ABSTRACT

Title of Document:	MAGNETIC DRUG TARGETING: DEVELOPING THE BASICS

Aleksandar Nacev, Ph.D., 2013

Directed By:	Associate Professor Benjamin Shapiro, Fischell Department of Bioengineering

Focusing medicine to disease locations is a needed ability to treat a variety of pathologies. During chemotherapy, for example, typically less than 0.1% of the drugs are taken up by tumor cells, with the remaining 99.9% going into healthy tissue. Physicians often select the dosage by how much a patient can physically withstand rather than by how much is needed to kill all the tumor cells. The ability to actively position medicine, to physically direct and focus it to specific locations in the body, would allow better treatment of not only cancer but many other diseases.

Magnetic drug targeting (MDT) harnesses therapeutics attached to magnetizable particles, directing them to disease locations using magnetic fields. Particles injected into the vasculature will circulate throughout the body as the applied magnetic field is

used to attempt confinement at target locations. The goal is to use the reservoir of particles in the general circulation and target a specific location by pulling the nanoparticles using magnetic forces.

This dissertation adds three main advancements to development of magnetic drug targeting. Chapter 2 develops a comprehensive ferrofluid transport model within any blood vessel and surrounding tissue under an applied magnetic field. Chapter 3 creates a ferrofluid mobility model to predict ferrofluid and drug concentrations within physiologically relevant tissue architectures established from human autopsy samples. Chapter 4 optimizes the applied magnetic fields within the particle mobility models to predict the best treatment scenarios for two classes of chemotherapies for treating future patients with hepatic metastatic breast cancer microtumors.

MAGNETIC DRUG TARGETING: DEVELOPING THE BASICS

By

Aleksandar Nelson Nacev

Dissertation submitted to the Faculty of the Graduate School of the

University of Maryland, College Park, in partial fulfillment

of the requirements for the degree of

Doctor of Philosophy

2013

Advisory Committee:

Associate Professor Benjamin Shapiro, Chair

Professor Elisabeth Smela

Associate Professor Silvia Muro

Assistant Professor Ian White

Dr. Michael Emmert-Buck

Dedication

To my parents who instilled within me the greater love for the pursuit of knowledge

by feeding my childhood mind with the strangely wonderful realities of the cosmos.

Acknowledgements

I would like to acknowledge the tireless work of my advisor Dr. Benjamin Shapiro for his guidance and support over my years at the University of Maryland.

In addition, I would like to thank my entire committee for their individual guidance and support during my doctoral studies, and for never refusing to answer a question of mine. Thank you Dr. Elisabeth Smela, Dr. Silvia Muro, Dr. Ian White, and Dr. Michael Emmert-Buck.

Lastly, thank you to all who have assisted in my research. Thank you Dr. Catherine Beni, Dr. Oscar Bruno, Skye Kim, Dr. Jaime Rodriguez-Canales, Dr. Michael Tangrea, Dr. Irving Weinberg, and Dr. Didier Depireux. Thank you to my fellow lab mates Dr. Roland Probst, Dr. Azeem Sarwar, Dr. Zhaolong Shen, Dr. Sandip Kulkarni, Zach Cummins, Bharath Ramaswamy, and Ryan Hilaman.

Table of Contents

List of Figures and Tables

Chapter 1:   Introduction

1.1   Overview

1.1.1   Introduction to Magnetic Drug Targeting

A need exists to be able to focus medicine to disease locations. During chemotherapy, for example, typically less than 0.1 to 1% of the drugs are taken up by tumor cells, with the remaining 99% going into healthy tissue [1], [2]. Chemotherapy encompasses treating patients with a diverse collection of drugs that attempt to preferentially destroy cancer cells either by inhibiting cellular division (which kills fast growing cancers, but also bone marrow, hair, skin, gut, and immune system cells) or by interrupting essential cell signaling pathways [3]–[8]. Physicians often combine drugs into chemotherapy cocktails that can compound side effects, and the dosage is usually selected by how much a patient can physically withstand rather than by how much is needed to kill all the tumor cells [3], [9], [10]. The ability to actively position medicine, to physically direct and focus it to specific locations in the body, would allow better treatment of not only cancer but other diseases [11]–[14].

Magnetic drug targeting (MDT) refers to the attachment of therapeutics to magnetizable particles, and then applying magnetic fields to concentrate them to disease locations such as to solid tumors, regions of infection, or blood clots [14]–[20]. Even though in some specialized cases the magnetizable particles can be introduced into the body outside the blood flow, e.g. as in magnetic treatment of the inner-ear where a small gel containing nanoparticles is placed on the round window membrane [21], [22] or intranasally [23],

[24], usually ferromagnetic particles are directly injected into the circulation by a vein or artery [11], [14], [25]–[32]. Particles so injected will circulate throughout the vasculature as the applied magnetic field is used to attempt confinement at target locations. Depending on the vessel into which the particles were injected (vein or artery), MDT will occur before the particles pass through the liver (first pass method [32]–[34]) or after the particles pass through the liver, lung and heart [14], [26], [35], [36]. The latter is more common, but reduces the drug amount available that can be targeted since a large portion of the drug is filtered by the liver and kidneys [11], [37], [38]. The goal of magnetic drug targeting is to use the reservoir of particles in the general circulation and target a specific location by pulling the particle and drug complexes using magnetic forces.

There are several other targeting techniques capable of directing therapy to desired locations. These include the use of magnetic fields [11], [12], ultrasound [39], [40], electric fields [41], [42], photodynamic therapy [29], [43], environment reactive targeting [44], and antigen recognition [45]–[49]. While this thesis focuses on magnetic drug targeting, it is important to note that there are synergies between these targeting techniques. Multifunctional particles capable of exploiting the benefits from each technique can be used to increase targeting ability. For example, transport of particles across the blood brain barrier using magnetic fields was assisted by first damaging the blood brain barrier using ultrasound [50]. Magnetic drug targeting could add specificity and improved therapeutic benefit if combined with other techniques.

Magnetic fields – more so than light, electric fields, and ultrasound [39]–[43] – are desirable for directing therapeutics inside patients because they can penetrate deep into the body, are routinely applied through the body in magnetic resonance imaging (MRI), and are considered safe even up to very high strengths (8 Tesla in adults, 4 T in children) [51]–[54]. Magnetic fields can both sense and actuate magnetic particles, although achieving both at once is an engineering challenge [55]–[57]. In contrast, light and ultrasound have limited tissue penetration depths [43], [58], [59], while strong electric fields (> 60 V/cm) are able to damage nerve and muscle cells [52], [60], [61].
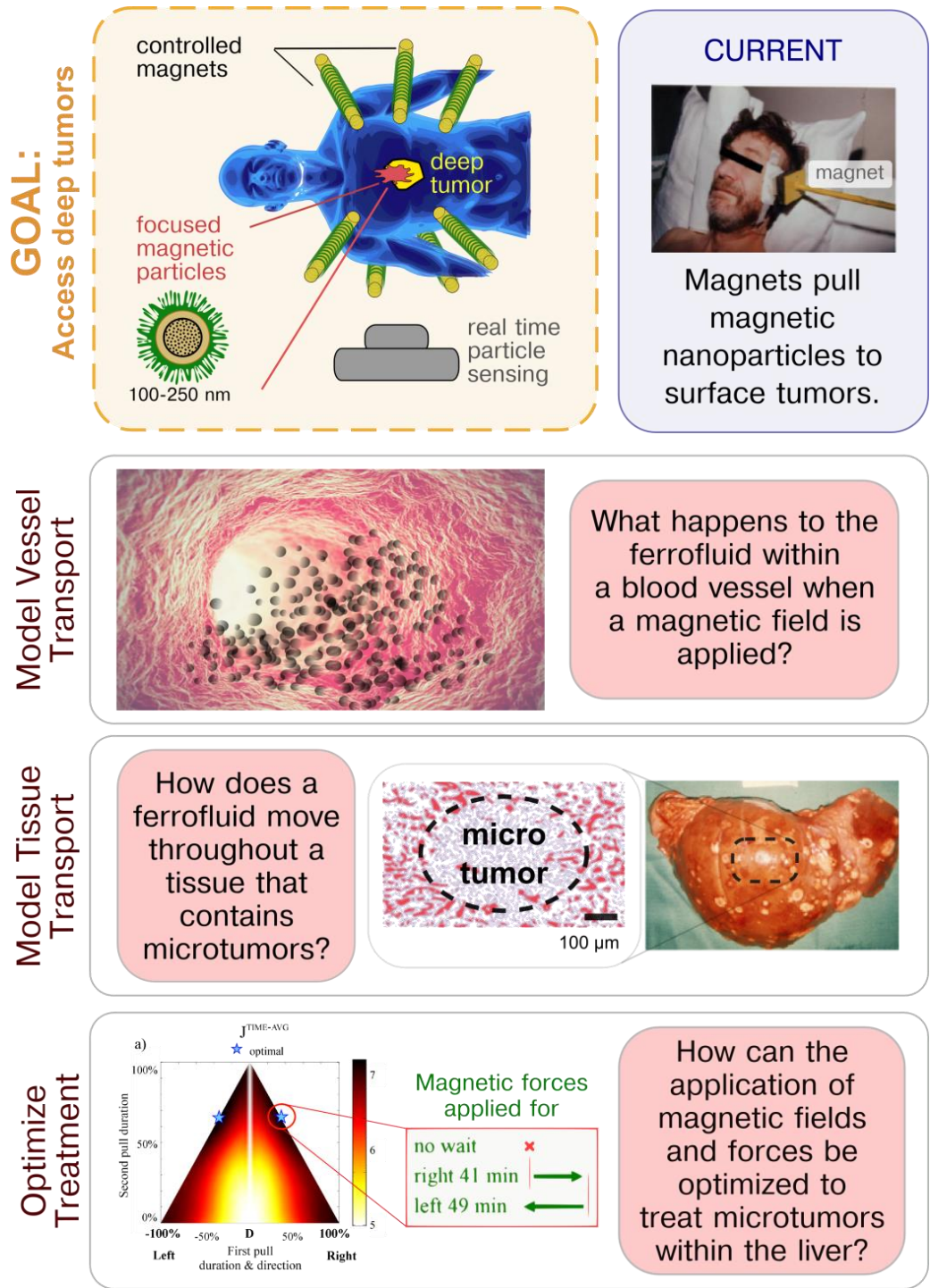
Figure 1: Overview of contributions presented. The ultimate goal of magnetic drug targeting is to direct therapeutics to disease locations deep within the body. The current state of the art still relies upon static magnets that are only capable of pulling magnetic nanoparticles to surface locations [14]. The three main contributions presented within this dissertation are the 1) modeling of ferrofluid transport within blood vessels, 2) within tissues, and the 3) optimization of a treatment scheme for hepatic metastatic breast cancer micro-tumors.

4

1.1.2 Applications of Magnetic Drug Targeting

Therapeutic magnetic elements have been created by the attachment of chemotherapy [3], [10] or gene therapy [62]–[64] to ferromagnetic particles [12], [13], [65]–[71], by filling polymer capsules or micelles (capsules that self-assemble from lipid molecules [72]) with both drugs and magnetic materials [71], [73], or by growing cells in a cell-culture medium with magnetic nanoparticles to let the cells ingest the particles and thereby become magnetic [74], [75]. A bare iron oxide nanoparticle is the simplest example of a magnetic carrier [76]. Magnetic particles can also consist of magnetite (Fe_3O_4) or maghemite (Fe_2O_3) nano-crystals embedded in a polymer core, and are usually coated with a layer of molecules (often starch or polyethylene glycol (PEG) molecules) to make the particles more biocompatible [68], [71], [73]. In more sophisticated particles, this coating is optimized to better hide the particles from the human immune system, so that the particles have a longer circulation time in the body before they are removed to the liver, kidneys, and spleen [71], [77]. Particle sizes can be controlled by various fabrication processes [68], [71], [78] and are made from nanometer to micrometer sizes.

They are usually injected into an animal or a patient as a ferrofluid, which is an emulsion of magnetic particles in water. Such magnetic nanoparticles have been tested in animals [12], [13], [26], [28], [31], [32], [34], [36], [50], [77], [79]–[107] and humans [16], [108]–[110]. Other entities besides particles – such as polymer capsules [111], flexible rods [96], lipid micelles [44], [112], [113], and live cells (such as stem cells) [74], [75], [114] – can also be loaded with magnetic materials and thus made magnetic. Stem cells are being magnetized so that they can be directed to regions of cardiovascular disease,

5

such as hardened blood vessels in diabetic patients, to help restore tissue function [75], [114]–[116], or to the retina for ocular regeneration [117]. All of these magnetized carriers, from nanoparticles to cells, can then be manipulated inside the body by externally applied magnetic fields. It takes a lot of development to ensure that magnetic carriers are safe, effective, and therapeutic [71]. Due to stringent regulatory approval requirements, so far only a few magnetic particles have been commercialized and approved for human use, and not yet as therapeutic carriers but only as imaging agents [118]–[121]. While magnetic particles have been used in clinical trials, the field of magnetic drug targeting is still new, and important information about the particles' biodistribution, especially while being targeted, is still unknown.

During magnetic drug targeting, magnetic carriers must be safely and effectively controlled inside the human body. The body consists of a heterogeneous and complex environment, which varies widely from person to person, and is not well understood. Many relevant and significant issues for effective control of particles remain unanswered, including uncertainty about the mechanisms of ferrofluid transport within the body, how nanoparticles can or cannot cross blood vessel walls, and how much force is required to direct them from blood into tissue. Similarly, there is a lack of knowledge of basic internal body parameters. The location of most blood vessels, the blood flow velocities in each vessel, the resistance of different tissue types to particle motion, and many other biological parameters are not known in general or for the case of each specific patient. Yet, even though the situation is highly uncertain, prior magnetic drug delivery has already been shown to effectively focus therapy to some desired locations in animals and

humans. For example, in the Lübbe 1996 phase I human clinical trials, a single permanent magnet was able to concentrate chemotherapy to inoperable but shallow (≤ 5 cm below skin depth) head, neck, and breast cancer tumors [14], [31], [122].

Since the success of the Lübbe trials [14], many groups have extended magnetic drug targeting for other applications. Pankhurst et al. has been targeting magnetically loaded mesenchymal stem cells to sites of vascular injury [114]. Häfeli et al. have used implanted magnets located behind the cornea to collect stem cells for retina regeneration [117]. Magnetic nanoparticles have been able to deliver therapeutics across the blood brain barrier when combined with ultrasound, which mechanically disrupts the blood brain barrier [50]. Due to the magnetic response characteristics of super paramagnetic iron oxide nanoparticles (SPIONs), there is a growing interest in using SPIONs for delivering thermal energy to tissue [16], [17], [84], [123]–[130]. This thermal application has been used to create targeted hyperthermia in prostate cancers [16], [110].

1.1.3   Challenges with Magnetic Drug Targeting

The depth, precision, and utility of magnetic targeting has been limited by particle material and surface properties [68], [71], by an insufficient understanding of particle transport in the human body [131]–[134], by the strength and design of magnets [51], [135]–[137], by a lack of deep-body real-time nanoparticle sensing capabilities [79], and by control algorithm development and implementation [138]–[140]. Magnetic nanoparticle fabrication and the resulting material and surface properties have been surveyed [12], [68]–[71], [141]. Essentially, material magnetization properties, χ, set the

strength of the magnetic forces for a given particle size and applied magnetic field [76], [96], [142]–[144], whereas surface coatings, particle size, and particle shape regulate biocompatibility and particle circulation times [12], [68], [71]. Understanding how various particle parameters impact ferrofluid transport is key, however, visualization techniques are currently limited. Real-time and sensitive measurement of nanoparticle distributions *in vivo* is challenging [16], [25], [68], even in small animals where depth of imaging is less of an issue [107], [128], [145], and has made it difficult to collect sufficient data to adequately validate models of ferrofluid transport.

Impossibility of a Stable Magnetic Trap

If it would be possible, the easiest, robust, and simplest way to implement magnetic drug targeting would be to create a magnetic trap. This would consist of some arrangement of magnets, either spatial or temporal, that pushes ferrofluid to one small concentrated region. Therefore, the patient would only have to be positioned properly underneath this magnetic trap to target a specific region within the body. Then over time, without the aid of a visualization technique, the ferrofluid would concentrate at a single site thereby increasing the drug concentration. This optimal scheme is unfortunately impossible for a collection of magnets and ferromagnetic/paramagnetic particles as shown by Samuel Earnshaw in 1839 [146].

Samuel Earnshaw's result on "the nature of molecular forces which regulate the constitution of the luminiferous ether" was read to the Cambridge Philosophical Society in March 1839, but was not printed until 1842 [146]. The result considers particles

attracted to each other by an inverse square law, and proves that "instability cannot be removed by arrangement (of the particles); for though the values of $d_f^2 V$, $d_g^2 V$, $d_h^2 V$ depend upon the arrangement of the particles, the fact that one at least must be positive and one negative depends only upon the equation $d_f^2 V + d_g^2 V + d_h^2 V = 0$, which is true for every arrangement. And consequently, whether the particles be arranged in cubical forms, or in any other manner, there will always exist a direction of instability." Earnshaw's function V is the potential energy of a single particle being attracted by many others. The proof proceeds by showing that the equation for V is "that of an hyperboloid" (a saddle), with the result that the sum of its three second derivatives must equal zero. Even if two derivatives are negative (corresponding to particle stability in a plane), the third derivative must then be positive (instability along a line).

Earnshaw's result equally applies to nanoparticles in a magnetic field. Although nanoparticles do not attract each other strongly, the potential energy created by an imposed magnetic field is also, at best, an energy saddle. It is not possible to create an energy well between magnets, no matter how they are arranged.

This result has implications for magnetic drug delivery; no arrangement of magnets can create an energy well between them to focus ferromagnetic particles to an interior target. Diamagnetic particles could be focused, in principle, but diamagnetism is six orders of magnitude weaker than ferromagnetism ($\chi \sim -10^{-5}$ instead of +20) and the forces created would be too tiny to move particles against tissue or blood resistance. Even if sufficient forces could be created on diamagnetic particles, the susceptibility of human

tissue is similar to that of diamagnetic materials in particles ($|\chi| \approx 10^{-6} - 10^{-4}$) [11] but its volume is far greater; thus the tissue would experience orders of magnitude greater forces than diamagnetic nanoparticles, which would harm patients. Thus Earnshaw's 1839 theorem, which shows that no static magnetic field can focus ferromagnetic particles to an interior target, remains a key and fundamental limitation for magnetic drug targeting. The solution is to bypass the assumptions of the theorem, for example, by introducing feedback control and varying the magnetic fields in time and space to control ferrofluid dynamics.

1.2 Physics of Magnetic Drug Targeting

1.2.1 Magnetic Fields and Forces Acting upon a Particle

Magnetic nanoparticles are small and experience small forces even under strong magnetic fields. In prior magnetic drug delivery experiments, magnet strengths have ranged from 70 milli-Tesla [142] to 2.2 Tesla [147], and corresponding magnetic gradients have varied from 0.03 T/m [148] to 100 T/m [86], a range that reflects magnet cost, complexity, safety, and ease-of-use versus desired (or possible) depth of targeting. For comparison, modern neodymium-iron-boron ($Nd_{12}Fe_{14}B$) permanent magnets can be purchased in strengths of up to 1.48 Tesla [149], [150] and the electromagnets used in magnetic resonance imaging systems create fields of 1 - 4.7 T, with some commercially-available MRI systems going as high as 9.4 T [51], [79]. In the 1996 human trials, 0.2 - 0.8 T permanent magnets were used to target 100 nm diameter particles to 5 cm depths [14], [31]. Targeting depths of up to 12 cm have been reported in animal experiments using larger 500 nm to 5 μm diameter particles and a 0.5 T permanent magnet [32]. Both

permanent and electromagnet designs can be optimized to extend magnetic fields and gradients further out, to increase the depth of magnetic forces.

1.2.2   Directing Magnetic Particles

Precision magnetic control of a single object has been demonstrated in animals and humans. Gentle magnetic manipulation of a rigid implanted permanent magnet through the brain, with a view to scan and burn out brain tumors by subsequently heating the magnet using RF (radio-frequency) magnetic fields, has been presented [151], [152] and tested in dogs [153]. Based on market opportunities, the focus of this effort changed to magnetically assisted cardiovascular surgical procedures and led to the founding of Stereotaxis (www.stereotaxis.com). This company now uses magnetic control to guide catheters, endoscopes, and other surgical tools with magnetic tips for precision treatment of cardiac arrhythmias and other cardiovascular procedures [154]–[156]. To date, Stereotaxis has carried out over 40,000 successful patient procedures in nearly 200 facilities around the world. Systems to magnetically steer implantable devices and microrobots, for gut, eye, cardiac, endovasculature, and lung surgery [157]–[164] have been tested in pigs and chicken embryos [165]–[168]. Conventional MRI machines have also been used as the control system to manipulate microscale particles [98], [158], [169]–[172], as well as magnetotactic bacteria [140], [173] or magnetized cells [116], [174]–[176], in pigs and mice [170], [174]. While MRIs are attractive due to their magnetic strength and clinical availability, the difficulty is that MRIs are designed to create a strong uniform magnetic field, but spatially varying magnetic fields are required to create forces on particles. Unless the MRIs are substantially modified [177]–[179],

they do not create sufficient magnetic spatial gradients to effectively manipulate nanoscopic particles. The control algorithms used in the above single-object manipulation systems have ranged from PID [158], [167] to point-wise optimization [151], [152], least-squares inversion [180], robust nonlinearization with backstepping [172], [181], a generalized predictive controller [171], and model predictive control [182].

Precise manipulation of a fluid of nanoparticles is more difficult than control of a single object. In prior ferrofluid trials, a magnet held outside the body drew in and concentrated particles to shallow breast, head and neck, and brain tumors [14], [17], [26], [31], [34]–[36], [50], [68], [80], [85], [94], [99], [100], [102], [105], [106], [109], [183], [184] (Figure 1b). There was no dynamic magnet control and the magnets accumulated the particles to targets beneath the skin or skull. Implantation of magnets or magnetic material into patients, such as within blood vessel walls, has been suggested as a way of reaching deeper tissue [87], [91], [97], [185]–[193]. The implanted materials serve to locally increase magnetic field gradients, and thus forces, when an external magnetic field is applied. Such a treatment envisions bringing magnetized endothelial cells to blood vessel walls and could also be appropriate for treating tumors that cannot be surgically removed but when magnetizable implants can be inserted into or near the tumor [87], [97], [185]–[187]. Overall, although the field of magnetic drug targeting is advancing towards commercial particles approved for human use [16], [115], [118]–[121], it remains open for significant improvements in modeling, design, and control, especially for non-invasive methods to effectively target deeper tissue. This dissertation takes the next step in developing the basics for magnetic drug targeting: 1) how can

magnetic drug targeting be properly modeled and designed for any situation; 2) how can magnetic drug targeting be correctly modeled and designed for the specific treatment of hepatic metastatic breast cancer.

1.3 Prior Work

1.3.1 Prior Modeling

Particle Targeting Models

The current state of magnetic drug targeting modeling has typically been limited to individual particle dynamics within the blood or to fluid dynamics within a single impermeable vessel. Rosensweig began the theory of magnetic drug targeting by investigating the forces acting upon a single magnetic entity (either a particle or magnetic bolus) [194]. This was further investigated and extended to capture efficiency in various vessels for a single object [36], [106], [131], [195]. The basis of these modeling schemes rely on comparing magnetic force to blood drag forces. All of these models lack modeling extravasation or membrane-tissue dynamics in addition to ignoring diffusion characteristics. They only model the magnetic and blood forces and not the movement of particles through vessel walls or membranes. This, however, is a major component in drug targeting since the particles must leave the vessels and enter tissue, to deliver therapeutics within tissue.

Particle Mobility Models

The partial differential equations for the time dynamics of nanoparticle concentration are stated in Section 3.4, and there the particle movement for any condition is described. However, the specific movement that occurs in a given organ or biological environment is completely dependent upon the parameters of that biological space. Chief among these biological parameters is the diffusion coefficient of the tissue and how it depends upon size. The following is the Brownian diffusion equation

(1) $\quad D_B = \frac{k_B T}{6 \pi \eta a}$

that relates the diffusive flux to the concentration gradient of the particles [37], [38], [131], [196]. Here k_B is the Boltzmann constant, T is the absolute temperature, η is the fluid viscosity, and a is the particle radius. While equation (1) does describe the diffusion coefficient as a function of particle size, it is only relevant for fluids and not tissues where the interstitial spaces can further inhibit particle diffusion and potentially mobility. In addition, the size dependence of the diffusion of particles through tissues is not a simple inverse relationship but instead exhibits behavior consistent with cut-off thresholds [37], [38]. This change in passive diffusion of a particle as it traverses between blood and tissue is described by an effective diffusion coefficient, which is the ratio of diffusion within the tissue to that within blood. This effective diffusion coefficient can then extend to approximate the relationship between the mobility of the particles as they traverse through tissue (see equation (7)). There have been many models to describe the decrease in the particle diffusion coefficient including the Renkin pore model [37], [38], [197] and the fiber-matrix model [37], [38]. These models, however, were developed for

small molecules (less than 100 nm) and do not accurately describe large particle diffusion.

The two classical models to approximate particle diffusion through tissues that will be described next are: 1) the Renkin reduced coefficient model [197]; and 2) the fiber matrix model [198]. These models examine nanoparticle movement through tissues or membranes, but they do not deal with the how the particles arrived within the tissue space. If the particles are within the circulatory system, then they must be able to extravasate and enter the tissue before these models are applicable. If the vessels within the target tissue do not have pores or there is no active transport, then the mobility through tissues is not applicable. While they have limitations, they still provide valuable insight into nanoparticle behavior when within tissues.

Renkin Reduced Diffusion Coefficient Model

(2) $\frac{D_e}{D_B} = (1 - \alpha)^2 \left(1 - 2.1044\alpha + 2.089\alpha^3 - 0.948\alpha^5 \right), \quad \alpha = \frac{a}{r_{pore}}$

(3) $\frac{D_e}{D_B} = K(\alpha) \times \omega_r(\alpha)$

The Renkin equation (equation (2), where D_e is the effective diffusion coefficient, and r_{pore} is the pore radius) approximates the apparent diffusion of a molecule attempting to travel through a membrane with a specific pore size. It was derived from a theoretical model [197] and only depends upon the particle radius and the average pore size of the membrane. Equation (3) rewrites the Renkin equation for simplicity. Equation (3) has two components. The first term, $K(\alpha)$ (first component on the right hand side), is a measure of how much the size of a pore 'excludes' a particle from entering. If the particle

or solute is already within the membrane, then $K(\alpha) = 1$. The second term on the right hand side, $\omega_r(\alpha)$, is a measure of the movement once the particle is within a membrane's pore and accounts for the increase in hydrodynamic drag as the particle moves through the membrane.

These equations are consistent with measurements made by Beck and Schultz [199] who constructed membrane sheets with well-defined pore sizes and near unity tortuosity. These membranes allowed for careful measurements of the diffusion through the membranes for various solutes ranging from 0.52 nm to 4.3 nm. While the results supported the Renkin equation, they were not able to investigate larger pore sized membranes that would be consistent with some biological membranes and structures (i.e. the glomerulus of the kidney) [199].

For the considered treatment case of the liver, pore sizes of the fenestrated capillaries found in the livers of humans have been measured on the order of 120 nm in diameter ([200]) to several microns ([38]). Assuming the smallest pore size is similar to the spaces within the extracellular matrix and a 100 nm diameter particle, the effective diffusion coefficient within the liver would be on the order of $0.07\,D_B$, an order of magnitude lower than that in blood.

There have been several further extensions on the Renkin equation. Deen et al. extended the equation to include tortuosity and for larger particles. The reduced diffusion coefficient introduced is as follows:

(4) $\quad \frac{D_e}{D_B} = \left(\frac{A_P}{S}\right)\frac{K\omega_r}{\tau} = \frac{\varepsilon}{\tau}K\omega_r$

where A_P is the pore surface area, S is the total membrane surface area, τ is the tortuosity, and ε is known as the porosity or the void volume fraction of the membrane [37], [201]. The tortuosity term is defined as the diffusion path length divided by membrane thickness [37], [38], [199]. It is a measure of the amount of additional movement a particle has to travel once inside a tissue or membrane to reach the opposing end. If the tortuosity term is large, then the particle has to traverse pores that are long winding channels. If the term is near unity, than the channels instead are straight passageways through the membrane or tissue.

Equation (4) shows another method of calculating the effective diffusion coefficient for a given tissue and particle type. However, it requires knowledge of three crucial tissue parameters: 1) the porosity of the tissue; 2) the tortuosity; and the 3) tissue pore size. The later has been estimated for several types of tissues a measure of the extracellular spaces of the tissue. However, the first two are not known for tissues that are not engineered with specific characteristics, limiting its usage.

Fiber Matrix Model

Another method of describing the diffusion of a solute through a tissue is the fiber matrix model. This model (developed in [198]), extends upon a model by Ogston [202]. It assumes that the tissue space contains a given concentration of long cylindrical fibers with a radius of a_f. From this assumption the following equation can be written

17

(5) $\quad \frac{D_e}{D} = \exp\left[-\left(1+\frac{a}{a_f}\right)v^{1/2}C_F^{1/2}\right] = \exp\left[-\left(1+\frac{a}{a_f}\right)\phi^{1/2}\right],$

where v is the specific volume of the fibers, and C_F is the fiber concentration, and ϕ is the volume fraction. Since this model starts with the assumption of long cylindrical fibers comprising the tissue architecture, it has the potential to better approximate the tissue properties.

The parameters in equation (5) can be estimated based upon collagen content in various tissues. Most tissues have a discretized preferred fibril diameter at 11 nm increments (11, 22, 33, 44, 55, etc. [203], [204]) and the collagen content and function are intertwined. For example the cornea has approximately a fiber diameter of ~ 20 nm with a very organized structure ensuring opacity, compared with the larger fiber bundles in tendons of ~ 500 nm providing structural support [203]. Continuing with the treatment case of liver, volume fractions have been measured in human livers to be on the order of 0.7 [205] with measured fibril diameters between 0.2 to 5 μm [206]. Considering a 100 nm diameter nanoparticle, the worst case effective diffusion coefficient would be 0.29 D_B, approximately an order of magnitude less than the diffusion coefficient in blood. This value for the effective diffusion coefficient is similar in magnitude to what is predicted from the Renkin pore model.

Limitations of Mobility Models

These two theoretical models have been compared to experimental measurements of small molecule diffusion. Nugent et al. [207] compared these two models with measured diffusivities of small molecule solutes in normal and tumor tissue. However, the main

18

limitation in utilizing these or other models predicting particle movement is the size choice of the solutes tested. Most experimental studies have only examined solutes below 10 nm [37], [197], [199], [207], [208]. As magnetic nanoparticles can be orders of magnitude larger than this, it is invaluable to know specifically how these larger particles will move through tissue.

Another more subtle limitation of these and previous models of particle motion is the assumption made linking the decrease in diffusion coefficient to the decrease in the magnetic drift coefficient. The magnetic velocity (described more fully later in equation (14)) is

(6) $\quad \vec{V}_R = k \nabla \left(|\vec{H}|^2 \right),$

where the magnetic drift coefficient, k, describes the mobility of the magnetic nanoparticle under an applied magnetic field, $\vec{H}$, in a certain fluid. Einstein's relation suggests that any physical barriers, such as membrane pores, that impact particle diffusion will also equivalently impact particle mobility [37], [38]. This would be represented by the following equation:

(7) $\quad \dfrac{D_e}{D_B} = \dfrac{k_e}{k}$

where k_e is the effective magnetic drift coefficient. However, this analogy considers only passive motion of the particles. It does not include the ability to exert an external force upon the magnetic nanoparticles and thus deforming the surrounding tissue space. While the tissue architecture might create barriers to particle motion, it is conceivable that the magnetic forces could pull the particles through a weakly formed extracellular matrix.

This would negate the assumption described in equation (7) as the effective magnetic drift coefficient could be much greater than approximated.

There are limitations and caveats to the above two models, however, absent relevant experimental measurements, they are the best current methods to approximate nanoparticle movement through tissues.

1.3.2 Animal and Clinical Trials

While magnetic nanoparticles have been approved for use in patients for MR imaging agents [118]–[121], there have been a limited number of clinical trials involving magnetic drug targeting. Most notably, Lübbe et. al have performed simplistic targeting with magnetic nanoparticles (from Chemicell GmBH) conjugated with doxyrubicin in clinical trials involving several patients with inoperable facial tumors [14]. There have been only a few patient trials since that have either involved using the magnetic field outside of an MRI to target nanoparticles [109], [209], or using nanoparticles as thermotherapy [16].

There are, however, a multitude of MDT experiments performed *in vivo* in animals. These range from dogs [28], hamsters [91], [95], mice [84], [86], [89], [104], rabbits [26], [80]–[83], [98], [103], [105], rats [31], [36], [50], [85], [87], [90], [94], [97], [99], [100], [106], sheep [102], to swine [32], [34]. These have progressed the development of MDT, however, they still rely on static magnetic fields to concentrate particles at a desired 'surface' location. This introduces targeting limitations and reduces the potential benefit

of MDT. By applying a closed-loop feedback strategy, the particles can be specifically targeted at a designated region deeper within the body able reach sites greater than 5 cm depth (the current limitation in human trials [14]).

1.4   Contributions Presented

This dissertation adds three main advancements to the magnetic drug targeting field. 1) The creation of a comprehensive ferrofluid transport model within any vessel, membrane and tissue space under an applied magnetic field verified by available published works. 2) A ferrofluid mobility model used to predict ferrofluid and drug concentrations within physiologically relevant histological samples from human autopsies. 3) An optimization of applied magnetic fields using the particle mobility models to predict the best treatment scenarios for two classes of chemotherapeutic drugs.

1.4.1   Blood Vessel Simulations

There are two categories of forces acting upon magnetic particles as they traverse throughout the body: those that are induced; and those that are a consequence of the environment. In the first, the magnetic force generated by an external magnetic field pulls particles towards the magnet creating a resultant drag force resisting this motion [194], [210]. In the second, the biological system transports particles through the blood and scatters particles as they interact with red blood cells [131]. Starting with physical first principles, Chapter 2 predicts the possible ferrofluid behaviors that can occur within any given blood vessel with any surrounding tissue space. Very few assumptions of

nanoparticle characteristics were made and the developed model encompassed the entire space of what is experimentally and biologically feasible (see Table 1).

By accurately describing the forces acting upon a magnetic nanoparticle and starting with physical first principles, the transient concentration of nanoparticles is described within a blood vessel including the surrounding tissue by a set of equations. Using these equations and custom finite element solver built in collaboration with California Institute of Technology, the entire realistic parameter space is exhaustively surveyed uncovering three fundamental magnetic nanoparticle behaviors: magnetic dominated; velocity dominated; and boundary layer formation. The behavior of a ferrofluid within a blood vessel and tissue was determined to be governed by only three non-dimensional parameters. These behaviors remain even as the constraints upon the simulation are relaxed. Therefore, an experiment can be correctly designed to create a desired magnetic nanoparticle behavior.

1.4.2 Tissue Simulations

While an open loop trap cannot exist (see section 1.1.3 where Earnshaw's theorem is discussed), open loop control still can be used for specific treatment scenarios. Metastatic breast cancer often results in hundreds of micro-tumors in a patients' liver. Contrary to primary tumors, these metastases often have low blood perfusion and chemotherapy often cannot accumulate to therapeutic levels within these micro-tumors [211]. These untreated tumors lead to cancer reoccurrence. Chapter 3 introduces a new method by which to equalize chemotherapies throughout the liver parenchyma (the functional tissue of the

liver). This method, coined dynamic magnetic shift (DMS), uses external magnetic fields to pull chemotherapy loaded magnetic nanoparticles throughout the liver.

Our collaborators at the National Cancer Institute started with histological patient data from NIH autopsy studies of terminal breast cancer patients. They then stained and marked the liver sections for blood vessels and cell nuclei. Using these histological sections, we took blood vessel density measurements to characterize the blood vessel population of either normal or tumor tissue. These measurements confirmed the existence of small micro-tumors containing fewer blood vessels compared to the surrounding normal tissue. It is these micro-tumors that are problematic for treating with chemotherapeutic agents. Therefore the treatment target for DMS was aimed at improving the drug concentrations throughout these micro-tumors.

To understand and quantify how DMS will improve the drug concentration within these micro-tumors, we created a ferrofluid transport model through tissue architectures. This model utilized the blood vessel distribution from actual autopsy sections and focused the treatment target on the problematic micro-tumors. By comparing the ferrofluid distribution that would occur naturally due from diffusion to the distribution from applying shifting magnetic fields, the potential therapeutic increase in ferrofluid concentration was determined. By using magnetic shift, the concentration of ferrofluid within these small micro-tumors increased by $> 86\%$ on average compared to natural diffusion.

1.4.3 Optimization of Dynamic Magnetic Shift

Chapter 3 introduced the idea of DMS and quantified the potential impact that the treatment scenario could have on the micro-environment of metastatic breast cancer within the liver. However, while the benefit was significant in Chapter 3 (> 86% improvement over diffusion), the question remains if we can improve it. What combination of transient magnetic fields would be the best to pull the ferrofluid throughout the liver to achieve therapeutic treatment goals?

Chapter 4 examines the optimal parameters necessary to deliver the ferrofluid throughout the liver architecture. The therapeutic treatment goals were defined for two classes of chemotherapeutic agents: 1) those drugs that only act during a specific phase of the cell cycle and must therefore be available for the cells as long as possible; and 2) those drugs that are insensitive the current phase of the cell cycle. These two goals led to the development of two distinct metrics to quantify the benefit a specific treatment scheme has upon the tissue architecture.

Using these two metrics as a way to compare the treatment scenarios, the optimal treatment was determined for shifting in two-directions by exhaustively simulating the various treatment scenarios. Not only was the optimal treatment searched over the direction of magnetic movement, but 140 micro-tumor cases were examined from 16 patients. Lastly, the robustness of these optimal treatment schemes was tested as the mobility parameters of the ferrofluid were relaxed. The robustness experiments examined the method by which the optimal treatment schemes change as the particles decrease in

tissue mobility. This optimal control scheme can then be used as a technique for treating metastatic breast cancer present within the liver for future patients.

Chapter 2: Modeling Magnetic Nanoparticle Transport through a Blood Vessel under an Applied Magnetic Field

This work originally appeared in [212] *and* [213].

This work was done in collaboration with Catherine Beni and Oscar Bruno from the California Institute of Technology. They developed the finite element solver, termed the vessel-membrane-tissue (VMT) solver, used to solve the model. I created the VMT model, and identified and investigated the treatment space. Lastly, I used prior experimental studies to validate the model.

2.1   Introduction

Magnetic drug targeting refers to the attachment of therapeutics to magnetizable particles, and then applying magnetic fields to concentrate them to disease locations such as to solid tumors, regions of infection, or blood clots [11], [12], [18], [25], [108], [134], [142], [214]. In some cases, however, the magnetizable particles can be introduced into the body outside the blood flow, e.g. as in magnetic treatment of the inner-ear where a small gel containing nanoparticles is placed on the round window membrane [21], [22], [215], usually ferromagnetic particles are injected into a vein or artery [11], [108], [25], [26], [80], [28]–[31], [14], [125], [216], [192], [102], [109], [106]. Particles so injected will circulate throughout the vasculature as the applied magnetic field is used to attempt confinement at target locations. Two main considerations arise from the *in vivo* use of these particles. First, the particles must be small enough to make it out from the blood vessels into surrounding tissue (they should be no larger than approximately $400 - 600$ nm to extravasate out from even 'leaky' tumor vessels [11], [37], [38], [133], [216],

26

[217]), and, more subtly and crucially, they must be small enough to have sufficiently long *in vivo* residence times (larger particles are removed faster by the mononuclear phagocyte system; in human clinical trials [30], [108] Chemicell's 100 nm particles were shown to have 30 min plasma residence times). Second, the magnetic force on these small particles is minimal. Magnetic force scales with particle volume [194], decreasing the size of a particle by a factor of 10 decreases the magnetic force on it by 1000. Even with strong magnetic fields (> 1 Tesla) and high magnetic gradients ($\approx$ 0.5 T/cm), the forces on ferro-magnetic nanoparticles remain extremely small, in the range of pico-Newtons [194], [218], [219].
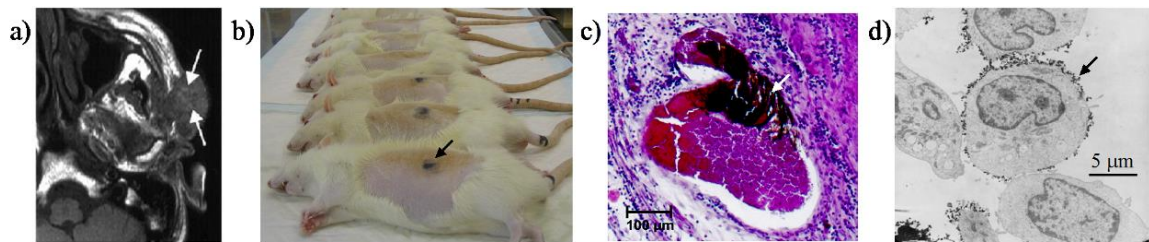
Figure 2: Verification of magnetic drug delivery from the body to the cellular scale in animal and human clinical trials. a) Magnetic resonance (MR) image for a cancer patient, magnetic nanoparticle (ferrofluid) accumulation can be seen as lighter regions at the arrow tips (due to the MR extinction phenomena [53]) [14], [30], [31], [108], [209]. b) Rat studies: concentrated ferrofluid is visible under the skin [31], [220]. c) Ferrofluid concentrated in rabbit tumor micro-vessels (white arrow) [26], [35]. d) Magnetic nanoparticles at the membrane of mouse epithelial cells (e.g. black arrow) [221].

Thus a key issue in magnetic drug delivery is whether the applied magnetic forces can compete with convective blood (drag) forces that tend to wash particles away. The questions are: can particles be confined to target regions against blood flow? In which blood vessels and where do they concentrate? How deep within the body can targeting occur? Past animal experiments [21], [26], [28], [31], [32], [34], [36], [50], [80]–[87],

[89]–[92], [94], [95], [97]–[106], [222] and phase I human clinical trials [14], [31], [109], [209] have observed the accumulation of magnetic nanoparticles by visual inspection, magnetic resonance imaging, and histology studies. These have shown that magnetic forces can concentrate micro- and nanoparticles *in vivo* near magnets, but the details of that concentration cannot be seen experimentally. MRI and visual inspection do not have the resolution to show in which vessels magnetic forces have exceeded blood drag forces, and they certainly cannot show where in the vessel accumulation is occurring. Equally, histology studies are carried out after the animal has been sacrificed and blood flow stopped; they speak only partially to where in the blood vessels the particles might have been. Thus, in this chapter, we address this issue via simulations. We map the parameter space and characterize what should happen in an idealized blood vessel in terms of applied magnetic force strength and blood flow velocity. Our goal is to forecast and characterize the type of behaviors that will occur.

We note that the usual back-of-the-envelope analysis is not sufficient; it does not predict what is observed experimentally. Consider the rat experiments shown in Figure 2b. Here our collaborators (Lübbe and Bergemann) used a 0.5 Tesla, 5 cm long, 5 mm wide permanent magnet to focus 250 nm diameter iron-oxide nanoparticles. Even for a particle at a distance of just 1 mm away from the magnet (just below skin depth), the magnetic force on this particle (see equation (11) and [194], [218]), including the effect of particle magnetic saturation and using an exact solution [223] for the magnetic field around the magnet, is only about $\approx 1 \times 10^{-13}$ N. By comparison, the Stokes blood drag force [224] on the same particle, for the slowest measured 0.1 mm/s blood-flow velocities in rat

capillaries [225]–[227], is $\approx 7 \times 10^{-13}$ N, a factor of $\times 7$ greater. This simple comparison suggests that the field gradient near the magnet cannot capture a 250 nm particle against even the weakest blood flow in a rat. Yet in Figure 2b the dark spots where the particles have been focused can be clearly seen. This focusing was carried out while the rats were alive and their blood was flowing, and it has been repeated even with 100 nm diameter particles where the magnetic forces are $2.5^3 = 15.625$ times smaller. Clearly, a crude comparison of magnetic forces per particle to Stokes drag is insufficient to match *in vivo* behavior. This mismatch is also apparent in the literature both for *in vitro* and *in vivo* experiments. In *in-vitro* studies (eg. [106], [228]), particles were focused even when centerline stokes drag forces exceeded magnetic forces. In the *in vivo* cases (eg. [26], [36], [95]), Stokes drag due to the slowest blood flow in the animals/humans exceeded maximum magnetic forces yet particle focusing was still observed.

The rough calculation above is deficient for two main potential reasons. 1) The blood flow drag forces on the particle vary with its position in the blood vessel. A particle at the vessel center-line will experience a higher blood velocity and hence a higher drag force, but a particle near the blood vessel wall will be surrounded by a near zero blood velocity. This decrease in velocity is due to the flow resistance provided by the vessel wall, the 'no-slip' boundary condition [38], [229], [230]. Thus a particle near the vessel wall will experience a much smaller drag force and can potentially be held by a much smaller magnetic force (see Figure 3, this effect is also noted in [219] for micro-channels). Alternatively 2) the particles might agglomerate to some degree even though they are typically engineered to minimize agglomeration [11], [12], [216]. This will increase the

magnetic force, which grows with volume, much faster than the Stokes drag, which grows with diameter, thus increasing trapping. In this chapter, we will focus on examining the first issue in detail, as it is the next crucial question. Item 2) is addressed approximately by considering an agglomerated clump as simply a larger 'super-particle' (see Section 2.15.5). Consideration of agglomeration thus folds into our non-dimensional numbers for size and force (discussed in Section 2.8.1). A more sophisticated, analysis of agglomeration will be carried out in future work.

This chapter focuses on systematically characterizing the behaviors of ferromagnetic nanoparticles in a single idealized blood vessel under the action of an applied magnetic force, blood drag, diffusion within the blood, and transport of particles from blood to surrounding tissue (modeled simply as diffusion, as in [37], [38]). It includes an ability to predict what happens in shallow and deep, small and large blood vessels, and it resolves the mismatch between experiments and the usual, but simplistic, back-of-the-envelope centerline Stokes drag versus magnetic force calculation described above. It is organized from the simplest scenario to cases that include added features such as spatially varying magnetic forces, blood pulsatility, curved vessel geometry, and skin boundary conditions. These added features do not qualitatively change the three types of nanoparticle behaviors observed: blood velocity dominated, magnetic force dominated, and boundary layer formation regimes. In addition, we do not consider cases where the concentration of ferromagnetic nanoparticles is sufficiently high to obstruct the flow within a blood vessel. We find that the observed nanoparticle concentration behavior in *in-vitro* and *in vivo* studies is correctly predicted by a single three-parameter non-

dimensional map (Figure 9 and Figure 11) that delineates the blood velocity dominated, magnetic force dominated, and boundary layer formation behaviors. Our summary result is simple to use and will enable a more systematic design of future magnetic *in vivo* drug delivery systems.

Simulating ferrofluid behavior, even in a single straight vessel, is challenging. We created an in-house vessel-tissue-membrane (VMT) numerical solver based on the Alternating Directions Implicit (ADI) method [231]–[234]. The VMT solver was both more accurate and 500 times faster than COMSOL (a general-purpose commercially available partial differential equation solver often used in the magnetic drug delivery literature, e.g. [228], [235]), and it was able to solve cases that COMSOL could not (see Section 2.8). Using VMT we were able to solve all cases, though the most challenging cases still took a long time (the case of mass Péclet number equal to 1×10^8 in Section 4.3 took 48 hours). There are ways to further improve VMT to make these cases run much faster and this will be reported in future publications as part of our effort to create a general-purpose fast and accurate simulation environment for magnetic drug delivery.

The current study is essential to better forecast what happens *in vivo* in shallow and deep blood vessels under varying circumstances. Our modeling is the next needed major step: it goes beyond a naive back-of-the-envelope calculation but is still tightly focused on the issue of blood convection versus magnetic forces. It necessarily cannot include all the complex details of magnetic particle phenomena *in vivo*, because much of that behavior is still not well understood at a physiological and physical level and therefore cannot yet be

quantified mathematically. For example, extravasation [11], [37], [38], [133], [216], [236]–[238] is an active research field in its own right and the mechanisms that drive it are not yet fully known or characterized. Since extravasation cannot be included in detail at our level of modeling, we represent it here by a diffusion term (from blood to tissue) that is folded into the effective diffusion coefficient (as is done in [37]). Even with this limitation, our model still provides accurate and effective results that are hard to attain any other way. It is necessary for our larger effort to design controllers that will achieve deep tissue magnetic drug targeting [218], [239]–[241], and its ability to simply but accurately predict *in vivo* behavior will aid the research efforts of the broader magnetic drug delivery community.

2.2   The Three Parameters

We consider the scenario of a single blood vessel with an inflow of blood and ferro-magnetic nanoparticles that are actuated by an externally applied magnetic force. We find that the nanoparticles exhibit three distinct and specific behavioral patterns: either velocity dominated (they are washed out of the back of the blood vessel), magnetic force dominated (magnetic forces overcome the blood vessel membrane and surrounding tissue barriers), or they form a boundary layer at the blood/tissue interface. Three non-dimensional numbers are required to determine which behavior is occurring. These three numbers are:

The Non-Dimensional Magnetic Force Strength (the Magnetic-Richardson Number): This number quantifies the ratio between the applied magnetic force and the

32

blood Stokes drag at the vessel centerline. When this number is greater than unity then the magnetic force is larger than the blood Stokes drag force at the vessel centerline.

The Renkin Reduced Diffusion Coefficient: This quantifies the ratio between diffusion in the blood vessel membrane and diffusion in the blood. If this number is smaller than unity then particles in the blood vessel membrane diffuse much slower than the same particles in blood.

The Mass Péclet Number: This number quantifies the ratio between the maximum centerline blood flow velocity times the average blood vessel width to the total particle diffusion coefficient. When this number is much greater than unity then particle convection occurs much faster than diffusion across the blood vessel width.

2.3   Domain Geometry

Figure 3 shows the model geometry: an idealized straight blood vessel contained by an endothelial layer next to an underlying tissue layer. This geometry is a simplified version of the Krogh tissue cylinder [37]. Similar to the Krogh cylinder model, the tissue space is a region between adjacent vessels and the model only applies to capillaries because it does not incorporate a vascular muscle layer. This restriction, however, can be relaxed by substantially lowering the diffusion coefficient of the membrane layer (see section 2.15.1) thus better approximating non-capillary vasculature. The vessel has an inlet at the left-hand side and an outlet at the right-hand side. Blood and a constant concentration of

ferro-magnetic nanoparticles enter from the left. A magnet is held below the blood vessel

and creates a downwards magnetic force.
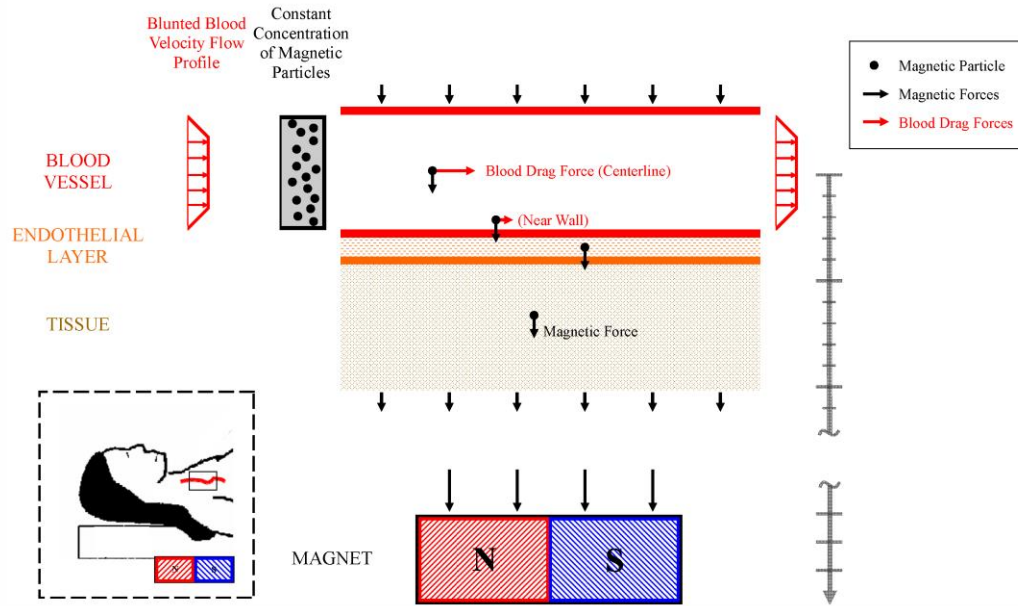
Figure 3: The simulated blood vessel geometry. The blood vessel is idealized as a straight channel. Blood and a constant concentration of magnetic nanoparticles enter from the left. The magnetic particles (black circles) within the blood vessel experience diffusion, migration under blood flow, and magnetic forces. Magnetic particles in the surrounding endothelial and tissue layer experience diffusion and magnetic drift but no blood flow forces. The magnet can be a long distance from the blood vessel (deep targeting) and here this is denoted by the break in the length bar on the right of the figure. Inset: The simulated domain around a blood vessel in deep tissue.

2.4   Governing Forces

We consider the three main forces acting upon the ferro-magnetic nanoparticles. These

include blood advection forces induced by blood plasma convection [37], [196], [224],

magnetic drift induced by the applied magnetic field [210], [242], [243], and diffusion

forces induced both by Brownian diffusion [196] and the scattering effect that colliding and shearing red blood cells have on the nanoparticles [131].

2.4.1 Maxwell's Equations for the Magnetic Field

Electromagnetic fields are classically described by Maxwell's equations [244]. We specialize to the case of magneto-static equations that are appropriate for stationary, or slowly varying, magnetic fields.

(8) $\quad \nabla \times \vec{H} = \vec{J}$

(9) $\quad \nabla \cdot \vec{B} = 0$

(10) $\quad \vec{B} = \mu_0 (\vec{H} + \vec{M}) = \mu_0 (\vec{H} + \chi \vec{H})$

Here $\vec{B}$ is the magnetic field [T], $\vec{H}$ is the magnetic intensity [A/m], $\vec{J}$ is the current density [A/m^2], $\vec{M}$ is the material magnetization [A/m], χ is the magnetic susceptibility, and μ_0 is the permeability of a vacuum [$4\pi \times 10^{-7}$ N/A^2]. These equations hold true in vacuum and in materials, for permanent magnets (magnetization $\vec{M} \neq 0$), and for electromagnets (current $\vec{J} \neq 0$) [194], [210], [245]. Through the human body, magnetic fields propagate essentially unchanged because the magnetic susceptibility of tissue is close to zero ($\chi \approx 10^{-6} - 10^{-4}$ [246], [247]). In contrast, the magnetite cores (e.g. Fe$_3$O$_4$) of ferro-magnetic particles have magnetic susceptibilities 5 to 7 orders of magnitude higher than that of tissue ($\chi \approx 20$), therefore these particles are strongly influenced by magnetic fields [194], [210], [245].

2.4.2 Magnetic Forces on a Particle

A single ferro-magnetic particle in a magnetic field will experience a force that depends upon the magnetic field and field gradient around it [87], [185], [210], [239].

$$(11) \quad \vec{F}_M = \frac{4\pi a^3}{3} \frac{\mu_0 \chi}{1+\chi/3} \left[\frac{d\vec{H}}{d\vec{x}} \right] \vec{H} = \frac{2\pi a^3}{3} \frac{\mu_0 \chi}{1+\chi/3} \, \nabla \left(|\vec{H}|^2 \right).$$

Here a is the radius of a nanoparticle [m] and ∇ is the gradient operator [with units 1/m]. For simplicity, the hydrodynamic radius is considered to be the same size as the magnetic core radius (the case where they differ is discussed in Section 2.15.8). The first relation is more familiar and clearly shows that a spatially varying magnetic field ($d\vec{H}/d\vec{x} \neq 0$) is required to create a magnetic force. The second equivalent relation states that the magnetic force on a ferro-magnetic particle is always from low to high magnetic fields and proportional to the gradient of the magnetic field intensity squared. The two relations are equal by the chain rule and it is evident that the magnetic force is also proportional to the particle volume.

If the applied magnetic field is sufficient to saturate the nanoparticle, then $[d\vec{H}/d\vec{x}]\vec{H}$ in equation (11) is modified to $[d\vec{H}/d\vec{x}]\vec{M}_{sat}$ where $\vec{M}_{sat}$ is the saturated magnetization of the particle. Since $\vec{M}_{sat}$ lines up with $\vec{H}$, this does not change the direction of the force, only its size. Thus, this case is considered within our framework simply by modifying the size of the magnetic force used.

As shown in Figure 4, when the magnet is held at a long distance compared to the blood vessel width, we can assume that the magnetic force is constant in space throughout the blood vessel width and length. This negates the need to solve the magneto-static

equations; it is true to within a few percent even for wide blood vessels near magnets, and it does not qualitatively change the resulting nanoparticle behaviors (Section 2.15.3 analyses the case where the magnetic force does vary in space according to the magneto-static equations).
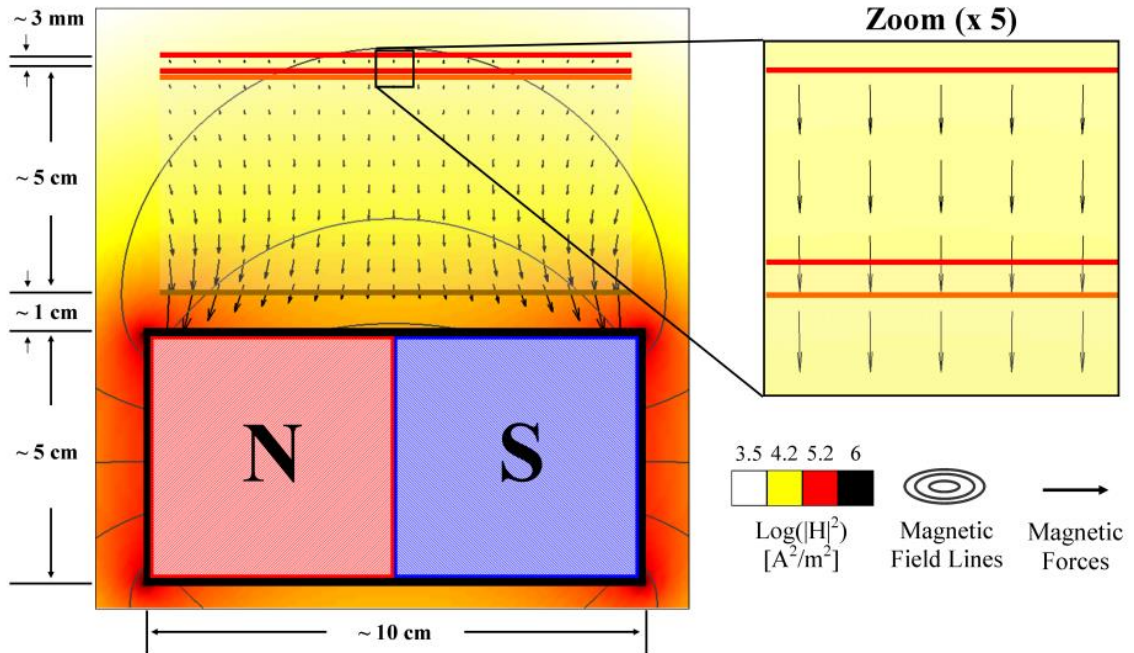
Figure 4: Magnetic forces are usually constant within the tissue-vessel system. Here even though a magnet is held close to the blood vessel (at a distance that is less than its length) the resulting magnetic force within the blood vessel is still essentially constant: the maximum error of $|F_{const}-F_{exact}|/|F_{exact}| < 10\%$.

For the rat experiment shown in Figure 2b, the force acting upon a single iron oxide 125 nm radius particle at a 1 mm depth is given by equation (11) to be $F_M \approx 0.1$ pN. (Here the 0.5 T permanent magnet produces a magnetic field intensity of 3.7×10^5 A/m and a magnetic spatial gradient of $\approx 1 \times 10^7$ A/m^2 at a distance of 1 mm, the particles had a magnetic susceptibility of roughly $\chi \approx 20$ and saturated at $\vec{M}_{sat} \approx 448$ kA/m [106].)

2.4.3   Magnetic Forces on a Concentration of Particles (on a Ferrofluid)

A ferrofluid is composed of many magnetizable nanoparticles and is essentially super-paramagnetic. Ferrofluids are strongly magnetized in the presence of an external field and then lose their magnetization once the external field is removed due to rapid random particle reorientation [194], [210], [245]. Neglecting particle-to-particle interactions, which are small due to particle reorientations and anti-agglomeration coatings [11], the magnetic force on each elemental volume of ferrofluid is given by [38], [196]

(12) $\vec{F}_M = \frac{2\pi a^3}{3} \frac{\mu_0 \chi}{1+\chi/3} \ C \ \nabla\left(\left|\vec{H}\right|^2\right)$

where C is the concentration of the particles [number/m^3].

2.4.4   Magnetic Drift Velocity: Magnetic Forces versus Stokes Drag

When the magnetic force of equation (11) is applied to a particle, it will accelerate the particle in the direction of this force until it reaches an equilibrium velocity $\vec{V}_R$ relative to the surrounding blood (or surrounding tissue). The opposing Stokes drag force on a spherical particle is given by [38], [196]

(13) $\vec{F}_S = 6\pi a\eta \vec{V}_R$

were η is the dynamic viscosity of blood [kg m/s]. When the Stokes drag force first equals the applied magnetic force, then the particle has reached its equilibrium relative velocity (magnetic velocity)

(14) $\vec{V}_R = \frac{a^2}{9\eta} \frac{\mu_0 \chi}{1+\chi/3} \ \nabla\left(\left|\vec{H}\right|^2\right) = k\nabla\left(\left|\vec{H}\right|^2\right)$

where $k = a^2 \mu_0 \chi/9\eta(1 + \chi/3)$ is the magnetic drift coefficient. This relative velocity adds to the fluid velocity (equation (15) below) and together they give the net convection plus

magnetic drift velocity. (Equation (13) does not include wall effects that modify the drag force on a particle within a few particle diameters of an external obstruction [248], [249]. Equation (14) also does not include magnetic particle-to-particle interaction forces. For an initial discussion of the effects of agglomeration see Section 2.15.5 or [250]–[252].)

Within the membrane and tissue layers, Stokes drag is not the only limitation to the maximum velocity induced by magnetic forces. There are many obstacles in the form of cells and extracellular matrix components that inhibit particle movement [37], [38], [237], [253]. These obstacles lead to an analogous magnetic drift coefficient for the membrane and tissue layers. Einstein's relation assumes that these obstacles also inhibit diffusion in a similar manner [37], [38]. Therefore the analogous magnetic drift coefficient for the membrane and tissue layer is generated by scaling k by the Renkin Reduced diffusion coefficient described in Section 2.8.4 [37].

Using the same rat example as before (Figure 2b) and a blood viscosity of 0.003 Pa s, the magnetic drift velocity of the 250 nm diameter iron oxide particles in blood is then $V_R \approx$ 1.4 x 10^{-5} m/s, i.e. it is 14 μm/s.

2.4.5 Advection Forces

The fluid velocity profile in a channel is curved - it is highest at the centerline and is zero at the walls due to the no-slip boundary condition. For Newtonian fluids in straight channels at steady state, this curved profile is parabolic [196], [254]. Blood, however, is a non-Newtonian fluid due to the presence of the clotting protein fibrinogen, which

causes red blood cells to aggregate at low shear rates. This creates a blunted flow profile known as plug flow [37]. Such a profile can be fit empirically by [255]

(15) $\qquad \vec{V}_B = V_{Bmax}\left(1 - \left(\frac{r}{R}\right)^{\xi}\right)$

where $\vec{V}_B$ is the velocity in [m/s], V_{Bmax} is the maximum centerline velocity [m/s], r is the radial location [m], R is the radius of the vessel [m], and ξ is a constant for a particular profile. A value of $\xi = 9$ is usually chosen to fit experimental data of the cardiac cycle [255]. This equation removes the need to solve the Navier-Stokes equations for the blood flow profile. In rat vessels the smallest centerline blood velocity is on the order of 0.1 mm/s [225]–[227], in humans it is 0.5 mm/s [37].

2.4.6   Diffusion Forces

There are two main types of particle diffusion that occur within a blood vessel: Brownian thermal motion and particle scattering due to collisions with blood cells.

Brownian Diffusion

Brownian motion refers to the random motion of particles under the action of thermal fluctuations and is quantified by a diffusion coefficient [37], [196]

(16) $\qquad D_B = \frac{k_B T}{6\pi\eta a}$

that relates the diffusive flux to the concentration gradient of the particles. Here k_B is the Boltzmann constant and T is the absolute temperature. For 250 nm diameter particles in blood at body temperature (37°C), the diffusion coefficient is $D_B \approx 6 \times 10^{-13}$ m^2/s [102], [210], [216], [239].

Diffusion from Blood Cell Scattering

Collision of blood cells with nanoparticles causes the particles to scatter and can be modeled as additional diffusion [131]. The scattering diffusion coefficient is on the order of $D_S \approx 10^{-11}$ - 10^{-10} m^2/s and can therefore be greater than the diffusion due to thermal motion. The total particle diffusion is the sum of thermal and scattering diffusion hence $D_{Tot} = D_B + D_S$.

2.4.7 Additional Forces not Considered within the Model

Several additional forces are neglected for simplicity. These include additional forces that occur when particles concentrate near the blood vessel boundary. If the particles concentrate to significant levels at the vessel boundary, the resultant concentration can extend into the vessel where blood velocity forces are high. It is possible for the collection of particles to then impact the blood flow and change the blood velocity flow profile. This effect is neglected within this model.

In addition, the effect of objects within the blood flow imparting an additional force as they collide with the particles is not considered. These objects include red blood cells, white blood cells, or platelets. While this is approximated for red blood cell interactions with the addition of a scattering diffusion coefficient, it does not completely describe the scenario for all vessel types or objects. One such un-described scenario is within capillaries or other small vessels where red blood cells encompass the entire vessel lumen (interior area) thereby pushing any particles along with the transient red blood cells.

41

2.5   Summary of Governing Equations and Boundary Conditions

The concentration of ferrofluid at each location is a function of time: it increases when the flux of particles to that location is positive and decreases when it is negative [196], [248]. The flux is the summation of the three effects discussed above: diffusion, convection by blood flow, and magnetic drift. Thus

$$(17)\quad \underbrace{\tfrac{\partial}{\partial t} C(x,y,t)}_{\substack{\text{Ferrofluid}\\\text{Concentration}}} = -\nabla \cdot \left[\underbrace{-D_{Tot}\nabla C}_{\text{Diffusion}} + C \underbrace{\vec{V}_B(y)}_{\substack{\text{Blood}\\\text{Convection}}} + C \underbrace{k\nabla\big(\big|\vec{H}(x,y)\big|^2\big)}_{\text{Magnetic Drift}} \right]$$

where $\vec{V}_B$ is the blood flow velocity. Considering a constant magnetic force acting only in the negative y-direction and the specific blunted blood flow profile of equation (8), the concentration can then be described by the partial differential equation

$$(18)\quad C(x,y) = -\nabla \cdot \left[D_{Tot}\nabla C + C\left(V_{Bmax}\big[1-\big(\tfrac{y}{R}\big)^9\big],0\right) + C\big(0,-k\nabla H^2\big)\right]$$

stated in two spatial dimensions, in x and y. The concentration inside the tissue is defined more simply by the equation

$$(19)\quad C(x,y) = -\nabla \cdot \left[-D_{T,Tot}\nabla C + C\big(0,-k_T\nabla H^2\big)\right].$$

Boundary conditions are required to complete the model. At the blood flow inlet, a constant concentration of magnetic particles is imposed (see also Figure 3). At all external boundaries of the tissue-vessel system, the normal diffusive flux is set to zero $(n \cdot D\nabla C = 0)$ enforcing the requirement that the total flux at those boundaries is exactly the convective flux (so that ferrofluid correctly convects out of the vessel outlet with the blood flow). The interior boundaries between the vessel and endothelial layer, and the endothelial layer and tissue, satisfy two conditions: the ferrofluid concentration is

continuous across each interface (no concentration discontinuities), and the ferrofluid that leaves one domain enters another (no ferrofluid is lost or created).

Since in magnetic drug delivery a magnet is often held outside the skin, and nanoparticles then concentrate closest to it but do not leave the body, it can be desirable to include a 'skin' boundary condition that prevents nanoparticles from leaving the tissue (this would be placed at the bottom of the tissue layer in Figure 3). We do not consider this added feature for the majority of the chapter because we are interested in ferrofluid behavior in, immediately around, and between blood vessels. Therefore we permit the nanoparticles to leave this focused inspection domain. Skin introduces a new complication, the pile-up of nanoparticles in the tissue next to it, and it can distort the behavior around blood vessels in a way that depends on tissue thickness. It necessitates a 4th non-dimensional number thus requiring a 4-dimensional visualization of the prototypical behavior of ferrofluids. A skin boundary condition is included in Section 2.15.6 and correctly causes ferrofluid to pile-up near the magnet.

2.6   Range of Physical Parameters

2.6.1   Magnetic Parameters

Magnetic nanoparticles are usually defined as a moiety between 1 nm and 1 μm that contain a magnetic core [11]. The magnetic core is usually composed of magnetite or maghemite [11], [80], [102], [104], [106], [108], [228], [256], [257] but other exotic materials can be used including cementite [32], [34]. For *in vivo* studies the size of particles used ranges from ≈ 10 nm (small carriers) [102] to 5 μm (large carriers) [32],

[34]. Smaller particles (size < 25 nm) usually exhibit superparamagnetic behavior that helps reduce agglomeration when the magnetic fields are removed [11]. Larger particles (size > 60 nm) benefit from not passing through normal fenestrated capillaries where the pore cut-off size is approximately 60 nm [11], [216].

The magnetic fields generated by external magnets in *in-vitro* studies have ranged anywhere from $\approx$ 70 mT [142] to $\leq$ 1.5 T [214], [228]. Animal trials have had ranges between 0.1 T and 1.5 T [31], [36], [80], [102], [109]. While the FDA has approved magnetic strengths up to 8 T for use with humans [11] and human clinical trials have utilized 0.2 to 0.8 T magnet field strengths [14], [30], [31], [108]. Most often permanent magnets have been used with sizes ranging from tens of millimeters to tens of centimeters [32], [34], [80], [108], [142], [228]. Occasionally electromagnets were utilized [214], [257]. The distance of particles from magnets has ranged from $\approx$ 1 mm to $\approx$ 12 cm in the literature [14], [32], [36], [106], but we consider up to 30 cm distances to examine the possibility of deep tissue magnetic targeting [218], [239], [241].

2.6.2   Advection Parameters

In humans, typical centerline blood velocities range from 0.5 mm/s in capillaries to the largest value of 40 cm/s in the aorta [37], [38], [131]. Average vessel diameters vary between 7 μm for capillaries to 3 cm in the vena cava [11], [37], [131].

2.6.3 Diffusion Parameters

Particle size and vessel radii impact the diffusion of nanoparticles. The largest diffusion coefficients occur in large vessels (arterioles and arteries) where cell scattering effects are high and with small particles where Brownian diffusion is large. The smallest diffusion coefficients occur in small vessels (capillaries) where scattering effect are negligible and with large particles where Brownian diffusion is small. The typical range in humans of total particle diffusion coefficients is between 1×10^{-14} to 6×10^{-10} m^2/s [37], [131].

Table 1: Human physical parameters encountered in magnetic drug delivery. (Essential quantities needed for the sub-sequent non-dimensionalization are bolded.)

Parameter	Symbol	Parameter Range
Particle Radius	a	1 nm – 5 µm
Distance from Magnet	d	1 mm – 30 cm
Magnetic Field Strength (or Magnetic Intensity)	$\|\vec{B}\|$ $\|\vec{H}\|$	0.1 – 1.5 T $8 \times 10^4 – 1.2 \times 10^6$ A/m
Magnet Length	L_M	1 - 30 cm
Magnetic Drift Velocity	$\|\vec{V}_R\|$	9×10^{-15} m/s – 3.8×10^{-4} m/s
Magnetic Force on a Particle	$\|\vec{F}_M\|$	$\mathbf{5 \times 10^{-25} – 1.1 \times 10^{-11}}$ **N**
Maximum Centerline Blood Velocity	V_{Bmax}	**0.5 mm/s – 40 cm/s**
Vessel Diameter	d_B	**7 µm – 3 cm**
Blood Viscosity	η	0.003 Pa s
Centerline Stokes Drag on a Particle	$\|\vec{F}_S\|$	$\mathbf{3 \times 10^{-14} – 1.1 \times 10^{-7}}$ **N**
Temperature	T	310 K (body temperature)
Brownian Diffusion Coefficient Scattering Diffusion Coefficient	D_B D_S	1×10^{-14} - 1×10^{-12} m^2/s 3.5×10^{-12} - 6×10^{-10} m^2/s
Total Diffusion Coefficient (in blood)	D_{Tot}	$\mathbf{1 \times 10^{-14} – 6 \times 10^{-10}}$ **m^2/s**
Diffusion Coefficient (in membrane)	D_M	**0 (particles > pores) - 1.5×10^{-12}**
Diffusion Coefficient (in tissue)	D_T	**0 (particles > interstitial spaces) - 1.2×10^{-14}**

2.7 Non-dimensionalization of Governing Equations

In a model with dimensional parameters, like equation (17), the numerical parameter values used depend on the chosen units (meters versus millimeters), there are typically multiple parameters associated with each phenomena (with diffusion, convection, and magnetic drift), and their effects are coupled together (for example, changing the particle radius changes both the diffusion coefficient D and the magnetic drift coefficient k).

Non-dimensionalizing (i.e. normalizing) the model reduces the number of parameters to those that are actually independent [248]. The resulting non-dimensional numbers capture the ratio between competing physical effects; they remain the same even if a different system of units is chosen; and they are uncoupled in the sense that each non-dimensional number is the ratio between two competing effects and is independent from parameters that make up any third effect (e.g. the Renkin number is a ratio of diffusion in tissue versus in blood and does not depend on particle size).

As described in section 2.2, for our idealized blood vessel system, nanoparticle behavior is uniquely determined by three non-dimensional numbers: the magnetic-Richardson number, the Renkin reduced diffusion coefficient, and the mass Péclet number. If we consider two situations A and B in which the blood vessel width, particle size, and magnetic field strength differ dramatically, but these two situations share the same three non-dimensional Richardson, Renkin, and Péclet numbers, then these two different situations will exhibit identical behavior because they will both have exactly the same balance of magnetic, diffusion, and convection phenomena.

We now formally derive the non-dimensional form of our model (upcoming equations (24), (25), and (26)) from the dimensional form. Repeating equation (17) for clarity

(20) $\frac{\partial C}{\partial t} = -\nabla \cdot \left[-D_{Tot}\nabla C + C\vec{V}_B + C\vec{V}_R \right]$

let $\hat{x} = x/d_B$, $\hat{y} = y/d_B$, $\hat{C} = C/C_0$, $\hat{\vec{V}}_B = \vec{V}_B/V_{Bmax}$, and $\hat{\vec{V}}_R = \vec{V}_R/V_{Bmax}$ so each non-dimensional variable (hatted) is the dimensional variable divided by a characteristic quantity. Here d_B, C_0, and V_{Bmax} are the characteristic length (the width of the blood

47

vessel), characteristic concentration (the inlet magnetic particle concentration), and the characteristic velocity (the maximum centerline velocity in the blood vessel). Using these three characteristic quantities, it is further possible to consistently define all other needed non-dimensional variables and derivative operators as $t = t(V_{Bmax}/d_B) = t/t_0$, $\partial t/\partial t = 1/t_0$ and $\nabla = \partial/\partial(x) = \partial/\partial(d_B x) = \hat{\nabla}/d_B$.

Table 2 summarizes the non-dimensional transformations for all variables. The five essential dimensional variables (those variables that are bolded in Table 1) reduce down to just two non-dimensional numbers, as predicted by the classical theorem of non-dimensional analysis: the Buckingham Pi Theorem [248]. These two non-dimensional numbers are the magnetic-Richardson number and the mass Péclet number. The third non-dimensional number considered in the chapter, the Renkin reduced diffusion coefficient of the endothelial membrane or the tissue, is required because diffusion in the endothelium or the tissue differs from diffusion in the blood.

Table 2: The non-dimensionalized variables.

Parameter	Dimensional Symbol [and units]	Non-Dimensional Version	Characteristic Quantity Used for Non-Dimensionalization
Particle Radius	a [m]	$a = a/d_B$	d_B the average width of the blood vessel, e.g. $d_B = 0.03$ mm for an arteriole
X Length	x [m]	$x = x/d_B$	
Y Length	y [m]	$y = y/d_B$	
Velocity	$\vec{V}$ [m/s]	$\vec{V} = \vec{V}/V_{Bmax}$	V_{Bmax} the maximum centerline blood velocity, e.g. $V_{Bmax} = 1$ cm/s for an arteriole
Concentration	C [mol/m^3]	$C = C/C_0$	C_0 the inlet concentration, e.g. $C_0 = 2$ to 4 mol/m^3
Time	t [s]	$t = t\dfrac{V_{Bmax}}{d_B} = \dfrac{t}{t_0}$	Non-dimensionalized by the composite quantity $t_0 = d_B/V_{Bmax}$
Diffusion Coefficient	D_{Tot} [m^2/s]	$\hat{D}_{Tot} = D_{Tot}\dfrac{t_0}{d_B^2} = \dfrac{D_{Tot}}{d_B V_{Bmax}}$	Non-dimensionalized by the composite quantity $d_B V_{Bmax}$

Substituting the non-dimensional variable (or derivative operator) multiplied by the constant characteristic quantity for each dimensional variable (or operator) rewrites equation (20) as

(21)
$$\frac{\partial(C_0 C)}{dt}\frac{\partial t}{dt} = -\frac{\hat{\nabla}}{d_B}\cdot\left[-D_{Tot}\frac{\hat{\nabla}(C_0 C)}{d_B} + (C_0 C)(V_{Bmax}\vec{V}_B + V_{Bmax}\vec{V}_R)\right]$$
$$\frac{C_0}{t_0}\frac{\partial C}{\partial t} = -\frac{1}{d_B}\,\hat{\nabla}\cdot\left[-D_{Tot}\frac{C_0}{d_B}\hat{\nabla}C + C_0 V_{Bmax}(\vec{V}_B + \vec{V}_R)C\right].$$

Multiplying both sides by t_0/C_0

(22)
$$\frac{\partial C}{\partial t} = -\frac{t_0}{d_B C_0}\,\hat{\nabla}\cdot\left[-D_{Tot}\frac{C_0}{d_B}\hat{\nabla}C + C_0 V_{Bmax}(\vec{V}_B + \vec{V}_R)C\right].$$

Canceling and grouping terms, and recalling that t_0 is defined to be d_B/V_{Bmax} gives

(23)
$$\frac{\partial C}{\partial t} = -\hat{\nabla}\cdot\left[-\underbrace{\left(\frac{D_{Tot}}{d_B V_{Bmax}}\right)}_{\text{Diffusion}}\hat{\nabla}C + \underbrace{(\vec{V}_B + \vec{V}_R)C}_{\text{Advection}}\right].$$

Defining the mass Péclet number to be $Pe = d_B V_{Bmax}$ and the magnetic Richardson number to be the downward component of the non-dimensional magnetic velocity yields

equation (24) (where the sub-script B has been added to denote nanoparticles in blood and the hats have been dropped). Equations for the membrane and tissue are derived in exactly the same way.

2.8   Simulation Development

2.8.1   Non-Dimensional Governing Equations: The 3 Key Numbers

Non-dimensionalization of the mathematical model is crucial for mapping out ferrofluid behaviors; it reduces the number of parameters from the 16 in Table 1 to three key independent numbers and it prevents repeatedly solving self-similar cases that have differing dimensional parameters but share the same behavior [248]. Non-dimensional numbers achieve this saving by capturing the ratios between competing physical effects thus illustrating which effects win when and by how much.

As done previously in section 2.7, we non-dimensionalize equation (17) by choosing a characteristic length scale (the width of the blood vessel d_B), a characteristic velocity (the maximum centerline velocity in the blood vessel V_{Bmax}), and a characteristic concentration (the nanoparticle concentration at the blood vessel inlet C_0), and then normalize each variable with respect to these three characteristic quantities. Section 2.7 defines all the resulting non-dimensional variables and provides a detailed derivation of the final equations. After non-dimensionalization, equation (17) becomes

(24) $\quad \frac{\partial C_B}{\partial t} = -\nabla \cdot \left[-\frac{1}{Pe} \nabla C_B + \left(\vec{V}_B + (0, -\Psi) \right) C_B \right]$

now where C_B is the non-dimensional concentration of nanoparticles in the blood and $\vec{V}_B$ is the non-dimensional blood velocity. Equations (25) and (26) are the non-dimensional analogs for transport of magnetic particles in the endothelial membrane and in tissue respectively

(25) $\quad \frac{\partial C_M}{\partial t} = -\nabla \cdot \mathcal{D} \left[-\frac{1}{Pe} \nabla C_M + (0, -\Psi) C_M \right]$

(26) $\quad \frac{\partial C_T}{\partial t} = -\nabla \cdot \mathcal{D}_T \left[-\frac{1}{Pe} \nabla C_T + (0, -\Psi) C_T \right].$

This normalized model is completely parameterized by 4 non-dimensional numbers: the magnetic-Richardson number Ψ, the mass Péclet number Pe, the Renkin reduced diffusion coefficient $\mathcal{D}$ for endothelial membrane diffusivity compared to blood, and the Renkin reduced diffusion coefficient $\mathcal{D}_T$ for the diffusivity of tissue compared to that of blood. The thin endothelial membrane either effectively acts as a barrier to nanoparticles or not, thus it suffices to vary either $\mathcal{D}$ (when the membrane limits transport) or $\mathcal{D}_T$ (if tissue limits transport). Since there is little need to vary both, 3 non-dimensional numbers are sufficient to completely characterize nanoparticle behavior.

2.8.2 Magnetic-Richardson Number

Based on the Richardson number [196], [258], we define a magnetic-Richardson number as the ratio of the magnetic force to the Stokes drag force that would act upon a single stationary particle at the centerline of a blood vessel. The magnetic-Richardson number is thus the ratio

(27) $$\Psi = \frac{\text{Magnetic Force at Centerline}}{\text{Stokes Drag Force at Centerline}} = \left|\frac{\vec{F}_M}{\vec{F}_S}\right| = \frac{6\pi a\eta k \nabla\left(|\vec{H}|^2\right)}{6\pi a\eta V_{Bmax}} = \frac{\vec{V}_R}{V_{Bmax}}$$

As the magnetic-Richardson number increases to a value greater than unity, the magnetic forces experienced by a particle are much higher than the drag forces created by the blood velocity. As the number decreases below unity, the blood velocity forces dominate.

For the smallest rat blood vessels, the magnetic force upon an iron oxide 250 nm diameter particle at 1 mm depth was 0.1 pN. The Stokes drag force on that same particle in a rat blood vessel with a centerline velocity of 0.1 mm/s is 0.7 pN. Therefore the magnetic-Richardson number in this case is $\Psi = 0.14$.

2.8.3 Mass Péclet Number

Here the mass Péclet number [37], [196], [254] is defined as the ratio of the blood vessel width multiplied by the maximum centerline blood velocity to the total diffusion coefficient of the nanoparticles within the vessel. At large Péclet values, the blood advection of nanoparticles far exceeds their diffusion.

(28) $$Pe = \frac{(\text{Blood Vessel Width})\times(\text{Maximum Blood Velocity})}{\text{Total Diffusion Coefficient of Particles}} = \frac{d_B V_{Bmax}}{D_{Tot}}$$

Continuing with our rat example, with a centerline velocity of 0.1 mm/s (the slowest measured in a rat capillary), a vessel diameter of $d_B \approx 6$ μm, and a nanoparticle in blood diffusion coefficient of $D_{Tot} \approx 6 \times 10^{-13}$ m^2/s, the mass Péclet number is $Pe \approx 1000$.

2.8.4 The Renkin Reduced Diffusion Coefficient

The behavior of semi-permeable membranes, such as the blood vessel wall, can be modeled by the Renkin reduced diffusion coefficient [37], [38]. This coefficient is the ratio of the diffusion coefficient in the membrane to the diffusion coefficient in the blood.

(29) $\quad \mathcal{D} = \dfrac{\text{Diffusion Coefficient in Membrane}}{\text{Total Diffusion Coefficient in Blood}} = \dfrac{D_M}{D_B + D_S} = \dfrac{D_M}{D_{Tot}}$

As this ratio decreases towards zero, the ferrofluid increasingly remains within the blood vessel. As the ratio increases towards unity, the ferrofluid begins to leave the vessel and enters the membrane. When this ratio is one, the ferrofluid behaves as if the vessel wall did not exist. With this number the permeability of the endothelial membrane can be varied in a simple manner.

If pore diameters of a membrane are known, the following equations can be used to estimate the ratio of blood to tissue diffusion coefficients

(30) $\quad \dfrac{D_M}{D_B} = (1 - \alpha)^2 \left(1 - 2.1044\alpha + 2.089\alpha^3 - 0.948\alpha^5\right), \alpha = \dfrac{a}{r_{pore}}$

where r_{pore} is the average radius of the pores in a membrane [37], [38], [197]. For normal endothelial pores of size $r_{pore} \approx 60$ nm in rat capillaries [225]–[227], $\mathcal{D} \approx 0$, while in leaky blood vessels where $r_{pore} \approx 600$ nm, $\mathcal{D} \approx 0.36$.

Not only is the ratio of membrane to blood diffusion coefficients important, but the ratio of tissue to blood diffusion coefficients impacts particle behavior. Similar to the semi-permeable vessel wall, tissue diffusivity is highly dependent upon particle size and the extra-cellular spacing. Therefore it is necessary to vary this number as well, and this is accomplished in Section 2.15.7.

$$(31) \quad \mathcal{D}_T = \frac{\text{Diffusion Coefficient in Tissue}}{\text{Total Diffusion Coefficient in Blood}} = \frac{D_T}{D_{Tot}}$$

Tissue diffusivity is usually greater than the membrane diffusivity but is typically less than the total blood diffusivity. In the rat example, for a tumor extracellular space of 1 μm, $\mathcal{D}_T \approx 0.56$ [37].

2.9 Numerical Implementation

Magnetic particle behavior was simulated by using both the commercial multi-physics package COMSOL (www.comsol.com) and by an algorithm designed specially to meet the significant challenges posed by the Vessel-Membrane-Tissue (VMT) convection diffusion problem. The second method is based on a combination of: 1) a graded mesh to adequately resolve thin boundary layers; 2) the Alternating Directions Implicit (ADI) method [234]; 3) an on-and-off fluid-freezing methodology that allows for efficient treatment of the multiple-time scales that exist in the problem; and 4) a change of unknowns that enables evaluation of steady states in tissue and membrane layers through a highly accelerated time-stepping procedure [231]–[234]. The resulting linear-time unconditionally-stable numerical methodology, called the VMT solver, is both significantly more accurate and up to four orders of magnitude faster than the COMSOL simulation, in addition to being capable of resolving thin boundary layers for cases where COMSOL fails. For example, considering the case of $Pe = 1000$, $\Psi = 0.001$, $\mathcal{D} = 0.01$, $\mathcal{D}_T = 0.01$, on a Intel Xenon quad core 3.1 GHz processor with 80 GB of available memory, COMSOL obtained a solution within 48 hours while our VMT solver obtained a steady state solution with 5 digits of accuracy in only 5 minutes and using 32.7 MB of memory. For another, much more difficult case using $Pe = 10000$, $\Psi = 0.00001$,

$\mathcal{D} = 0.001$, $\mathcal{D}_T = 0.01$, our VMT solver obtained a steady state solution with 5 digits of accuracy in under 8 minutes and using just 98.3 MB of memory while COMSOL was unable to provide a solution.

Full details of the numerical methodology (with additional accuracy and computing improvements resulting from use of the novel Fourier Continuation-Alternating Directions method [259]) used in the VMT solver will be presented in a forthcoming contribution [260].

Below we provide details of both the COMSOL and VMT numerical implementations, then a comparison of the two to show that they give the same answer (up to the poorer solution accuracy possible with COMSOL is shown in section 2.11).

2.9.1   COMSOL Implementation

Software Implementation

For implementing the model, the software package COMSOL Multiphysics version 3.4 was chosen initially. This package allowed the geometry specified in Figure 3 to be constructed. Equations (24), (25), and (26) were solved for the entire control volume using the prescribed blood velocity and magnetic velocity (equations (15) and (14)). Simulation times ranged from 15 minutes for the easy cases with $Pe \leq 100$, up to 36 hours for $Pe \approx 1000$, and were unsolvable for $Pe \geq 3000$ even when using a high-end quad-core 32 GB RAM computer (a typical 2009 desktop PC or laptop has only 4 GB of RAM available).

Meshing Parameters

COMSOL computes the solution by using the finite element method; that is by meshing the region and numerically integrating the approximate solution of the PDE at all mesh points until converged [261]. The mesh sizing must be sufficiently small to capture any physics being modeled in the domain. In systems with both advection and diffusion, the cell Péclet number sets the mesh sizing dependence on the modeled physical phenomena to ensure numerical stability. The cell Péclet number is defined as

(32) $Pe_{cell} = \mathbf{\Psi} Pe\ dx$

where dx is the mesh size in any primary coordinate direction. When $Pe_{cell} \leq 2$, the solution is guaranteed to be numerically stable [262]. This requirement for stability demands small mesh elements due to small diffusion coefficients (for a $\mathbf{Pe} \approx 1000$ simulation, this requirement translated into 4.7×10^7 required mesh points and 80 GB of available memory, either random access or virtual memory). The COMSOL simulations were solved using a computer that contained a quad-core processor. Using COMSOL and this high-end computer we were able to solve cases up to $\mathbf{Pe} \leq 1300$ but higher Péclet number cases remained unsolvable (a $\mathbf{Pe} = 1 \times 10^8$ would have required 4.7×10^{17} mesh points to ensure numerical stability corresponding to a 2000 Terabytes $\approx 2 \times 10^6$ Gigabytes of required memory, an infeasible amount).

2.9.2   Vessel-Membrane-Tissue (VMT) Solver

The VMT solver provided far more capabilities than COMSOL and was both over 500 times faster than COMSOL and able to solve cases that COMSOL could not. Using the VMT solver we were able to resolve all the needed cases to sufficient accuracy to

56

accurately and unambiguously locate the delineations between our 3 observed behaviors. The VMT solver is comprised of four distinct components used in combination: 1) a graded mesh to adequately resolve thin boundary layers; 2) a change of unknowns that enabled evaluation of steady states in tissue and membrane layers through a highly accelerated time-stepping procedure [231]–[234]; 3) an on-and-off fluid-freezing methodology that allowed for efficient treatment of the multiple-time scales that exist in the problem; and 4) the Alternating Directions Implicit (ADI) method for solving PDEs [234].

To resolve the thin boundary layer that can form at the interface between the vessel and the endothelial layer, a typical Cartesian mesh was not adequate. Instead, the VMT method used a graded mesh implemented through an exponential change of unknowns of the form

(33) $\xi_j = e^{-\Psi Pe}$, and

(34) $\begin{aligned} x_i &= (i-1)h_x & i &= 1, \ldots, N & h_x &= 1/(N-1) \\ y_j &= (j-1)h_y, & j &= 1, \ldots, M, & h_y &= 1/(M-1). \end{aligned}$

To numerically resolve advection in the vessel, we began by using a small time step, $\Delta t = 0.1$. This presented a problem, however, because diffusion in the membrane and tissue can be small. Therefore using this time step required a long simulation time in order for the concentration to reach steady state. If the time step was taken to be much larger, we risked being unable to resolve ferrofluid advection in the vessel. To overcome this difficulty, we periodically 'froze' and 'un-froze' the concentration in the blood vessel. Freezing occurred once the concentration in the blood vessel approached steady state allowing for only the concentration in the membrane and tissue to be evolved.

Evolution of the concentration in only the membrane and tissue continued until the freezing approximation was no longer accurate, at which time we unfroze the concentration in the blood, and evolved the entire system at a significantly reduced time-step until freezing could be performed again. The process was repeated until steady-state in the complete system was reached.

In order to quickly obtain steady states in the membrane and tissue regions for each frozen vessel concentration, we performed a transformation that allowed us to take advantage of a fast steady-state solver based on selection of adequately chosen, very large time-steps. The required transformation was a change of unknowns

$$(35) \quad \begin{aligned} C_M(x, y, t) &= \omega_M(x, y, t) e^{-\Psi y Pe/2} \\ C_T(x, y, t) &= \omega_T(x, y, t) e^{-\Psi y Pe/2} \end{aligned}$$

that eliminated the magnetic term in the PDE for the membrane and tissue, converting the convection diffusion spatial operator to a spatial operator of Helmholtz type

$$(36) \quad \begin{aligned} \frac{\partial \omega_M}{\partial t} &= -\nabla \cdot \mathcal{D}\left[-\frac{1}{Pe}\nabla \omega_M\right] - \frac{\Psi^2}{4}\omega_M \\ \frac{\partial \omega_T}{\partial t} &= -\nabla \cdot \mathcal{D}_T\left[-\frac{1}{Pe}\nabla \omega_T\right] - \frac{\Psi^2}{4}\omega_T \end{aligned}.$$

We then selected time-steps in a form described in [263], that is (36)

$$(37) \quad \Delta t_n = \frac{h_M^2}{b}\left(\frac{b}{a}\right)^{\frac{n+1}{100}}$$

where

$$(38) \quad a = 4\sin^2\left(\frac{\pi h_M}{2}\right), \quad b = 4\cos^2\left(\frac{\pi h_M}{2}\right)$$

h_M is the step size in the y-direction in the membrane, and n is the iteration number. This was done in conjunction with freezing the concentration in the vessel to obtain fast convergence.

An essential element of the overall VMT solver was the Alternating Directions Implicit (ADI) methodology first introduced in [231]–[234]. Based on reducing a given PDE into separate ODEs through the factorization of terms associated with a particular variable, ADI methods require line-by-line solutions of small sets of simultaneous equations. The key feature of these methods is their unconditional stability, thus permitting our VMT solver to avoid the extremely small time-steps imposed for stability by explicit schemes in the presence of small diffusion coefficients and allowing the use of the efficient time-stepping scheme described earlier. The ODEs generated from this method can be solved by using a variety of methods. Because of the rectangular geometry being considered for the VMT solver, a standard Finite Difference approach was used. For general (e.g. curved) domains, another approach is required. The only available methodology that gives rise to unconditionally stable numerics for the Alternating Directions method in general non-rectangular domains is the Fourier Continuation-Alternating Directions (FC-AD) approach introduced in [259]. By solving the ODEs generated in the ADI algorithm through the use of Fourier Continuation methods [264], the FC-AD algorithm has the ability to yield high-order accurate, unconditionally stable solutions in essentially linear time. The FCAD algorithm is currently being implemented for future simulations of flow through more complex vasculature geometries and will be presented in a forthcoming chapter, [260].

2.10   Determination of Experimental Domains

In vivo experiments often contain a wide range of physical variables that fold into the development of the three non-dimensional numbers. These numbers are dictated by the

biology of the system studied and include items such as varying blood vessel widths, blood vessel velocities, and diffusion coefficients within various tissues, membranes, and blood vessels. Typically, information is not known about the exact physical variables experienced by every nanoparticle within the animal or human at any specific time. Some particles can be within liver regions, while others are floating within skin tissue. Therefore, the analysis of the entire biological system must include educated estimates for the expected range of all the key non-dimensional numbers. Our three non-dimensional numbers are written again below with the biologically varying parameters marked by a double underline:

(39) $\quad \Psi = \dfrac{\text{Magnetic Force at Centerline}}{\text{Stokes Drag Force at Centerline}} = \left| \dfrac{\vec{F}_M}{\vec{F}_S} \right| = \dfrac{6\pi a \eta k \nabla \left(|\vec{H}|^2 \right)}{6\pi a\, \eta V_{Bmax}} = \dfrac{\vec{V}_R}{\underline{\underline{V_{Bmax}}}}$

(40) $\quad Pe = \dfrac{\text{Blood Vessel Width} \times \text{Maximum Blood Velocity}}{\text{Total Diffusion Coefficient of Particles}} = \dfrac{d_B V_{Bmax}}{D_B + \underline{\underline{D_S}}}$

(41) $\quad \mathcal{D} = \dfrac{\text{Minimum Diffusion Coefficient in Membrane or Tissue}}{\text{Total Diffusion Coefficient in Blood}} = \dfrac{\min\left(\underline{\underline{D_M}}, \underline{\underline{D_T}} \right)}{D_B + \underline{\underline{D_S}}}$

2.10.1 Magnetic-Richardson Number Range

As shown in equation (39), the magnetic-Richardson number is only dependent upon one biological variable: the centerline blood velocity. Therefore the range of the magnetic-Richardson number is as follows

(42) $\quad \dfrac{\vec{V}_R}{V_{Bmax}|_{\max}} \le \Psi \le \dfrac{\vec{V}_R}{V_{Bmax}|_{\min}}$

where V_{Bmax} is the centerline (maximum) velocity in the blood vessel and $|_{\max}$ and $|_{\min}$ denote the maximum and minimum of this velocity across physiological conditions, at major veins versus capillaries respectively.

2.10.2 Renkin Reduced Diffusion Coefficient Range

Equation (41) illustrates the fact that the Renkin reduced diffusion coefficient is dependent upon the diffusion in the membrane, the diffusion in the tissue, and the scattering diffusion coefficient due to blood vessel size and velocity. The tissue and membrane diffusion coefficients are properties of the tissue and can range from a lower bound of 'zero' when the particle is larger than the membrane pores or tissue interstitial spaces, to an upper bound equal to the diffusion coefficient within the blood. The scattering diffusion coefficient can be estimated by using the following formula [131]

$$(43) \qquad D_S \approx K_{sh}(r_{RBC})^2\gamma \approx 8K_{sh}(r_{RBC})^2 \frac{V_{Bmax}}{d_B}$$

where the dimensionless coefficient is $K_{sh} = 5 \times 10^{-2}$, the red blood cell radius is $r_{RBC} = 4.26 \times 10^{-6}$ m, and γ is the shear rate at the vessel wall. Therefore the range for all Renkin reduced diffusion coefficients is

$$(44) \qquad \frac{\min(D_M|_{\min}, D_T|_{\min})}{D_B + D_S|_{\max}} \leq \mathcal{D} \leq \frac{\min(D_M|_{\max}, D_T|_{\max})}{D_B + D_S|_{\min}}$$

2.10.3 Mass Péclet Number Range

The mass Péclet number varies with more complexity than the other two numbers as is evident from equation (40). The numerator varies not only with the centerline velocity of a vessel but also with the diameter of that vessel. Physiologically the velocity is also dependent upon the diameter of the vessel and the exact shape of this dependency is not linear. In addition the denominator is also dictated by the scattering diffusion coefficient that is governed by the vessel diameter. From equations (39) and (41), the needed dependencies and bounds on the Péclet number are

(45) $\quad Pe = \frac{d_B(V_{Bmax}) \times V_{Bmax}}{D_B + D_S(V_{Bmax})}$

(46) $\quad \frac{d_{Bmin}(V_{Bmax}|_{min}) \times V_{Bmax}|_{min}}{D_B + 8K_{sh}(r_{RBC})^2 \frac{V_{Bmax}|_{max}}{d_{Bmin}(V_{Bmax}|_{min})}} \leq Pe \leq \frac{d_{Bmax}(V_{Bmax}|_{max}) \times V_{Bmax}|_{max}}{D_B + 8K_{sh}(r_{RBC})^2 \frac{V_{Bmax}|_{min}}{d_{Bmax}(V_{Bmax}|_{max})}}$

To understand the shape of the mass Péclet curve, the relationship between the vessel diameter and centerline blood velocities must be known or estimated. For some organisms, i.e. humans, this relationship is well known [265] and appropriate bounds for these data points can be determined. For other organisms, i.e. rats, the relationship is not well known and bounds must be estimated more roughly to allow all possibilities. Figure 5 shows the relationship within humans for the vessel diameter to the vessel velocity [265] with our two chosen bounding curves for the data shown.
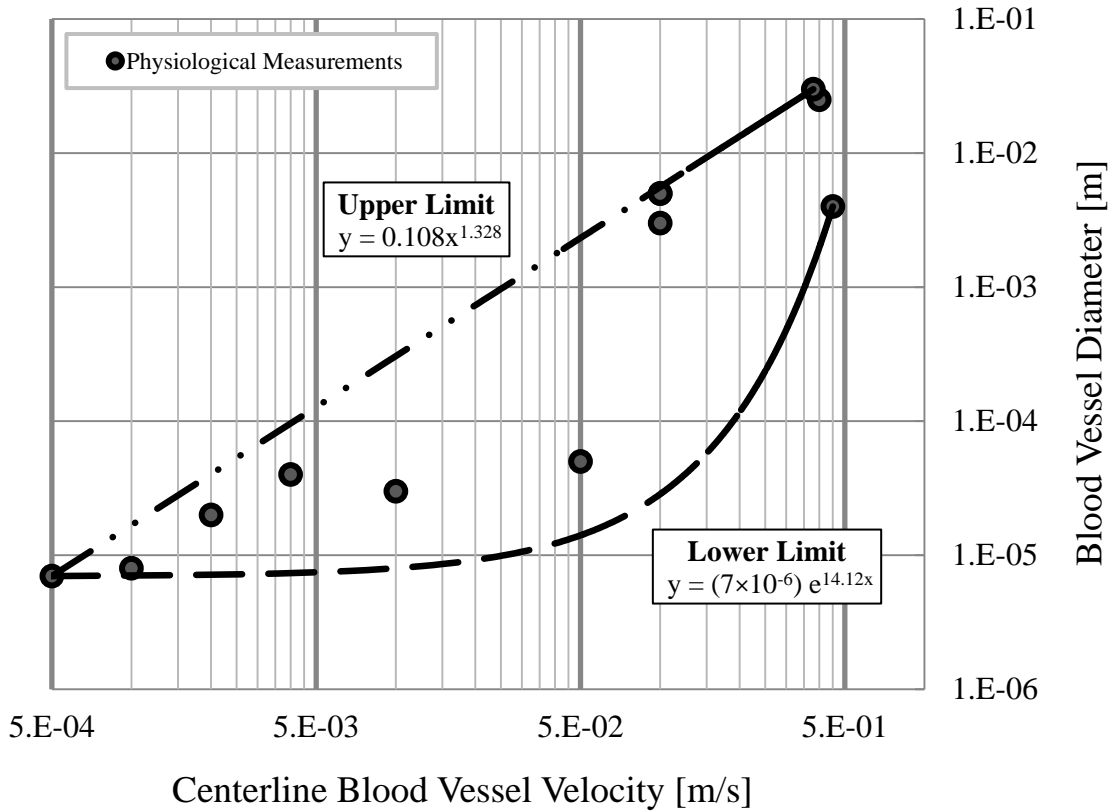
Figure 5: Relationship between vessel diameter and blood vessel velocity within humans [265]. Our chosen upper and lower limits to bound the data are shown.

The combination of these ranges for the non-dimensional numbers generates the shape of the experimental domains seen in Figure 15 of the main text. These domains are simple (conservative) rectangles when only general physiological information is known (Bergemann, Widder), they are tighter curved domains for the situation in humans (Lübbe) where more specific physiological information is available.

2.11   Comparison of COMSOL versus VMT

Up to the accuracy possible in COMSOL, the two numerical methods provide the same answers. Below we show two side-by-side comparisons: one easy case in which the COMSOL solution accuracy is sufficient (here there is a very good match between COMSOL and VMT) and one medium-difficulty case where COMSOL was able to find a solution but the accuracy of VMT is better. For hard (high Péclet number) cases, COMSOL cannot provide a solution and VMT is the only option.
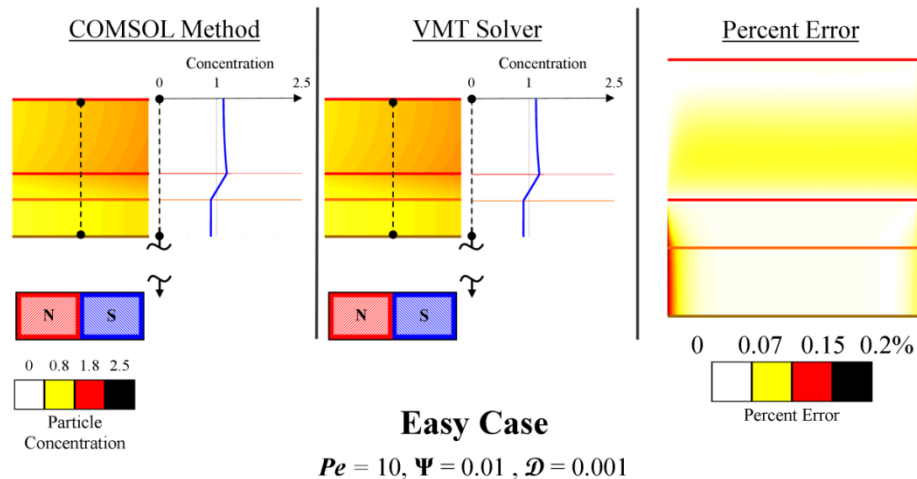
Figure 6: Easy case at a $Pe = 10$, $\Psi = 10^{-2}$, $\mathcal{D} = 10^{-3}$. Cross-sectional magnetic nanoparticle concentration for steady state for both COMSOL and the VMT method. The percent error is calculated by $(C_{Comsol} - C_{VMT})/C_{VMT}$.

COMSOL Method   VMT Solver   Percent Error

Medium Case
$Pe = 1000,\ \Psi = 0.0001,\ \mathcal{D} = 0.001$
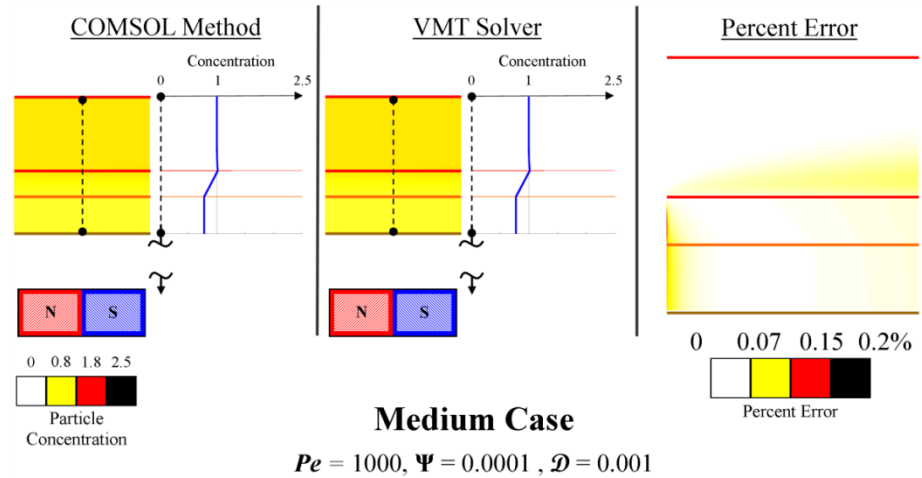
Figure 7: Medium case at a $Pe = 1000$, $\Psi = 10^{-4}$, $\mathcal{D} = 10^{-3}$. Cross-sectional magnetic nanoparticle concentration for steady state for both COMSOL and the VMT method. The percent error is calculated by $(C_{Comsol} - C_{VMT})/C_{VMT}$.

2.12   The Three Prototypical Behaviors

Each simulation of equations (24), (25) and (26) calculated the time sequence and ending equilibrium concentration of ferromagnetic nanoparticles as a function of location in blood and tissue. From this concentration data, cross-sectional plots spanning the diameter of the tissue-vessel system were generated. By varying the three non-dimensional numbers, three distinct particle behaviors were observed. These behaviors were then delineated on a plot of Renkin reduced diffusion coefficient versus magnetic-Richardson number for a given mass Péclet number (Figure 9). Péclet number dependence is subsequently shown in Figure 10 and Figure 11.

The three prototypical behaviors are shown below with an early, intermediate and steady state time snapshot.
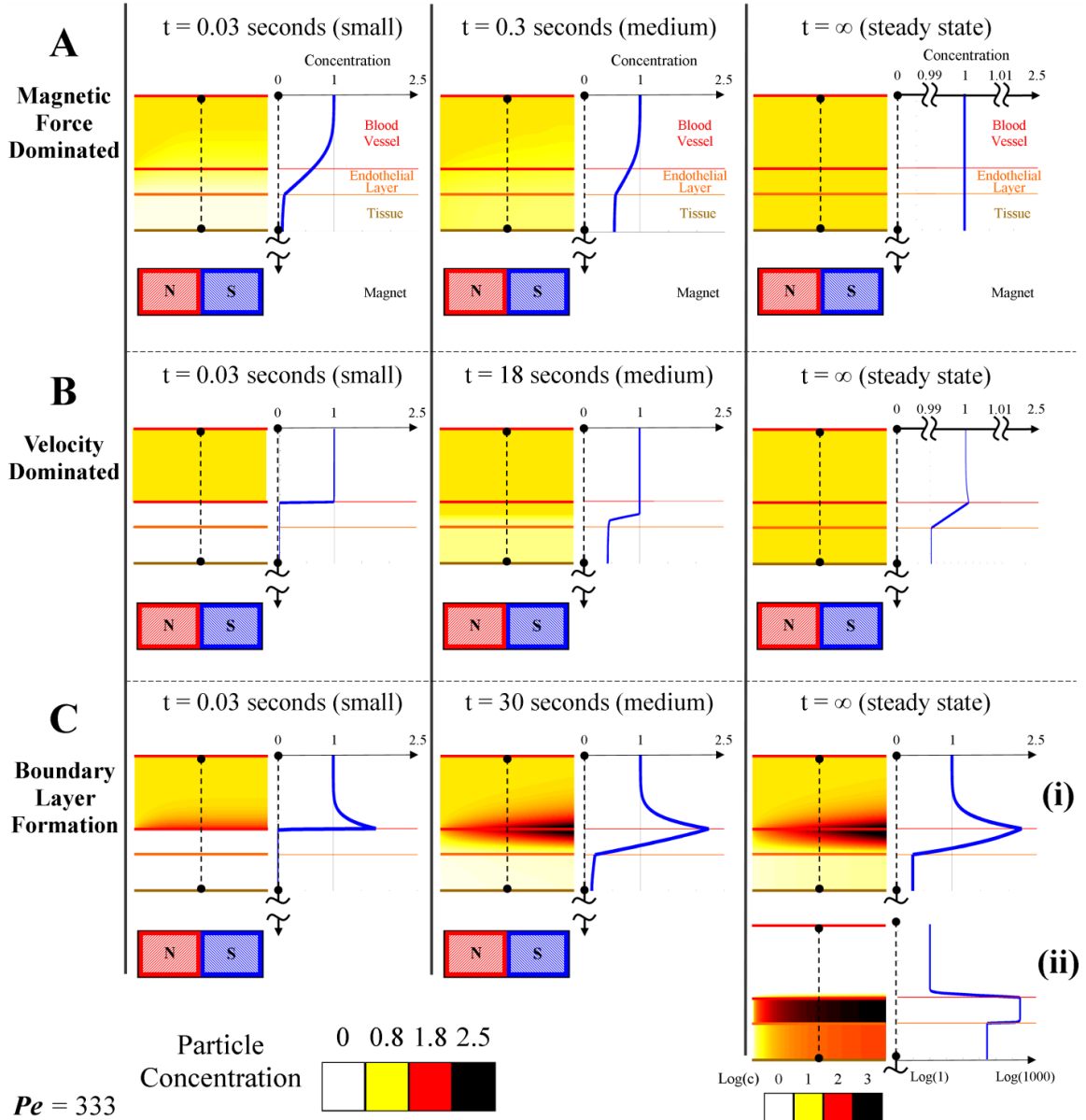
Figure 8: The three prototypical behaviors: A) magnetic force dominated case ($\Psi = 10^{-3}$, $\mathcal{D} = 1$), B) velocity dominated case ($\Psi = 10^{-5}$, $\mathcal{D} = 10^{-3}$), and C) boundary layer formation ($\Psi = 10^{-2}$, $\mathcal{D} = 10^{-3}$). (A) The magnetic force dominated case shows a cross-sectional concentration of the magnetic nanoparticles for three times at $t = 0.03$ seconds (early), 0.3 seconds (middle), and at equilibrium, at $Pe = 333$. Particles are pulled towards the magnet and out through the bottom of the tissue resulting in a constant concentration equal to the blood inlet concentration. Here the tissue diffusion is set to equal the diffusion in the endothelial membrane. (B) Velocity dominated shows a cross-sectional concentration of the magnetic nanoparticles for three times at $t = 0.03$ seconds (early), 18 seconds (middle), and at equilibrium, at $Pe = 333$. Particles are washed out before they generate a significant boundary layer along the vessel wall. At long times diffusion equilibrates the concentration between tissue and blood. Here the tissue Renkin number is set at $\mathcal{D}_\mathcal{T} = 10\mathcal{D}$, which means it is ten times as easy for particles to diffuse through tissue than through the endothelial membrane. (C) Boundary layer formation shows a cross-sectional magnetic

65

nanoparticle concentration for three times at $t = 0.03$ seconds (early), 30 seconds (middle), and at equilibrium, at $Pe = 333$. (i) The steady state profile for $\Psi = 10^{-2}$. Here the particle concentration is shown on the same linear scale as in other time snap shots. (ii) The steady state profile for a higher magnetic-Richardson number, for $\Psi = 10^{-1}$. Here both the particle concentration and the cross-sectional plot are shown on a log scale. In both boundary layer cases ($\Psi = 10^{-2}$ and 10^{-1}) the particles build-up along the vessel membrane on both the vessel side and within the membrane. The boundary layer forms very rapidly. In (ii) the membrane particle concentration is sufficiently high to cause a concentration in the tissue greater than the vessel inlet concentration. In both (i) and (ii) the tissue Renkin number is set at $\mathcal{D}_T = 10\mathcal{D}$ which means it is ten times as easy for particles to diffuse through tissue than through the endothelial membrane.

2.12.1 Magnetic Force Dominated Behavior

In this regime the applied magnetic forces dictate particle behavior. Here the magnetic forces control the transport of the particles irrespective of the blood drag forces. It turns out that when the magnetic force is dominant and is constant, the equilibrium concentration will approach a constant value throughout the tissue-vessel system being considered. The constant downward magnetic force pulls the nanoparticles from the blood vessel inlet downwards into the tissue and out the bottom, and any transient concentration gradients are smoothed out by diffusion. Here the maximum concentration never exceeds the inlet concentration, as shown in Figure 8(A). This is a reasonable result since we are assuming the blood vessel sees a constantly replenished supply of nanoparticles (from the rest of the body). The applied (approximately constant) magnetic force and diffusion then serve to distribute that concentration of nanoparticles equally throughout the region of tissue below the blood vessel and above the magnet. Here the applied magnetic field does not concentrate particle concentration in the blood vessel or surrounding tissue.

2.12.2 Velocity Dominated Behavior

In velocity or Stokes drag dominated behavior the blood drag force on a stationary particle far exceeds the magnetic and diffusion forces. Here the blood velocity washes the particles out the back of the vessel before magnetic forces have had a chance to affect them, as shown in Figure 8(B). Since the inlet of the vessel is always refreshing the fluid flow with the inlet concentration, the overall concentration in the blood remains near that of the inlet concentration. Particle concentration in the tissue is much lower even for long times but eventually, by diffusion, reaches a steady state where the concentration in the tissue is equal to that in the blood vessel. This case acts as if there is no magnet at all since blood forces far exceed its effect. Due to the speed of each effect, different time scales for the 'early' and 'middle' frames were chosen in Figure 8 so that the middle panels could illustrate the intermediate concentrations of each behavior.

2.12.3 Boundary Layer Formation

The boundary layer regime occurs when the magnetic and blood drag forces are comparable; it is the most interesting case. Figure 8(C) illustrates this case. In this regime, the nanoparticles build-up near the vessel wall, either inside the vessel where the blood velocity is near zero and/or in the membrane next to the vessel build-up (by diffusion). The concentration elsewhere in the blood essentially remains at the set inlet concentration. In this case the concentration of nanoparticles near the vessel wall can exceed the inlet concentration by double or higher. Compared to the previous velocity dominated behavior, which also exhibits a slight build-up of particles along the vessel wall, we define the ferrofluid behavior as forming a boundary layer when

67

(47) $C_{B,vessel-wall} \geq 1.01 C_{B,inlet}.$

In addition, it is this case which has the potential to increase the nanoparticle concentration within the tissue to above the unit (blood inlet) concentration, Figure 8(C(ii)). It is this boundary layer regime that illustrates how a focusing of nanoparticles is possible even if the magnetic force is substantially smaller than the centerline drag force (as in the rat example of Figure 2b).

While this behavior is desired for magnetic drug targeting, there are important considerations when a large concentration build-up occurs within the vessel membrane. If the particles carry a therapeutic compound, it is possible that undesired treatment of the vessel membrane will occur. This potential side effect is important to evaluate while developing a magnetic drug targeting treatment.

2.12.4 Mapping the Behavioral Space

Summary of Behaviors under Non-dimensional Number Variations

For ferro-magnetic nanoparticles under the action of diffusion, blood convection, and a magnetic force in a straight idealized blood vessel surrounded by tissue, we find three behavior regimes: magnetic dominated, blood velocity dominated, and a boundary layer formation regime. Only in the boundary layer case is the ferrofluid concentrated by the applied magnetic field (Figure 8(C)). In the magnetic and velocity dominated cases it escapes, either out the bottom of the tissue or through the blood vessel outlet. In these two cases it is only the constant re-supply of ferrofluid at the vessel inlet that provides the steady state ferrofluid concentrations shown in Figure 8(A and B).

68
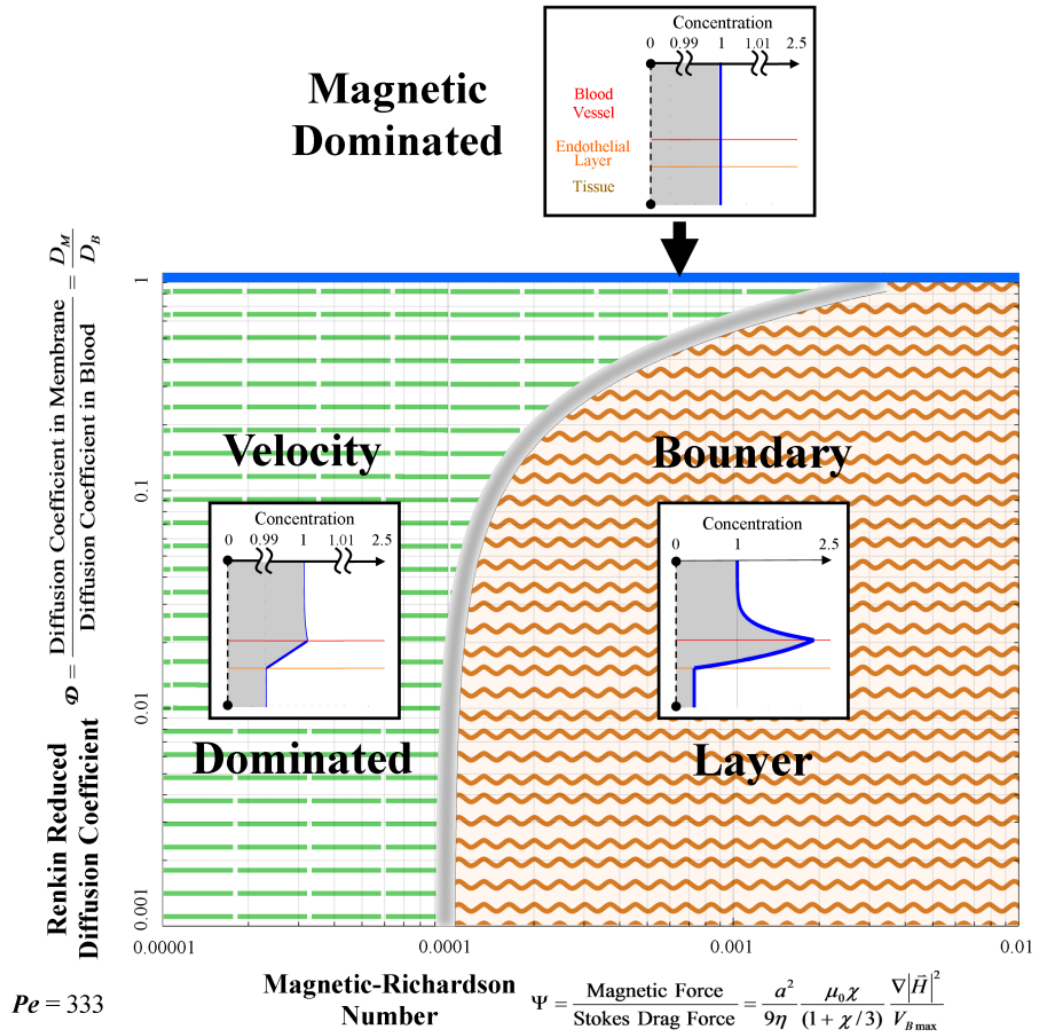
Figure 9: Magnetic nanoparticle behaviors as a function of the magnetic-Richardson and Renkin reduced diffusion coefficient non-dimensional numbers. The mass Péclet number was held constant. Three regions are shown: the magnetic dominated region at the top (the thin solid blue region); the velocity (Stokes drag) dominated region on the left (dashed lines region); and the boundary layer formation region on the right (wavy lines region). Notice that boundary layer build-up behavior is still possible even if the magnetic force is just 0.01% of the Stokes drag force at the vessel centerline, i.e. at $\Psi \geq 0.0001$. The boundary between the velocity and boundary layer build-up regions is diffuse as shown schematically by the thickness of the fuzzy gray line separating them.

For the simulation results below, the behavior of any case is grouped into one of these 3 regimes by analyzing the equilibrium concentration profile across the vessel cross-section. If the steady state cross-sectional concentration is uniformly equal to the inlet

concentration then the behavior is classed as magnetic dominated; if the steady state vessel wall concentration build-up is less than + 1% of the inlet concentration then it is classed as velocity dominated; and if the cross-sectional concentration exhibits high vessel wall concentration build-up then it is classed as boundary layer formation. In all cases, this classification exactly matches the qualitative classification based on transient and equilibrium behavior shown in Figure 8.

According to the range of dimensional parameters given in Table 1, the three key non-dimensional numbers were correspondingly varied between 10^{-8} and 30 for the magnetic-Richardson number, between 10^{-4} and 1 for the Renkin reduced diffusion coefficient, and between 30 and 1×10^{8} for the mass Péclet number. To examine the behaviors at a constant mass Péclet number, simulations were conducted over a logarithmically-spaced grid of 7 magnetic-Richardson and 5 Renkin numbers. Then, to determine the dependence on the Péclet number, the Péclet number was varied over 7 values while the Renkin number was held constant and the Richardson number was varied. This provided a general understanding of the non-dimensional number space. To precisely identify the locations of delineations between the 3 behavioral domains, simulations were completed over two fine grids. First, a fine grid of 10 magnetic-Richardson, 1 Renkin, and 9 Péclet numbers was used. Then, a grid of 13 Renkin, 6 magnetic-Richardson, and 7 Péclet numbers was used. In total, this yielded 720 cases that were simulated and analyzed. Figure 9 and Figure 11 below summarize the results and show the behavior delineations. Then random cases were simulated to verify the defined delineation regions.
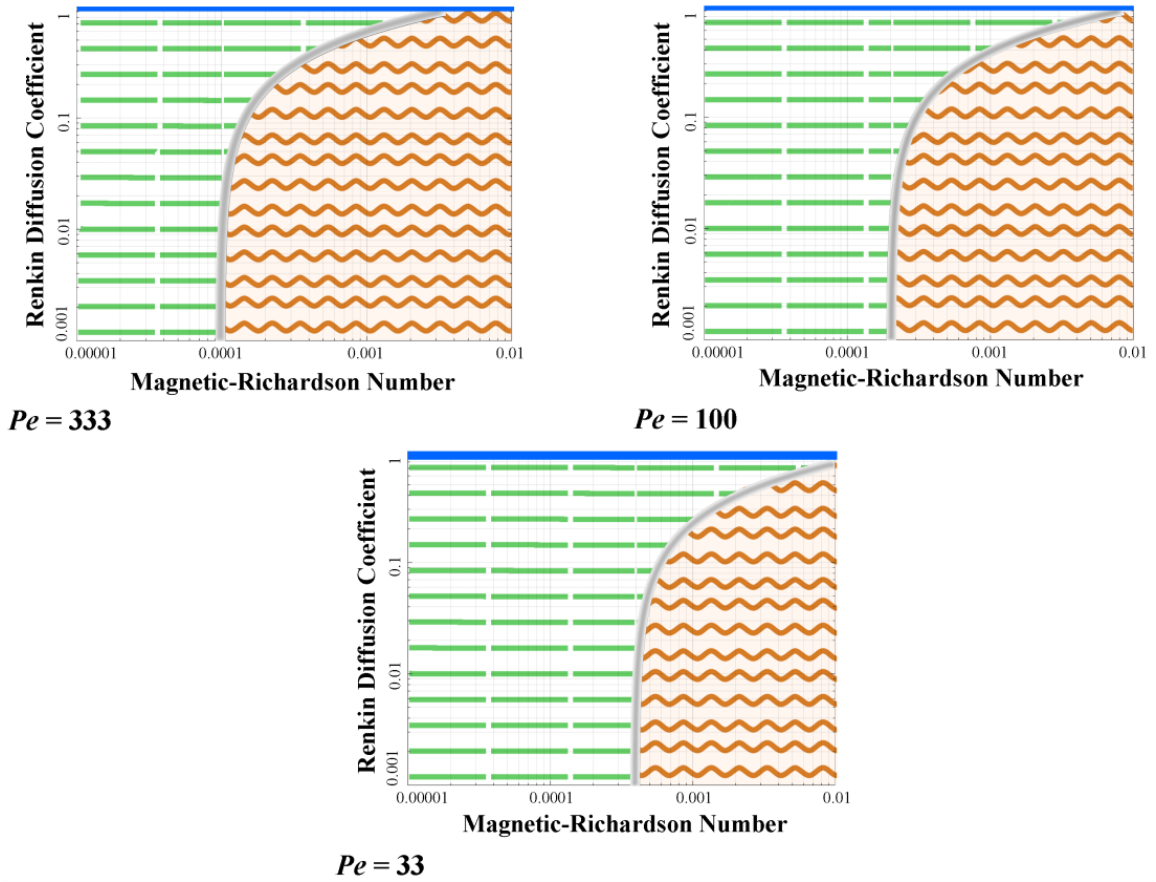
Figure 10: Behavioral dependence upon mass Péclet number. As the mass Péclet number decreases, the delineation between behavior types shifts to the right (to larger magnetic-Richardson numbers). In addition, at lower mass Péclet numbers, the magnetic dominated region increases in size towards lower Renkin reduced diffusion coefficients.

Figure 9 illustrates the behavior trends at a mass Péclet number of 333 (i.e. the convection of the nanoparticles is 333 times faster than their diffusion through the blood vessel width). It shows the regions in which the three behavior types occur. The velocity dominated region occurs at low magnetic-Richardson numbers where the Stokes drag forces are much larger than the magnetic forces. Meaning, there is a cutoff value at which the Stokes drag forces are able to overcome the magnetic forces sufficiently so that concentration build-up within the vessel is negligible. In contrast, at moderate and higher magnetic-Richardson numbers, the Stokes drag forces are not as effective and a highly

concentrated boundary layer develops. However, as the Renkin reduced diffusion coefficient is increased, this ferrofluid boundary layer region occurs less readily, because any build-up of particle concentration in the endothelium can more easily diffuse out into the vessel and be swept away by blood convection. Thus the velocity dominated behavior will also occur in circumstances where the membrane provides a weaker barrier to particle movement described by a larger Renkin reduced diffusion coefficient. This is shown by the curving gray line in Figure 9. But, at near unity Renkin reduced diffusion coefficients, the diffusion coefficients in the blood, endothelial membrane, and tissue are approximately the same and the particles see no difference between these three media leading to magnetically dominated behavior where magnetic forces pull particles downwards through the membrane and tissue towards the magnet.

Figure 10 illustrates the shift in behavior regimes with changing mass Péclet number. The changing Péclet number moves the behavior regimes on the magnetic-Richardson and Renkin axes. As the mass Péclet number decreases, i.e. as particle diffusion increases compared to their convection, the boundary between the velocity dominated and the boundary layer region shifts towards larger magnetic-Richardson numbers where larger magnetic forces are required to overcome the Stokes drag forces. As the particles are able to move more freely due to higher diffusion effects, they do not easily concentrate within the vessel and require larger magnetic forces to retain them near the vessel wall. In addition, it can be seen that at low mass Péclet numbers (< 50), the magnetic dominated region begins to grow in size and stretch to lower Renkin reduced diffusion coefficients.
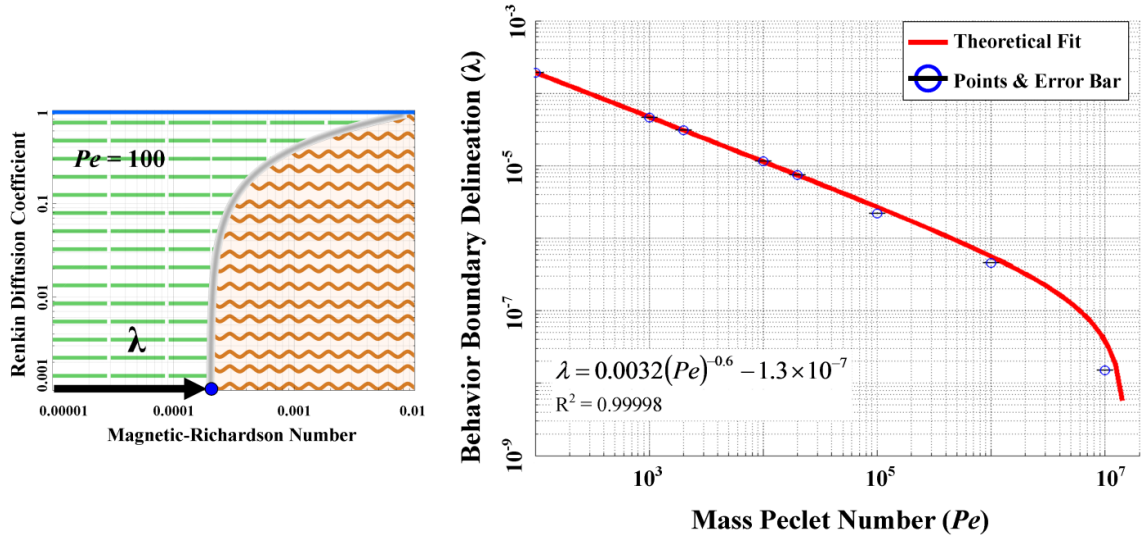
Figure 11: The delineation of the boundary between the velocity dominated and boundary layer formation regimes is denoted by λ (left panel, it is measured along the magnetic-Richardson axis at a Renkin coefficient of 10^{-3}) and it depends on the mass Péclet number (right panel). The stated equation provides a convenient fit of λ versus $\boldsymbol{Pe}$ for the curve shown in red.

The shift in the velocity-dominated/boundary formation behavior delineation, λ, due to a mass Péclet number change can be approximated by a power law fit $\lambda \approx 0.0032\boldsymbol{Pe}^{-0.6} - 1.3 \times 10^{-7}$ that has an R^2 value of 0.99998 (Figure 11). As the mass Péclet number increases, the delineation shifts to smaller magnetic-Richardson numbers. At a mass Péclet number of $\boldsymbol{Pe} > 2.1 \times 10^7$, $\lambda = 0$ and the characteristic behavior will be boundary layer formation. This suggests that at very large mass Péclet numbers (at very high blood velocities in big vessels) the nanoparticles will build-up along the blood vessel even with very small applied magnetic forces. This is because we assume that the particles continue to be supplied at a constant concentration at the inlet of the blood vessel (Figure 3) from the rest of the body. As they flow quickly to the right, the downward magnetic force brings them to the blood vessel wall predicting a sharp boundary layer due to the now, in comparison, small effect of diffusion. In practice when there are very large blood

73

velocities, only few nanoparticles immediately near the blood vessel wall will be captured during the short time that the nanoparticles remain within the vessel before they flow out the back. This leads to a very thin boundary layer formation of only a few particles at high mass Péclet numbers.
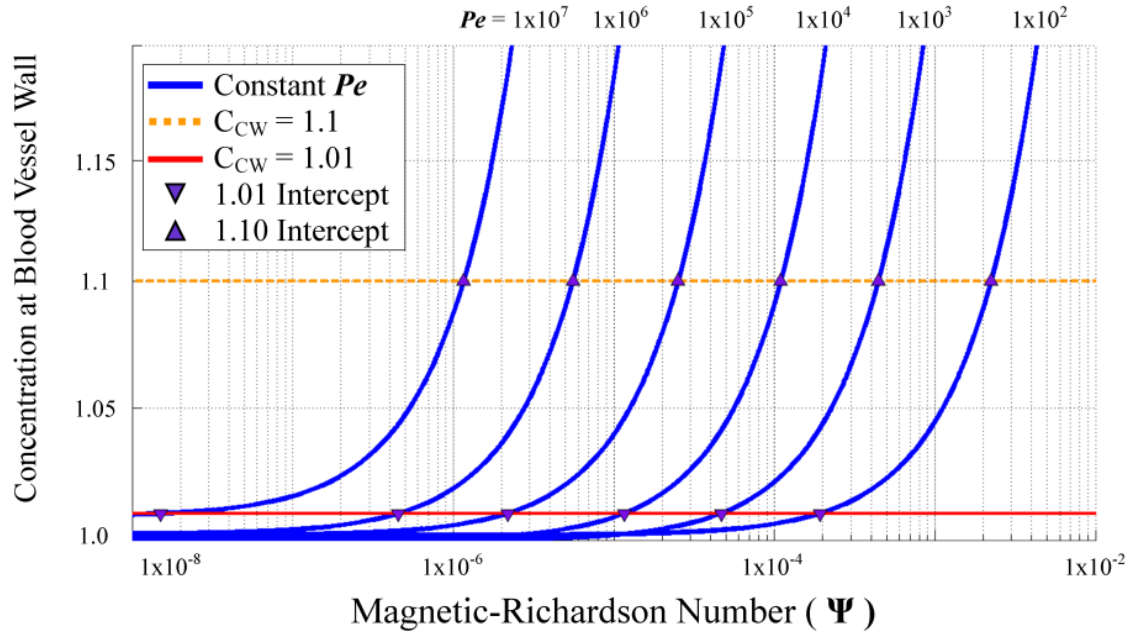
Figure 12: Concentration at the blood vessel wall ($C_{B,vessel-wall}$) versus magnetic-Richardson number for a given mass Péclet number. Curves associated with each constant mass Péclet number are shown in blue. The red line illustrates a concentration cutoff requirement of $> +1\%$ for boundary build-up behavior. Any magnetic-Richardson number larger than the intercept between the red line and blue curve for a given Péclet number (shown by a downwards purple triangle) will exhibit a boundary build-up behavior. The dotted orange line shows cutoffs for a higher vessel wall concentration requirement of $> +10\%$.

Figure 12 can be used to determine the blood vessel concentration ($C_{B,vessel-wall}$) for a given magnetic-Richardson number and mass Péclet number. The blue curves correspond to constant mass Péclet numbers and illustrate the blood vessel wall concentration's dependence upon magnetic-Richardson number. The concentration cutoff requirement of $> +1\%$ (equation (47)) is depicted by a red line, while an alternate equally-valid cutoff

requirement of $> +10\%$ is depicted by a dotted orange line. While equation (47) was used to define the behavior boundary delineation, a larger blood vessel wall concentration could easily be chosen and determined by Figure 12.

Figure 9, Figure 10, Figure 11, and Figure 12 can be used to quickly look up the expected behavior of any magnetic drug focusing experiment. For an *in vivo* setting, from a knowledge or expectation of the experimental parameters, the magnetic field strength, the magnetic field gradient, particle size, considered blood vessel depth, width, blood centerline velocity, and membrane pore size, the designer should compute or estimate the magnetic-Richardson number (equation (27)), the Renkin reduced diffusion coefficient (use the smaller of the two Renkin numbers between the endothelial membrane (29), and the tissue (31)), and the Péclet number (equation (28)). Then look up the resulting expected behavior in Figure 9 or Figure 10. (Use the λ fit equation of Figure 11 to find the location of the boundary between the velocity and boundary layer formation cases if your Péclet number is not one of those shown in Figure 10.)

The analysis above predicts experimental results in the literature extremely well, for both *in-vitro* and *in vivo* cases (see the next section). However, it still treats an idealized case. Additional model features, such as pulsatile blood flow, curved blood vessels, particle agglomeration, and skin boundary conditions are included in Section 2.15. Except for the effect of skin, which can significantly distort the ferrofluid concentration profile for blood vessels very near it, we find that none of these effects make a substantial difference

– the behavior is still magnetic dominated, velocity dominated, or forms a boundary layer essentially as outlined in Figure 9 and Figure 11.

2.13   Comparison with Experiments

Several experimental studies currently published ranging from *in-vitro* glass vessels to *in vivo* animal targeting have been studied and compared to our predicted behavior. Each experiment can be compared against Figure 9, Figure 10, Figure 11, and Figure 12. We find excellent agreement between prior published experimental observations and our predictions – in fact, there are multiple cases where we can now explain behavior that was not previously understood.

Table 3: Parameters for experimental studies reviewed in Sections 2.13.1 to 2.13.5. Bolded items are quantities used to determine our three characteristic non-dimensional numbers. Here 'cp' and 'M' are used to denote capillary and major blood vessel properties respectively. 'Sm' and 'Lg' denote small and large ranges. 'N/A' denotes inapplicable variables because the experiments were completed within glass tubes. '--' denotes unknown variables that are not needed because the magnetic forces were either supplied or could be otherwise be calculated.

Parameter			Ganguly	Xu	Widder	Bergemann	Lübbe
Particle Radius	a		5 nm	10 nm	7 nm[a] |0.5 μm[b]	125 nm	50 nm
Distance to Magnet	d		1 mm	--	5 mm	1 mm	0.5 cm
Field Strength Magnetic Intensity	$\|\vec{B}\|$ $\|\vec{H}\|$		1.3 T 1 x 10^6 A/m	--	0.55 T 4.3 x 10^5 A/m	0.5 T 3.9 x 10^5 A/m	0.8 T 6.3 x 10^5 A/m
Magnet Length	L_M		6 cm	--	--	5 cm	3 cm
Magnetic Force	$\|\vec{F}_M\|$		**4 x 10^{-5} pN**	**2.6 x 10^{-5} pN**	**0.12 pN**	**0.1 pN**	**3 x 10^{-2} pN**
Maximum Blood Velocity	V_{Bmax}	cp	4.8 mm/s	5.3 mm/s *	≈ 0.1 mm/s	≈ 0.1 mm/s	≈ 0.5 mm/s
		M		100 mm/s **	≈ 20 cm/s	≈ 20 cm/s	≈ 10 cm/s[#]
Vessel Diameter	d_B	cp	10 mm (3effective)	2 mm	≈ 6 μm	≈ 6 μm	≈ 7 μm
		M			≈ 1 mm	≈ 1 mm	≈ 5 mm
Fluid Viscosity	η		0.001 Pa s	0.001 Pa s	0.003 Pa s	0.003 Pa s	0.003 Pa s
Stokes Drag Force	$\|\vec{F}_S\|$	cp	**0.5 pN**	**1 pN ***	**3 pN**	**0.7 pN**	**1.4 pN**
		M		**20 pN ****	**6 nN**	**1.4 nN**	**0.28 nN**
Blood Diff. Coeff.	D_B		4x10^{-11} m²/s	2x10^{-11} m²/s	1x10^{-13} m²/s	6x10^{-13} m²/s	1x10^{-12} m²/s
Scattering Diff. Coef.	D_S	cp	N/A	N/A	0	0	0
		M			1x10^{-9} m²/s	1x10^{-9} m²/s	6x10^{-10} m²/s
Membrane Diff. Coef.	D_M	Sm	N/A	N/A	0	0	0
		Lg			1x10^{-13} m²/s	6x10^{-13} m²/s	6x10^{-13} m²/s
Tissue Diff. Coef.	D_T	Sm	N/A	N/A	0	0	0
		Lg			1x10^{-13} m²/s	6x10^{-13} m²/s	6x10^{-13} m²/s
Diffusion Coefficient	D_{Tot}	cp	**4x10^{-11} m²/s**	**2x10^{-11} m²/s**	**1x10^{-13} m²/s**	**6x10^{-13} m²/s**	**1x10^{-12} m²/s**
		M			**1x10^{-9} m²/s**	**1x10^{-9} m²/s**	**6x10^{-10} m²/s**
Magnetic-Richardson Number	Ψ	cp	*9 x 10^{-5}*	*2.5 x 10^{-5} **	*0.04*	*0.14*	*0.025*
		M		*1.3 x 10^{-6} ***	*2 x 10^{-5}*	*1.5 x 10^{-4}*	*1.3 x 10^{-4}*
Mass Péclet Number	***Pe***	cp	*3.6 x 10^5*	*5.3 x 10^5*	*4 x 10^3*	*1 x 10^3*	*3.5 x 10^3*
		M		*1 x 10^7*	*2 x 10^5*	*2 x 10^5*	*8.3 x 10^5*
Renkin Reduced Diffusion Coefficient	$\varPhi$	Sm	*N/A*	*N/A*	*≈ 0*	*≈ 0*	*≈ 0*
		Lg			*≈ 0.05*	*≈ 0.56*	*≈ 0.8*
Behavior Boundary Position	λ	cp	*1.6 x 10^{-6}*	*1 x 10^{-6}*	*2.2 x 10^{-5}*	*5 x 10^{-5}*	*2.4 x 10^{-5}*
		M		*7.2 x 10^{-8}*	*2.2 x 10^{-6}*	*2.2 x 10^{-6}*	*4.4 x 10^{-7}*

(*) 100% retention of particles; (**) 15% retention of particles; ([#]) ignores vena cava and aorta velocities; ([a]) radius of magnetite particle; ([b]) radius of microsphere or liposome.

2.13.1 Analyzing Ferrofluid Transport for Magnetic Drug Targeting [228]

Ganguly *et al.* attempted to capture ferrofluid particles within a glass tube containing a moving fluid by using a permanent magnet located beneath the tube. The set-up is analogous to the one presented in this chapter allowing for an easy comparison. Table 3 shows the parameters used in this experiment and the corresponding values of our three non-dimensional numbers.

It is important to note that in this experiment, the particles are injected into the bottom $1/16^{th}$ section of the glass pipe. They continue axially along this radial location until they encounter the magnet. Therefore, although the maximum velocity of the fluid within the pipe is 2.5 cm/s, the maximum fluid velocity experienced by the particles is 4.8 mm/s (assuming a parabolic velocity profile). This produces the Ψ, *Pe*, and $\mathcal{D}$ non-dimensional numbers noted in the 'Ganguly' column of Table 3.

Here the Renkin reduced diffusion coefficient is not applicable because there is only a single vessel domain. Thus, the behavior of the particle concentration is dependent solely upon the magnetic-Richardson and mass Péclet numbers. The mass Péclet number leads to the estimation of the velocity/ boundary layer delineation position λ. By comparing this value to the magnetic-Richardson number, the behavior type can be determined. Since $\Psi = 9 \times 10^{-5} \gg \lambda = 1.6 \times 10^{-6}$ this places the predicted behavior squarely within the boundary layer formation regime (even though the centerline Stokes drag far exceeds the maximal applied magnetic force, $\Psi \ll 1$). We thus correctly predict the experimentally observed boundary-layer formation region where the usual Stokes drag vs. magnetic forces back-of-the-envelope analysis fails.

2.13.2 Site-directed Research of Magnetic Nanoparticles in Magnetic Drug Targeting [106]

Similar to the experiment described above, Xu *et al.* captured moving nanoparticles within a glass tube using a permanent magnet. Xu's experiment, in contrast to Ganguly, includes a magnet located farther away and a spherical capturing chamber is used (the glass tube spreads out into a spherical bulb and then goes back to a straight tube). The bulk fluid velocity was adjusted, and the retention percentage within the capturing chamber was quantified for various speeds. The authors noted that the retention was 100% at a 5.3 mm/s and $\approx$ 15% at 100 mm/s. The parameter values for these cases are shown in Table 3 under 'Xu'.

Similar to Ganguly's experiment, due to a single vessel domain the Renkin reduced diffusion coefficient is not applicable. As above, the delineating boundary position λ and the magnetic-Richardson number Ψ are compared for the two cases Xu *et al.* considered. When the fluid velocity is 5.3 mm/s, the magnetic-Richardson number is x 25 larger than the behavior delineation λ. This comparison implies behavior well within the boundary layer regime. However, to correlate this behavior to the measured capture percentage requires determination of the boundary thickness that develops before the capture region. Since nanoparticles were not pre-mixed with the fluid but instead injected into the flow, the particles retain their initial injection position within the flow section. If the particles are assumed to be in the lower quarter of the flow near the magnet (a reasonable assumption if the particles were injected with minimal velocity), then the boundary layer that is swept into the spherical capturing chamber can be determined. If the particles are

79

flowing at 5.3 mm/s then the capture percentage predicted by a simulation of this case was ≈ 100% which matches the measured 100% retention by Xu *et al.* When Xu set their velocity to the higher 100 mm/s value, only 15% of the particles were captured in their experiment. In this case the delineating boundary position λ is a little closer to the magnetic-Richardson number (λ is $\times 18$ greater then Ψ). The percentage captured predicted by a simulation of this case was 13%, which closely matches the 15% retention measured by Xu *et al.*

Xu et al. commented that the standard force comparison (capture force requirements versus magnetic forces) did not predict the occurrence of their observed behavior. They suggested that the particles agglomerated to generate large magnetic forces. While agglomeration may increase magnetic force upon the concentration of particles (see Section 2.15.5), our more subtle comparison of magnetic forces versus Stokes drag forces away from the channel centerline is sufficient to correctly predict Xu's results.

2.13.3 Tumor Remission in Yoshida Sarcoma-Bearing Rats by Selective Targeting of Magnetic Albumin Microspheres Containing Doxorubicin [36], [266]

Widder *et al.* conducted *in vivo* experiments on rats to target tumors located on the tail using magnetically responsive microspheres and an external magnet. These microspheres are composed of a coat of albumin surrounding magnetic material (magnetite nanoparticles with 10-20 nm diameters) and a chemotherapy agent (doxorubicin). Magnetic material composition within microspheres has a wide range but is typically

between 20% to 50% by weight (w/w) [195]. Knowing the density of the albumin shell (1.36 g/ml [267]), the number of particles within a 1-micron sized microsphere can be approximated ($\approx$ 6000 for 20% w/w). They injected the ventral caudal artery near the rat tail tumors with these magnetically responsive albumin microspheres. The permanent bipolar adjustable gap magnet was positioned around the tumor and held for 30 minutes. For cases in which the magnet was applied, the rats saw decreased tumor size over the length of the experiment. Without a magnet, the rats usually had an increased tumor size and eventually died during the experiment. These data suggests that the magnetic particles were concentrated by the magnet at the tumor location.

Table 3 shows the numbers for this experiment. There is a range of appropriate magnetic-Richardson numbers here, from $\Psi \approx 0.04$ (for small capillaries) to $\Psi \approx 2 \times 10^{-5}$ (for major vessels). Likewise, the Péclet number varies from 4×10^3 to 2×10^5. Finally, the Renkin diffusion coefficient, determined from Equation (30), ranges between $\mathcal{D} \approx 0.05$ when in sinusoidal capillaries (liver, spleen and bone marrow) and essentially zero when in continuous capillaries and fenestrated capillaries. For tumors with leaky vessels that have an average membrane pore size of 600 nm, the maximum Renkin number is $\mathcal{D} \approx 0.002$. Based on this, we predict that the behavior delineation position will be $\lambda \approx 2.2 \times 10^{-5}$ for capillaries and $\lambda \approx 2.2 \times 10^{-6}$ in large vessels. Since the delineation position is well to the left of the magnetic-Richardson number, the behavior will primarily be boundary layer formation. We thus predict, except for situations where the Renkin number approaches unity (for damaged or sinusoidal vessels), that the particles can be accumulated to higher concentrations due to a boundary layer formation in the tail

for all physiological conditions – for small and large vessels, with fast and slow blood vessel velocities. Since the rat tumors decreased in size due to magnetic forces, it is reasonable to conclude that the magnetic particles were targeted into and around the tumor location. This matches our theoretical predictions above.

2.13.4 Preclinical Trials Experiences with Magnetic Drug Targeting [31], [220]

The rat experiments of Figure 2b are used as an example throughout this chapter. The non-dimensional numbers for these experiments are summarized in Table 2 under 'Bergemann'. Here, for a 1 mm focusing depth, the magnetic-Richardson number Ψ varies from 0.14 in capillaries to 1.5×10^{-4} in large vessels and the Péclet number varies similarly from 1000 to 2×10^{5}. The Renkin reduced diffusion coefficient is effectively zero for continuous and fenestrated capillaries. In sinusoidal capillaries, the Renkin value is approximately $\mathcal{D} \approx 0.56$ and within leaky vessels with an average pore size of ≈ 600 nm the Renkin value is $\mathcal{D} \approx 0.36$. From these values, the behavior delineation position is predicted to be $\lambda \approx 5 \times 10^{-5}$ in capillaries and $\lambda \approx 2.2 \times 10^{-6}$ in large vessels.
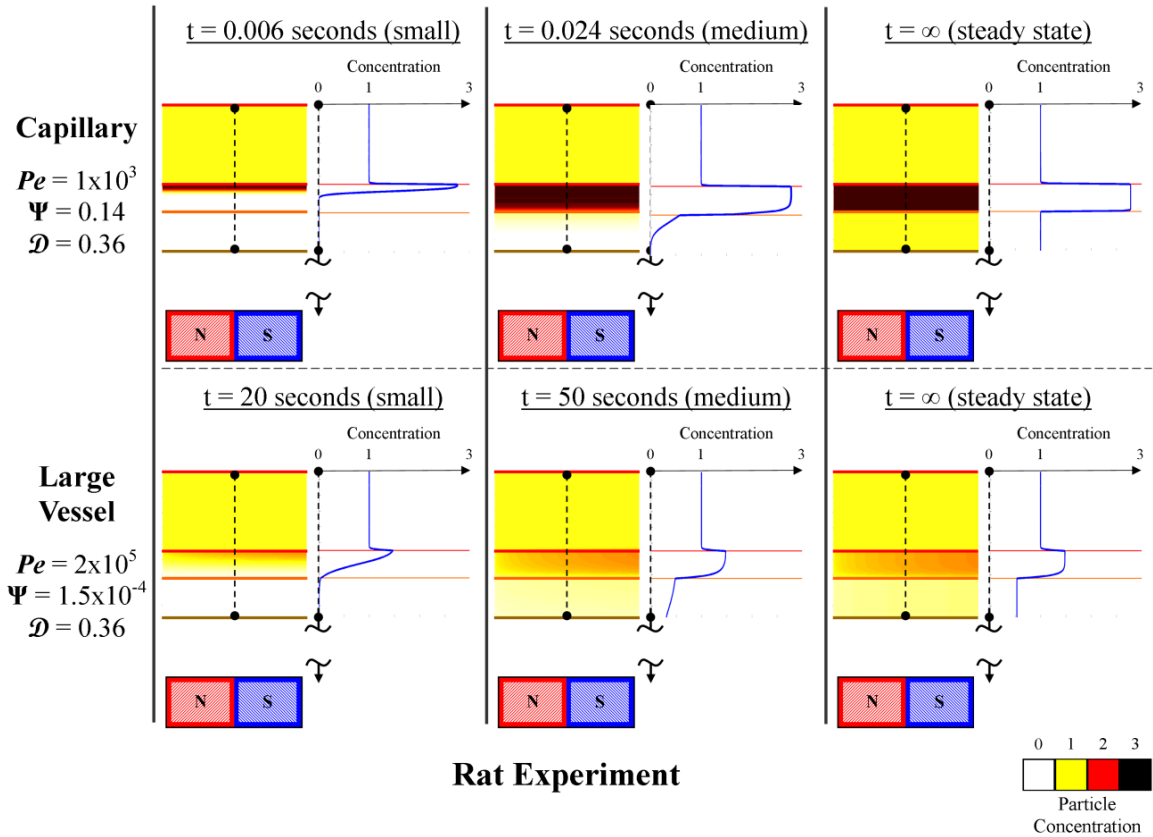
Figure 13: Predicted ferrofluid concentrations for 1 mm deep magnetic targeting in the rat experiments of Figure 2b. An initial, intermediate, and final (steady-state) time are shown for capillary (slowest blood flow, $V_{Bmax} = 0.1$ mm/s) and a major blood vessel (fastest blood flow, $V_{Bmax} = 20$ cm/s). Contrary to the crude estimate in the introduction, magnetic focusing is predicted even in the major blood vessels.

Since Ψ far exceeds λ, both capillaries and large vessels at ≤ 1 mm depth will experience a boundary layer formation behavior, except for situations where the Renkin number closely approaches unity (for damaged vessels) then velocity dominated behavior occurs. Figure 13 shows the predicted transient and equilibrium ferrofluid concentration for a capillary and major blood vessel at 1 mm depth near the magnet. Ferrofluid focusing is seen near the blood vessel wall for both the slowest (capillary) and the fastest (major artery) blood flow.

2.13.5 Clinical Experiences with Magnetic Drug Targeting [14]

Lübbe has performed phase I human clinical trials for the treatment of head, neck and breast cancer shallow (near the skin) tumors (last column in Table 3 under 'Lübbe'). At the surface of the tumor (at a 0.5 cm distance from the magnet) the magnetic-Richardson number varies from 0.025 in capillaries to 1.3×10^{-4} in large vessels and the Péclet number varies similarly from 3500 to 8.3×10^5. The Renkin reduced diffusion coefficient is effectively zero for continuous capillaries. In fenestrated capillaries and sinusoidal capillaries the Renkin value is respectively $\mathcal{D} \approx 0.002$ and $\mathcal{D} \approx 0.8$. Within leaky vessels with an average pore size of ≈ 600 nm the Renkin value is $\mathcal{D} \approx 0.7$. From these values, the boundary position delineation is predicted to be $\lambda \approx 2.4 \times 10^{-5}$ in capillaries and $\lambda \approx 4.4 \times 10^{-7}$ in large vessels.

We find that the magnetic-Richardson number Ψ is several orders of magnitude larger than the behavior delineation position value λ at the surface of the tumors. Therefore, a boundary layer formation behavior is predicted at tumor surfaces. A boundary behavior, however, will still occur at some distance within the tissue as long as the magnetic force upon those deeper particles keeps the magnetic-Richardson number within the boundary layer formation regime. The depth of boundary layer formation can be determined within a given force field for physiological blood velocities (capillaries and large vessels) as shown in Figure 14. Up to a depth of 5 cm and 7.9 cm for large vessels and capillaries respectively, the particles will exhibit a boundary layer behavior. After these cutoff distances, the nanoparticles will exhibit a velocity dominated behavior and will be washed away by blood flow in major and minor blood vessels respectively. Between a

distance of 5 cm and 7.9 cm, the particles will transition from a complete boundary layer behavior to a velocity dominated behavior getting washed away first in larger vessels that exhibit a higher blood velocity.
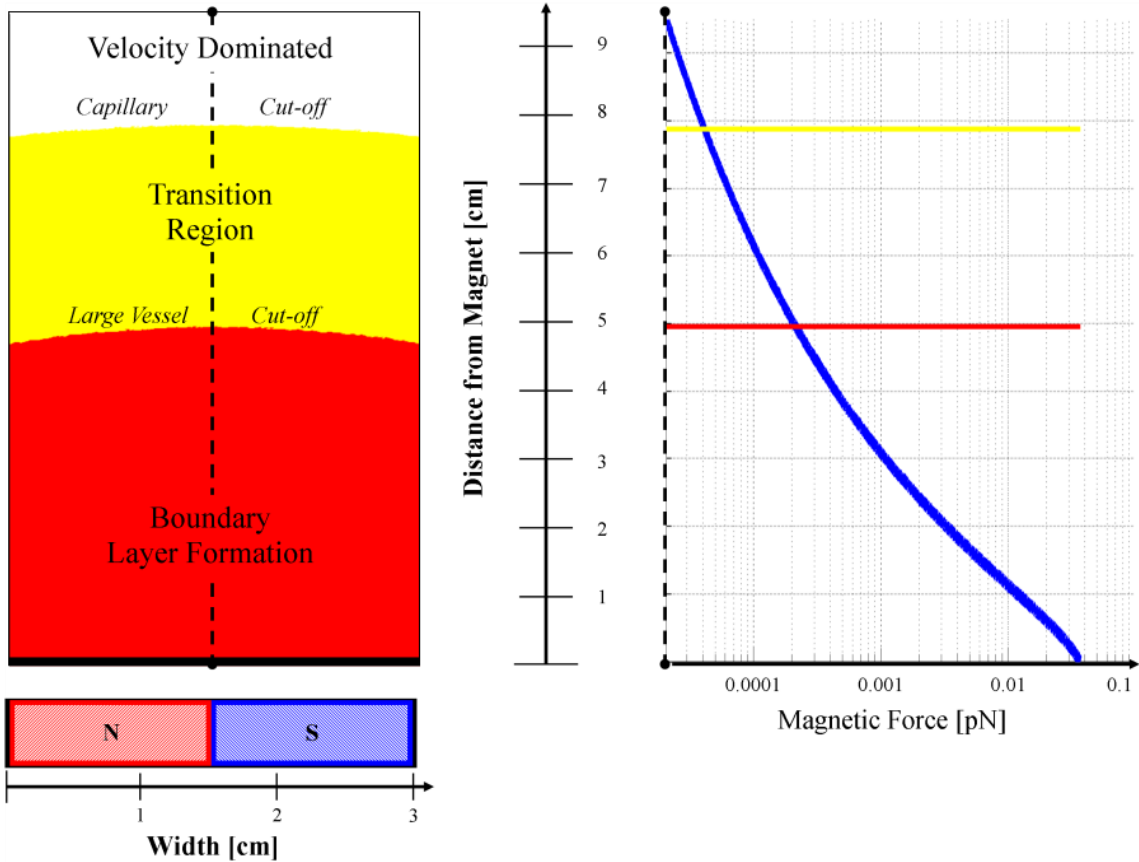
Figure 14: Focusing depth for the Lübbe 0.8 Tesla human clinical trials experiments. The magnet is positioned a distance of 0.5 cm from the skin. The predicted depth of the boundary layer formation, transition, and velocity dominated regions is shown. For particles deeper inside the body, the magnet is unable to exert a sufficient magnetic force (shown on the right) to generate a ferrofluid boundary layer behavior. Focusing of magnetic nanoparticles is predicted to be possible in major vessels up to a 5 cm depth, and in capillaries to a greater 7.9 cm depth.

During Lübbe's clinical trials, nanoparticles were observed to be targeted approximately within 5 cm [268] of the magnet located at the tumor site by magnetic resonance imaging immediately after treatment (Figure 2a), a finding that is consistent with our predictions here [31]. If the same sized particles with a stronger and larger magnet were used, such as

a 2 Tesla (MRI strength) electromagnet with a 25 cm diameter, 20 cm length and 5 cm air core, then we predict that targeting would be possible to a depth of 20 cm in large vessels and to a depth of 30 cm in capillaries.

2.14   Summary of Cases

Figure 15 shows a graphical representation of all the experimental cases considered in this chapter and compares them to our predicted behavior. For the human clinical trials (Lübbe), the experimental domain is represented more accurately as being curved because the magnetic-Richardson number and the mass Péclet number both vary together across human physiological conditions: blood velocity is higher in bigger blood vessels [265]. This affects both the Richardson and Péclet numbers (see equations (27) and (28)). It was possible to quantify the upper and lower bound curves for human experiments (Lübbe), but not for animal experiments (Widder and Bergemann), because more published physiological data is available for humans. A detailed analysis and derivation of the curves used is provided in the Section 2.10.
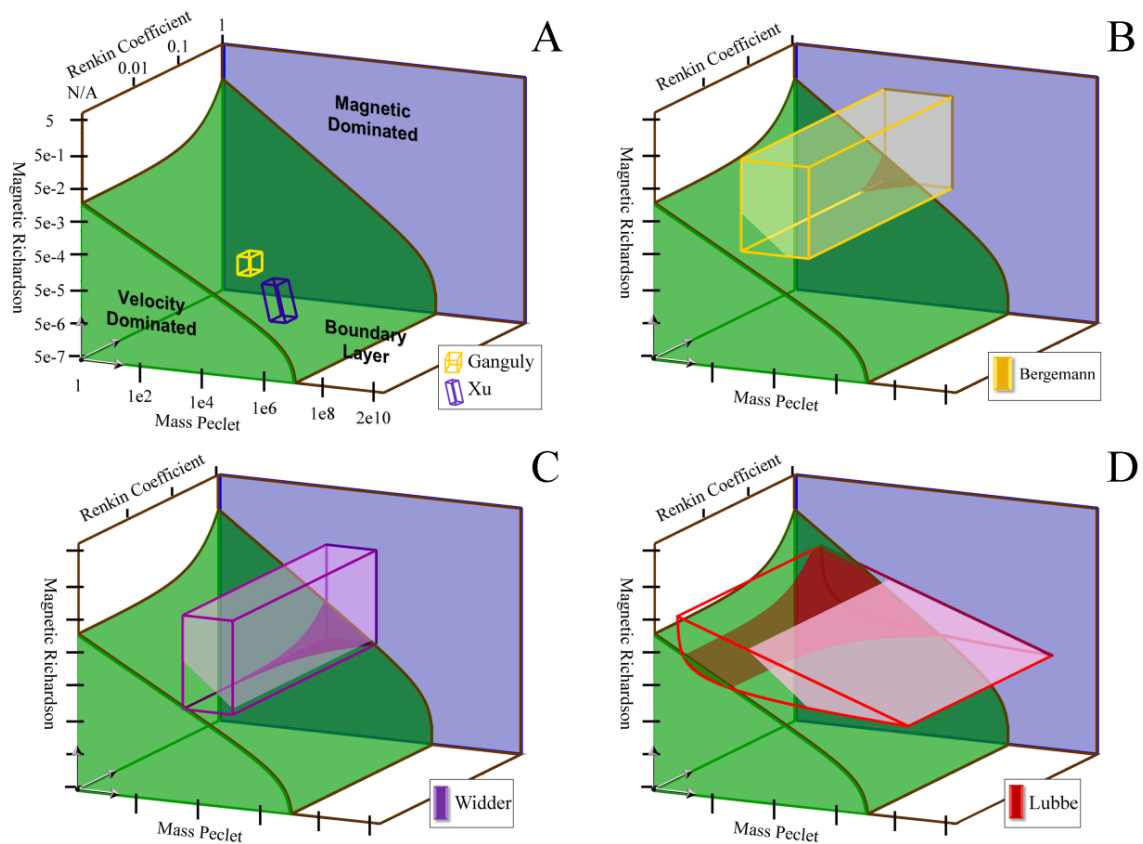
Figure 15: Summary of experimental studies. The firmly shaded regions in green and blue denote the magnetic and velocity behavior domains. The boxed or curved boxed regions show the values spanned by each experiment. The dark shading (dark yellow in B, purple in C, and dark red in D) shows the region of the corresponding experiment that exists in the velocity dominated region. The light shading (light yellow in B, light purple in C, and pink in D) shows the region of the experiments where the concentration created in the tissue is greater than the vessel inlet concentration. The *in-vitro* experiments (A) exist entirely in the boundary layer regime. Widder (B) and Bergemann (C) have small portions in the velocity dominated region, only at small magnetic-Richardson numbers and high Renkin coefficients. Lübbe (D) extends into the velocity behavior domain when mass Péclet numbers and magnetic-Richardson numbers are small, and this extent increases as the Renkin coefficient increases.

Figure 15 also shows where the magnet creates a concentration in the tissue that is greater than the systemic injected concentration. In the boundary layer domain, even though particles accumulate at the blood/membrane interface, there are some cases where that accumulation is high enough to create a $C > 1$ in the surrounding tissue, and others

where the accumulated amount is insufficient. The cases where more tissue accumulation occurs are influenced by the endothelium thickness to blood vessel diameter ratio, and this additional geometric consideration adds a further non-dimensional number that can be varied. In Figure 15, the lightly shaded regions (light yellow in B, light purple in C, and light pink in D) show the extent of the experimental domains that are predicted to have a tissue concentration greater than unity. Here we assumed a representative endothelium thickness to vessel diameter ratio, a ratio that corresponds to a typical arteriole.

2.15   Relaxing Simulation Parameters

Additional features can be added to relax simulation idealizations. These features sometimes make a quantitative difference to the nanoparticle concentration profiles but, with the exception of the skin boundary condition, they do not make a qualitative difference. The three behavioral forms still occur though their delineations can shift moderately depending upon the features added.

2.15.1 No Extravasation through Blood Vessel Membrane

First, there is a trivial case to consider when the blood vessel will not allow any particles to pass through the membrane into the surrounding tissue: i.e. no extravasation. This case can be modeled by forcing the flux normal to the blood vessel membrane surface to be equal to zero. Figure 16 shows how the two characteristic behaviors (velocity dominated and boundary layer formation) remain in effect in this case. The magnetic dominated

behavior, however, which requires particles to move from the blood into the tissue, is no longer possible.
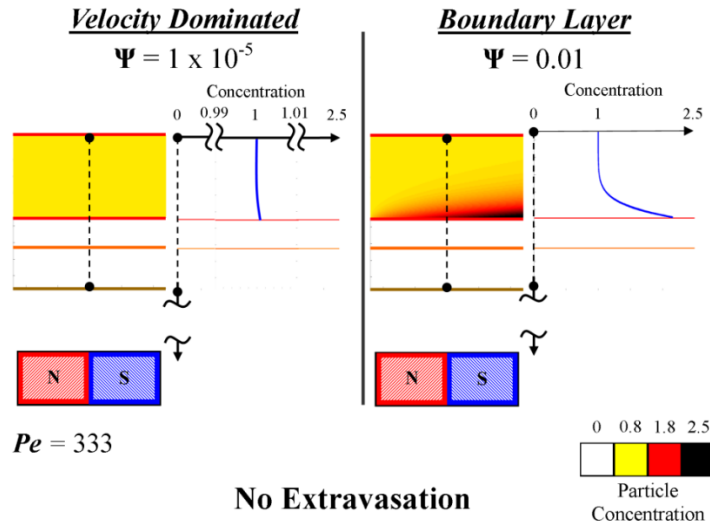
Figure 16: No extravasation through the blood vessel membrane. The characteristic behaviors still exhibit their defining characteristics within the blood vessel. The magnetic dominated case is no longer possible. Instead, when there is no extravasation (e.g. for particles bigger than blood vessel fenestrations) magnetic dominated behavior is replaced by a boundary layer type behavior.

2.15.2 Pulsatile Blood Flows

Flow in blood vessels is pulsatile [255], [269]–[272], its forward velocity increases and decreases as the heart pumps (see Figure 5(a) in [269] of an archetypal peak velocity waveform complied from 3560 cardiac cycles). We now include this blood velocity oscillation and show that it does not qualitatively change the 3 types of behavior we see – we still find a magnetic dominated, velocity dominated, and boundary layer regime.

The waveform associated with high pulsatile cardiac blood flow was used to set the blood velocity in time. A choice of three heart rates was used (a resting heart rate of 1 Hz, 1.5 Hz, and a rat heart rate of 6.75 Hz) and applied to three cases that produce the three

characteristic behaviors. Since magnetic drug targeting localizes particles to a region by use of a magnet held locally for minutes, e.g. [108], but blood pulsation occurs once every second, it is appropriate to consider the averaged effect that the pulsating blood flow will have on particle concentration. Figure 17 shows the time averaged concentration profiles taken for three heartbeats after a treatment window of one hour for the 9 chosen cases.

In comparison to [273], we do not consider a significant ferrofluid inlet concentration where the ferrofluid can then become an obstacle to the incoming flow and therefore we do not expect recirculation regions to be created. This phenomenon can make the average of the pulsatile case differ from the steady inlet flow case. Based on the range of biological parameters, the relevant non-dimensional numbers possible range between 0.01 (in capillaries) and 27 (in the largest vessels) for the Womersly number and the Reynolds number varies between 0.001 (in capillaries) and 3900 (in the largest vessels such as the aorta or vena cava).
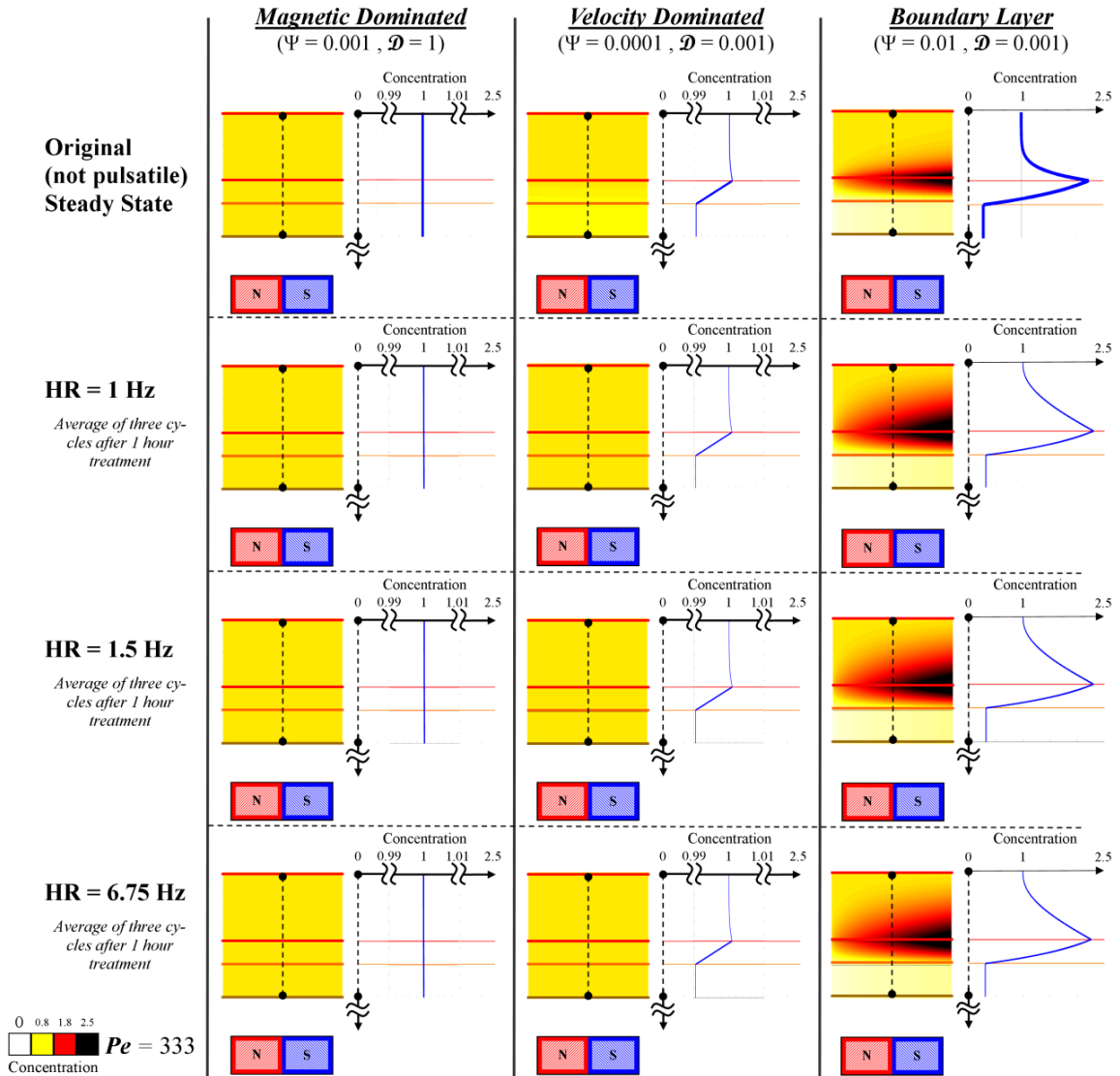
Figure 17: Pulsatile blood flow concentration profiles for the three characteristic behaviors experiencing three different heart rates (HR). For each pulsatile case, the concentration profile consists of the time average for three heartbeats after a treatment window of one hour. This concentration can be compared to the prior steady state concentrations when blood flow pulsatility is not considered. The three behaviors are qualitatively the same and further are also similar quantitatively. (For this 333 Péclet number case, the Womersley and Reynold numbers can vary between 0.01 to 0.19 and 0.001 to 2.6 respectively for physiological and practical engineering conditions, according to the parameters in Table 1.)

Figure 17 shows that blood pulsatility under a uniform magnetic force field does not impact behavior delineation: the time-averaged concentration profiles remain in the magnetic dominated, velocity dominated, or boundary layer regime as they were in the

91

constant blood flow case. This result has allowed for the simplification of the physiological model to the cycle-averaged blood velocity experienced within that vessel, a simplification we have used throughout the chapter.

2.15.3 Non-Uniform Magnetic Force Fields

Previously, we treated the magnetic force as constant (see Figure 4). Here the exact magnetic field and the spatial variation in the resulting magnetic force on the magnetic particles is used. The magnetic force increases as the particles move closer to the magnet. Various parameters for a particular experiment will adjust how much the magnetic force increases in the blood vessel and surrounding tissue. These parameters include the size of the magnet, the size of the considered tissue-vessel system, and the distance of the tissue-vessel system from the magnet. In this section we exactly solve the magneto-static equations (8) to (10) and plug the computed magnetic field $\vec{H}(x, y)$ into equation (17) to state and solve the PDE for particle transport (previously the magnetic force $F \sim \nabla H^2$ was assumed to be a constant pointing downwards). To quantify the deviation from a uniform magnetic force, we use the metric $R_M = F_{M,max} / F_{M,centerline}$ where $F_{M,centerline}$ is the magnetic force along the blood vessel centerline and $F_{M,max}$ is the maximum magnetic force within the considered vessel-tissue domain (it occurs at the bottom of the domain nearest the magnet corners where the magnetic field gradients are the highest). To examine how non-uniform magnetic force fields affect the three prototypical behaviors, three case studies were simulated for a varying magnetic force ratio of $\mathbf{R_M}$ = 2 and 10. $\mathbf{R_m}$ was varied by increasing the size of the magnet and reducing the distance between the vessel and magnet.
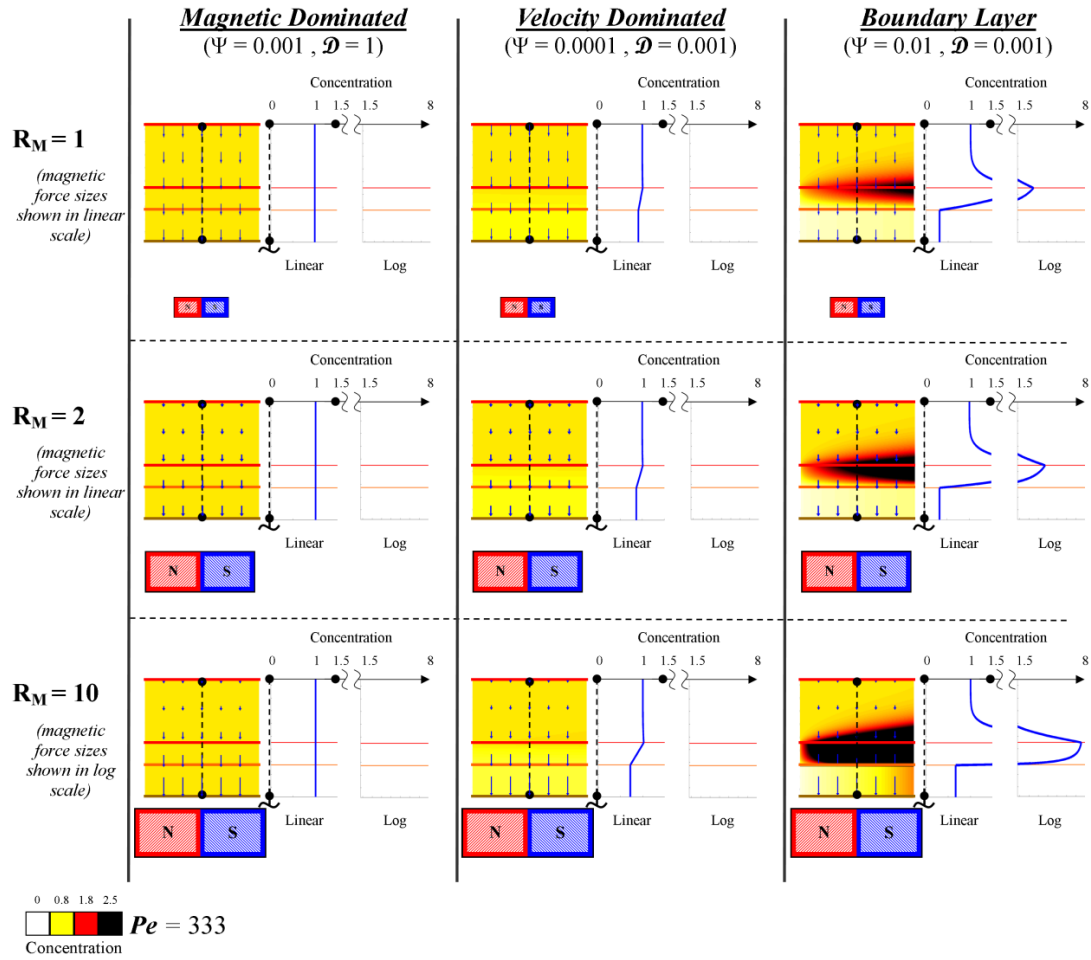
Figure 18: Concentration profiles for various magnetic force ratios. Three cases were chosen that illustrated the prototypical behaviors (magnetic dominated, velocity dominated, and boundary layer formation behavior) and the magnetic force ratio was changed from $R_M = 1$ to 2 and 10 by increasing the size of the magnet and reducing the distance between the vessel and magnet. The exact magnetic forces are shown as blue arrow overlays within each plot. The case of $R_M = 1$ and 2 show the arrow magnitudes in linear scale, while the case of $R_M = 10$ shows the arrow magnitudes in log scale (an arrow with twice the length will have ten times the magnitude).

Figure 18 shows how the magnetic force ratio does not affect the prototypical behavior. When $R_M = 1$, the simulation is exactly equivalent to the cases considered in the main chapter. As R_M increases, the maximum magnetic force at the bottom edge of the tissue-vessel system increases. In the case of a magnetic dominated behavior, the magnetic force ratio has very little to no effect on the solution. For velocity dominated cases, the

vessel still maintains the inlet concentration value but the concentration in the tissue and membrane decreases due to increased pull from the magnet. Lastly, in the boundary layer formation cases, the vessel wall concentration simply increases. Since the vessel wall concentration at a given magnetic-Richardson number increases with the magnetic force ratio $\mathbf{R_m}$, the behavior delineation position (λ) will shift left in Figure 11 as the magnetic force ratio increases.

2.15.4 Curved Blood Vessels

Blood vessels within any organism are rarely, if ever, straight. The idealized straight blood vessel used throughout the chapter was relaxed and two different curvatures were utilized to determine the variance of the characteristic behaviors. The blood vessel length in each case was kept constant, and the only geometric parameter that changed was the radius of curvature. As can be seen in Figure 19 below, the characteristic behaviors retained their defining qualities. The only difference in cross-sectional concentration was seen in the boundary layer formation cases where the slight curvature case experienced a modest increase in concentration compared to no curvature or large curvature. This was because a slight curvature contained a longer segment of blood vessel in which the particles are able to form a boundary layer leading to a higher concentration build-up over that particular segment. However, this increase in concentration only shifts the boundary behavior delineation and does not change the overall observed behavior.
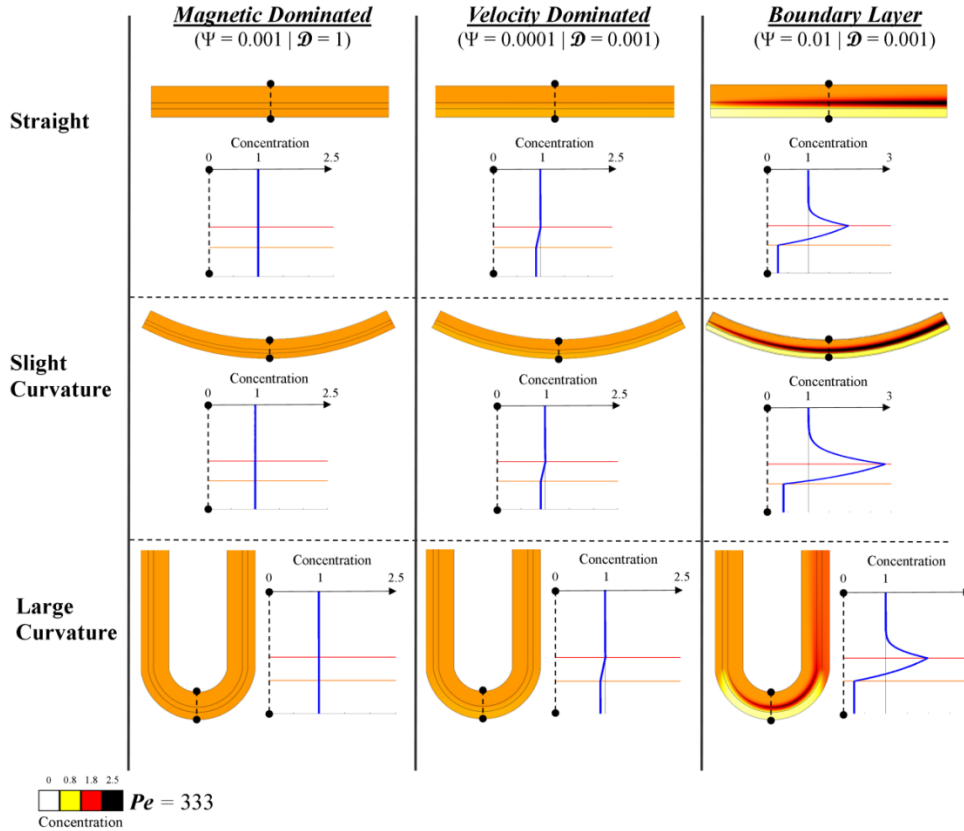
Figure 19: Curved blood vessels and the three prototypical behaviors. The curvature of the blood vessels does not affect the characteristic trend of the behaviors, but it can shift the behavior boundary delineation curve slightly.

2.15.5 Particle Agglomeration

Agglomeration of particles can be considered approximately within our current framework. To do so, we think of a 'super-particle' composed of n ferro-magnetic particles stuck together. The magnetic force on such a particle increases by a factor of $\times\, n$. However, the diameter of the particle goes only as $\sqrt[3]{n}$ since it takes $2 \times 2 \times 2$ or $\times 8$ particles to make a twice-as-big super-particle. Thus, the Stokes drag force increases by $\sqrt[3]{n}$ and so the magnetic-Richardson number increases by $n^{2/3}$ (see equation (27)). For the nanoparticles used in the rats of Figure 2b, if we consider a super-particle made up of 125

particles, the magnetic-Richardson number increases from 0.14 to 3.5. Since the super-particle has a larger radius, the blood and membrane diffusivities, D_B and D_M, will be smaller decreasing from 6×10^{-13} and 2×10^{-13} (for leaky capillaries with 600 nm pores) to 1×10^{-13} and 0 respectively. The scattering diffusion coefficient, D_S, will stay the same, however, since it is only dependent upon the type of blood vessel. This causes the mass Péclet number to increase from 1000 to 6000. The Renkin coefficient will instead decrease from 0.36 to 0. One can now read-off the behavior of such a particle from Figure 9 and Figure 10 as before: clearly, a case that was previously velocity dominated could now fall into the boundary layer regime. In reality, during agglomeration there will be a statistical distribution of particle sizes, and chains can form instead of our simplified 'super particles'. To analyze such cases correctly requires additional research.

2.15.6 Skin Boundary Condition

In animal and human trials, skin prevents magnetic particles from leaving the tissue. To model this case we enforce a boundary condition at the bottom of the tissue closest to the magnet that does not allow a flux of magnetic nanoparticles across it. As expected, this causes a pile-up of particles just inside the skin nearest the magnet. Depending on the width of the tissue section being considered, this build-up can extend into the vessel region qualitatively distorting the three prototypical behaviors. Three case studies were chosen to examine the effect that the skin boundary has upon the solution.
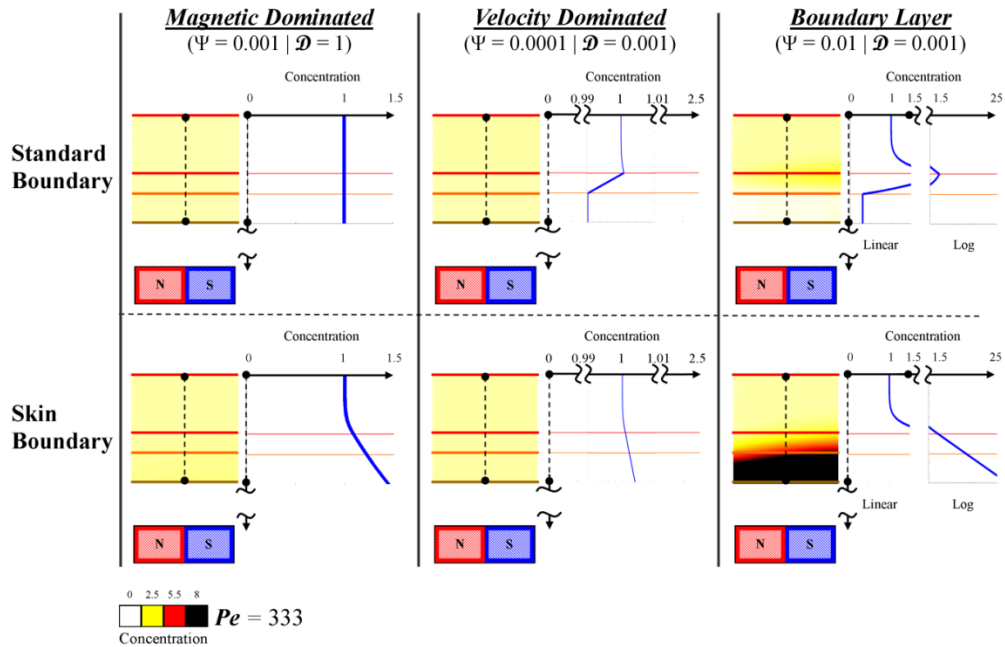
Figure 20: The effect that the skin boundary condition has upon the three prototypical behaviors can be seen by comparing the lower row to the top row of cases. The particles, once pulled through the vessel, travel to the skin boundary and then build-up along this interface and can extend back into the vessel region. This is most apparent in the magnetic dominated case where there is a build-up within the blood vessel membrane due to the presence of the skin boundary condition.

For any situation, if the blood vessel is close to the skin, the accumulation of ferrofluid at the skin can build up and can extend back through the tissue and into the vessel overwhelming any boundary layer that may otherwise have formed at the blood vessel wall. The magnetic dominated case saw an increase at the skin boundary, and a slight increase in particle concentration in the blood vessel due to the ability of the particles to build up at the skin. The velocity dominated case saw only a slight concentration build-up near the skin and a negligible change within the blood vessel. This is because particles are constantly washed out of the vessel and not captured by the magnetic field thus they do not readily arrive at the skin interface. The boundary layer case had a significant increase in the particle concentration near the skin and vessel membrane, but very little

change within the blood vessel. Particles in this case are pulled through the membrane and into the tissue with build-up near the skin only slightly affecting the blood vessel.

2.15.7 Varying of Tissue Diffusivity

In section **Error! Reference source not found.**, the Renkin tissue coefficient, $\mathcal{D}_{\mathcal{T}}$ (equation (31)), was always larger than the membrane Renkin coefficient, $\mathcal{D}$ (equation (29)), so that the limit to particle diffusion out of the vessel was the membrane. This behavior is consistent with many tissue-vessel systems but not all [37]. There are physiological conditions were the underlying tissue might not allow diffusion of particles as easily as a membrane, the Renkin tissue coefficient would then be smaller than the membrane Renkin coefficient. Therefore, the effect on particle concentration for changing the Renkin tissue coefficient (a fourth non-dimensional number) must be examined. Two cases were chosen to explore the effect changing tissue diffusivity has upon the steady-state concentration: boundary layer formation and velocity dominated behavior. Since the magnetic dominated behavior occurs only at Renkin reduced diffusion coefficients that are near unity, it does not make sense to vary the tissue diffusivity significantly for a magnetic dominated case.
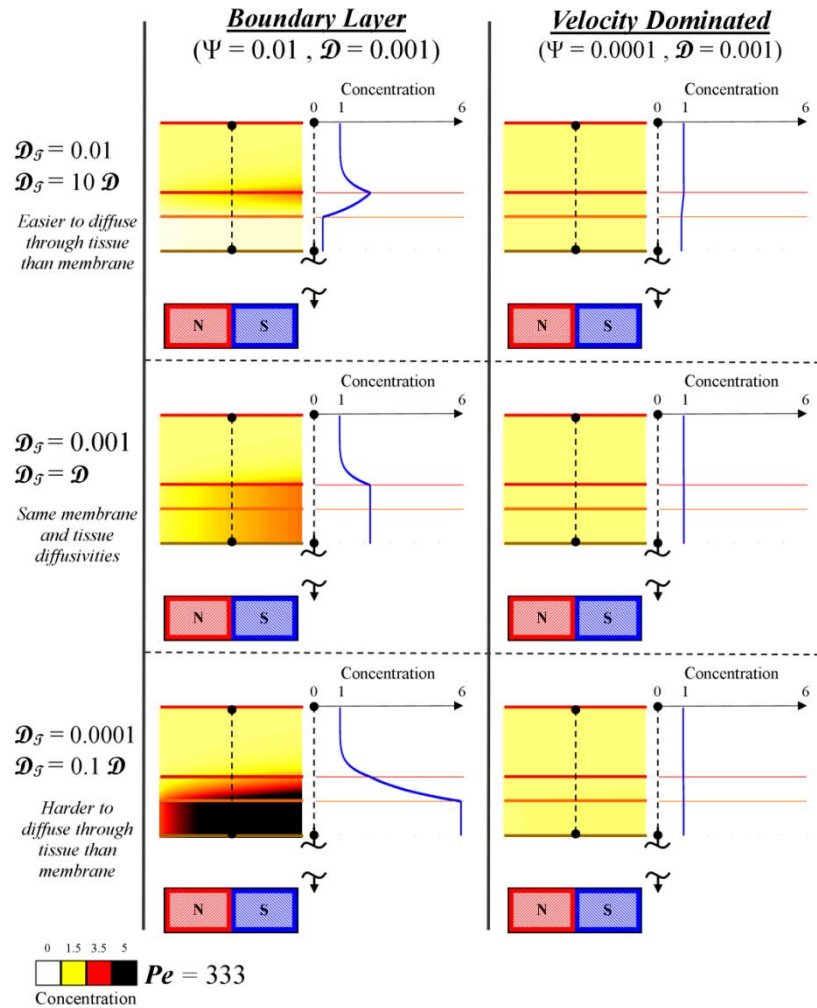
Figure 21: The effect on two prototypical behaviors by varying the Renkin reduced diffusion coefficient for tissue ($\mathcal{D}_{\mathcal{T}}$). The non-dimensional number cases used in section **Error! Reference source not found.** are shown on the top row. The Renkin tissue coefficient is decreased in each subsequent row so that the membrane Renkin coefficient is the same as the Renkin tissue coefficient in the second row. The last row signifies a Renkin tissue coefficient an order of magnitude less than the membrane Renkin coefficient.

The above figure shows cases where the Renkin reduced diffusion coefficient for the tissue is changed while the regular (endothelial membrane) Renkin reduced diffusion coefficient is held constant at $\mathcal{D} = 0.001$. The first row ($\mathcal{D} = 0.01$) corresponds to the typical cases used in this chapter where we have assumed that diffusion in the tissue is $\times 10$ greater than the diffusion in the endothelium (diffusion in the tissue is $1/100^{th}$ that of

blood while diffusion in the membrane is $1/1000^{th}$ that of blood). The second row ($\mathcal{D}_\mathcal{T} = 0.001$) shows the concentration if the two Renkin values are equal (diffusion in the both tissue and membrane is $1/1000^{th}$ that of blood). Here it is possible to see that the tissue space becomes an extension of the membrane space with an equivalent behavior (because $\mathcal{D}_\mathcal{T} = \mathcal{D}$). The third row ($\mathcal{D}_\mathcal{T} = 10^{-4}$) shows the solution when the diffusion in the tissue is x 10 smaller than the diffusion in the endothelium (diffusion in the tissue is $1/10000^{th}$ that of blood while diffusion in the membrane is $1/1000^{th}$ that of blood). Now the tissue space holds the primary concentration of particles. In all cases, the steady state vessel wall concentration remains essentially constant as we change the tissue Renkin value. This suggests that the relationship between these two Renkin values merely effects the distribution of particles between the membrane and the tissue and not the vessel concentration. Since the vessel wall concentration is not easily effected, the three prototypical behaviors and their delineation boundaries do not change.

2.15.8 Different Particle Hydrodynamic and Magnetic Core Radii

For simplicity, typically the hydrodynamic and magnetic core radii are assumed to be equal. Most often this is not exactly the case and there is a slight mismatch between the two values due to particle coatings that are added onto either affix therapeutics or immune system evading mechanisms [11], [14]. Then the hydrodynamic radius is slightly larger than the magnetic core radius leading to an increase in the Stokes drag force compared to the magnetic force. In this case, equation (11) would remain the same and equations (13) and (14) would change to

(48) $\vec{F}_S = 6\pi r\eta \vec{V}_R$

(49) $\vec{V}_R = \frac{a^3}{9\eta r}\frac{\mu_0 \chi}{1+\chi/3}\, \nabla\!\left(|\vec{H}|^2\right)$

where r is the hydrodynamic radius of a particle. Therefore, the non-dimensional magnetic-Richardson number changes in addition to a slight change in the Péclet and Renkin numbers. Using the same rat example as throughout the chapter, if the 250 nm diameter particle had a 300 nm hydrodynamic diameter, the magnetic force acting upon this particle would remain constant while the Stokes drag force changes from 0.70 pN to 0.84 pN. This would cause a slight decrease in the magnetic-Richardson number from 0.14 to 0.12. Since the particle has a larger radius, the blood and membrane diffusivities, D_B and D_M, will be smaller decreasing from 6×10^{-13} and 2×10^{-13} (for leaky capillaries with 600 nm pores) to 5×10^{-13} and 1.4×10^{-13} respectively. The scattering diffusion coefficient, D_S, will stay the same, however, since it is only dependent upon the type of blood vessel. This causes the mass Péclet number to increase from 1000 to 1200. The Renkin coefficient will instead decrease from 0.36 to 0.28.

2.15.9 Non-Perpendicular Magnetic Force

For blood vessels in animal or human vasculature, the alignment of the blood vessels obviously varies and the applied magnetic force may not be perpendicular to the blood flow. We considered this case in the main text because it is the least complex scenario to think about, and because it represents a best case (the magnetic force is lined up to extract as many particles as possible). A simple first approximation of the ferrofluid behavior for the case when a blood vessel is not aligned perpendicular to the magnet force is to separate the magnetic force into the perpendicular (*y*-direction in Figure 3) and parallel (*x*-direction in Figure 3) components. Then the perpendicular magnetic force component

101

can be used as the magnetic force in equation (23), while the parallel component can be added to the Stokes drag force to be used as a 'net' Stokes drag force in equation (23) to compute a modified magnetic-Richardson number that takes into account the magnetic force misalignment.

2.16   Conclusion

It is not enough to compare Stokes drag at the centerline to magnetic forces to conclude whether particles can or cannot be magnetically captured against blood flow. Such a comparison dramatically under-predicts the ability of magnetic forces to capture particles because it does not account for the near-zero velocity of blood near vessel walls nor the effects of diffusion. We have carried out a detailed analysis to better understand and quantify the behavior of magnetizable particles *in vivo*. We find that there are three types of behaviors (velocity dominated, magnetic dominated, and boundary-layer formation) uniquely identified by three essential non-dimensional numbers (the magnetic-Richardson, mass Péclet, and Renkin numbers). Figure 9, Figure 10, Figure 11, and Figure 12 allow magnetic drug delivery researchers to readily determine which behavior should occur in their experiments. These three behaviors remain present even if we consider additional realistic and complicating features, such as blood flow pulsatility, non-uniform magnetic fields, curved blood vessels, and particle agglomeration; although these added effects can modestly shift the delineations between the behaviors. Only the presence of skin, which creates a new interface where particles can build up, adds a qualitatively new behavior and it would require the addition of a fourth non-dimensional number to map out its effect. A comprehensive comparison to prior published *in-vitro*

and *in vivo* experiments shows excellent agreement and explains results that were not previously understood.

Contribution to the Field and Clinical Applications

Previous authors have created models investigating magnetic nanoparticle behavior within a single non-permeable blood vessel. These groups have considered either the capture efficiency of single particles (non-interacting individual nanoparticles) or the concentrations of disperse ferrofluids. However, since only the blood vessel itself is modeled, these models do not include particle transport through membranes and into the surrounding tissue space. In addition, most models do not include the blood vessel velocity profiles and instead simplify this profile to a constant drag force thereby neglecting a non-trivial contribution to nanoparticle behavior. Lastly, these models are only applicable for specific geometries, magnetic fields, and blood vessel types, and therefore do not examine what occurs throughout any region of the body nor any experimental condition.

We have created a more realistic and widely applicable FEM model of the blood vessel, blood vessel membrane, and outlying tissue section. This model treats nanoparticles as a fluid and not individual elements and therefore can handle concentrations specifically as they develop large boundary layers between the model domains (vessel, membrane or tissue). In addition, the model included blood velocity profiles and diffusion effects (either due to Brownian motion or due to blood cell scattering). We wrote equations from physical first principles that combined the Navier-Stokes equations, the magneto-static

103

Maxwell equations, Fick's diffusive flux equations, and Einstein's Brownian motion approximation. We reduced the number of experimental parameters from 24 by simplification and non-dimensionalization to four crucial independent parameters that dictate nanoparticle fluid concentration within this system. These independent parameters and not the experimental parameters define the ferrofluid concentration. It is possible to change a set of experimental parameters (e.g. the particle radius and magnet shape) and not change ferrofluid concentration, but it is not possible to change the independent parameters and maintain a constant the ferrofluid concentration.

Our collaborators at the California Institute of Technology created a custom-built solver to resolve the boundary layers between the vessel, membrane and tissue domains. With this solver, we then examined the entire realistic experimental space. From this, we determined there were only three fundamental behavior regimes of the ferrofluid. By mapping the non-dimensional parameters to the fundamental behaviors, we developed a method to predict the nanoparticle behavior for any experimental condition. We then verified the mapping by comparing it to available in-vitro and *in vivo* experimental data.

For a clinical and experimental use, the above model is able to predict the type of behavior a researcher will experience. All the details and necessary information has been provided in this Chapter. However, for a complete summary and easy reference, the following flowchart, Figure 22, can be used to employ the models predictions for a given experimental case.

STEP 1: Measure

Start by establishing the following variables, which include magnet, particle and *in-vivo* parameters. The magnetic field experienced at the target location is determined by the magnet strength, the dimensions of the magnet, and the distance from the magnet. The composition of the particles determines the magnetic core radius, hydrodynamic diameter, and magnetic susceptibility. The location of the target region within the body determines the type of tissue, target depth, and the proximity, size and type of blood vessels.

Magnet Parameters

Magnet strength
B [Tesla]

Magnet dimensions
$L_M \times w_M \times h_M$ [meters]

Distance from magnet to target
d [meters]

Permeability of free space
$\mu_o = 4\pi \times 10^{-7}$ N/A^2

Particle Parameters

Magnetic core radius[1]
a [meters]

Hydrodynamic diameter
d_{hydro} [meters]

Particel material magnetic susceptibility
χ

In-vivo Parameters

Body temperature
T [Kelvin]

Pore sizes for tissue and membrane
$d_{p,mem}$, $d_{p,tiss}$ [meters]

Max blood speed
$V_{B\,max}$ [meters/second]

Blood vessel diameter
d_B [meters]

Blood viscosity
η [Pascal seconds]

Below are the parameters for the rat example in Figure 2. The membrane pore diameters correspond to leaky tumor vessels.

$B = 0.5$ T
$L_M \times w_M \times h_M = (0.05 \times 0.05 \times 0.01)$ m
$d = 0.001$ m
$a = 125 \times 10^{-9}$ m
$d_{hydro} = 250 \times 10^{-9}$ m
$\chi = 20$
$T = 310$ K
$d_{p,mem} = 600 \times 10^{-9}$ m
$d_{p,tiss} = 600 \times 10^{-9}$ m
$V_{B\,max} = 0.0001$ m/s
$d_B = 6 \times 10^{-6}$ m
$\eta = 0.003$ Pa·s

STEP 2: Calculate

Using the parameters established in Step 1, the following equations can calculate the forces and diffusion coefficients necessary to predict the ferrofluid behavior. The magnetic field and gradient are to be evaluated at the target position (x*,y*,z*) from a simulated or measured magnetic vector field. Then calculate the magnetic force. Determine the Stokes drag force by the blood flow speed at the target location. The diffusion coefficients are calculated for the corresponding target region in the biological system.

Magnet Field

Use modeling software to compute the magnetic field and its derivative.

$\vec{H}(x,y,z) = \begin{bmatrix} Hx & Hy & Hz \end{bmatrix}$

$$\frac{\partial \vec{H}}{\partial \bar{x}} = \begin{bmatrix} \frac{\partial(Hx)}{\partial x} & \frac{\partial(Hy)}{\partial x} & \frac{\partial(Hz)}{\partial x} \\ \frac{\partial(Hx)}{\partial y} & \frac{\partial(Hy)}{\partial y} & \frac{\partial(Hz)}{\partial y} \\ \frac{\partial(Hx)}{\partial z} & \frac{\partial(Hy)}{\partial z} & \frac{\partial(Hz)}{\partial z} \end{bmatrix}$$

Evaluate at the target location (x*,y*,z*) that is located a distance d from the magnet.

Magnetic Force

Compute the magnetic force

$$\vec{F}_M = \frac{4}{3}\pi a^3 \frac{\chi}{1+\chi/3}\mu_0\left(\frac{\partial \vec{H}^T}{\partial \bar{x}}\vec{H}\right)$$

Stokes Drag Force

Given the blood flow speed at the target location, compute the Stokes drag:

$$\left\|\vec{F}_S\right\| = 3\pi d_{hydro}\eta V_{B\,max}$$

Check that forces are in SI units [Newtons].

Diffusion Coefficients

Calculate the blood diffusion coefficient:

$$D_B = \frac{k_B T}{6\pi\eta a}$$

Calculate scattering coefficient (D$_S$) in SI units [m^2/s] using [10].

Calculate total coefficient:

$$D_{Tot} = D_B + D_S$$

Calculate membrane and tissue diffusion coefficients using [10,11]

By COMSOL[2]:

$\vec{H}(x,y,z) = \begin{bmatrix} 0.2 & 1.3 \times 10^5 & 0.3 \end{bmatrix}\frac{A}{m}$

$\frac{\partial \vec{H}}{\partial \bar{x}} = \begin{bmatrix} 2.9 \times 10^7 & 160 & 150 \\ -210 & -5.9 \times 10^7 & -750 \\ 68 & -400 & 2.9 \times 10^7 \end{bmatrix}\frac{A}{m^2}$

$\vec{F}_M = \frac{4}{3}\pi(125 \times 10^{-9}\,\text{m})^3\left(\frac{20}{1+20/3}\right)(4\pi \times 10^{-7}\,\text{N/A}^2)$
$(\begin{bmatrix} -2E7 & -7.7E12 & -8.6E7 \end{bmatrix}\text{A/m}^3)$

$\left\|\vec{F}_M\right\|_{y-direction} = F_M = 1 \times 10^{-13}$ N

The stokes drag force is for a capillary near tumors.

$\left\|\vec{F}_S\right\| = 3\pi(250 \times 10^{-9}\,\text{m})(0.003\,\text{Pa s})(0.0001\,\text{m/s})$

$\left\|\vec{F}_S\right\| = F_S = 7 \times 10^{-13}$ N

The diffusion coefficients are associated with leaky capillaries near tumors. As noted in [11], the scattering coefficient is not applicable.

$D_{Tot} = 6 \times 10^{-13}$ m^2/s $D_B = 6 \times 10^{-13}$ m^2/s
$D_M = 2.16 \times 10^{-13}$ m^2/s D_S = N/A
$D_T = 2.16 \times 10^{-13}$ m^2/s

STEP 3: Predict

From the variables calculated in Step 2, determine the following four non-dimensional numbers. Using these four non-dimensional numbers, the coordinate location within the non-dimensional space can be determined. This location will reveal the ferrofluid behavior.

MAGNETIC RICHARDSON NUMBER $\quad \Psi = \dfrac{F_M}{F_S}$

MASS PECLET NUMBER $\quad Pe = \dfrac{d_B V_{B\,max}}{D_{Tot}}$

RENKIN DIFFUSION COEFFICIENT $\quad \mathcal{D} = D_M/D_{Tot}$

TISSUE RENKIN DIFFUISION COEFFICIENT $\quad \mathcal{D}_T = D_T/D_{Tot}$

$(\Psi, Pe, \min(\mathcal{D}, \mathcal{D}_T))$

Magnetic Dominated

Velocity Dominated

Boundary Layer Formation

Renkin Coefficient

Magnetic Richardson Number
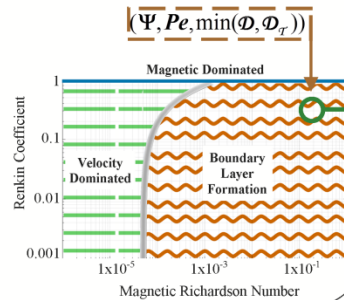
The four non-dimensional numbers are

$\Psi = (1/7) \times 10^{-13} = 0.14$

$Pe = \dfrac{(0.001\,\text{m})(0.0001\,\text{m/s})}{6 \times 10^{-13}\,\text{m}^2/\text{s}} = 1 \times 10^3$

$\mathcal{D} = 2.16 \times 10^{-13}/6 \times 10^{-13} = 0.36$

$\mathcal{D}_T = 2.16 \times 10^{-13}/6 \times 10^{-13} = 0.36$

Rat Capillaries
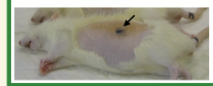
The rat capillary example falls into the boundary layer formation region.

Figure 22: The process flow for determining the ferrofluid behavior in and around a blood vessel under an external magnetic field. With step 1 the critical parameters are established; step 2 calculates the required variables from the described formulas; and step 3 predicts the ferrofluid

behavior based upon the four non-dimensional numbers derived from the calculated variables. All units are in standard international (SI) format. Double bars ($\|\cdot\|$) denotes the Euclidean norm of a vector. Brackets within equations ($[\,\cdot\,]$) denote a vector or matrix quantity. ∇ denotes the gradient operator. [1]The magnetic core radius is a radius of the region enclosing the magnetic components of the magnetic particle. [2]When developing the theoretical model to predict the magnetic field and its derivative, it is beneficial to take advantage of any symmetry inherent within the problem. In our convention, we align the blood vessel with the x-axis and consider a magnet placed symmetrically along the y-axis.

Chapter 3: Dynamic Magnetic Shift to Improve Therapeutic Transport through Tissue

This work originally appeared in [274].

This work was done in collaboration with colleagues at the National Cancer Institute of the National Institutes of Health. Skye Kim, Michael Tangrea, and Mike Emmert-Buck collected the samples from the NIH autopsy database. In addition, they fixed, mounted, and stained the samples to identify vessel locations. Jaime Rodriguez-Canales, a trained pathologist, identified the tumor and normal regions within the liver. These collaborators performed the first comparison of normal to tumor tissue, which I further extended with image processing. I designed, developed, and examined the magnetic nanoparticle tissue transport model and then used it to create the dynamic magnetic shift treatment scheme.

3.1 Introduction

Given the multitude of potential treatment targets for magnetic drug targeting (MDT), it is vital to first choose a desired treatment target before engineering a magnetic drug targeting schema. As mentioned in Chapter 1, the initial MDT case was the treatment of cranial surface primary tumors [14]. These results have been extended to sensitize tumors using thermotherapy [16]. Outside of oncology, advances include using magnetized stem cells to treat regions of cardiovascular disease to help restore tissue function [75], [114]–[116], or to the retina for ocular regeneration [117]. However, a previously unconsidered target by MDT that has significant impact on patient quality of life is metastatic disease.

The three-dimensional tumor microenvironment introduces an additional level of complexity as the rapid and uncontrolled growth of tumor cells can result in a disorganized and only partially functional biological milieu, an environment that favors tumor growth over normal physiological processes. One outcome of this process is an abnormal vascular system [275]. Unlike the well-structured series of small vessels that create a fine meshwork of capillaries in normal tissues to deliver oxygen and nutrients within a diffusion-limited distance of cells, tumors often exhibit a complex and disordered blood supply resulting in diminished perfusion to some or all parts of the tumor microenvironment and reduced delivery of blood borne components, including systemically administered therapeutic agents [211], [276]–[280].

The full complement of reasons for poor chemotherapeutic efficacy in metastases are not understood [276], [277]; however, to improve drug delivery functionalized nanoparticles are being developed to target cancers and increase local drug concentrations, cellular uptake, and clinical effectiveness [45]–[49], [281]–[284]. Unlike small drug molecules that equilibrate quickly through tissue space by diffusion alone [37], [38], larger functionalized nanoparticles (including targeting antibodies [45]–[49], environmental reactive drugs [44], or imaging reagents [285], [286]) are unable to diffuse as easily [37], [38]. Several *in vivo* studies have shown that with targeted carriers, even if the cellular uptake is increased, the tumor drug concentration remains unchanged compared to untargeted carriers [46], [47], [281]. This poor penetration can reduce the efficacy of large nanoparticle carriers, particularly within poorly vascularized cellular regions in the tumor environment.

In order to provide adequate nanoparticle concentrations to breast and other metastatic tumors, we are evaluating a new method of normalizing nanotherapy termed dynamic magnetic shift (DMS) [185], [287]–[293] (see Figure 23) that is designed to achieve two important goals: a) Increase nanoparticle levels in poorly vascularized tumors or tumor sub-regions by equalizing the concentration between tumor and normal tissues; and, b) Improve tumor nanoparticle levels simultaneously in *all* tumor foci across a given anatomical region, without the need for imaging-based, positional information of lesions. To accomplish these objectives, magnetic nanoparticles would be given systemically and allowed to distribute throughout the body. A magnetic force would then be applied in one direction over a specified anatomical zone of the body to promote movement of the therapeutic particles into the tumor space from adjacent, well-vascularized normal tissue (an effective external nanoparticle reservoir) and also from sub-regions within the tumor that contain high levels of nanoparticles (e.g. internal vessels). The externally applied magnetic forces would overcome diffusion limits by physically displacing ferromagnetic drug carriers across nano- or micro-meter distances (Figure 23). This displacement can be driven in one direction only, but our studies show that it is advantageous to repeat the process in at least two directions to more uniformly distribute the nanoparticles due to the complex geometries of vessels within tumor foci. Since the nanoparticles have a finite circulation time *in vivo*, there is a balance between magnetically actuating for as long as possible in one direction versus successively applying magnetic forces in multiple directions to better redistribute drugs into and throughout metastatic tumors. Our finding

109

is that two directions is a practical compromise between shift distance and number of shift directions, and we examine that case here.
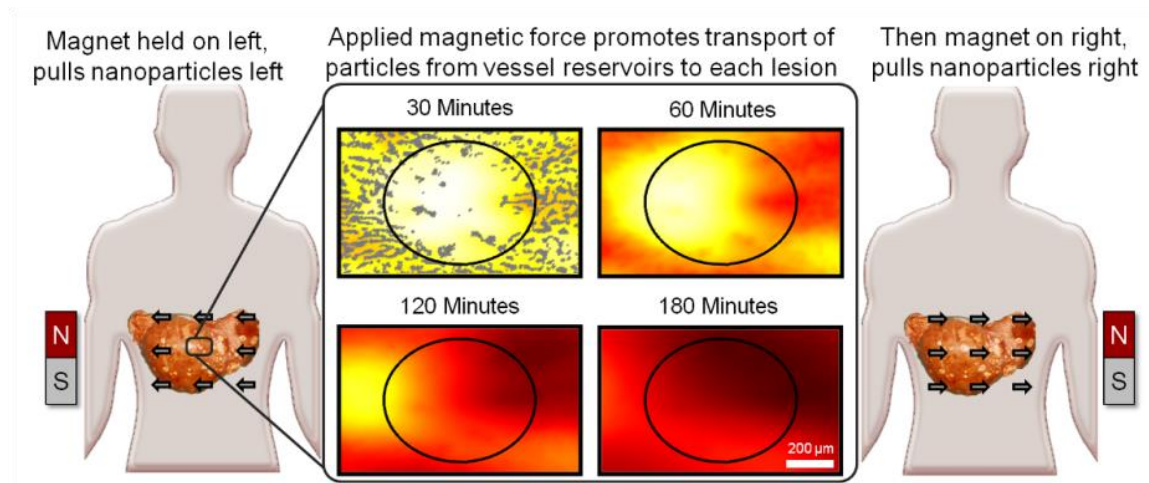
Figure 23: Schematic illustration of magnetic left-then-right shift option to increase nanoparticle levels into and throughout liver metastatic tumor foci. Left and right panels: appropriately chosen (strong and correctly sized) magnets can create sufficient magnetic gradients on therapeutic magnetic nanoparticles to displace them from dense distributions in normal tissue into adjacent poorly-vascularized tumor regions. In this example, magnetic shift is shown in just two successive directions, but the process can be repeated in multiple spatial planes. Middle panel: computer simulations of the resulting therapeutic particle distributions in a 1 mm wide tissue region using blood vessel geometry taken from autopsy data (gray markings). The color gradient shows the resulting nanoparticle concentration at each tissue location (red is high, white is low). Magnetic actuation increases nanoparticle concentration in the tumor area (marked by the black circle, also clearly visible by a lack of blood vessels) at 30, 60, 120 and 180 minutes after systemic injection.

The natural motion of nanoparticle complexes within a tissue space is diffusion and small convective bulk flow. If the convective flow is tiny, than the nanoparticle movement through a tissue space or tumor can be described purely by diffusion. Using the particle mobility models discussed in section 1.3.1 and a representative size of tumor, it is possible to predict the natural diffusive distance of a nanoparticle over a treatment window.

If the particle is small, this distance is large and the particles are able to perfuse through the entire tumor. If the particle is large then the diffusive distance is tiny, and the particles will not reach far into the tumor. As given by equation (14), the distance traveled by a magnetic particle due to a magnetic field is also related to size. The larger the particle the further it will travel. Using these two competing effects and models of tissue resistance, it is possible to generically predict the regimes in which DMS would provide a significant improvement over natural diffusion. Figure 24 gives an overview using these models of the potential regions where DMS would provide a significant mobility increase over natural diffusion. However, this generic prediction does not incorporate any information about the tumor architecture. Incorporating the tissue architecture is the next step to determine if DMS would have any impact.
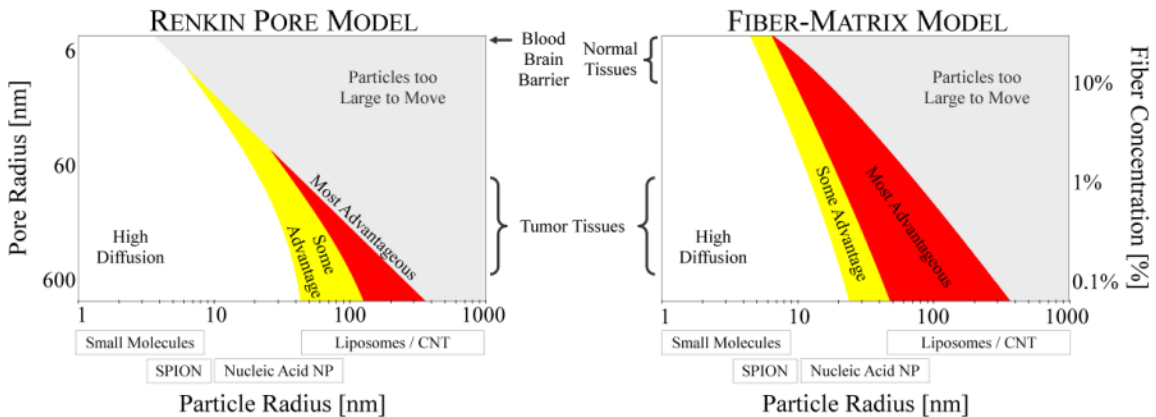
Figure 24: A map of when DMS is predicted to be advantageous over diffusion alone for poorly perfused liver metastases (for a sample 0.5 mm diameter tumor, therapeutic particles are assumed to have a 45 minute *in vivo* residence time). For two common types of tissue models, a Renkin Pore model [37], [38], [197] or a Fiber-Matrix model [37], [38], [202], the coloring shows when DMS treatment will improve drug delivery to the tumor. Here, 'High Diffusion' refers to the region where diffusion alone should suffice: it is the region where particle diffusion is predicted to create a concentration of therapy in all tumor cells that is ≥ 85% of the concentration of therapy in the blood stream. 'Some Advantage' (yellow) and 'Most Advantageous' (red regions) is where diffusion will not suffice and DMS has the potential to improve therapy concentration to all cells in the tumor by > 17% and > 100% respectively compared to diffusion alone. Thus, DMS will be advantageous for mid-range 10 – 500 nm particle sizes, when the particles are big enough so that

diffusion alone is no longer effective but small enough so they can be magnetically moved through tissue. Particles of this size include heat shock protein cages (< 16 nm) [294], polymeric micelles (< 50 nm) [295], colloidal suspensions of albumin-Taxol (Abraxane, 130 nm) [296], and functionalized carbon nanotubes (0.1 - 4 μm) [297].

To evaluate the histological and vascular features of metastatic foci in human subjects and their implications for magnetic drug delivery, a series of autopsy cases from women who died from metastatic breast cancer were analyzed. Blood vessel density and geographic distribution were quantitatively measured and these data used for mathematical simulations of the distribution of magnetic particles within tumors with and without magnetic actuation, to assess the feasibility of DMS and also to describe and understand the critical elements that affect the process. In brief, strong magnets of a carefully selected size (20 cm $\times$ 40 cm) that create substantial magnetic gradients inside the body (magnetic fields fall of with distance creating a spatial gradient) were evaluated; the magnetic fields, gradients, and forces were computed by standard methods [131], [185], [228], [298]; the best available parameters were used for human tissue resistance to particle motion [37], [38], [197]; and, DMS parameters (strength and timing for a 2-direction shift) were varied to evaluate different treatment regimens. Finally, since one of the most common sites for metastasis of breast cancer is the liver and there is clinical evidence suggesting that treatment of metastatic hepatic lesions can lead to improvement in patient outcome, we focused our attention on hepatic metastasis [299]–[302].

3.2   Domain Geometry

Autopsies from eighteen women with metastatic breast cancer who died at the NIH Clinical Center were initially evaluated. The liver (89%) and lungs (89%) were the organs

most commonly affected in this cohort of patients, although a majority of the women also had widespread systemic metastases. The most common causes of death were overall tumor burden and respiratory compromise, often associated with infections that were secondary to therapy and immune suppression. The chemotherapeutic treatment history in the patients varied; however, in all cases the drugs received were standard regimens. Grossly, the metastatic tumor foci appeared as firm white nodules, in contrast to the adjacent, dusky, liver parenchyma (Figure 25).

Figure 25: Photograph of metastatic breast cancer in liver. The lesions appear grossly as firm, white nodules, consistent with a host desmoplastic response and poor vascularization.

(Note - the image is representative of the pathological descriptions in the autopsy cases in the study, but is not an actual image from one of the cases. Photo provided courtesy of Drs. Hanne Jensen and Robert D. Cardiff, Center for Comparative Medicine, University of California, Davis.)

3.3   Vessel Measurements – Normal Liver and Metastases

Ten autopsies were chosen for vessel analysis based on the quality of CD31 immuno-staining. All ten patients had liver metastases, ranging from micro-metastases that were only a few millimeters in diameter, to grossly visible lesions that were a centimeter or more across. At the microscopic level, the metastases were comprised of sheets of

irregularly shaped tumor cells with pleomorphic nuclei. Foci of chronic inflammation, necrosis, and micro-hemorrhage were variably observed in the tumors.
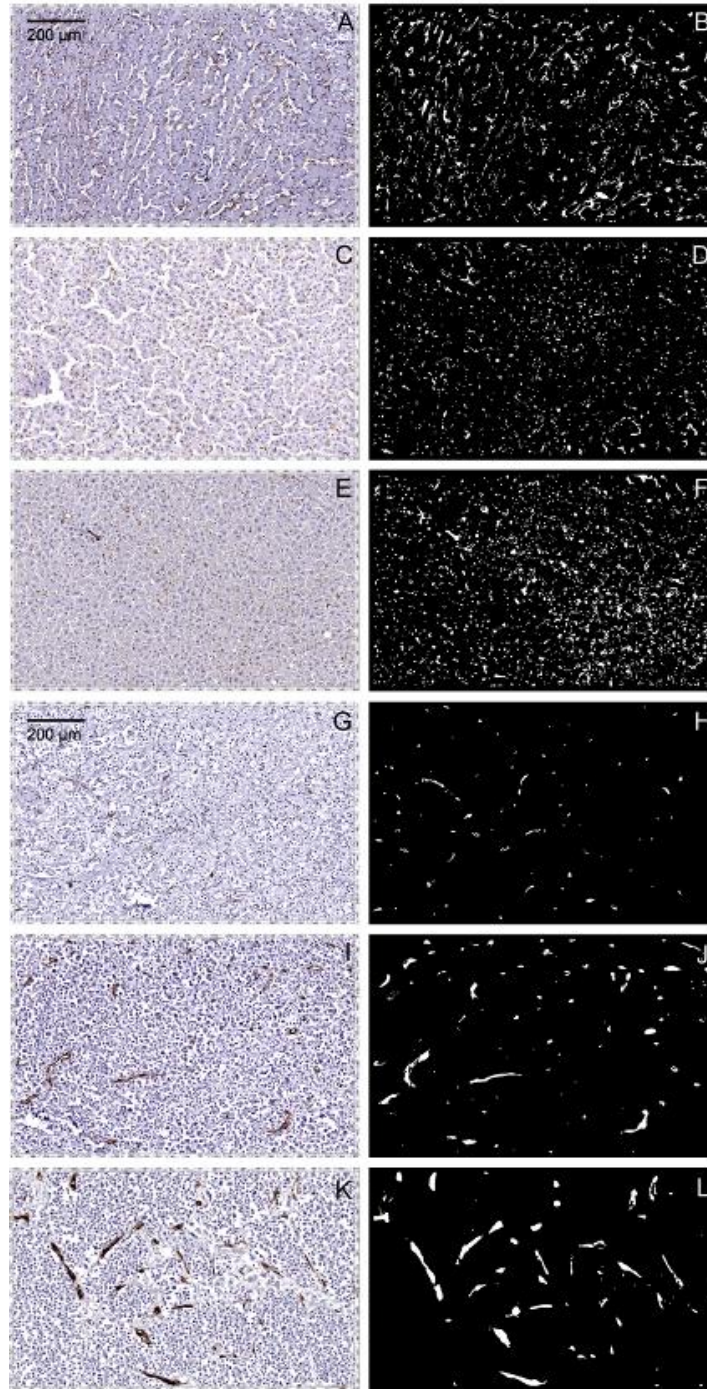
Figure 26: Photomicrographs of vessel staining in three cases of metastatic breast cancer in liver. Images on the left are immunostained histological sections. On the right are the same sections

visualized in black and white to highlight the CD31 stained vasculature. Panels A-F are from normal liver and panels G-L are from matched tumors. At low power, the normal sections show a fine meshwork of capillaries. In contrast, tumors exhibit vessels that are generally larger in size and fewer in number.

Normal liver in the patients contained a fine meshwork of small vessels and capillaries interspersed throughout the parenchyma, an architectural pattern consistent with an even distribution of blood flow and diffusion-based delivery of oxygen and nutrients to hepatocytes and associated support cells. In contrast, the tumor vessels were generally larger in diameter but fewer in number than in the adjacent normal liver, with a more random distribution and a greater vessel-to-vessel spatial separation. This difference in tumor vasculature is evident in the low power histological views shown in Figure 26 and was observed in the metastases from nine of the ten patients analyzed.
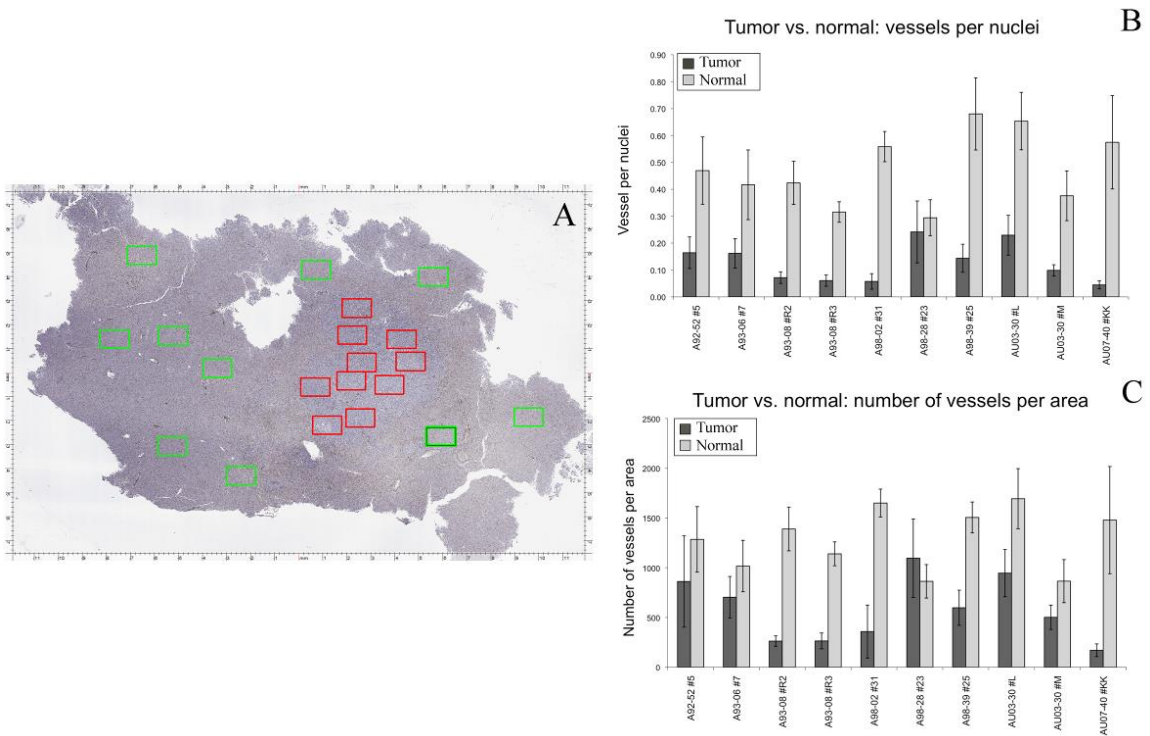
Figure 27: Quantitative measurement of vessels in normal liver and adjacent metastatic breast cancer in 10 cases. Panel A: representative whole slide images of a histological liver section

containing both normal tissue and tumor. Each rectangle represents a randomly chosen region (green = normal, red = tumor; dimensions = 1.2×0.75 mm; 100X magnification). Panel B: the vessels-to-nuclei ratio in tumor regions is lower and more variable than in normal areas. Panel C: tumor regions have a lower number of blood vessels per area than in normal.

To quantitatively assess the vasculature patterns of both normal tissue and tumor, twenty arbitrary histological regions were chosen for each case: ten that contained normal liver (green rectangles) and ten with tumor (red rectangles). As an example, a low power microscopic view of one case and geographic regions selected for analysis is shown in Figure 27A. Overall, the measurements revealed that tumors contained fewer vessels and had more vascular heterogeneity than normal tissue, consistent with the visual observations seen in Figure 26. Except for outlier case A98-28 (the only lobular breast cancer case in the series, see Discussion section), all tumor cases had fewer vessels than normal tissue as measured using vessel count per cell number (Figure 27B) or using vessel count per area (Figure 27C).

We next assessed the tumor microenvironment in terms of regions with the fewest number of vessels. In other words, we purposefully looked for and measured sub-regions of tumors with the lowest vascular density, then compared these sub-regions against normal tissue of the same patient by computing the distance to the nearest blood vessel for every location within the tissue image. As seen in the panels across the top of Figure 28, in a normal region the average of the distance from each cell to its nearest blood vessel is 5.3 ± 2.7 μm (the maximum is = 67.8 μm; n $\approx$ 5500). In contrast, in the selected tumor region, the average was observed to be 43.8 ± 6.9 μm (the maximum was = 287 μm; n $\approx$ 5500). These results indicate that in addition to a lower average vascular density than normal tissue, there exist specific sub-regions of tumors that are far away from all

vessels, regions that are likely poorly perfused and difficult for systematically administered particles to access.
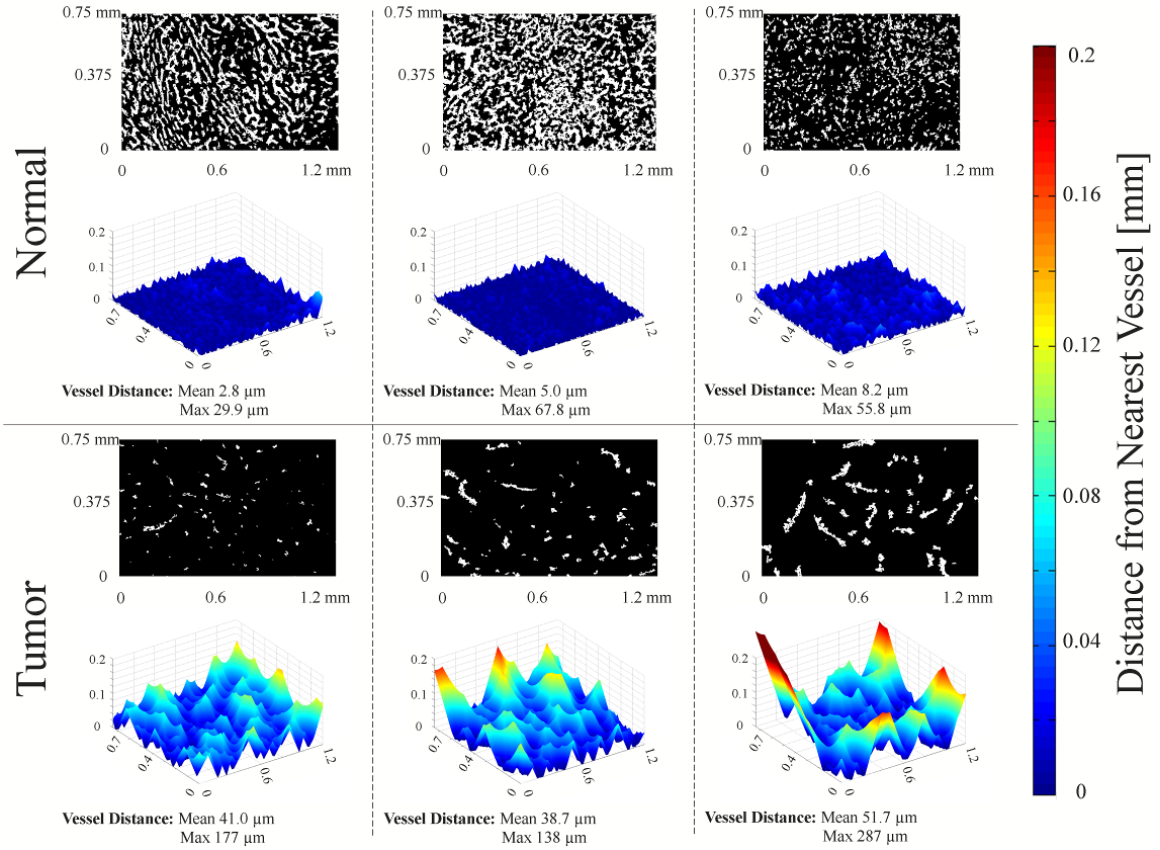
Figure 28: Computation of the distance of normal liver cells (panels across top) or tumor cells (bottom) to their nearest blood vessel. The black and white images indicate tissue (black) and vessel (white) locations. Each normal and tumor region was selected for analysis based on the fewest number of vessels observed at low magnification. The three-dimensional relief graphs show the distance in microns to the nearest blood vessel for a given tissue location. As the graphs increase in height, that tissue location is further from its nearest blood vessel. In all examples, the tumor cases have cells located further away from nearest blood vessels (indicated by larger mean and max values).

3.4   Governing Equations

To examine the effect that low vascular density has upon magnetic targeting procedures, simulations were constructed using the histology of a representative small metastatic

tumor (diameter ≈ 0.5 mm, inset of Figure 29) and the surrounding normal liver parenchyma. Using finite element modeling software, the behavior of magnetic nanoparticles was examined with and without the application of magnetic actuation (Comsol Multiphysics) [261]. All magnetic fields, gradients, resulting forces and particle motions, were computed from physical first principles [131], [185], [228], [244], using the best available parameters for particle diffusivity and resistance to motion in human tissue [37], [38].

Simulation Domain
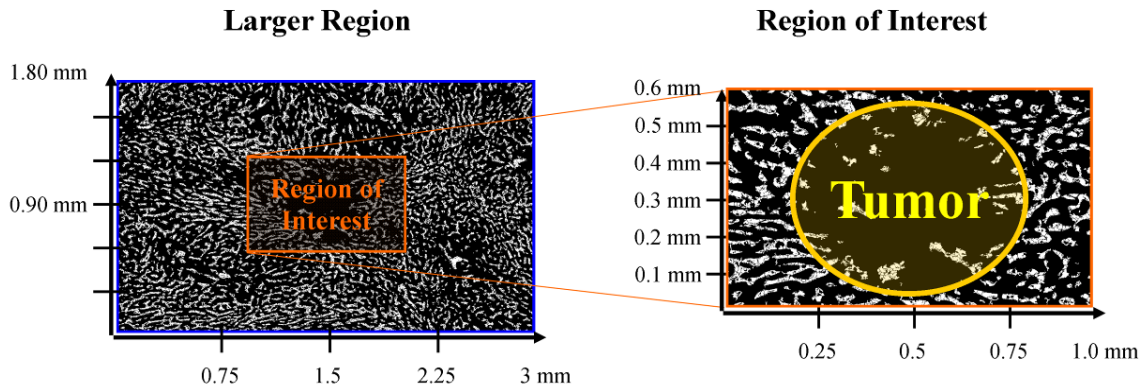
Figure 29: Simulation domain showing the larger region (left panel) that encompasses the smaller region of interest (right panel). The yellow ellipse represents tumor.

The evolution of particle distributions in media was described by partial differential equations (PDEs). Here, for diffusion and magnetic transport in tissue, the appropriate PDE with boundary and initial conditions is shown below [194], [303].

(50) $\quad \frac{\partial C}{\partial t} = -\nabla \cdot \left\{ - \underbrace{D\nabla C}_{\text{Diffusion}} + C \underbrace{\vec{V}_{magnetic}}_{\text{Drift Velocity}} \right\}$

(51) $\quad C(x,y,t)_{Vessels} = C_0(x,y)e^{-\lambda t}, \; \lambda \equiv \ln \frac{2}{t_{half-life}}$.

This type of formulation is standard, and the properties of tissue (D, $\vec{V}_{magnetic}$, $t_{half-life}$, C_0) were chosen to match the properties of drug-coated 60 nm diameter magnetic particles in human tissue [37], [38], [131], [196]. The decay constant, λ, defines how the particle concentration in blood is related to the nanocarrier half-life, $t_{half-life}$. A fiber matrix model with a 1 nm radius fiber volume concentration of $C_F = 0.3\%$ [37], [38], [202], was chosen to evaluate the worst-case situation for DMS where the diffusion coefficient of the particles is high thus reducing the benefit of DMS (for this $C_F = 0.3\%$, the reduced diffusion coefficient of the Fiber-Matrix model is $D_T \approx 0.15$) [37], [38], [202]. The magnetic field and magnetic gradient around a 20 cm × 40 cm magnet (2.5 T remnant magnetization) was solved using COMSOL [228], which gave the magnetic force at a depth of ≈ 11 cm in the body as $F_{mag} \approx 0.34$ fN. Comparing this force to tissue resistance, $F_{resistance} \approx (1/D_T)6\pi a\eta V_{magnetic}$, where a is the particle radius, η is the fluid viscosity and $V_{magnetic}$ is the speed at which nanoparticles are transported through the region of tissue by the applied magnetic force, yielded a particle magnetic drift velocity of $V_{magnetic} \approx 0.09$ μm/s [131].

3.5 Boundary Conditions

Two sets of boundary conditions are necessary to solve equation (50): one set to describe the extravasation from the blood vessels into the tissue (equation (51)), and the second to describe the movement of nanoparticles out of the simulated region.

The first set of conditions is determined by the diffusion of particles from the vessels into the adjacent tissue governed by the nanoparticle concentration gradient (high in blood, low in tissue). Therefore, the movement of particles into the tissue is dependent upon the blood plasma concentration. Here we describe the concentration of nanoparticles within blood plasma as one that decays over time as described by equation (51). This decay models the known physiological plasma concentration of systemically injected nanoparticles. From this equation, the half-life ($t_{half-life}$) of nanoparticles in the blood plasma can be chosen to mimic physiological parameters in humans (here, $t_{half-life} = 45$ min was used) [11], [14], [31].

The second set of boundary conditions defines the free movement, the flux, of nanoparticles out of the region of interest (Figure 29). Nanoparticles leave only when the magnetic force pulls them out of the simulated region; therefore, the total flux of particles out of the tissue is equal to the convective flux created by the magnetic forces as described by the following equation:

(52) $\underbrace{\vec{n} \cdot (-D \nabla C_i)}_{\text{Diffusion out of the histolocial region}} = 0$, therefore

(53) $\underbrace{\vec{n} \cdot (\vec{V}_i C_i)}_{\text{Convective flux from magnetic forces}} = \underbrace{\vec{J}_i}_{\text{Total flux}}$

3.6   Simulation Region

Nanoparticles are swept out of the simulated region then re-enter during treatment. We addressed the effects of particle re-entry on the accuracy of our simulation results by tripling the simulated region (inset of Figure 29) to 3 mm × 1.8 mm, which centered on the original region of interest (Figure 29). The increase in size was sufficient to accurately track all particles passing through the original region at any time. This did not change the results. In other words, all particles near the exterior boundary of the expanded region that would either enter or leave (i.e., particles that would not be correctly tracked by our simulation) were too far away from the original region to contribute to its nanoparticle concentration.

3.7   Simulation Development

Each case simulated consisted of solving the constitutive equation (50) over the entire image and marching it forward through time. Nanoparticles enter the surrounding tissue (shown in black in Figure 29 top row) from the identified blood vessels (white regions in Figure 29) over time. The amount of nanoparticles moving from the vessels into the adjacent tissue is described by equation (51), from which equation (50) generates the distribution of particles at the next time instant across the region of interest. This

calculation is marched through time for 3 hours, creating a complete solution of the nanoparticle distribution for the entire treatment window.

Three treatment scenarios were considered: Case a) No applied magnetic forces (for a treatment duration of t = 3 hrs); Case b) A constant unidirectional West magnetic force (t = 3 hrs); and Case c) A sequence of magnetic forces chosen by intuition that begins with no magnetic force (for t = 45 min) followed by a unidirectional East force (for t = 1.5 hrs) which then switches to a unidirectional West force (for t = 45 min). Case c) was chosen to test the effects of switching magnetic force directions on both the average and maximum over time nanoparticle concentration achieved in the tumor region to see whether it could be improved over the results of Case b). Subsequently, we carried out a comprehensive search over magnetic force duration and number of pull directions (single or bi-directional pull?) to go beyond case c) and to find optimal DMS treatment parameters for a 1.5 hour treatment.

Equation (50) describes the basic physics of nanoparticle transport inside the body and shows that accumulation or depletion of particles at any location is due to transport by diffusion and applied magnetic forces. This type of formulation is standard [196]. Parameters are chosen to reflect the tissue properties of the region of interest (e.g. the diffusion coefficient can be changed to reflect parameters of normal or tumor tissue), and it is this equation that is simulated below. Equation (51) reflects our knowledge about the residence time of nanoparticles in vivo and states that the amount of particles that extravasate from blood to tissue at a given time is linked to the plasma concentration,

which decays exponentially over time due to uptake of the nanoparticles by the reticuloendothelial system (RES).

3.7.1   Magnetic Fields, Gradients, and the Resulting Forces on Nanoparticles

For any electromagnet or permanent magnet, a magnetic field is present surrounding the magnet with field lines leaving the north pole and re-entering the south pole [244]. The field generated will be stronger closer to the magnet (specifically at the corners) and weaker as the distance from the magnet increases [186], [244], [298]. The magnetic field falls off very quickly further from the magnet relative to its size (larger magnets will have a slower decreasing magnetic field strength [304]) creating a magnetic field gradient, and it is this gradient that creates a force that attracts particles towards the magnet. For a 20×40 cm magnet with a remnant magnetization of 2.5 T, the field at 11 cm distance (along the long axis of the magnet) will be $B \approx 0.43$ T, or $H \approx 3.4 \times 10^5$ A/m. The gradient of the magnetic field at that distance will be $\partial H / \partial x \approx 2.7 \times 10^6$ A/m^2. Using these values and considering a magnetic nanoparticle with a diameter of 60 nm, the magnetic force (see equation (11)) acting on this particle will be $F_{magnetic} \approx$ $(2/3)\, a^3 \mu_0 [\chi / (1 + \chi / 3)](\partial H / \partial x) \approx 0.34$ fN $\approx 0.34 \times 10^{-15}$ Newtons (a femto-Newton is 10^{-15} Newtons). Considering a Fiber-Matrix model with $C_F = 0.3\%$, as discussed in the Materials and Methods section, the reduced diffusion coefficient of the described Fiber-Matrix model will be $D_T \approx 0.15$. Assuming that the reduced diffusion coefficient impacts forced particle movement in a similar manner as diffusion (Einstein's relation [37], [38], [197]), the tissue resistance can be expressed as follows $F_{tissue-resistance} =$ $(1/ D_T)6\pi a \eta V_{magnetic}$. At equilibrium, the magnetic force and the tissue resistances equal,

therefore the expected speed of a particle through a tissue space will be $V_{magnetic} \approx$ 0.09 μm/s, or $\approx$ 90 nm/s.

3.7.2 Parameters for Nanoparticle Diffusion and Magnetic Transport through Human Tissue

At present, nanoparticle diffusivity and tissue resistance are not well known or characterized, especially within metastatic tumors in humans [37], [38]. However, several models can be used to predict the relative movement of nanoparticles through tissue based on the size of the particles and relevant tissue parameters. Two traditional models (the Renkin Pore model [37], [38], [197] and the Fiber-Matrix model [37], [38], [202]) were examined to determine the range of both diffusivity and tissue resistance.

The classical method of describing particle motion through different media is by a reduced diffusion coefficient that scales both the blood diffusion coefficient [37], [38] and the magnetic drift coefficient (by assuming Einstein's relation [38]). This reduced coefficient usually depends upon particle size (it decreases as the size increases) and the properties of the tissue (denser tissues increase particle resistance). Conversely, the magnetic force increases with particle size – it simply scales with particle volume [185], [244]. Thus, there is an optimal particle size for different tissue properties – the particle should be big enough so that the magnetic force is substantial, but small enough to effectively move through the tissue (Figure 30).
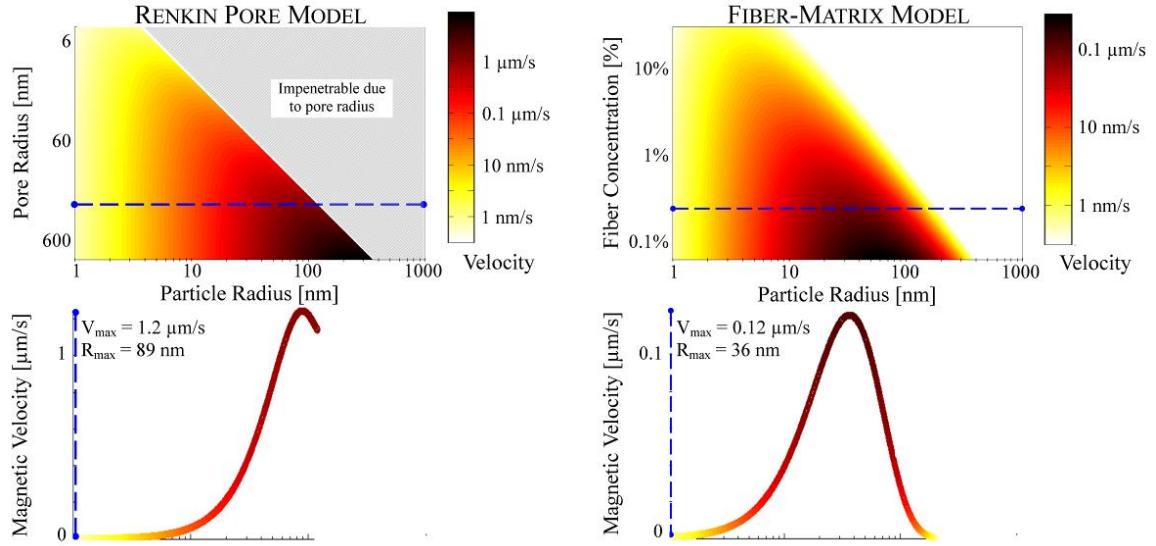
Figure 30: Optimal particle size for DMS. Two classical models of tissues (Renkin Pore and Fiber-Matrix model) are used to determine the maximum velocity for a given particle size. The top panels show the nanoparticle magnetic velocity (by a color scale with black being the fastest and white the slowest) for a given particle radius and tissue characteristic (pore size or fiber concentration). A cross-section was taken (dashed line) to show the magnetic velocity for either a pore radius of 200 nm or a fiber concentration of 0.3%. A 20×40 cm magnet with a 2.5 Tesla remnant magnetization held 11 cm away was used to calculate the magnetic velocity of the nanoparticles. There is a clear optimal particle size choice, for this tissue density it is 89 nm or 36 nm according to the Renkin or Fiber-Matrix model respectively.

Using Figure 30 and assuming a physiologically worst-case scenario for DMS of a very diffusive metastatic tumor (where the diffusion of nanoparticles is high, reducing the potential beneficial impact of the magnetic actuation, see Figure 24), a fiber concentration $C_F \approx 0.3\%$ using the Fiber-Matrix model [37], [38] was chosen that lead to an optimal particle diameter of 60 nm and a maximum particle magnetic drift velocity of ≈ 0.09 µm/s. The associated tissue diffusion coefficient, via the particle's size and Einstein's relation, is $D \approx 9 \times 10^{-13}$ m^2/s. These parameters were used to evaluate the DMS methodology.

3.7.3 Physiological Modifications

The simulation framework presented can be modified and detail can be added to address additional questions and to examine different treatment options. Variations in histology, changes to nanoparticles, and alterations in magnetic treatment correspond to changing the parameters in equation (50) and choosing their variation in time and space. For instance, the initial distribution of magnetic particles in blood vessels after systemic injection, but not yet in surrounding tissue by subsequent extravasation, diffusion, and magnetic forces, is reflected by choosing the initial condition $C_0(x, y)$ to match the geometric distribution of blood vessels measured from the histology (Figure 26). Likewise, computing the magnetic forces and including the migration velocity they cause for nanoparticles in each location in the body, including the effect of varying magnetic fields during treatment, can be included in $\vec{V}_{magnetic}(x, y, t)$. The impact particle and physiological parameters have upon specific terms in equation (50), however, is not always obvious. For example, varying the particle size will affect not only the diffusion coefficient D but also the magnitude of the particle migration velocity, $\vec{V}_{magnetic}$, as discussed in the Materials and Methods section. The diffusion coefficient, as is described by Brownian motion, decreases as the particle size increases [196]. The magnetic forces on particles scales with the volume of the particles but is opposed by the viscous resistance to nanoparticle motion offered by blood, interstitial fluid, or tissue, and that scales nominally with particle size. However, assuming various tissue models, as particle size increases above the geometrical thresholds of the tissue (i.e. above the pore size in a Renkin model), the tissue resistance climbs very quickly [37], [38], [197]. The net result is that the migration velocity increases with the square of particle diameter for an optimal

126

range and then decreases dramatically [37]. Variations in tissue properties also affect both the diffusion and the migration velocity parameters. Nanoparticles have more difficulty moving through dense cellular networks than through interstitial fluid [37], [38]; thus, tissue morphology effects both the diffusion and magnetic migration of the particles. Extravasation modifies how these particles move out from blood into surrounding tissue. In summary, although quantifying tissue properties of diffusion, migration, and extravasation is challenging and these parameters are often poorly known or uncertain, the mathematical model provides the ability to change them in simulations, to rapidly see the consequences, and to thus better understand how these tissue properties can affect nanoparticle distribution in tissue.

3.8 Magnetic Drug Transport Simulation Results

To evaluate the utility of externally applied magnetic forces in equilibrating nanoparticle levels in tumors, a series of simulations of equations (50) and (51) were performed. The rate of nanoparticle extravasation through capillary walls, the decay constant λ in equation (51), was inferred from the measured half-life ($t_{half-life}$) of nanoparticles in patients in the clinical trials of Lübbe et al. [11], [14], [31] (For additional details on the simulations and mathematics, please see the Supplementary Section.)

Figure 31 and Table 4 compare the time progressed behavior of the magnetic nanoparticles for the three treatment scenarios. Figure 31(a) represents the change in particle concentration with no applied magnetic forces over 3 hours for a tissue sample that includes a small metastasis. Locations with high vascular densities (normal tissue)

produced regions with high particle concentrations, while regions with lower vascular densities (tumor) experienced lower concentrations. In Figure 31(b), a constant West magnetic force was applied for 3 hours. The increase in particle concentration in the tumor is especially evident at the end of the second hour (at 120 minutes). Single direction shift yielded a 15.8% (compared to in blood) time-averaged nanoparticle concentration in the tumor, instead of the prior 9.9% value − a ×1.6 fold improvement; while time-averaged particle concentration in the normal tissue remained almost the same as for diffusion only (19.6% instead of 20.4%). Thus, magnetic shift in just one direction partially re-normalized particle concentration from normal to tumor tissue. Figure 31(c) simulated an alternating bi-directional magnetic treatment. This simulation began with no magnetic forces (for 45 min), then a unidirectional East magnetic force (for 1.5 hours), which then switched to a unidirectional West force (for 45 min). Alternating the direction of magnetic forces more effectively normalized particle concentration between normal and tumor tissue as the time-averaged concentration of particles in the tumor was 18.0%, which is close to the 19.7% concentration in normal tissue, a ×1.99 fold improvement compared to no magnetic actuation. The time-averaged metric is appropriate for time-dependent therapies or phase-specific therapies [305], like paclitaxel [4] and topotecan [5], where it is important to ensure that cancer cells experience a higher dosage of therapy over a long time window to continue treating them until they enter the correct phase of their cell cycle. For phase-nonspecific therapies or dose-dependent drugs [4], like gemcitabine [8] and carboplatin [6], it would suffice to increase the dose in cancer cells for just a short time since the drug efficacy is not dependent upon the cancer's cell cycle phase. In this phase-nonspecific case, it is more appropriate to consider the time

maximum concentration at each tissue location. If such a time-maximum metric is considered, then even a single direction shift is sufficient to normalize the maximum-over-time nanoparticle concentration from normal to tumor regions (see Table 4).
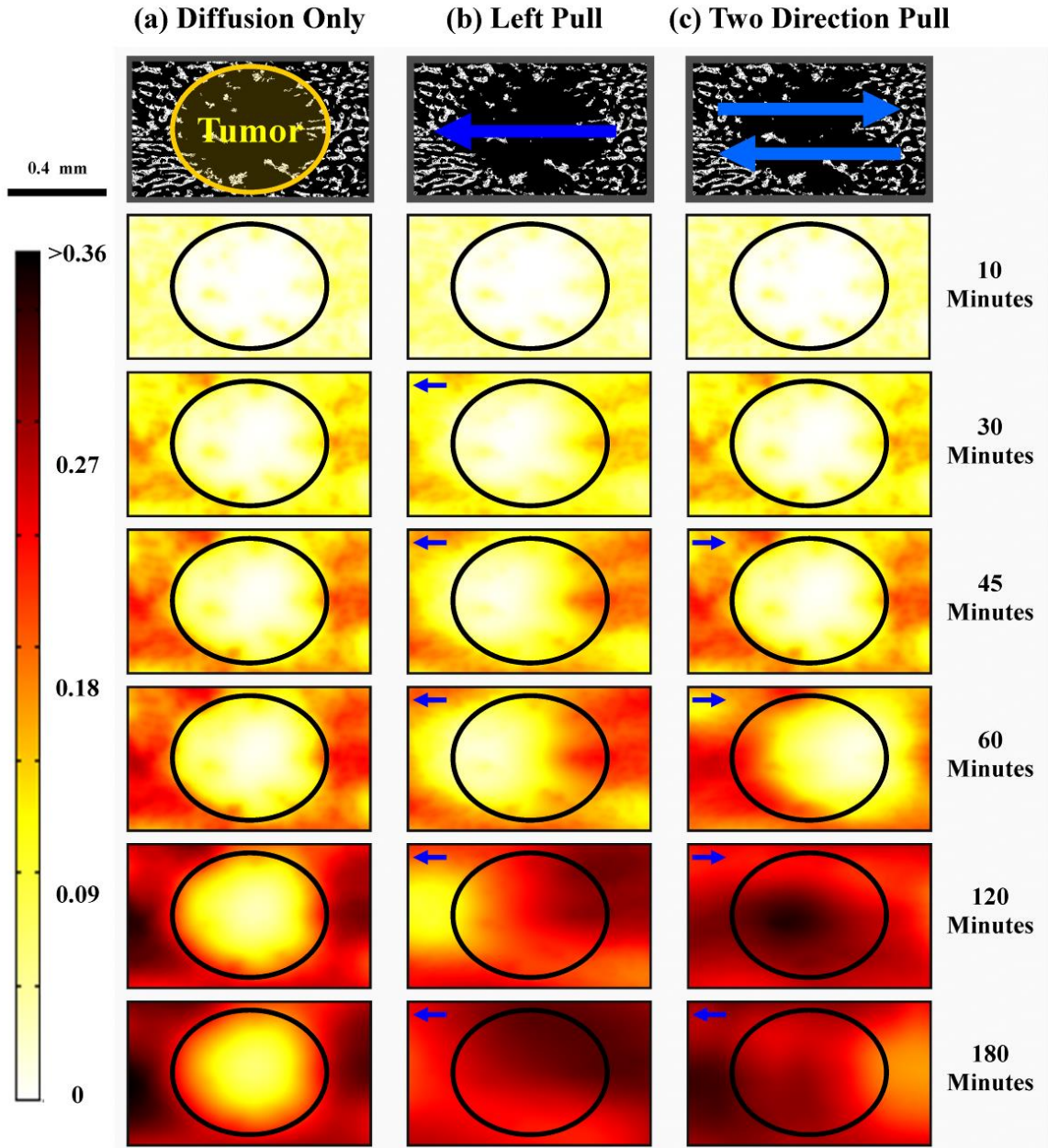
Figure 31: Time progression of nanoparticle concentration for the three treatments. The panels across the top were from a histological image of normal liver containing a small metastasis (marked by the circle). (a) Nanoparticle concentration with no magnetic forces and only diffusive

effects. The tumor region had a low nanoparticle concentration even after 180 min. (b) Nanoparticle concentration with a constantly applied magnetic force to the left (West). The nanoparticles were displaced to the left, increasing the particle concentration in the tumor. (c) Nanoparticle concentration with an alternating magnetic force first to the right (East) and then to the left (West). Nanoparticles from surrounding normal tissue were effectively brought into the tumor region by DMS.
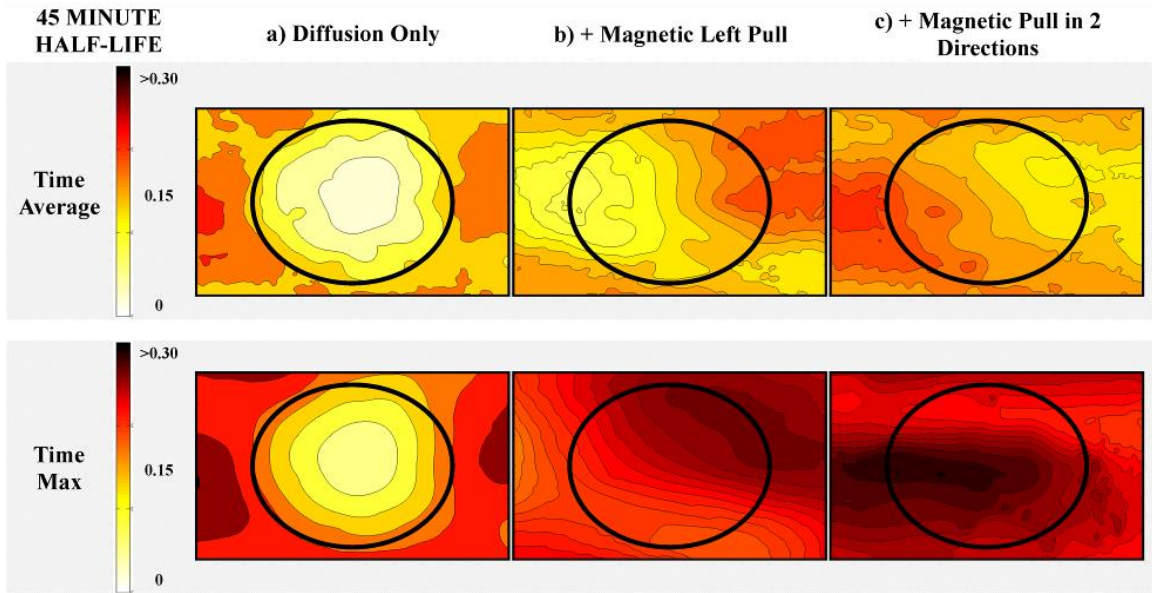
Figure 32: Visualization of the time-averaged (for slower acting therapies) and time-maximum (for fast acting therapies) concentration of therapy in normal and tumor tissue for the 3 cases from Figure 31. The top shows the time-averaged nanoparticle concentrations achieved across the tissue section over the 3 hour treatment window using: a) Diffusion only, b) A left magnetic pull only, and c) A two-directional magnetic pull. The bottom row represents the maximal nanoparticle concentration over time. Note that the tumor in the center of the image receives both significantly higher average and time-maximal nanoparticle levels when dynamic magnetic shift (DMS) is applied.

Figure 32 plots the results from the simulations, showing the average and maximum nanoparticle concentration over time in the tissue for three scenarios: Case a) no applied magnetic forces (diffusion only); Case b) West-only magnetic force; and Case c) a sequence of alternating magnetic forces (East then West). In Case a), diffusion only with no magnetic forces applied, both the time averaged and the time maximum nanoparticle concentration in the tumor region was half what it was in the normal tissue ($Ave_{[Normal]a} = 20.4\%$, $Ave_{[Tumor]a} = 9.9\%$; $Max_{[Normal]a} = 28.9\%$, $Max_{[Tumor]a} = 15.8\%$) (Figure 32a). In

Case b), a constant unidirectional (West) magnetic force improved the maximum nanoparticle concentration over time significantly in the tumor but the average over time increased only moderately compared to the surrounding normal tissue ($\text{Ave}_{[Normal]b} = 19.6\%$, $\text{Ave}_{[Tumor]b} = 15.8\%$; $\text{Max}_{[Normal]b} = 27.4\%$, $\text{Max}_{[Tumor]b} = 27.4\%$) (Figure 32b). Finally, Case c), a bidirectional sequence of magnetic forces (East then West), was shown to be the most effective and improved both the average and maximum tumor nanoparticle concentrations relative to normal tissue ($\text{Ave}_{[Normal]c} = 19.7\%$, $\text{Ave}_{[Tumor]c} = 18.0\%$; $\text{Max}_{[Normal]c} = 29.0\%$, $\text{Max}_{[Tumor]c} = 30.1\%$ in tumor) (Figure 32c). Overall, Case c) increased the $\text{Ave}_{[Tumor]}$ ratio for magnetic actuation vs. diffusion by 1.86 fold, and increased the $\text{Max}_{[Tumor]}$ ratio by 1.89 fold. In essence, magnetic shift was able to normalize the concentration of nanoparticles between normal and tumor cells, both according to the time-averaged (flow slow acting therapies) and time-maximum (for fast acting therapies) metrics.

Table 4: Time averaged and time maximum particle concentrations in tumor vs. surrounding normal tissue. The time average 'normal' and 'tumor' values for the three treatment cases were computed by taking the average concentration over time within each tissue region (normal or tumor). Likewise, the time maximum 'normal' and 'tumor' values were computed by taking the maximum over time at each location, and then spatially averaging that value across the normal and tumor regions, respectively. In the table below: time average 'T:N' ratio = 'Tumor Average' / 'Normal Average', and the 'Fold Increase' = 'T:N Average (Left Magnet or Shift 2 Directions)' / 'T:N Average (Diffusion Only)', likewise, the time maximum ratio 'T:N' = 'Tumor Max' / 'Normal Max', and the 'Fold Increase' = 'T:N Max (Left Magnet or Shift 2 Directions)' / 'T:N Max (Diffusion Only)'. The standard deviations are shown beneath each percentage to quantify the spatial variance around the time averaged or time maximum region concentrations. 'T:N' values close to unity correspond to effective therapy normalization between tumor and normal tissue, 'Fold Increases' quantify the benefit of DMS.

CASE	TIME AVERAGE				TIME MAX			
	Normal	Tumor	T:N	Fold Increase	Normal	Tumor	T:N	Fold Increase
a) Diffusion Only	20.4 % ± 3.7 %	9.9% ± 4.5 %	0.49	--	28.9% ± 4.3 %	15. 8% ± 5.2 %	0.55	--
b) Left Magnet	19.6% ± 3.2 %	15.8% ± 3.5 %	0.81	1.65	27.4% ± 4.1 %	27.4% ± 2.9 %	1.00	1.81
c) Shift 2 Directions	19.7% ± 2.8 %	18.0% ± 2.6 %	0.91	1.86	29.0% ± 3.3 %	30.1% ± 2.4 %	1.04	1.89

The cases above show that DMS can normalize nanoparticle concentrations across tumors by effectively transporting particles from well-vascularized normal tissue to poorly vascularized tumor regions. In the above example, the bi-directional mode timing was chosen based on intuition – it was thought beneficial to wait for some time to allow nanoparticles to first accumulate around vessels, and then to pull in the two different directions.

Going further, it is possible to examine the cells furthest from the blood vessels and compare the drug concentrations that these cells experience versus those that are near the vessels. Figure 33 shows the fold increase in the time-average and time-maximum

concentration for those cells furthest from the surrounding blood vessels for case b) and case c) compared to natural diffusion (case a)).
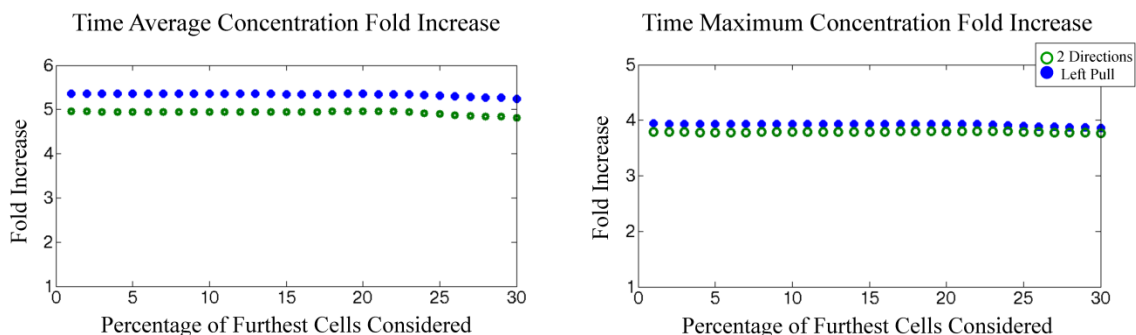
Figure 33: Fold increase for the furthest cells from the vasculature. The fold increase in the time-averaged and time-maximum drug concentration for case b) and case a) versus natural diffusion are shown for the cells furthest from the vasculature.

The cell that are furthest away see an increase in the drug concentration of > 5 times higher for time-averaged drug concentrations, and > 3.8 times higher for time-maximum drug concentrations. The clinical effect of this drug concentration increase within the tumor would have to be determined by animal trials. While this drug concentration increase may or may not improve the concentration within the tumors to therapeutic levels, DMS introduces the potential to lower systemic dosages. If a patient can currently receive therapeutic levels of chemotherapy at dose X, using DMS that dosage could potentially be reduced by a factor of 5 to X/5 and retain the same therapeutic effect. This systemic reduction in dosage would reduce the side effects experienced by the patient. To improve on case c), based on the collected autopsy data, we sought to determine the best DMS parameters by optimizing the timing and direction of the applied magnetic force.

133

3.9   Discussion

Metastatic tumors exhibit a diverse set of cellular, pathological, and structural features that make them a challenging target for therapeutic intervention [299], [300]. Evaluation at the microscopic level shows a variety of histopathologies, both within and among different cancer foci. For example: tumor grade, cellularity, degree of inflammation, desmoplastic host response, micro-hemorrhages, and necrosis can vary from lesion to lesion and even from sub-region to sub-region within a neoplasm. Moreover, the vascular characteristics of metastatic tumors differ from normal tissues and among cancer sites, both spatially and temporally [211]. Tumor vessels are often dilated, saccular, tortuous, and disorganized in their patterns of interconnection, producing a geometric resistance to blood flow and a decrease in perfusion [278]. The dysfunctional vasculature is evident at the gross pathological level as a striking feature of metastatic lesions is their firm, white appearance, suggesting that blood perfusion is less than that of most normal organs (Figure 25).

The chaotic nature of the vasculature and the subsequent increase in interstitial fluid pressure can result in uneven, fluctuating blood flow in tumors and prevent exposure to conventional nanotherapies that rely on the blood supply for diffusion-based distribution throughout the body, since the highest concentration of systemically delivered therapeutics are achieved at sites closest to the blood vessel and the concentration falls as the distance increases. As an example of this phenomenon, a study of local concentration of 5FU in liver metastases models as compared to adjacent normal tissue revealed limited 5FU penetration in areas of poor blood flow [276]. Inadequate tumor perfusion can also

result in hypoxia, postulated to be a central feature of cancer that is important to the physiological functioning and survival of the tumor cells and associated host cells. Historically, hypovascular tumor foci have been indirectly observed by their resistance to ionizing radiotherapy that relies on tissue oxygen content at the time of treatment [277]. More recently, hypoxic regions have been described to produce genomically unstable, clinically aggressive tumor cells that thrive in these regional microenvironments [280]. Thus, poorly vascularized tumors or tumor sub-regions can be clinically problematic based on both the inability to achieve therapeutically effective drug levels as well as the hypoxic microenvironment that is favorable to tumor cell growth and progression.

In the present study, we found that metastatic breast tumors in liver consistently had a lower number of blood vessels on average across the lesions than adjacent normal liver tissue (see Figure 26). Moreover, specific tumor sub-regions contained little or no vasculature, with vessel-to-tumor cell distances as large as 287 μm (see Figure 27). The one exception to this pattern was the outlier case A98-28. Interestingly, A98-28 is a liver metastasis of lobular carcinoma, the only non-ductal cancer that was included in the study. Detailed histopathological inspection of this tumor revealed large, poorly differentiated cells that did not grow in solid sheets, but rather in clusters that invaded the liver through the sinusoidal system, expanding it rather than replacing the normal tissue. The endothelium of the expanded sinusoids continues to express CD31; however, the majority of the CD31 positive cells are not blood vessels. Thus while case A98-28 appears well-perfused, it may in fact be the least vascularized tumor in the series due to the pathological features associated with metastatic lobular carcinoma.

To date, magnetic drug delivery has been used for focusing anti-neoplastic agents to primary, superficial tumors and has been evaluated in phase I clinical trials by placing a strong permanent magnet (0.8 Tesla) near the tumor [14], [31], [209]. While this approach is promising to treat single inoperable tumors in known, near-skin surface locations, it does not solve the larger clinical problem of increasing therapeutic levels in widespread metastatic disease, including lesions that are not near the skin surface. For nano-therapy, this is especially problematic since nanocarriers will diffuse substantially less effectively than small drug molecules. Simulations of the effect magnetic gradients have upon nanoparticle movement in tissue revealed it is possible to use DMS to transport nanoparticles from vessel reservoirs in normal tissue to avascular tumor areas. Both single and two directional dynamic shift were able to better distribute nanoparticles over the tissue space, with the bi-directional approach achieving a more even concentration throughout the tumor, showing the promise of using magnetic actuation for reaching into regions of the body inaccessible to pure diffusive movement of nanocarriers. Of particular note, the DMS method described and simulated here can be applied simultaneously to all metastatic foci in a given anatomical region of the body, as the magnets used would create sufficient gradients and forces on nanoparticles across all target locations, without the use of radiological imaging to identify lesions. This is important in breast cancer and other common epithelial tumors where many hundreds of metastatic sites typically exist in patients with advanced disease, ranging in size from grossly visible tumors to small, micro-metastatic foci (as an example in liver, see Figure 25). A one-by-one approach to visualize each tumor by radiological imaging and then

136

using magnetic control to target them individually would be impractical; however, DMS does not require such imaging and can be applied simultaneously to all lesions within a defined anatomical zone.

While there are other organs that will contain metastatic sites, we began with the treatment of the liver. Liver was a good candidate for DMS since it has large vessel gaps, is relatively homogenous in nature, and is the body's natural filtration system. DMS was capable of improving the nanoparticle concentration in the furthest cells by a factor of 5. This could further be improved if the micro-tumor is larger or denser and particles are unable to reach the isolated cells by natural diffusion.

DMS appears to be a promising solution to the problem of low blood supply in tumors. However, there are specific caveats that must be considered regarding this approach and the results described above. First, we used vascular density as a surrogate marker of perfusion and this assumption may not be accurate – in other words, the decrease in vessel number in metastatic lesions and the focal sub-regions with few or no vessels are consistent with decreased perfusion, but it is also possible that the unique nature of the tumor microenvironment, or other factors we have not yet considered, can compensate for the disordered vasculature and so perhaps therapeutic levels of drugs or nanoparticles may reach most or all tumor cells by diffusion alone. Ultimately, measurement of actual drug levels in clinical cancer samples will be necessary to gauge the effect of the abnormal tumor vasculature on drug concentration close to and distant from vessels and such studies will be undertaken in future work.

The second caveat is that the liver tissue utilized as a 'normal control' in our study may not be an appropriate metric for evaluating tumor vessels. Liver is richly vascularized with vessels and sinusoids in order to support the extensive metabolic functions of hepatocytes and has a high degree of vascular input and output. The fact that metastases have fewer vessels than adjacent liver tissue does not necessarily indicate the tumor vasculature is incapable of providing therapeutic nanoparticle levels to cancer cells.

The third caveat is that applying a magnetic force and moving the particles through the tissue space might cause damage to the tissue itself as the particles force their way through the extracellular space. This damage might be detrimental if it affects healthy tissue causing inflammation and loss of proper tissue function. On the other hand, this effect might be beneficial if it affects tumorous tissue as it could damage the tumor extracellular spaces, widening the gaps between densely populated cells, allowing more drug to perfuse through the micro-tumors.

Finally, the use of external magnets as a nanoparticle delivery system requires particles of large enough size to generate sufficient force to displace them in tissue – the larger the particle, the larger the force. However, as the size of the particle increases, the diffusability (D in the differential equation described in the Results section above) will decrease due to mechanical constraints in the microenvironment. These constraints include: physical barriers of cell-to-cell adhesion; the composition and density of stromal constituents; and, the nature of the tumor cell-stromal interactions. Overall, the balance of

magnetic force vs. tissue resistance favors medium sized particles (> 10 nm, but < 200 nm). Magnetic forces increase with particle volume (radius cubed) while the tissue resistance initially increases slowly with particle size, until the particle size nears a defining characteristic of the tissue (i.e. pore radius for the Renkin Pore model) making the resistance grow exponentially thereafter [37], [38]. In normal, highly organized and tightly compartmentalized tissues, the characteristics that define a tissue will favor smaller particles (i.e. small pore radii ~ 10 nm). But within the disorganized and haphazard structure of the tumor microenvironment, the tissues can be described to have much larger pore sizes that allow relatively unimpeded movement of even large sized nanoparticles (~ 200 nm) through substantial areas of tumor space.

Clearly though, all of these critical aspects of magnetic drug delivery will need to be carefully evaluated both in future simulations and in model systems designed to test and optimize the method in the laboratory. The goal of this chapter was to present the motivation and initial proof-of-concept for DMS based on autopsy studies of vasculature in human metastases and using mathematical modeling that has been validated against both *in-vitro* and *in vivo* experiments in prior studies.

3.10   Conclusion

In summary, DMS simulations based on quantitative analysis of the tumor vasculature in women who died of metastatic breast cancer indicate that improved nanoparticle concentrations can be achieved using magnetic gradients generated by one or two externally held strong magnets. Depending on the desired therapy, slow or fast acting, we

showed a DMS strategy for improving the nanoparticle normalization throughout the entire tumor space within the treated anatomical region. The next steps of this effort are to optimize DMS for future patients within unknown microtumor architecture.

Contribution to the Field and Clinical Applications

Metastasis is often a terminal diagnosis for cancer patients and current chemotherapy or radiotherapies have a limited beneficial impact on the patients' quality of life. Due to the physiological differences between primary tumors and metastatic sites, chemotherapy, which works well for primary tumors, often fails to effectively treat metastases due to the physical differences and cellular resistance of chemotherapeutics. To improve upon small drug molecules, researchers have developed various nanotherapeutics designed to target cancer cells more specifically and improve cellular uptake of these compounds. However, these nanotherapeutics often have a decreased and limited mobility in tissues due to their larger size created by the addition of targeting moieties or engineered coatings. Most targeted nanotherapeutics designed for metastatic cancers have a very promising outlook, but have in a clinical setting failed to live up to expectations. The discrepancy between expected therapeutic benefit and actual clinical results is an open question but a suggested factor includes limited drug perfusion into metastatic sites either from increased affinity of nanotherapeutics to peripheral metastatic cells or the decreased diffusional mobility of these large nanotherapeutics. We aimed to address this limited mobility by examining the physiology of the tissue microenvironment and then overcoming the limit of diffusional movement by pulling the ferrofluid using external magnets from vessel sources into otherwise inaccessible regions of the tissue.

140

Previous modeling has been conducted for non-magnetic particles diffusing into tumor spheroids or into various tissues cavities. However, there has been a lack of modeling for magnetic nanoparticles under an applied magnetic field in different tissues using anatomical data (i.e. actual blood vessel distributions). Our collaborators at the National Cancer Institute gathered images of unique liver histological sections obtained from NIH patients who died from metastatic breast cancer. We analyzed the vessel distribution in normal and metastatic cancer tissue. We presented a relationship between the blood vessel distribution and the tissue type (normal versus cancerous). We used these blood vessel distributions, available analytical particle diffusion models within tissues, and simulations of magnetic forces to determine in which tissues and particle sizes the use of magnetic forces could provide a clinical benefit. We developed an FEM model that incorporates the particle diffusion, magnetic forces, and particle half-life in the circulatory system, and is uniquely initialized with blood vessel distribution data of isolated breast cancer liver metastases in surrounding tissue (the exact situation in which we are trying to improve treatment). We created an open-loop control treatment scheme, which is designed to increase particle concentration at the metastatic sites that incorporates bi-directional magnetic forces, a specified treatment time, and particle size.

Chapter 4:   Optimizing Dynamic Magnetic Shift for Future Patients

Portions of this work originally appeared in [240].

This work utilized the same database of samples originally gathered by our collaborators at the National Cancer Institute (Skye Kim, Michael Tangrea, Mike Emmert-Buck, and Jaime Rodriguez-Canales). A finite element solver was developed by our collaborators at the California Institute of Technology (Aditya Viswanathan and Oscar Bruno). I developed the optimization scheme and performed the optimization upon the samples.

4.1   Introduction

Chapter 3 developed a novel model of the transport of ferrofluid within a tissue architecture. The model began from physical first principles of nanoparticle diffusion and magnetically induced velocities (equations (52) and (53)). Particle parameters were estimated from available theoretical models that predict the diffusive and mobility parameters within various tissues (see section 1.3.1). Then histological samples of breast cancer liver metastases were cultivated from a NIH autopsy database. These images became the basis for the tissue architectures used within the transport model. These histologically derived images provided a physiological relevance of the desired disease target, metastatic breast cancer.

Using the developed model, blood vessel distribution statistics were calculated and simple diffusion simulations conducted (column (a) of Figure 31 and Figure 32). Supporting previously observed results [211], [279], the regions where particles were unable to effectively reach by diffusion were small microtumors. As has been suggested

[211], [279], the adequate treatment of these microtumors is difficult and inadequate treatment leads to cancer reoccurrence.

To treat these small microtumors, the novel treatment scheme of DMS was introduced to assist diffusive transport by pulling magnetic nanoparticles through these avascular microtumors. The developed model was then used to investigate the potential impact DMS would have in treating these avascular microtumors. Using two treatment schemes, the benefit on the micro-environment of metastatic breast cancer within the liver by using DMS was quantified (see Table 4). However, while the benefit was significant in Chapter 3 (> 86% improvement over diffusion), the question remained if the proposed treatment strategies used were the best strategies available. In addition, if there are many variations of microtumors throughout the entire liver, what treatment strategy would provide the best results for the whole liver? What combination of magnetic fields overtime would be the best to pull the ferrofluid throughout the liver to achieve therapeutic treatment goals for any given patient with any given microtumor distribution?

Chapter 4 takes the next logical step and examines the optimal parameters necessary to deliver the ferrofluid throughout the liver architecture by applying a magnetic force to the nanoparticles. As with most optimization problems, the most challenging aspect to determining the optimal results is properly formulating the optimization problem [306]. For optimizing DMS, choices have to be made about which magnetic fields and in which directions these fields should be applied. In addition, what is the proper metric to measure and compare the beneficial impact of one treatment scheme to another?

From our initial simulations in Chapter 3, DMS saw substantial improvement by applying the magnetic field in two directions versus a single direction, but not for three directions over two. This allowed us to focus the optimization problem on pulling the magnetic nanoparticles only in two opposite directions (left and right). Combined with a fixed total treatment time (1.5 hours, as determined by the nanoparticle circulation half-life of 45 minutes), the only choice needed to be optimized is the amount of time the particles are pulled in any given direction (as a function of the total treatment time).

Considering the wide range of metrics available (a sample of which are shown in Table 4), it was necessary to develop robust metrics that capture the treatment potential of a given scheme. In addition, it is impractical that a clinician would know the precise location of all microtumors within a patient's liver and even if these positions were known, it would be impractical for a clinician to spot treat each site. Therefore, the metrics used to find the optimal treatment could not rely upon knowledge of the exact microtumor locations. Lastly, the therapeutic treatment goals were defined for two classes of chemotherapeutic agents: 1) those drugs that only act during a specific phase of the cell cycle and must therefore be available to the cells for as long as possible [4], [5], [305]; and 2) those drugs that are insensitive to the current phase of the cell cycle [4], [6], [8]. All of these requirements led to the development of two distinct metrics to quantify the benefit a specific treatment scheme has upon the tissue architecture. These metrics are discussed in section 4.2.3.

4.2   Methodology

To determine the optimal treatment scheme, four requirements are needed: a tissue transport model; a defined optimization space; a chosen set of metrics; and an optimization technique. Each of these elements will be discussed in the following section. Sacrificing time, physical storage space, and computer memory for simplicity allowed a simple exhaustive search technique to be used to find the optimal treatment parameters, simplifying the fourth requirement.

4.2.1   Tissue Transport Model

The tissue transport model of the ferrofluid is almost identical to the one developed in Chapter 3, section 3.7.2. Equations (52) and (53) were used to describe the time dependent transport behavior through a prescribed tissue space. The diffusive and magnetic velocity parameters used in Chapter 3 were again used for determining the optimal treatment scheme. Repeated again for clarity, these are a particle size of $a = 60$ nm, a diffusion coefficient of $D = 9 \times 10^{-13}$ m^2/s, and a magnetic drift velocity of $V = 0.09$ µm/s. The same half-life of 45 min was used but the treatment time was reduced to 1.5 hours. This treatment time was reduced for two reasons: 1) after a time period of twice the half-life has passed, the majority of available nanoparticles have extravasated out of the blood vessels and into the tissue; 2) patients are unwilling to submit to treatment for a prolonged period of time and even a treatment period of an hour and a half might be near the limit that a patient would withstand.

Lastly, the most important aspect of the tissue transport model comes from the physiologically relevant tissue architectures used to initialize the model. For examining an optimal treatment scheme, it is important to utilize a variety of similar microtumors from various patients. To this end, 142 samples from 16 patients were extracted from the library of whole organ histological slices. These samples had small microtumors centered within larger liver sections. A representative section is shown in Figure 34.
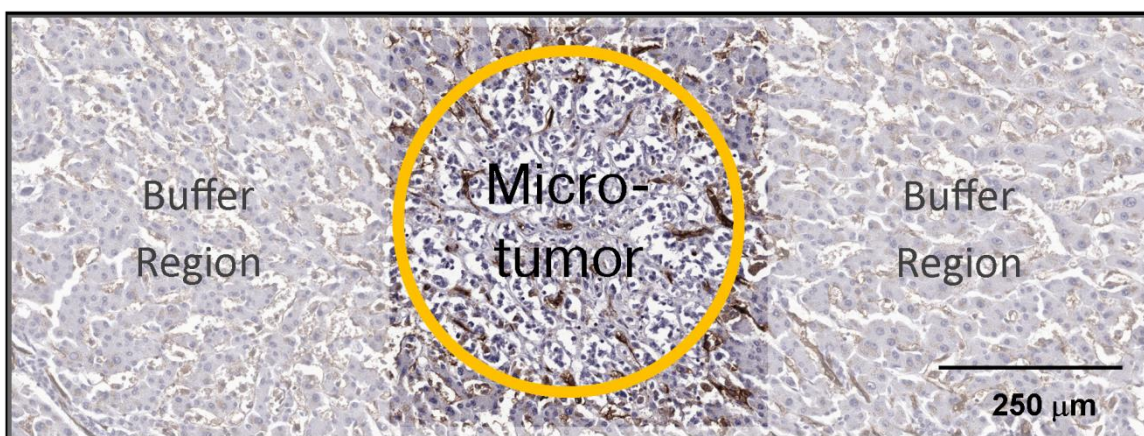
Figure 34: Representative section collected for the sample set used to find the optimal treatment scheme. Here there is a microtumor located at the center of the section denoted by the yellow circle. The un-shaded middle section is the region of interest and the metrics are calculated only over that specified un-shaded region. The lightly shaded buffer regions on all borders are necessary to properly account for nanoparticle movement into and out of the region of interest (see section 3.5).

To ensure that the physiological characteristics of these microtumors were similar, statistics of the blood vessel distribution were examined. Only two samples from the larger group were rejected because they contained very high concentrations of blood vessels within the treatment region (microtumor). This is exactly *not* the desired treatment case because these samples would receive high concentrations of nanoparticles regardless if a magnetic field was applied. The remaining samples comprised the sample

set of cases. This sample set was then used as the basis for determining the optimal treatment scheme.

4.2.2 Treatment Vectors

As discussed in section 4.1, only two magnetic field directions were examined. For further simplification, only two treatment vectors were considered. These are as follows:

$$(54) \quad \vec{U}_1 = \begin{cases} 1) \text{ Diffusion} \\ 2) \text{ Pull to the left} \\ 3) \text{ Pull to the right} \end{cases} = [0 \quad -1 \quad 1]$$

$$(55) \quad \vec{U}_2 = \begin{cases} 1) \text{ Diffusion} \\ 2) \text{ Pull to the right} \\ 3) \text{ Pull to the left} \end{cases} = [0 \quad 1 \quad -1] \quad .$$

There are many other combinations of treatment vectors possible with the constraint of only pulling in two directions, however, to maintain simplicity to decrease simulation time and physical storage, these two vectors were chosen. Treatment vector $\vec{U}_1$ begins by allowing the particles to diffuse a certain amount of time, followed by pulling the particles to the left for a period, and then the remaining portion to pull to the right. Treatment vector $\vec{U}_2$ allows the particles to diffuse, and then pulls to the right, followed by a pull to the left. Since the total time amount of time spent in each stage (diffusion, left or right pulling) must be equal to the total treatment time of 1.5 hours, it is sufficient to express the treatment scheme as a function of only two time periods. The two 'active' stages where magnetic forces are applied were chosen to describe a treatment scheme. Therefore, it is possible to plot any given metric within the following shape, shown in Figure 35.
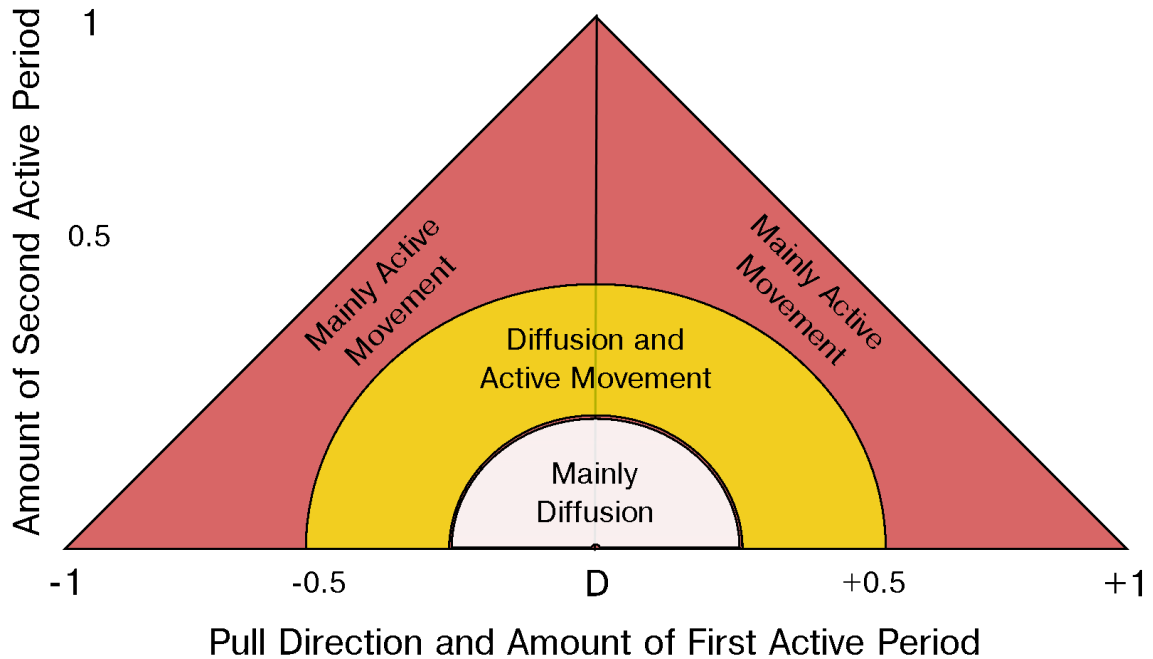
Figure 35: Optimization space as a function of the two defining time periods. The *x*-axis defines both the initial pull direction and the duration of the first active period. A negative *x*-value would correspond to a $\vec{U}_1$ treatment scheme, while a positive *x*-value would correspond to a $\vec{U}_2$ treatment scheme. The *y*-axis corresponds to the second active period's duration. If in the second quadrant, the second active direction would be to the right. If in the first quadrant, the second active direction would be to the left. All values have been given as a fraction of the total treatment window. Regions near the origin consist mainly of treatment schemes that primarily allow the particles to diffuse for the majority of the treatment window. Regions near the extremities of the triangle rely on constant manipulation of the particles by applied magnetic fields.

By plotting the metrics from the various treatment schemes onto Figure 35, the optimal scheme can be determined. In addition, these types of plots will easily allow identification of any symmetry between the two treatment vectors. Ideally if the sample set has sufficient randomness, the plot should exhibit symmetry across the *y*-axis. This can easily explained because the samples do not have a biologically predetermined coordinate system. Moving the particles left through a sample is equivalent to moving the particles right through a sample if a patient is reversed within the machine. Therefore, absolute directional choices do not matter, only the relative directions.

148

4.2.3 Metric Calculations

Beyond considering a single sample tumor, magnetic sweep sequences were optimized based on autopsy data across multiple tumors and patients. During sweep, there is a fundamental tradeoff; since the nanoparticles have a finite circulation time *in vivo*, there is a balance between magnetically pulling in one direction for as long as possible to sweep therapy as far as possible versus applying magnetic pulls in multiple different directions to bring drugs into poorly vascularized tumors from a variety of adjacent locations. A third pull direction did not add much value, so the timing of sweep was optimized only in two opposite directions. Vessel distribution autopsy data is only available for deceased patients, so there is a need to choose treatment for future patients based on autopsies of similar past patients. Hence, bidirectional sweep is optimized based on one set of samples (group A) and then tested on a second set of samples (group B).

The optimization metric has to be chosen with care. The goal of sweep is to normalize the distribution of therapy, to avoid therapy cold spots at thousands of metastatic tumors. Moreover, for a single small tissue area (for example, the 1.5 mm wide sample shown in Figure 34), a trained pathologist can identify the micro-tumor location and its extent (the yellow circle). However, it is not feasible for a pathologist to visually identify thousands of tumors per liver autopsy, and to do so over many patients. There is also a need to continue to consider both slow-acting and fast-acting therapies, for which, respectively, time-averaged and time-maximum particle concentrations are more appropriate. Thus, two metrics are considered

149

$$(56) \quad J^{time-avg} = \frac{\text{Spatial average of the time averaged concentration}}{\text{Spatial variance of the time averaged concentration}} = \frac{avg\left(C^{avg-time}\right)}{std\left(C^{avg-time}\right)}$$

$$(57) \quad J^{time-max} = \frac{\text{Spatial average of the time maximum concentration}}{\text{Spatial variance of the time maximum concentration}} = \frac{avg\left(C^{avg-max}\right)}{std(C^{avg-max})}$$

where the numerator is the spatial average of the nanoparticle concentration across the entire tissue slice, for either the time average or the time maximum. The denominator of the metrics penalizes high spatial variance across tissue; if the spatial standard deviation is high (if the tissue has regions of both high and low particle concentration, an undesired situation since now some tumor regions remain untreated), then the denominator is high and the metric is low. Together, the numerator and denominator try to ensure a nonzero and uniform concentration of therapy across the entire tissue. In particular, if sweep-timing parameters can be chosen to create a uniform high nanoparticle concentration, then this metric will tend to infinity and sweep will have completely eliminated the problem that poorly vascularized tumors lack therapy.

4.3 Results

4.3.1 Exhaustive Search

The bidirectional sweep optimization considered 70 tissue samples in group A and another 70 for group B. Two parameters were optimized across group A: the duration of the first pull and the duration of the second pull. Since the treatment time was kept constant at 1.5 hours, this also defined the waiting period at the start by $t_{wait} = 1.5 \text{ hrs} - t_{\text{first pull}} - t_{\text{second pull}}$. Each of the two pull durations was varied across 25 values yielding 625 simulations per tissue slice, and thus a total of 87,500 simulations. It took 7 days to complete the simulations on a Core i7 2.6 GHz computer running Windows 7 with 32 GB

of RAM. Figure 36 shows the fold increases in the two metrics $J^{time-avg}$ and $J^{time-max}$ versus the diffusion-only case for group A.

In the top panels of Figure 36, the optimal strategies for slow- and fast-acting drugs are marked by the blue stars. To increase the degree of normalization for slow-acting therapies ($J^{time-avg}$), it was best to shift in one direction for ~ 45% of the time, and then shift in the opposite direction for the remaining ~ 55% of the time. This procedure corresponded to shifting in one direction until just before the half-life of the nanoparticles was reached, and it made no difference if the shift was to the right or left first. By comparison, in order to increase the degree of normalization for fast-acting therapies ($J^{time-max}$), it was best to shift the nanoparticles in only one direction (either only left or only right) for the entire duration of the 1.5 hour treatment. This procedure ensured that every region of tissue saw as many new nanoparticles as possible. Bringing the particles back in the opposite direction did not improve the maximum over time. Thus, depending on whether a fast- or slow-acting therapy was considered, a different sweep strategy was optimal.

The optimums of Figure 36ab were then tested on group B. Panels Figure 36cd show the histograms of $J^{time-avg}$ and $J^{time-max}$ for diffusion alone versus optimal bidirectional sweep. As can be seen, the group A sweep optima effectively shift the mean of the histograms of group B to better outcomes.
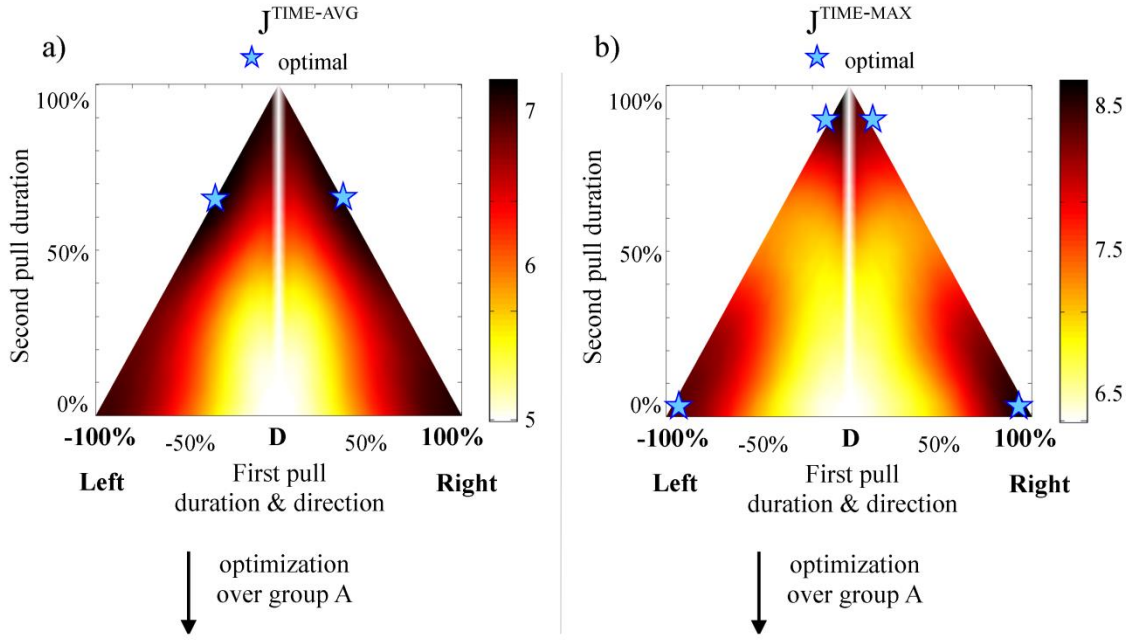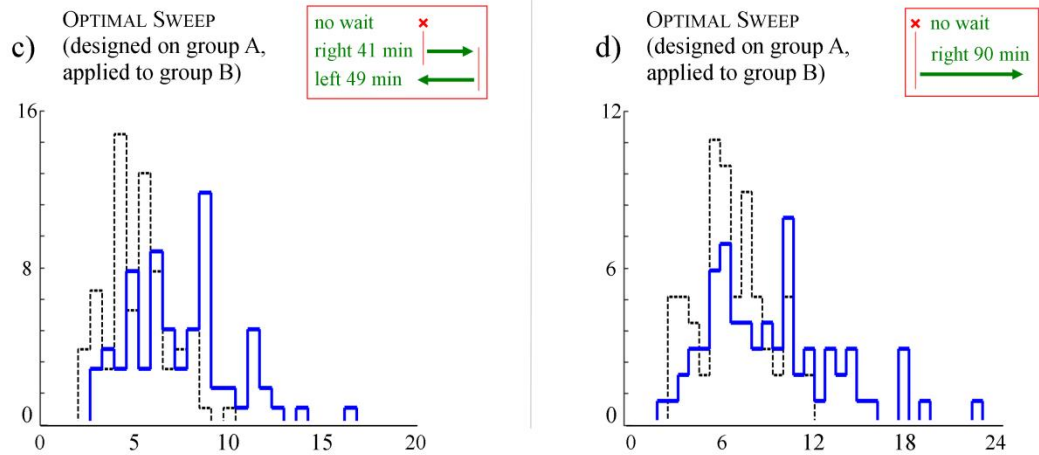
Figure 36: Sweep optimized over group A (first row) was then applied to group B (second row). a,b) Degree of nanoparticle normalization ($J^{time-avg}$ (56) and $J^{time-max}$ (57)) averaged over group A, as a function of pull left and right durations. Dark colors corresponded to high average concentrations and low spatial variances across group A tissue samples. Low values correspond to low concentrations or therapy hot and cold spots. In the triangles, the first pull duration is varied along the horizontal axis, the second along the vertical axis, with any remaining time spent waiting at the start of the treatment. For example, the location (+ 0.50, - 0.20) represents a 30% (27 minute) waiting time, followed by a 50% (45 min) pull to the right, then a final 20% (18 min) pull left. Pure diffusion (no pulling) corresponds to the center white vertical axes above D. Optimal strategies are marked by the blue stars. c,d) Dotted black lines shows the histogram of metrics $J^{time-avg}$ and $J^{time-max}$ across group B samples for diffusion only. When the optimal sweep sequences of group A are applied to group B samples, these metrics shift to higher values as shown by the solid blue histograms in panels c and d. The optimal sweep sequences are summarized within the red box at the top right of each panel: in both cases it is optimal to begin pulling immediately ("no wait") and the pull directions and optimal durations are shown by the

152

green arrows and text. In group c) the suboptimal and optimal means are 5.1 and 7.1 with a $p = 2.2 \times 10^{-7}$ (ANOVA). In group d) the suboptimal and optimal means are 6.3 and 8.7 with a $p = 8.4 \times 10^{-6}$ (ANOVA).

The following Figure 37 shows the optimal results for all 140 cases. In addition, since the improvement over passive diffusion is the standard, the fold increase over diffusion is shown. As is evident by the minimal differences between Figure 36 and Figure 37, the optimal solution has not changed with the addition of twice the number of samples. They are again represented as blue stars and correspond to $U_{avg,opt} = t(\vec{U}_1) = t(\vec{U}_2) = [0 \quad 0.45 \quad 0.55]$ for $J^{time-avg}$ and $U_{max,opt} = t(\vec{U}_1) = t(\vec{U}_2) = [0 \quad 1 \quad 0]$ for $J^{time-max}$.
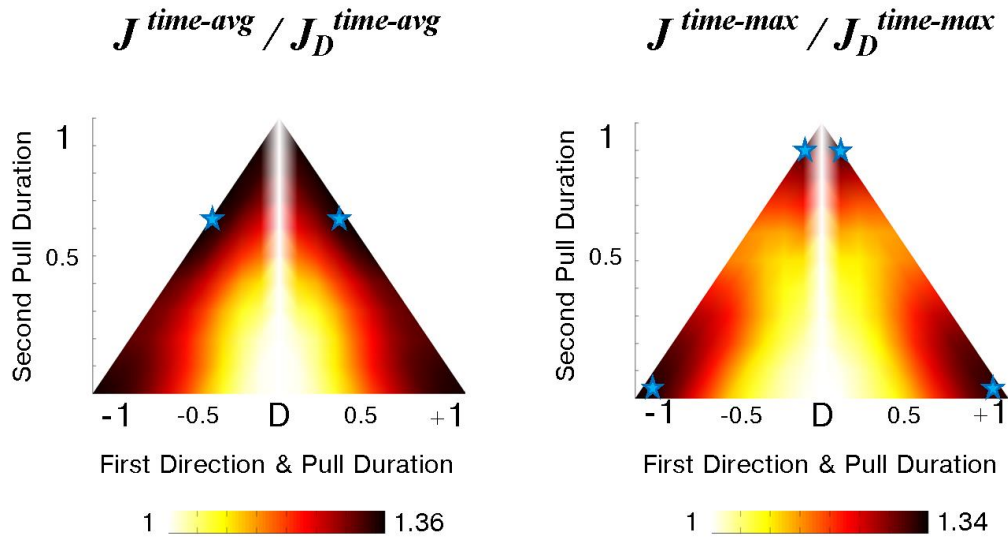
Figure 37: Treatment metrics for 140 cases for $D = 9 \times 10^{-7}$ mm^2/s, and $V_{magnetic} \approx 0.09$ μm/s. Here the treatment metrics are shown as a fold increase over the diffusion only case. Therefore, larger values correspond to regions where DMS improves the drug concentrations within the micro-tumors. The optimal treatment schemes are shown as blue stars. They represent $U_{avg,opt} = [0 \quad 0.45 \quad 0.55]$ for $J^{time-avg}$ and $U_{max,opt} = [0 \quad 1 \quad 0]$ for $J^{time-max}$.

4.3.2 *k*-Fold Cross Validation

The separation of the samples into two groups, the treatment group and the training group, can be extended to better predict the treatment potential of future patients. This process termed k-fold cross validation is a well-defined statistical technique to determine the applicability a sample set has to future sets [307]. Similar to Figure 36, *k*-fold cross validation begins by randomly separating the samples into *k* groups of roughly equal size, usually *k* is small and around 10. One of these *k* groups is then used as the treatment set while the rest are used together as the training set. The optimal treatment strategy is determined from the training set and then applied to the treatment set. In this way, the bias of knowing the details of the treatment sets is removed from determining the optimal treatment strategy.
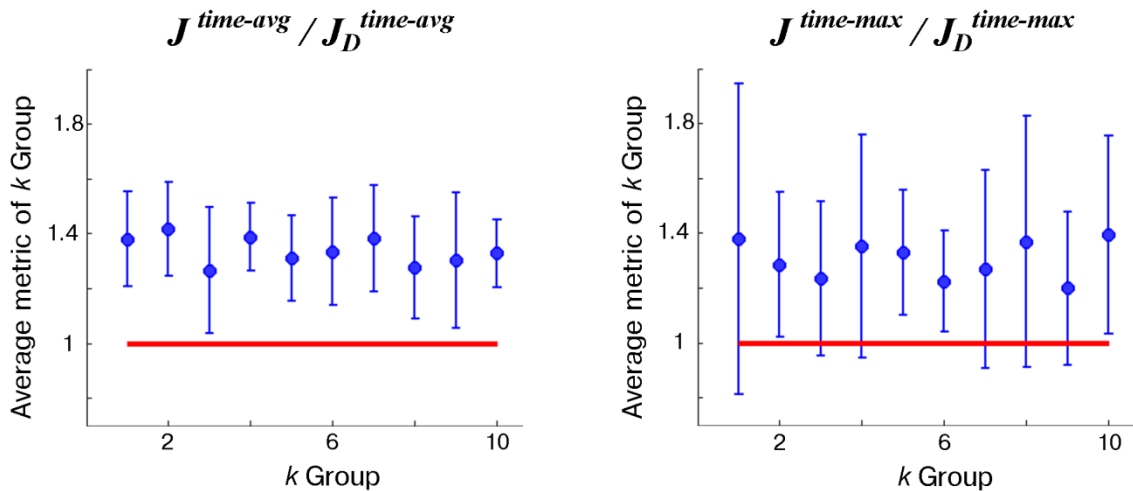
Figure 38: Treatment metrics of *k*-fold cross validation for 10 groups. The blue circles dictate the average treatment metric for the *k*[th] group. The standard deviation is illustrated by the associated error bars. The red line is the metric value associated with diffusion only movement. The average of all k groups is 1.34 and 1.30 for the ratios of $J^{time-avg}$ and $J^{time-max}$ to diffusion respectively.

This process is then repeated for each k group. The metrics achieved from the treatment sets are then averaged and are a reasonable approximation of the potential treatment gain for future samples. Figure 38 shows the results of a $k = 10$ cross validation. The average treatment metric for each k group are shown in blue with associated standard deviations. The red line denotes the diffusion only case. For each k group, the treatment strategy as determined by the training set produced on average better than diffusion treatment for the treatment groups. The average improvement to diffusion by using an optimized DMS strategy on the treatment groups was 34% and 30% for $J^{time-avg}$ and $J^{time-max}$ respectively.

4.3.3 Robustness

Figure 36 shows the optimum of the two treatment vectors, $\vec{U}_1$ and $\vec{U}_2$, for a given set of physical parameters as described in section 4.2.1. The next logical step is to examine the robustness of these optimums as the physical parameters relax. How do the optimums change if the nanoparticle diffusivity and mobility are an order of magnitude less? This could occur if the tissue architecture resists particle motion more than the models (sections 1.3.1 and 3.7.2) predict.

This complication was investigated by performing the same optimization procedure upon the sample set for varying Renkin reduced diffusion coefficients. As in equation (26), the Renkin reduced diffusion coefficient will change both the diffusion coefficient and magnetic velocity in equation (50) to the following

$$(58) \qquad \frac{\partial C}{\partial t} = -\nabla \cdot \mathcal{D}_{Robust} \left\{ - \underbrace{D\nabla C}_{\text{Diffusion}} + C \underbrace{\vec{V}_{magnetic}}_{\text{Drift Velocity}} \right\}$$

where the new addition is the coefficient $\mathcal{D}_{Robust}$ describing the unknown resistive tissue effects. This coefficient was varied over two orders of magnitude: $\mathcal{D}_{Robust} = 0.1$ to 0.01. In addition, the coefficient was adjusted to emulate the case where the particles are in blood, i.e. the tissue has no resistance to particle motion $\mathcal{D}_{Robust} = 6.6$. The results are shown in Figure 39. These consist of three additional cases investigated and each pair of triangular plots below represents 625 simulations. These simulations quadrupled the required amount of physical storage space and simulation time compared to those investigated in Section 4.3.1. An exhaustive search of all possible $\mathcal{D}_{Robust}$ would be infeasible and impractical.
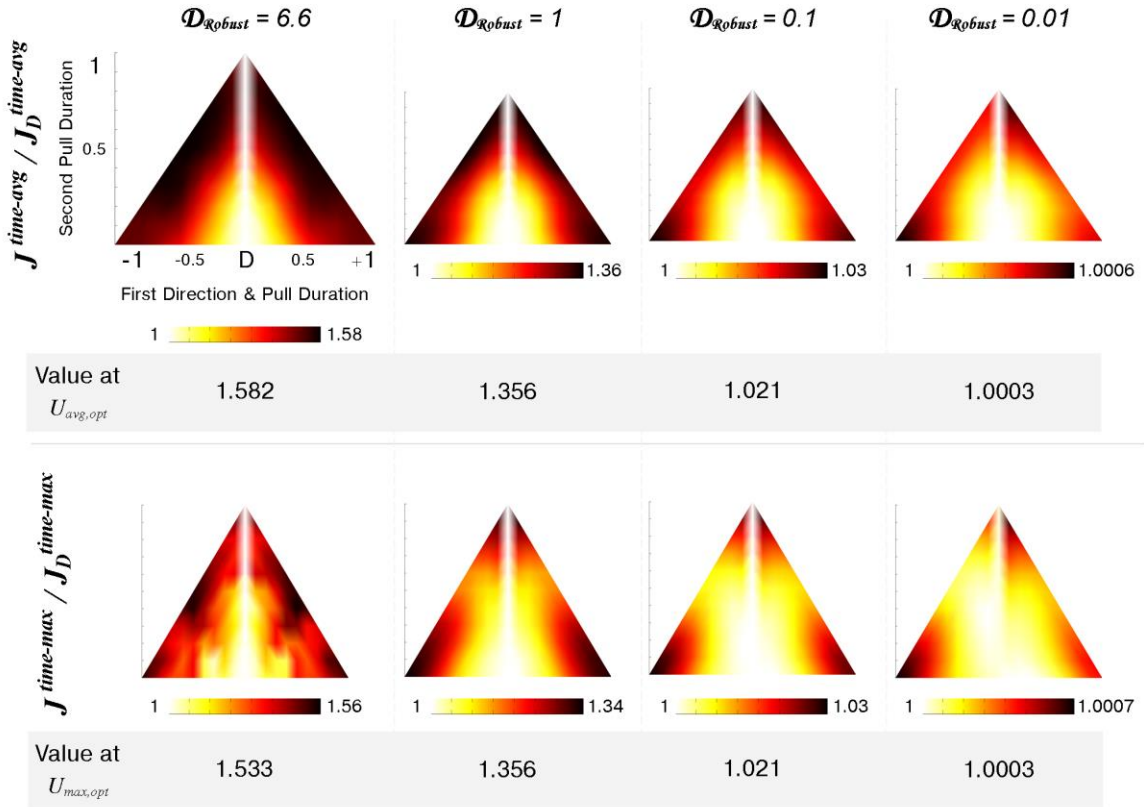
Figure 39: Robustness of optimization for various Renkin reduced diffusion coefficients. The optimal results are shown for various Reduced Renkin coefficients $\mathcal{D}_{Robust}$ and for the ratios of $J^{time-avg}$ and $J^{time-max}$ to diffusion. The second column represents the results as seen previously Figure 36. The first column represents the particles when they are within blood and not hindered by tissue. The third and fourth columns are with an increased tissue resistance increasing by an order of magnitude each time. Each triangle is shown on their own color scale as denoted beneath it where red is high and white is low values. In the gray panels beneath the triangular images, the metrics from each case taken at the previous optimum, $U_{avg,opt} = [0 \quad 0.45 \quad 0.55]$ and $U_{max,opt} = [0 \quad 1 \quad 0]$, are shown. This allows one to compare the optimums for every case to the previously obtained optimum.

The first row in Figure 39 shows the ratios to diffusion of the time-averaged metric, $J^{time-avg}$, for varying $\mathcal{D}_{Robust}$ coefficients, while the second row shows the time-maximum metrics, $J^{time-max}$. As $\mathcal{D}_{Robust}$ decreases, the optimal movement becomes biased to pulling the magnetic field in only one direction. At $\mathcal{D}_{Robust} = 6.6$, the optimal choice is similar to that for $\mathcal{D}_{Robust} = 1$, which is pulling in both directions for roughly

157

equal amounts of time. At $\mathcal{D}_{Robust} = 0.1$ the optimal choice is close to pulling in only one direction while at $\mathcal{D}_{Robust} = 0.01$, the optimal choice is to move the particles to the left the entire time. This transition to a single pull describes a bias that few samples have upon the optimal solutions.

Going further, it is possible to compare the magnitude of the metrics at the local and previous optimum locations. This is accomplished by examining the maximum value seen on the color scale (corresponding to the current optimum) compared to the value shown in the gray bar (compared to the prior cases' optimum). As $\mathcal{D}_{Robust}$ decreases the difference between these two values widens suggesting that the prior optimum scheme is not as effective. Lastly, it is important to note that the benefit achieved from DMS decreases dramatically as the particles are unable to move. This makes intuitive sense because as the particles are unable to move due to an applied field, they behave more like they would under diffusion only conditions. Table 5 shows the k-fold cross validation results for the cases in Figure 37 at their local optimums.

While Figure 39 describes the optimal behavior as tissue resistance is changed, it does not detail what would happen if the particles *could* be moved within a tissue. Even if the tissue resistance forces increase by orders of magnitude, it might be feasible for certain circumstances to apply significantly more magnetic force to counteract this increase in tissue resistance. How does the optimal solution change then?

The following Figure 40 details the optimal results of DMS for decreasing diffusion coefficients while keeping the magnetic velocity constant. This corresponds to a case where the particles have a lower than expected diffusional movement but maintain their magnetic velocities. Again, these are an additional three cases and each pair of triangular plots below represents 625 simulations. This brings the total simulation count to 612,500.
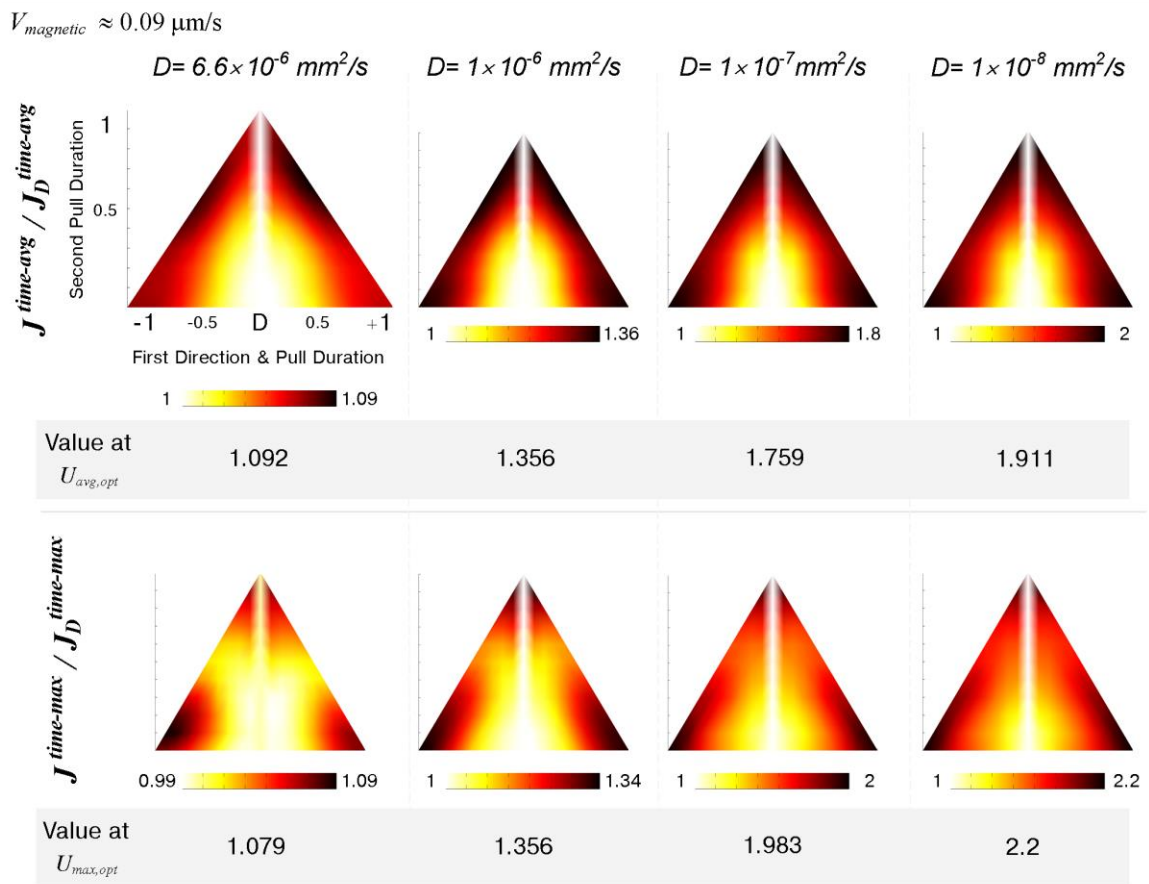
Figure 40: Optimal DMS treatment schemes as the diffusion coefficient decreases and the magnetic velocity remains constant for two treatment metrics. The second column represents the results as seen previously Figure 36. The first column represents the particles when they are within blood and not hindered by tissue. The third and fourth columns are with an increased tissue resistance increasing by an order of magnitude each time. Each triangle is shown on their own color scale as denoted beneath it where red is high and white is low values. In the gray panels beneath the triangular images, the metrics from each case taken at the previous optimum,

$U_{avg,opt} = [0 \quad 0.45 \quad 0.55]$ and $U_{max,opt} = [0 \quad 1 \quad 0]$, are shown. This allows one to compare the optimums for every case to the previously obtained optimum.

For both the $J^{time-avg}$ and $J^{time-max}$ metric ratios, Figure 40 shows that the optimal treatment scheme barely changes. This is evident by the difference seen in the maximum value of the color scale (corresponding to the current optimum) compared to the value shown in the gray bar (compared to the prior cases' optimum). This suggests that the optimal treatment schemes are robust when the magnetic velocities remain constant even when the diffusion coefficient decreases. As the diffusion coefficient decreased, the optimum scheme did spread to include more possibilities of magnetic movement as shown by a less confining region of high metric values along the exteriors of the triangular plots. This suggests that while there are defined optimums, constantly moving the particles by magnetic fields produces a near optimum solution.

In addition, as the diffusion coefficient decreases, the benefit achieved from DMS increases dramatically. When the diffusion coefficient is 100 times smaller than expected, the benefit from DMS is double that of diffusion only. This increase in DMS benefit as the diffusion coefficient decreases and the magnetic velocity remains constant shows that the DMS strategy can provide real benefit to those regions where magnetic forces have a significant impact on particle movement.

The results from k-fold cross validation for the robust investigation cases are shown in Table 5 below. This k-fold cross validation was performed using the local optimums for each case. As mentioned previously in Section 4.3.2, k-fold cross validation provides an

appropriate measure of the ability of a given optimal treatment scheme to treat future patients.

Table 5: k-fold cross validation for 10 groups of the additional parameters investigated for robustness.

Renkin Reduced Diffusion Coefficient $\mathcal{D}_{Robust}$	Fold Increase over Diffusion		Diffusion Coefficient D [mm^2/s]	Fold Increase over Diffusion	
	$J^{time-avg}$	$J^{time-max}$		$J^{time-avg}$	$J^{time-max}$
6.6	1.59	1.54	6×10^{-6}	1.094	1.078
1	1.34	1.30	1×10^{-6}	1.34	1.30
0.1	1.028	1.033	1×10^{-7}	1.79	1.92
0.01	1.0006	1.0007	1×10^{-8}	1.94	2.13

4.4   Conclusion

Chapter 3 introduced a novel model of ferrofluid transport within tissue architectures. The model began from physical first principles of nanoparticle diffusion and magnetically induced velocities. Well-developed theoretical models were used to predict the particle mobility parameters within a tissue. To obtain accurate and anatomically relevant tissue geometries, histological samples of breast cancer liver metastases were cultivated from a NIH autopsy database. These images became the basis for the tissue architectures used within the transport model. Using this image database, the chosen disease target of hepatic metastatic breast cancer was accurately modeled.

The ferrofluid mobility model through hepatic metastatic breast cancer identified the crucial lack of perfusion through microtumors. A proposed treatment strategy of dynamic

magnetic shift was introduced to simultaneously improve the perfusion of ferrofluid throughout the multitude of microtumors. Even with a naïve DMS treatment strategy, ferrofluid concentrations within microtumors were significantly increased versus passive diffusion. The next step was to determine the optimal treatment strategy for a multitude of microtumor samples in order to treat future patients within unknown microtumor architectures.

In order to determine the optimal treatment strategy for future patients with unknown microtumors, a dataset of available microtumor architectures was culled from the image dataset previously obtained. In addition, two metrics to quantify the benefit DMS provides to the treatment of the microtumors. These metrics describe the benefit of two classes of therapies: 1) cell-cycle sensitive therapies ($J^{time-avg}$); or 2) cell-cycle non-sensitive therapies ($J^{time-max}$). Then with the micotumor sample dataset, two DMS schemes (1: diffusion, left, and then right movement, or 2: diffusion, right and then left movement) were exhaustively searched to determine the optimum treatment.

Using the exhaustive search method with appropriate ferrofluid mobility parameters ($D = 9 \times 10^{-7}$ mm^2/s, $V_{magnetic} \approx 0.09$ μm/s), the optimal treatment strategy to treat the microtumor data set was determined for two treatment metrics. Two treatment vectors were investigated over the prescribed treatment window of an hour and a half. In total for the typical nanoparticle parameters associated with 60 nm particles, 87,500 simulations were conducted using the tissue mobility models. These simulations identified the optimal treatment scheme to maximize the two treatment metrics. These are shown in

Figure 36 and Figure 37. To extend this DMS scheme to future patients where the microtumor architecture may not be known, a *k*-fold cross validation was performed on the data set. The results from this cross-validation are shown in Figure 38. The potential benefit of DMS to future patients would be an improvement of 34% and 30% for $J^{time-avg}$ and $J^{time-max}$ therapies respectively.

Then extending upon this optimization technique, the particle parameters were relaxed. As the exact mobility parameters of the ferrofluid are difficult to determine for a given tissue, it was important to investigate the dependence of the optimum as the mobility is changed. An appropriate Renkin reduced diffusion coefficient, $\mathcal{D}_{Robust}$, was used to adjust the particle parameters within a range of the upper limit (mobility within blood) to a reduction by two orders of magnitude. With small decreases in the particle mobility, the optimum solutions remain in a similar region, see Figure 39. However, as the particle mobility decreases to two orders of magnitude, the optimum solutions start to favor a single direction of magnetic shift suggesting that individual samples bias the DMS treatment. In addition, as both the particle diffusive and magnetic mobility decrease so does the treatment potential of DMS.

Lastly, the DMS treatment optimum for cases where the magnetic velocity remains constant as the diffusion decreases was examined. All of these additional investigations increased the total simulation count to 612,500 simulations. The treatment schemes associated with the optimums, as the diffusion coefficient was reduced, were retained (see Figure 40). As the diffusion coefficient decreased, the optimum scheme did spread to

include more possibilities of magnetic movement as shown by a less confining region of high metric values. This suggests that near optimum results can be obtained by constantly moving the magnetic nanoparticles. In addition, as the diffusion decreased, DMS provided an increasing improvement over the diffusion only scenarios.

Contribution to the Field and Clinical Applications

Prior techniques to deliver therapeutics to metastatic and primary tumors rely upon active affinity moieties such as Herceptin [45], [47], [276]. However, these methods have significantly decreased perfusion rates when they encounter solid tumors. The reduction in perfusion into small metastatic micro-tumors leads to cancer reoccurrence. To potentially improve the treatment of these micro-tumors, a treatment strategy utilizing magnetic materials and external magnetic fields to improve perfusion was developed. DMS is a novel technique and could potentially improve treatment of these metastatic sites over normal diffusive behavior. This Chapter went further and investigated the optimal strategies needed to use DMS within a clinical setting. As DMS itself is novel, the optimal DMS treatment strategy has never before been investigated.

The optimal treatment schemes determined from this Chapter have been investigated for their potential future treatment of patient microtumors. The optimal behaviors suggest that there are cases when DMS is not clinically relevant or appropriate due to the low achievable benefit. This low benefit occurs when magnetic forces are unable to move nanoparticles sufficiently. However, there are also many circumstances were DMS would provide a clinically beneficial impact.

To appropriately use these optimized treatment schemes in the clinic, experiments in excised animal tissue sections (currently under way) and in live animals (planned) must be accomplished. Although it was consistently found, across more than a hundred micro-tumors, that liver metastases are poorly vascularized compared to normal tissue, the autopsy and simulation studies were carried out on a relatively small cohort (16 breast cancer patients). More data is needed to determine effective control strategies for different scenarios so that the optimal method can be chosen according to patient profiles (e.g., an advanced breast cancer patient with liver tumors).

Chapter 5: Conclusions

5.1 Looking Back

This thesis was aimed at understanding the magnetic nanoparticle behavior within blood vessels and tissues so that we could intelligently design the magnetic fields to place the nanoparticles where we want them. We developed a method to design appropriate magnetic fields to illicit nanoparticle boundary layer formation behavior within blood vessels and surrounding tissue. Using these concentrated nanoparticles at blood vessels as a reservoir, we showed how nanoparticles could be moved through bulk tissue. Finally, we explored the idea of utilizing this nanoparticle tissue transport to treat metastatic breast cancer liver metastases.

While magnetic drug targeting is not unique, the field had only a cursory understanding of the interaction between magnetic fields and the particles within biological structures. This thesis added the first in-depth analysis of how magnetic nanoparticles are transported within a biological environment. This transport is complex, and as noted earlier in sections 2.1 and 2.13.4, a simple analysis is not sufficient to predict how the nanoparticles will behave. This thesis showed that examining only the magnetic forces versus blood flow velocities led to an incorrect assessment of nanoparticle targeting ability. It is therefore necessary to include diffusion and profiles of the blood flow.

With these additions, the model correctly predicted experimental behavior. It offers a framework to begin to understand nanoparticle transport in a generic biological system. In practice when examining a specific treatment case, all of the biological factors unique

166

to the treatment scenario should be included within the analysis. Failure to include these factors might lead to a misunderstanding of the ability to magnetically target drugs. Many potential factors could be included, but the specific treatment case will dictate those that are important.

Generally, the two most important considerations are the extravasation ability of the nanoparticles and the diffusion coefficients of the tissue. How and by what method the nanoparticles extravasate from the target vessels needs to be understood so that it can be incorporated within the model. For example, if the particles are being targeted within large healthy intact vessels (e.g. aorta), extravasation will not occur. This may or may not matter for the specific treatment scenario. Similarly, the diffusivity and mobility through a specific tissue should be folded into the model. Nanoparticle mobility determines not only the particle behavior but also the treatment potential. Unfortunately, most of the mobility information of nanoparticles through specific tissues is not known and is quite complex. Nanoparticle mobility is dictated by particle size, tissue architecture, nanoparticle coating, tissue composition, cellular endocytosis and affinity, and potentially magnetic forces.

While other organs will show metastatic sites, we began with the liver as a first step and proof of principle. Since we examined the specific treatment case of the liver with breast cancer metastases, we were able to address these two main considerations. Extravasation within the liver is not an issue because the vasculature within the liver is primarily sinusoidal capillaries with larger holes (> 20 micron gaps) capable of allowing the

transport of cells [37]. This makes liver a perfect candidate to investigate magnetic drug targeting, as there are no limitations to particles leaving the vasculature. In addition, since the liver is the body's filtration system, most substances are transported to this organ making the particles' biodistribution favorable.

The second issue of particle mobility through the liver is more nuanced. Most organs have a well-ordered superstructure that lends directionality to the organ. For example, the lung is a highly ordered and well-defined structure with tightly controlled vessels for transporting oxygen and blood. While the liver has a structure, it is one of the more homogeneous organs within the body. This allowed us to approximate nanoparticle diffusion as an isotropic diffusion coefficient dependent upon the collagen content (see section 1.3.1).

These two factors are an example of how to apply the unique biological characteristics to the analysis but they are not the only specifications to consider. Other applicable factors include the blood vessel composition (the number and type of layers), and the ways in which the nanoparticles interact with the tissue itself. If extravasation does not occur, it could be important to understand in which vessel layers the particles accumulate. It is conceivable that without extravasation the particles would concentrate within the basement membrane of vessels next to the smooth muscle layers of vessels. In addition, for a given tissue the particles could potentially be endocytosed and degraded based upon the type of particle surface coating. The attached drugs, therefore, may not reach their desired target. Therefore, it is important to consider and understand the specific drug

type, drug-nanoparticle interaction, and the exact way in which cells within the tissue might affect this interaction.

There are a whole host of possible modifications to the generic model we have developed. Some of these modifications can be directly implemented, others require significant model adjustments, and the rest require an entirely new model. A subset of these modifications and possible changes to the model are discussed next.

Particle Coatings

Nanoparticles are designed with a myriad of coatings for specific purposes [68]–[71], [308], [309]. These coatings vary from polyethylene glycol (PEG) significant for its nonantigenic properties, dextran for biocompatibility, polyvinyl alcohol for preventing agglomeration, to polyacrylic acid for its increase in bioadhesion [309]. These coatings have a varied impact on their environment from how they change the nanoparticles' size to how they change the interaction of the nanoparticles with surrounding cells, extracellular matrix proteins, and plasma proteins. The change in the particles' size has been considered in section 2.15.8 and can easily be added into the model.

However, the change in particle "adhesive" properties has not been included in the model. One such adhesive property is the interaction of the antibody-functionalized particles to their associated antigen. Adhesive properties take two forms: 1) adhesiveness with the passive extracellular matrix, and 2) adhesiveness with cells due to surface protein interactions. The first effect could be accounted for by dramatically decreasing

169

the diffusion coefficient within the tissue. The second effect could be included in a simplified manner by adding a reaction term that removes nanoparticles as they come in contact with the cells (applicable if the cells endocytosis and degrade the particles). If more complexity is needed, then the model should be adjusted to keep track of individual cells and the amount of surface receptors on each cell that has interacted with a given nanoparticle.

Implanted Magnetic Devices

Implantable magnetic devices are being investigated for a variety of applications from the treatment of cardiovascular disease [97], [310] to ocular regeneration [117], [142]. While the principal of implantable magnetic devices is the same as an externally applied magnetic field, the local behaviors of the magnetic nanoparticles would change. The externally applied magnetic fields always concentrate the particles towards the direction of the magnet. However, due to biological barriers (such as the skin), the particles are not in direct contact with the magnet. Implantable devices typically have direct contact or nearly direct contact (separated by a permeable tissue layer) with the magnetic nanoparticles. To incorporate implanted magnetic devices to the model, a non-uniform magnetic field would have to be included that attracts magnetic particles to a solid object. This is a difficult modification to the model and should be done on a case-by-case basis.

Damage to Vessels and Tissues

Since magnetic particles are forcibly dragged through tissues and membranes by magnetic forces, there is a potential that the particles could cause damage to the

biological environment. This damage is a significant effect that is not considered in this model due to the lack of knowledge of how variously-sized particles at various forces will interact with the tissue environment. It is conceivable that small particles would damage their environment less than their larger counterparts because the magnetic forces and tissue resistance forces acting upon the larger particles is greater. However, this has not been characterized and is not known. There are various possible effects caused by damage to the tissue. Damage to membranes or biological barriers would not only allow more nanoparticles to traverse across the membrane, but also could potentially allow various plasma components to leak across the membrane. This could be potentially harmful as there are several plasma components that are purposefully separated from the tissue. For example, when blood plasma is exposed to sub-endothelial cells that express the blood clotting protein tissue factor, blood coagulation occurs [311]. These effects could be significant and should be investigated in future studies.

There are two ways to incorporate tissue damage into the model. A simplified approach would consist of introducing a time-dependent diffusion coefficient and mobility term. This would approximate the increase in mobility and natural diffusion as holes are created over time within membranes or tissues. A more complex scheme would require monitoring the specific holes and pathways created by pulling particles through biological barriers. Then created holes would have a higher diffusion and mobility coefficient allowing subsequent particles to follow the created path.

Concentration of Nanoparticles needed for Therapeutic Levels

There have only been a few clinical trials involving magnetic drug targeting in animals and even fewer in humans. The needed concentrations of magnetic nanoparticles to produce therapeutic levels of conjugated drugs are unknown. The drug elution profiles as they are released from the nanoparticles have been measured for *in vitro* conditions but have not been investigated *in vivo*. For example, it is not yet known how the forced movement of magnetic particles across a membrane will affect the association of conjugated drugs. Therefore, it might be necessary for the concentration of magnetic nanoparticles targeted within a tissue to be greater than is estimated from simple bound drug amounts.

In addition, endocytosis of the nanoparticles could reduce the available drug bound to the nanoparticle. Most drugs are not designed to withstand nor target the lysosomes within a cell and therefore would degrade once the particle-drug complexes are engulfed by a cell. These modifications to the model can be addressed by measuring and simulating the drug concentration as it elutes from the particles, diffuses through the tissue, and metabolized by the cells. To incorporate the removal of nanoparticle-drug complexes by the cells, a reaction term can be included that will decrease the available nanoparticle concentration over time. Both of these modifications are complex, but they are possible within the current model framework.

Unique Tissue Architecture Characteristics

Tissues architectures have various biological components and structures. Even when considering normal versus tumor tissue, these structures could have varying diffusion coefficients depending on tissue density. These variations between tissue types can be included by adding a spatially varying diffusion coefficient. While it is possible to add into the model, the diffusion and mobility of particles through the environment is not known. These values must be measured from animal experiments. Additionally, increased interstitial pressure within the tumor can be incorporated by adding a directional velocity to the particles. This velocity term would be centered at the tumor site and exert a force outwards from the tumor decreasing further away from the tumor. The pressure exerted can be measured and approximate velocities can be calculated from [37], [38].

The tissue mobility model is developed in only two dimensions, but a tissue is a complex three-dimensional system. Therefore, by simplifying the model to two dimensions, the mobility of the particles is underestimated. To incorporate three dimensions into the model would require new tissue architectures measured from the histological samples.

5.2   Future Experiments

Since validation of the model relied upon prior experimental studies that were good but not ideal for validation purposes, it would be beneficial to have an experiment designed specifically for this purpose. Two crucial *in vivo* experiments are needed to validate the vessel and tissue models respectively.

The first *in vivo* experiment consists of visualizing and quantifying the nanoparticle concentration flowing within a capillary and its surrounding tissue under a measured magnetic field. Knowing specifically how the nanoparticles are able to extravasate through capillaries and into the surrounding tissue space is crucial to validating the vessel-membrane-tissue model. Starting with capillaries simplifies the model by reducing the number of membrane components (there are no smooth muscle layers within capillaries). The most important measurement is how the particles build up along the vessel wall and within the tissue. Possible methods of measuring this concentration are with fluorescence, ultrasound, or magnetic particle imaging. The magnetic field strength and particle size should be changed to create various boundary layers. The varied boundary layers can be compared against the predicted boundary layers allowing for the validation of the transition region between velocity dominated and boundary layer formation cases. While live tissue is more realistic than *ex vivo* samples, it is more difficult to accurately control the experimental parameters. Therefore, initial experimental studies might have to be performed with *ex vivo* samples. Christoph Alexiou is already beginning experiments of this type [312].

The second recommended *in vivo* experiment is measuring the ability of magnetic fields to shift systemic magnetic nanoparticles millimeter distances through live tissue. This would validate the tissue transport model for hepatic metastatic breast cancer. These experiments are relatively simple but require significant preparation. Ideally, nanoparticles would be injected systemically into both healthy and diseased animals. The

particles would circulate through the animal and collect at the liver. A magnet held near the liver would be applied to a subset of these animals for a given treatment time. Afterwards histological sections of all sets of animals (normal versus diseased, with and without magnetic fields), would be taken of the liver. Then by visually inspecting these histological samples, the distribution of the magnetic nanoparticles throughout the tissue would be known and could be compared against the models for tissue movement. This comparison is crucial to knowing if and how the magnetic nanoparticles are able to be pulled into the diseased tissue within the liver. These experiments are currently under way as a collaboration between the University of Maryland and the National Cancer Institute.

Although not crucial, it would be beneficial to the model to be able to measure the natural diffusion of nanoparticles and the induced magnetic mobility of nanoparticles within various tissues for various particle types. This experiment can be performed using *ex vivo* samples. However, caution should be taken to ensure that the tissue is physiologically relevant. Tissues that have been frozen, while easy to procure, contain damaged extracellular matrixes due to ice crystal formation. Therefore, only fresh tissue should be used, but if they are not recently excised and kept cold before usage, there could be significant tissue digestion that occurs due to tissue death. This effort is currently under way at the University of Maryland. We are gathering information about the ability of nanoparticles to move through bulk tissue while maintaining physiologically relevant conditions. These mobility and diffusion parameters can then feed into the model to better account for particle movement.

Bibliography

[1]   R. Reszka, P. Beck, I. Fichtner, M. Hentschel, J. Richter, and J. Kreuter, "Body distribution of free, liposomal and nanoparticle-associated mitoxantrone in B16-melanoma-bearing mice," *J. Pharmacol. Exp. Ther.*, vol. 280, no. 1, pp. 232–237, Jan. 1997.

[2]   A. A. M. Veldt, N. H. Hendrikse, E. F. Smit, M. P. J. Mooijer, A. Y. Rijnders, W. R. Gerritsen, J. J. M. Hoeven, A. D. Windhorst, A. A. Lammertsma, and M. Lubberink, "Biodistribution and radiation dosimetry of 11C-labelled docetaxel in cancer patients," *Eur. J. Nucl. Med. Mol. Imaging*, vol. 37, no. 10, pp. 1950–1958, May 2010.

[3]   M. Perry, *The chemotherapy source book*, 2nd ed. Baltimore: Williams & Wilkins, 1996.

[4]   S. B. Horwitz, "Taxol (paclitaxel): Mechanisms of action," *Ann. Oncol. Off. J. Eur. Soc. Med. Oncol. Esmo*, vol. 5 Suppl 6, pp. S3–6, 1994.

[5]   D. Lorusso, A. Pietragalla, S. Mainenti, V. Masciullo, G. Di Vagno, and G. Scambia, "Review role of topotecan in gynaecological cancers: Current indications and perspectives," *Crit. Rev. Oncol. Hematol.*, vol. 74, no. 3, pp. 163–174, Jun. 2010.

[6]   S. B. Duffull and B. A. Robinson, "Clinical pharmacokinetics and dose optimisation of carboplatin," *Clin. Pharmacokinet.*, vol. 33, no. 3, pp. 161–183, Sep. 1997.

[7]   S. Rockwell and G. B. Grindey, "Effect of 2',2'-difluorodeoxycytidine on the viability and radiosensitivity of EMT6 cells in vitro," *Oncol. Res.*, vol. 4, no. 4–5, pp. 151–155, 1992.

[8]   E. Mini, S. Nobili, B. Caciagli, I. Landini, and T. Mazzei, "Cellular pharmacology of gemcitabine," *Ann. Oncol. Off. J. Eur. Soc. Med. Oncol. Esmo*, vol. 17 Suppl 5, pp. v7–12, May 2006.

[9]   T. . De Vita Jr., S. Hellman, and S. A. Rosenberg, *Cancer, principles and practice of oncology*, 8th ed. Philadelphia PA: Lippincott Williams and Wilkins, 2008.

[10]   B. Chabner and D. L. Longo, *Cancer chemotherapy and biotherapy : principles and practice*. Philadelphia: Wolters Kluwer Health/Lippincott Williams & Wilkins, 2011.

[11]   M. Arruebo, R. Fernandez-Pacheco, M. R. Ibarra, and J. Santamaria, "Magnetic nanoparticles for drug delivery," *Nano Today*, vol. 2, no. 3, 2007.

[12]   Q. A. Pankhurst, J. Connolly, S. K. Jones, and J. Dobson, "Applications of magnetic nanoparticles in biomedicine," *J. Phys. Appl. Phys.*, vol. 36, no. 13, p. R167, 2003.

[13] Q. A. Pankhurst, N. K. Thanh, S. K. Jones, and J. Dobson, "Progress in applications of magnetic nanoparticles in biomedicine," *J. Phys. Appl. Phys.*, vol. 42, pp. 224001–16, 2009.

[14] A. S. Lubbe, C. Bergemann, H. Riess, F. Schriever, P. Reichardt, K. Possinger, M. Matthias, B. Dorken, F. Herrmann, R. Gurtler, P. Hohenberger, N. Haas, R. Sohr, B. Sander, A. J. Lemke, D. Ohlendorf, W. Huhnt, and D. Huhn, "Clinical experiences with magnetic drug targeting: A phase I study with 4'-epidoxorubicin in 14 patients with advanced solid tumors," *Cancer Res.*, vol. 56, no. 20, pp. 4686–4693, 1996.

[15] J. Dobson, "Magnetic micro- and nano-particle-based targeting for drug and gene delivery," *Nanomed.*, vol. 1, no. 1, pp. 31–37, 2006.

[16] M. Johannsen, U. Gneveckow, B. Thiesen, K. Taymoorian, C. H. Cho, N. Waldöfner, R. Scholz, A. Jordan, S. A. Loening, and P. Wust, "Thermotherapy of prostate cancer using magnetic nanoparticles: feasibility, imaging, and three-dimensional temperature distribution," *Eur. Urol.*, vol. 52, no. 6, pp. 1653–1661, Dec. 2007.

[17] K. Maier-Hauff, R. Rothe, R. Scholz, U. Gneveckow, P. Wust, B. Thiesen, A. Feussner, A. von Deimling, N. Waldoefner, R. Felix, and A. Jordan, "Intracranial thermotherapy using magnetic nanoparticles combined with external beam radiotherapy: results of a feasibility study on patients with glioblastoma multiforme," *J. Neurooncol.*, vol. 81, no. 1, pp. 53–60, Jan. 2007.

[18] N. M. Orekhova, R. S. Akchurin, A. A. Belyaev, M. D. Smirnov, S. E. Ragimov, and A. N. Orekhov, "Local prevention of thrombosis in animal arteries by means of magnetic targeting of aspirin-loaded red cells," *Thromb. Res.*, vol. 57, no. 4, p. 611, 1990.

[19] P. K. Stoimenov, R. L. Klinger, G. L. Marchin, and K. J. Klabunde, "Metal Oxide Nanoparticles as Bactericidal Agents," *Langmuir*, vol. 18, no. 17, pp. 6679–6686, Aug. 2002.

[20] P. Gong, H. Li, X. He, K. Wang, J. Hu, W. Tan, S. Zhang, and X. Yang, "Preparation and antibacterial activity of Fe3O4@Ag nanoparticles," *Nanotechnology*, vol. 18, no. 28, p. 285604, Jul. 2007.

[21] R. D. Kopke, R. A. Wassel, F. Mondalek, B. Grady, K. Chen, J. Liu, D. Gibson, and K. J. Dormer, "Magnetic nanoparticles: inner ear targeted molecule delivery and middle ear implant," *Audiol Neurotol*, vol. 11, no. 2, pp. 123–133, 2006.

[22] B. Shapiro, I. Rutel, and K. Dormer, "A System to Inject Therapeutically-coated Magnetic Nano-particles into the Inner Ear: Design and Initial Validation," in *Proceedings of the 3rd International Conference on Micro- and Nanosystems, IDETC 2009*, San Diego, CA, 2009.

[23] L. Danielyan, R. Schäfer, A. von Ameln-Mayerhofer, M. Buadze, J. Geisler, T. Klopfer, U. Burkhardt, B. Proksch, S. Verleysdonk, and M. Ayturan, "Intranasal delivery of cells to the brain," *Eur. J. Cell Biol.*, vol. 88, no. 6, pp. 315–324, 2009.

[24] R. A. Guerrero, J. M. Ball, S. S. Krater, S. E. Pacheco, J. D. Clements, and M. K. Estes, "Recombinant Norwalk virus-like particles administered intranasally to mice induce systemic and mucosal (fecal and vaginal) immune responses," *J Virol*, vol. 75, no. 20, pp. 9713–22, 2001.

[25] M. Shinkai, "Functional magnetic particles for medical application," *J. Biosci. Bioeng.*, vol. 94, no. 6, pp. 606–613, 2002.

[26] C. Alexiou, W. Arnold, R. J. Klein, F. G. Parak, P. Hulin, C. Bergemann, W. Erhardt, S. Wagenpfeil, and A. S. Lubbe, "Locoregional cancer treatment with magnetic drug targeting," *Cancer Res.*, vol. 60, no. 23, pp. 6641–6648, 2000.

[27] C. Alexiou, R. Jurgons, R. Schmid, W. Erhardt, F. Parak, C. Bergemann, and H. Iro, "Magnetic Drug Targeting - A new approach in locoregional tumortherapy with chemotherapeutic agents. Experimental animal studies," *Hno*, vol. 53, no. 7, pp. 618–622, 2005.

[28] J. W. Barry, J. J. Bookstein, and J. F. Alksne, "Ferromagnetic embolization. Experimental evaluation," *Radiology*, vol. 138, no. 2, pp. 341–349, 1981.

[29] A. A. Kuznetsov, V. I. Filippov, R. N. Alyautdin, N. L. Torshina, and O. A. Kuznetsov, "Application of magnetic liposomes for magnetically guided transport of muscle relaxants and anti-cancer photodynamic drugs," *J. Magn. Magn. Mater.*, vol. 225, no. 1–2, pp. 95–100, 2001.

[30] A. S. Lubbe, C. Bergemann, J. Brock, and D. G. McClure, "Physiological aspects in magnetic drug-targeting," *J. Magn. Magn. Mater.*, vol. 194, no. 1–3, pp. 149–155, 1999.

[31] A. S. Lubbe, C. Bergemann, W. Huhnt, T. Fricke, H. Riess, J. W. Brock, and D. Huhn, "Preclinical experiences with magnetic drug targeting: Tolerance and efficacy," *Cancer Res.*, vol. 56, no. 20, pp. 4694–4701, 1996.

[32] S. Goodwin, C. Peterson, C. Hoh, and C. Bittner, "Targeting and retention of magnetic targeted carriers (MTCs) enhancing intra-arterial chemotherapy," *J. Magn. Magn. Mater.*, vol. 194, no. 1–3, pp. 132–139, 1999.

[33] T. Wu, H.-P. Lin, C.-N. Hu, J.-P. Chen, Y.-J. Chang, S.-T. Lee, and Y.-H. Ma, "Intra-Arterial Application of Magnetic Nanoparticles for Targeted Thrombolytic Therapy: A Rat Embolic Stroke Model," in *International Conference on the Scientific and Clinical Applications of Magnetic Carriers*, Rostock, Germany, 2010.

[34] S. C. Goodwin, C. A. Bittner, C. L. Peterson, and G. Wong, "Single-dose toxicity study of hepatic intra-arterial infusion of doxorubicin coupled to a novel magnetically targeted drug carrier," *Toxicol. Sci.*, vol. 60, no. 1, pp. 177–183, 2001.

[35] C. Alexiou, R. Jurgons, C. Seliger, S. Kolb, B. Heubeck, and H. Iro, "Distribution of mitoxantrone after magnetic drug targeting: Fluorescence microscopic investigations on VX2 squamous cell carcinoma cells," *Z. Phys. Chem.-Int. J. Res. Phys. Chem. Chem. Phys.*, vol. 220, no. 2, pp. 235–240, 2006.

[36] K. J. Widder, R. M. Morris, G. Poore, D. P. Howard, and A. E. Senyei, "Tumor remission in {Y}oshida sarcoma-bearing rats by selective targeting of magnetic albumin microspheres containing doxorubicin," *PNAS*, vol. 78, no. 1, pp. 579–581, 1981.

[37] R. L. Fournier, *Basic Transport Phenomena in Biomedical Engineering*. New York: Taylor & Francis, 2007.

[38] W. M. Saltzman, *Drug Delivery: Engineering Principles for Drug Therapy*. New York, NY: Oxford University Press, 2001.

[39] W. G. Pitt, G. A. Husseini, and B. J. Staples, "Ultrasonic drug delivery-a general review," *Expert Opin. Drug Deliv.*, vol. 1, no. 1, pp. 37–56, 2004.

[40] Z.-G. Gao, H. D. Fain, and N. Rapoport, "Controlled and targeted tumor chemotherapy by micellar-encapsulated drug and ultrasound," *J. Control. Release Off. J. Control. Release Soc.*, vol. 102, no. 1, pp. 203–222, Jan. 2005.

[41] B. W. Barry, "Novel mechanisms and devices to enable successful transdermal drug delivery," *Eur. J. Pharm. Sci.*, vol. 14, no. 2, pp. 101–114, 2001.

[42] A. R. Denet, R. Vanbever, and V. Preat, "Skin electroporation for transdermal and topical delivery," *Adv. Drug Deliv. Rev.*, vol. 56, no. 5, pp. 659–674, 2004.

[43] T. J. Dougherty, C. J. Gomer, G. Jori, D. Kessel, M. Korbelik, J. Moan, and Q. Peng, "Photodynamic therapy," *J. Natl. Cancer Inst.*, vol. 90, no. 12, pp. 889–905, 1998.

[44] N. Nasongkla, E. Bey, J. Ren, H. Ai, C. Khemtong, J. S. Guthi, S. F. Chin, A. D. Sherry, D. A. Boothman, and J. Gao, "Multifunctional polymeric micelles as cancer-targeted, MRI-ultrasensitive drug delivery systems," *Nano Lett.*, vol. 6, no. 11, pp. 2427–30, 2006.

[45] S. I. Rudnick, J. Lou, C. C. Shaller, Y. Tang, A. J. P. Klein-Szanto, L. M. Weiner, J. D. Marks, and G. P. Adams, "Influence of Affinity and Antigen Internalization on the Uptake and Penetration of Anti-HER2 Antibodies in Solid Tumors," *Cancer Res.*, vol. 71, no. 6, p. 2250, 2011.

[46] H. Hatakeyama, H. Akita, E. Ishida, K. Hashimoto, H. Kobayashi, T. Aoki, J. Yasuda, K. Obata, H. Kikuchi, T. Ishida, H. Kiwada, and H. Harashima, "Tumor targeting of doxorubicin by anti-MT1-MMP antibody-modified PEG liposomes," *Int J Pharm*, vol. 342, no. 1–2, pp. 194–200, 2007.

[47] D. B. Kirpotin, D. C. Drummond, Y. Shao, M. R. Shalaby, K. Hong, U. B. Nielsen, J. D. Marks, C. C. Benz, and J. W. Park, "Antibody targeting of long-circulating lipidic nanoparticles does not increase tumor localization but does

increase internalization in animal models," *Cancer Res*, vol. 66, no. 13, pp. 6732–40, 2006.

[48]   J. Hsu, D. Serrano, T. Bhowmick, K. Kumar, Y. Shen, Y. C. Kuo, C. Garnacho, and S. Muro, "Enhanced Endothelial Delivery and Biochemical Effects of [alpha]-Galactosidase by ICAM-1-Targeted Nanocarriers for Fabry Disease," *J. Controlled Release*.

[49]   O. C. Farokhzad, J. Cheng, B. A. Teply, I. Sherifi, S. Jon, P. W. Kantoff, J. P. Richie, and R. Langer, "Targeted nanoparticle-aptamer bioconjugates for cancer chemotherapy in vivo," *Proc Natl Acad Sci U S*, vol. 103, no. 16, pp. 6315–20, 2006.

[50]   H.-L. Liu, M.-Y. Hua, H.-W. Yang, C.-Y. Huang, P.-C. Chu, J.-S. Wu, I.-C. Tseng, J.-J. Wang, T.-C. Yen, P.-Y. Chen, and K.-C. Wei, "Magnetic resonance monitoring of focused ultrasound/magnetic nanoparticle targeting delivery of therapeutic agents to the brain," *Proc. Natl. Acad. Sci.*, vol. 107, no. 34, pp. 15205–15210, Aug. 2010.

[51]   J. F. Schenck, "Safety of Strong, Static Magnetic Fields," *J. Magn. Reson. Imaging*, vol. 12, no. 1, pp. 2–19, Jul. 2000.

[52]   D. J. Schaefer, J. D. Bourland, and J. A. Nyenhuis, "Review of patient safety in time-varying gradient fields," *J. Magn. Reson. Imaging Jmri*, vol. 12, no. 1, pp. 20–29, Jul. 2000.

[53]   E. D. Allen and J. H. Burdette, *Questions and Answers in MRI*, 2nd Ed. St. Louis, Missouri: Mosby, 2001.

[54]   E. Andersen, "Magnetic resonance imaging - safety and health issues," *Aaohn J. Off. J. Am. Assoc. Occup. Heal. Nurses*, vol. 55, no. 4, pp. 137–139, Apr. 2007.

[55]   S. Martel, O. Felfoul, J. B. Mathieu, A. Chanu, S. Tamaz, M. Mohammadi, M. Mankiewicz, and N. Tabatabaei, "MRI-based medical nanorobotic platform for the control of magnetic nanoparticles and flagellated bacteria for target interventions in human capillaries," *Int. J. Robot. Res.*, vol. 28, no. 9, pp. 1169–1182, 2009.

[56]   C. Catana, Y. Wu, M. S. Judenhofer, J. Qi, B. J. Pichler, and S. R. Cherry, "Simultaneous acquisition of multislice PET and MR images: {I}nitial results with a MR-compatible PET scanner," *J. Nucl. Med.*, vol. 47, no. 12, pp. 1968–76, 2006.

[57]   W. T. Katsiyiannis, D. P. Melby, J. L. Matelski, V. L. Ervin, K. L. Laverence, and C. C. Gornick, "Feasibility and safety of remote-controlled magnetic navigation for ablation of atrial fibrillation," *Am. J. Cardiol.*, vol. 102, no. 12, pp. 1674–1676, 2008.

[58]   A. Haake and J. Dual, "Contactless micromanipulation of small particles by an ultrasound field excited by a vibrating body," *J. Acoust. Soc. Am.*, vol. 117, no. 5, pp. 2752–2760, May 2005.

[59] S. Oberti, A. Neild, D. Möller, and J. Dual, "Strategies for single particle manipulation using acoustic radiation forces and external tools," *Phys. Procedia*, vol. 3, no. 1, pp. 255–262, Jan. 2010.

[60] C. Polk and E. Postow, *Handbook of Biological Effects of Electromagnetic Fields*. CRC Pr I Llc, 1996.

[61] Raphael C. Lee, "Cell Injury by Electric Forces," *Ann. N. Y. Acad. Sci.*, vol. 1066, no. Cell Injury: Mechanisms, Responses, and Repair, pp. 85–91, 2006.

[62] J. Villemejane and L. M. Mir, "Physical methods of nucleic acid transfer: general concepts and applications," *Br. J. Pharmacol.*, vol. 157, no. 2, pp. 207–219, 2009.

[63] R. G. Hawley, F. H. Lieu, A. Z. Fong, and T. S. Hawley, "Versatile retroviral vectors for potential use in gene therapy," *Gene Ther.*, vol. 1, no. 2, pp. 136–138, Mar. 1994.

[64] S. Li and L. Huang, "Nonviral gene therapy: promises and challenges," *Gene Ther.*, vol. 7, no. 1, pp. 31–34, Jan. 2000.

[65] S. W. Kamau, "Enhancement of the efficiency of non-viral gene delivery by application of pulsed magnetic field," *Nucleic Acids Res.*, vol. 34, no. 5, pp. e40–e40, Mar. 2006.

[66] S. C. McBain, H. H. P. Yiu, and J. Dobson, "Magnetic nanoparticles for gene and drug delivery," *Int. J. Nanomedicine*, vol. 3, no. 2, pp. 169–180, 2008.

[67] E. Stride, C. Porter, A. G. Prieto, and Q. Pankhurst, "Enhancement of Microbubble Mediated Gene Delivery by Simultaneous Exposure to Ultrasonic and Magnetic Fields," *Ultrasound Med. Biol.*, vol. 35, no. 5, pp. 861–868, May 2009.

[68] C. Sun, J. Lee, and M. Zhang, "Magnetic nanoparticles in MR imaging and drug delivery," *Adv. Drug Deliv. Rev.*, vol. 60, no. 11, pp. 1252–1265, Aug. 2008.

[69] C. C. Berry, "Progress in functionalization of magnetic nanoparticles for applications in biomedicine," *J Phys Appl Phys*, vol. 42, pp. 224003 – 12, 2009.

[70] A. G. Roca, R. Costo, A. F. Rebolledo, S. Veintemillas-Verdaguer, P. Tartaj, T. Gonzalez-Carreno, M. P. Morales, and C. J. Serna, "Progress in the preparation of magnetic nanoparticles for applications in biomedicine," *J. Phys. Appl. Phys.*, vol. 42, no. 22, p. 224002, Nov. 2009.

[71] O. Veiseh, J. W. Gunn, and M. Zhang, "Design and fabrication of magnetic nanoparticles for targeted drug delivery and imaging," *Adv. Drug Deliv. Rev.*, vol. 62, no. 3, pp. 284–304, Mar. 2010.

[72] D. C. Drummond, O. Meyer, K. Hong, D. B. Kirpotin, and D. Papahadjopoulos, "Optimizing liposomes for delivery of chemotherapeutic agents to solid tumors," *Pharmacol. Rev.*, vol. 51, no. 4, pp. 691–744, 1999.

[73] K. Cho, X. Wang, S. Nie, Z. Chen, and D. M. Shin, "Therapeutic Nanoparticles for Drug Delivery in Cancer," *Clin. Cancer Res.*, vol. 14, no. 5, pp. 1310–1316, Mar. 2008.

[74] U. Zimmermann and G. Pilwat, "Organ specific application of drugs by means of cellular capsule systems," *Z. Naturforsch. [C]*, vol. 31, no. 11–12, pp. 732–736, 1976.

[75] A. Solanki, J. D. Kim, and K.-B. Lee, "Nanotechnology for regenerative medicine: {N}anomaterials for stem cell imaging," *Nanomed.*, vol. 3, no. 4, pp. 567–578, Aug. 2008.

[76] R. Weissleder, A. Bogdanov, E. A. Neuwelt, and M. Papisov, "Long-circulating iron oxides for MR imaging," *Adv. Drug Deliv. Rev.*, vol. 16, no. 2–3, pp. 321–334, Sep. 1995.

[77] A. J. Cole, A. E. David, J. Wang, C. J. Galbán, H. L. Hill, and V. C. Yang, "Polyethylene glycol modified, cross-linked starch-coated iron oxide nanoparticles for enhanced magnetic tumor targeting," *Biomaterials*, vol. 32, no. 8, pp. 2183–2193, Mar. 2011.

[78] A. Figuerola, R. Di Corato, L. Manna, and T. Pellegrino, "From Iron Oxide Nanoparticles towards Advanced Iron-Based Inorganic Materials Designed for Biomedical Applications," *Pharmacol. Res.*, vol. 62, pp. 126–143, 2010.

[79] M. Mahmoudi, V. Serpooshan, and S. Laurent, "Engineered nanoparticles for biomolecular imaging," *Nanoscale*, 2011.

[80] C. Alexiou, R. Jurgons, R. Schmid, A. Hilpert, C. Bergemann, F. Parak, and H. Iro, "In vitro and in vivo investigations of targeted chemotherapy with magnetic nanoparticles," *J. Magn. Magn. Mater.*, vol. 293, no. 1, pp. 389–393, 2005.

[81] C. Alexiou, W. Arnold, P. Hulin, R. J. Klein, H. Renz, F. G. Parak, C. Bergemann, and A. S. Lubbe, "Magnetic mitoxantrone nanoparticle detection by histology, {X}-ray and MRI after magnetic tumor targeting," *J. Magn. Magn. Mater.*, vol. 225, no. 1–2, pp. 187–193, 2001.

[82] C. Alexiou, R. Jurgons, R. J. Schmid, C. Bergemann, J. Henke, W. Erhardt, E. Huenges, and F. Parak, "Magnetic drug targeting - Biodistribution of the magnetic carrier and the chemotherapeutic agent mitoxantrone after locoregional cancer treatment," *J. Drug Target.*, vol. 11, no. 3, pp. 139–149, 2003.

[83] C. Alexiou, A. Schmidt, R. Klein, P. Hulin, C. Bergemann, and W. Arnold, "Magnetic drug targeting: biodistribution and dependency on magnetic field strength," *J. Magn. Magn. Mater.*, vol. 252, no. 1–3, pp. 363–366, 2002.

[84] N. A. Brusentsov, T. N. Brusentsova, E. Y. Filinova, N. Y. Jurchenko, D. A. Kupriyanov, Y. A. Pirogov, A. I. Dubina, M. N. Shumskikh, L. I. Shumakov, and E. N. Anashkina, "Magnetohydrodynamic thermochemotherapy and MRI of mouse tumors," *J. Magn. Magn. Mater.*, vol. 311, no. 1, pp. 176–180, 2007.

[85] B. Chertok, B. A. Moffat, A. E. David, F. Yu, C. Bergemann, B. D. Ross, and V. C. Yang, "Iron oxide nanoparticles as a drug delivery vehicle for MRI monitored magnetic targeting of brain tumors," *Biomaterials*, vol. 29, no. 4, pp. 487–496, 2008.

[86] P. Dames, B. Gleich, A. Flemmer, K. Hajek, N. Seidl, F. Wiekhorst, D. Eberbeck, I. Bittmann, C. Bergemann, T. Weyh, L. Trahms, J. Rosenecker, and C. Rudolph, "Targeted delivery of magnetic aerosol droplets to the lung," *Nat Nano*, vol. 2, no. 8, pp. 495–499, 2007.

[87] Z. G. Forbes, B. B. Yellen, D. S. Halverson, G. Fridman, K. A. Barbee, and G. Friedman, "Validation of high gradient magnetic field based drug delivery to magnetizable implants under flow," *Ieee Trans. Biomed. Eng.*, vol. 55, no. 2 Part 1, pp. 643–649, 2008.

[88] U. O. Häfeli and G. J. Pauer, "In vitro and in vivo toxicity of magnetic microspheres," *J. Magn. Magn. Mater.*, vol. 194, no. 1–3, pp. 76–82, 1999.

[89] U. O. Hafeli, S. M. Sweeney, B. A. Beresford, J. L. Humm, and R. M. Macklis, "Effective targeting of magnetic radioactive 90Y-microspheres to tumor cells by an externally applied magnetic field. {P}reliminary in vitro and in vivo results," *Nucl. Med. Biol.*, vol. 22, no. 2, pp. 147–155, 1995.

[90] M. G. Krukemeyer, V. Krenn, M. Jakobs, and W. Wagner, "Mitoxantrone-Iron Oxide Biodistribution in Blood, Tumor, Spleen, and Liver-Magnetic Nanoparticles in Cancer Treatment," *J Surg Res*, 2012.

[91] T. Kubo, T. Sugita, S. Shimose, Y. Nitta, Y. Ikuta, and T. Murakami, "Targeted delivery of anticancer drugs with intravenously administered magnetic liposomes in osteosarcoma-bearing hamsters.," *Int. J. Oncol.*, vol. 17, no. 2, pp. 309–315, 2000.

[92] T. Matsuo, T. Sugita, T. Kubo, Y. Yasunaga, M. Ochi, and T. Murakami, "Injectable magnetic liposomes as a novel carrier of recombinant human BMP-2 for bone formation in a rat bone-defect model," *J. Biomed. Mater. Res.*, vol. 66A, no. 4, pp. 747–754, Sep. 2003.

[93] N. Morishita, H. Nakagami, R. Morishita, S. Takeda, and F. Mishima, "Magnetic nanoparticles with surface modification enhanced gene delivery of HVJ-E vector," *Biochem. Biophys. Res. Commun.*, vol. 334, no. 4, pp. 1121–1126, 2005.

[94] O. Mykhaylyk, A. Cherchenko, A. Ilkin, N. Dudchenko, V. Ruditsa, M. Novoseletz, and Y. Zozulya, "Glial brain tumor targeting of magnetite nanoparticles in rats," *J. Magn. Magn. Mater.*, vol. 225, no. 1–2, pp. 241–247, Jan. 2001.

[95] H. Nobuto, T. Sugita, T. Kubo, S. Shimose, Y. Yasunaga, T. Murakami, and M. Ochi, "Evaluation of systemic chemotherapy with magnetic liposomal doxorubicin and a dipole external electromagnet," *Int. J. Cancer*, vol. 109, no. 4, pp. 627–635, 2004.

[96] J.-H. Park, G. von Maltzahn, L. Zhang, M. P. Schwartz, E. Ruoslahti, S. N. Bhatia, and M. J. Sailor, "Magnetic Iron Oxide Nanoworms for Tumor Targeting and Imaging," *Adv. Mater.*, vol. 20, no. 9, pp. 1630–1635, May 2008.

[97] B. Polyak, I. Fishbein, M. Chorny, I. Alferiev, D. Williams, B. Yellen, G. Friedman, and R. J. Levy, "High field gradient targeting of magnetic nanoparticle-loaded endothelial cells to the surfaces of steel stents," *Proc. Natl. Acad. Sci.*, vol. 105, no. 2, pp. 698–703, 2008.

[98] P. Pouponneau, J.-C. Leroux, G. Soulez, L. Gaboury, and S. Martel, "Co-encapsulation of magnetic nanoparticles and doxorubicin into biodegradable microcarriers for deep tissue targeting by vascular MRI navigation," *Biomaterials*, vol. 32, no. 13, pp. 3481–3486, May 2011.

[99] S. K. Pulfer and J. M. Gallo, "Enhanced Brain Tumor Selectivity of Cationic Magnetic Polysaccharide Microspheres," *J. Drug Target.*, vol. 6, no. 3, pp. 215–227, Jan. 1998.

[100] S. L. Raut, B. Kirthivasan, M. M. Bommana, E. Squillante, and M. Sadoqi, "The formulation, characterization and in vivo evaluation of a magnetic carrier for brain delivery of NIR dye," *Nanotechnology*, vol. 21, no. 39, p. 395102, Oct. 2010.

[101] G. R. Reddy, M. S. Bhojani, P. McConville, J. Moody, B. A. Moffat, D. E. Hall, G. Kim, Y.-E. L. Koo, M. J. Woolliscroft, J. V. Sugai, T. D. Johnson, M. A. Philbert, R. Kopelman, A. Rehemtulla, and B. D. Ross, "Vascular Targeted Nanoparticles for Imaging and Treatment of Brain Tumors," *Clin. Cancer Res.*, vol. 12, no. 22, pp. 6677–6686, Nov. 2006.

[102] K. Schulze, A. Koch, B. Schopf, A. Petri, B. Steitz, M. Chastellain, M. Hofmann, H. Hofmann, and B. von Rechenberg, "Intraarticular application of superparamagnetic nanoparticles and their uptake by synovial membrane-an experimental study in sheep," *J. Magn. Magn. Mater.*, vol. 293, no. 1, pp. 419–432, 2005.

[103] H. Tanaka, T. Sugita, Y. Yasunaga, S. Shimose, M. Deie, T. Kubo, T. Murakami, and M. Ochi, "Efficiency of magnetic liposomal transforming growth factor-beta 1 in the repair of articular cartilage defects in a rabbit model," *J. Biomed. Mater. Res. A*, vol. 73A, no. 3, pp. 255–263, 2005.

[104] T. Tang, J.-W. Zheng, B. Chen, H. Li, X. Li, K.-Y. Xue, X. Ai, and S.-Q. Zou, "Effects of targeting magnetic drug nanoparticles on human cholangiocarcinoma xenografts in nude mice," *Hepatobiliary Pancreat Dist*, vol. 6, no. 3, pp. 303–307, 2007.

[105] R. Tietze, R. Jurgons, S. Lyer, E. Schreiber, F. Wiekhorst, D. Eberbeck, H. Richter, U. Steinhoff, L. Trahms, and C. Alexiou, "Quantification of drug-loaded magnetic nanoparticles in rabbit liver and tumor after in vivo administration," *J. Magn. Magn. Mater.*, vol. 321, no. 10, pp. 1465–1468, May 2009.

[106] H. Xu, T. Song, X. Bao, and L. Hu, "Site-directed research of magnetic nanoparticles in magnetic drug targeting," *J. Magn. Magn. Mater.*, vol. 293, no. 1, pp. 514–519, 2005.

[107] C. Zhang, M. Jugold, E. C. Woenne, T. Lammers, B. Morgenstern, M. M. Mueller, H. Zentgraf, M. Bock, M. Eisenhut, W. Semmler, and F. Kiessling, "Specific Targeting of Tumor Angiogenesis by RGD-Conjugated Ultrasmall Superparamagnetic Iron Oxide Particles Using a Clinical 1.5-T Magnetic Resonance Scanner," *Cancer Res.*, vol. 67, no. 4, pp. 1555–1562, Feb. 2007.

[108] A. S. Lubbe, C. Alexiou, and C. Bergemann, "Clinical applications of magnetic drug targeting," *J. Surg. Res.*, vol. 95, no. 2, pp. 200–206, 2001.

[109] M. W. Wilson, R. K. Kerlan, N. A. Fidelman, A. P. Venook, J. M. LaBerge, J. Koda, and R. L. Gordon, "Hepatocellular Carcinoma: Regional Therapy with a Magnetic Targeted Carrier Bound to Doxorubicin in a Dual MR Imaging/ Conventional Angiography Suite–Initial Experience with Four Patients," *Radiology*, vol. 230, no. 1, pp. 287–293, 2004.

[110] M. Johannsen, U. Gneveckow, L. Eckelt, A. Feussner, N. WaldÖFner, R. Scholz, S. Deger, P. Wust, S. A. Loening, and A. Jordan, "Clinical hyperthermia of prostate cancer using magnetic nanoparticles: Presentation of a new interstitial technique," *Int. J. Hyperthermia*, vol. 21, no. 7, pp. 637–647, Jan. 2005.

[111] T. Sato and R. Ruch, *Stabilization of Colloidal Dispersions by Polymer Adsorption*, vol. 9. Dekker New York:, 1980.

[112] V. P. Torchilin, "Recent advances with liposomes as pharmaceutical carriers," *Nat. Rev. Drug Discov.*, vol. 4, no. 2, pp. 145–160, Feb. 2005.

[113] S. Lecommandoux, O. Sandre, F. Checot, and R. Perzynski, "Smart hybrid magnetic self-assembled micelles and hollow capsules," *Prog. Solid State Chem.*, vol. 34, no. 2–4, pp. 171–179, Jul. 2006.

[114] J. Riegler, A. Liew, S. O. Hynes, D. Ortega, T. O'Brien, R. M. Day, T. Richards, F. Sharif, Q. A. Pankhurst, and M. F. Lythgoe, "Superparamagnetic iron oxide nanoparticle targeting of MSCs in vascular injury," *Biomaterials*, vol. 34, no. 8, pp. 1987–1994, Mar. 2013.

[115] P. G. Kyrtatos, P. Lehtolainen, M. Junemann-Ramirez, A. Garcia-Prieto, A. N. Price, J. F. Martin, D. G. Gadian, Q. A. Pankhurst, and M. F. Lythgoe, "Magnetic Tagging Increases Delivery of Circulating Progenitors in Vascular Injury," *Jacc Cardiovasc. Interv.*, vol. 2, no. 8, pp. 794–802, 2009.

[116] Z. Y. Huang, N. Pei, Y. Y. Wang, X. X. Xie, A. J. Sun, L. Shen, S. N. Zhang, X. B. Liu, Y. Z. Zou, J. Y. Qian, and J. B. Ge, "Deep magnetic capture of magnetically loaded cells for spatially targeted therapeutics," *Biomaterials*, vol. 31, no. 8, pp. 2130–2140, 2010.

[117] A. Yanai, U. O. Häfeli, A. L. Metcalfe, P. Soema, L. Addo, C. Y. Gregory-Evans, K. Po, X. Shan, O. L. Moritz, and K. Gregory-Evans, "Focused magnetic stem cell targeting to the retina using superparamagnetic iron oxide nanoparticles," *Cell Transplant.*, Mar. 2012.

[118] B. Bonnemain, "Superparamagnetic agents in magnetic resonance imaging: physicochemical characteristics and clinical applications. A review," *J. Drug Target.*, vol. 6, no. 3, pp. 167–174, 1998.

[119] M. G. Harisinghani, J. Barentsz, P. F. Hahn, W. M. Deserno, S. Tabatabaei, C. H. van de Kaa, J. de la Rosette, and R. Weissleder, "Noninvasive Detection of Clinically Occult Lymph-Node Metastases in Prostate Cancer," *N. Engl. J. Med.*, vol. 348, no. 25, pp. 2491–2499, Jun. 2003.

[120] A. Singh, T. Patel, J. Hertel, M. Bernardo, A. Kausz, and L. Brenner, "Safety of ferumoxytol in patients with anemia and CKD," *Am. J. Kidney Dis. Off. J. Natl. Kidney Found.*, vol. 52, no. 5, pp. 907–915, Nov. 2008.

[121] Y. X. Wang, S. M. Hussain, and G. P. Krestin, "Superparamagnetic iron oxide contrast agents: physicochemical characteristics and applications in MR imaging," *Eur. Radiol.*, vol. 11, no. 11, pp. 2319–2331, 2001.

[122] A. Lemke, B. Sander, A. Luebbe, H. Riess, N. Hosten, and R. Felix, "MR imaging after magnetic drug targeting in patients with soft-tissue tumors," *Radiology*, vol. 201, pp. 1421–1421, 1996.

[123] R. Beate, "Thermotherapy of oesophageal cancer with superparamagnetic iron oxide nanoparticles," in *8th International Conference on Scientific and Clinical Applications of Magnetic Carriers*, Rostock, Germany, 2010.

[124] R. Rand, H. Snow, D. Elliott, and M. Snyder, "Thermomagnetic surgery for cancer," *Appl. Biochem. Biotechnol.*, vol. 6, no. 4, pp. 265–272, 1981.

[125] P. Moroz, S. K. Jones, J. Winter, and B. N. Gray, "Targeting liver tumors with hyperthermia: ferromagnetic embolization in a rabbit liver tumor model," *J. Surg. Oncol.*, vol. 78, no. 1, pp. 22–29, 2001.

[126] C. L. Dennis, A. J. Jackson, J. A. Borchers, R. Ivkov, A. R. Foreman, P. J. Hoopes, R. Strawbridge, Z. Pierce, E. Goerntiz, J. W. Lau, and C. Gruettner, "The Influence of Magnetic and Physiological Behavior on the Effectiveness of Iron Oxide Nanoparticles for Hyperthermia," *J. Appl. Phys.*, vol. 41, no. D, pp. 134020–5, 2008.

[127] T. V. Samulski, *Non-invasive apparatus and method for providing RF energy-induced localized hyperthermia.* Duke University (Durham, NC), 2005.

[128] A. Natarajan, C. Gruettner, R. Ivkov, G. L. DeNardo, G. Mirick, A. Yuan, A. Foreman, and S. J. DeNardo, "NanoFerrite particle based radioimmunonanoparticles: binding affinity and in vivo pharmacokinetics," *Bioconjug. Chem.*, vol. 19, no. 6, pp. 1211–1218, Jun. 2008.

[129] S. J. DeNardo, G. L. DeNardo, A. Natarajan, L. A. Miers, A. R. Foreman, C. Gruettner, G. N. Adamson, and R. Ivkov, "Thermal dosimetry predictive of efficacy of 111In-ChL6 nanoparticle AMF induced therapy for human breast cancer in mice," *J. Nucl. Med.*, vol. 48, pp. 437–444, 2007.

[130] C. Gruettner, K. Muller, J. Teller, F. Westphal, A. Foreman, and R. Ivkov, "Synthesis and antibody conjugation of magnetic nanoparticles with improved specific power absorption rates for alternating magnetic field cancer therapy," *J. Magn. Magn. Mater.*, vol. 311, pp. 181–6, 2007.

[131] A. D. Grief and G. Richardson, "Mathematical modeling of magnetically targeted drug delivery," *J. Magn. Magn. Mater. - Proc. Fifth Int. Conf. Sci. Clin. Appl. Magn. Carriers*, vol. 293, no. 1, pp. 455–463, 2005.

[132] A. E. David, A. J. Cole, B. Chertok, Y. S. Park, and V. C. Yang, "A combined theoretical and in vitro modeling approach for predicting the magnetic capture and retention of magnetic nanoparticles in vivo," *J. Control. Release Off. J. Control. Release Soc.*, vol. 152, no. 1, pp. 67–75, May 2011.

[133] S. K. Hobbs, W. L. Monsky, F. Yuan, W. G. Roberts, L. Griffith, V. P. Torchilin, and R. K. Jain, "Regulation of transport pathways in tumor vessels: Role of tumor type and microenvironment," *PNAS*, vol. 95, no. 8, pp. 4607–4612, 1998.

[134] V. P. Torchilin, "Drug targeting," *Eur. J. Pharm. Sci.*, vol. 11, pp. 81–91, 2000.

[135] D. B. Montgomery, *Solenoid magnet design*. Wiley, 1969.

[136] H. Xu, S. M. Conolly, G. C. Scott, and A. Macovski, "Homogeneous magnet design using linear programming," *Magn. Ieee Trans.*, vol. 36, no. 2, pp. 476–483, 2000.

[137] K. Preis, O. Biro, M. Friedrich, A. Gottvald, and C. Magele, "Comparison of different optimization strategies in the design of electromagnetic devices," *Magn. Ieee Trans.*, vol. 27, no. 5, pp. 4154–4157, 1991.

[138] S. Martel, C. C. Tremblay, S. Ngakeng, and G. Langlois, "Controlled manipulation and actuation of micro-objects with magnetotactic bacteria," *Appl. Phys. Lett.*, vol. 89, no. 23, pp. 233904–3, 2006.

[139] S. Martel, J.-B. Mathieu, O. Felfoul, A. Chanu, E. Aboussouan, S. Tamaz, P. Pouponneau, L. Yahia, G. Beaudoin, G. Soulez, and M. Mankiewicz, "Medical and Technical Protocol for Automatic Navigation of a Wireless Device in the Carotid Artery of a Living Swine Using a Standard Clinical MRI System," in *Medical Image Computing and Computer-Assisted Intervention, MICCAI*, 2007, pp. 144–152.

[140] S. Martel, M. Mohammadi, O. Felfoul, Z. Lu, and P. Pouponneau, "Flagellated Magnetotactic Bacteria as Controlled MRI-trackable Propulsion and Steering Systems for Medical Nanorobots Operating in the Human Microvasculature," *Int. J. Robot. Res.*, vol. 28, no. 4, pp. 571–582, 2009.

[141] L. Qu, G. Shi, J. Yuan, G. Han, and F. Chen, "Preparation of polypyrrole microstructures by direct electrochemical oxidation of pyrrole in an aqueous solution of camphorsulfonic acid," *J. Electroanal. Chem.*, vol. 561, no. 1–2, pp. 149–156, 2004.

[142] D. L. Holligan, G. T. Gillies, and J. P. Dailey, "Magnetic guidance of ferrofluidic nanoparticles in an in vitro model of intraocular retinal repair," *Nanotechnology*, vol. 14, no. 6, pp. 661–666, 2003.

[143] U. O. Häfeli, M. A. Lobedann, J. Steingroewer, L. R. Moore, and J. Riffle, "Optical method for measurement of magnetophoretic mobility of individual magnetic microspheres in defined magnetic field," *J. Magn. Magn. Mater.*, vol. 293, no. 1, pp. 224–239, May 2005.

[144] E. B. Denkbaş, E. Kiliçay, C. Birlikseven, and E. Öztürk, "Magnetic chitosan microspheres: preparation and characterization," *React. Funct. Polym.*, vol. 50, no. 3, pp. 225–232, Feb. 2002.

[145] L. Josephson, M. F. Kircher, U. Mahmood, Y. Tang, and R. Weissleder, "Near-infrared fluorescent nanoparticles as combined MR/optical imaging probes," *Bioconjug. Chem.*, vol. 13, no. 3, pp. 554–560, Jun. 2002.

[146] S. Earnshaw, "On the nature of the molecular forces which regulate the constitution of the luminiferous ether," *Trans. Camb. Philos. Soc.*, vol. 7, pp. 97–112, 1842.

[147] C. Alexiou, D. Diehl, P. Henninger, H. Iro, R. Rockelein, W. Schmidt, and H. Weber, "A High Field Gradient Magnet for Magnetic Drug Targeting," *Ieee Trans. Appl. Supercond.*, vol. 16, no. 2, pp. 1527–1530, Jun. 2006.

[148] J. Ally, B. Martin, M. B. Khamesee, W. Roa, and A. Amirfazli, "Magnetic targeting of aerosol particles for cancer therapy," vol. 293, pp. 442–449, 2005.

[149] K. Magnetics, "K&J Magnetics - Neodymium Magnet Specifications," *Neodymium Magnet Physical Properties*, 2011. [Online]. Available: http://www.kjmagnetics.com/specs.asp. [Accessed: 15-Nov-2011].

[150] M. Sagawa, S. Fujimura, N. Togawa, H. Yamamoto, and Y. Matsuura, "New material for permanent magnets on a base of Nd and Fe," *J. Appl. Phys.*, vol. 55, no. 6, pp. 2083–2087, 1984.

[151] F. Creighton, "Control of Magnetomotive Actuators for an Implanted Object in Brain and Phantom Materials," University of Virginia, 1991.

[152] D. C. Meeker, E. H. Maslen, R. C. Ritter, and F. M. Creighton, "Optimal Realization of Arbitrary Forces in a Magnetic Stereotaxis System," *Ieee Trans. Magn.*, vol. 32, no. 2, pp. 320 – 328, 1996.

[153] M. S. Grady, M. A. Howard 3rd, J. A. Molloy, R. C. Ritter, E. G. Quate, and G. T. Gillies, "Nonlinear magnetic stereotaxis: three-dimensional, in vivo remote magnetic manipulation of a small object in canine brain," *Med. Phys.*, vol. 17, no. 3, pp. 405–415, Jun. 1990.

[154] R. C. Ritter, *Open field system for magnetic surgery*. 2001.

[155] P. R. Werp, *Methods and apparatus for magnetically controlling motion direction of a mechanically pushed catheter*. 2002.

[156] T. Bauernfeind, F. Akca, B. Schwagten, N. de Groot, Y. Van Belle, S. Valk, B. Ujvari, L. Jordaens, and T. Szili-Torok, "The magnetic navigation system allows safety and high efficacy for ablation of arrhythmias," *Eur. Eur. Pacing Arrhythm. Card. Electrophysiol. J. Work. Groups Card. Pacing Arrhythm. Card. Cell. Electrophysiol. Eur. Soc. Cardiol.*, vol. 13, no. 7, pp. 1015–1021, Jul. 2011.

[157] G. Ciuti, P. Valdastri, A. Menciassi, and P. Dario, "Robotic magnetic steering and locomotion of capsule endoscope for diagnostic and surgical endoluminal procedures," *Robotica*, vol. 28, no. 02, p. 199, Oct. 2009.

[158] S. Tamaz, R. Gourdeau, A. Chanu, J.-B. Mathieu, and S. Martel, "Real-time MRI-based control of a ferromagnetic core for endovascular navigation," *IEEE Trans. Biomed. Eng.*, vol. 55, no. 7, pp. 1854–1863, 2008.

[159] S. Yim and M. Sitti, "Design and analysis of a magnetically actuated and compliant capsule endoscopic robot," 2011, pp. 4810–4815.

[160] X. Wang and M. Q.-H. Meng, "A fast algorithm for field computation in magnetic guidance," 2008, pp. 1608–1613.

[161] O. Ergeneman, Gö. Dogangil, M. P. Kummer, J. J. Abbott, M. K. Nazeeruddin, and B. J. Nelson, "A Magnetically Controlled Wireless Optical Oxygen Sensor for Intraocular Measurements," *Ieee Sensors J.*, vol. 8, no. 1, pp. 29–37, Jan. 2008.

[162] S. Jeon, G. Jang, H. Choi, and S. Park, "Magnetic Navigation System With Gradient and Uniform Saddle Coils for the Wireless Manipulation of Micro-Robots in Human Blood Vessels," *Ieee Trans. Magn.*, vol. 46, no. 6, pp. 1943–1946, Jun. 2010.

[163] S. Martel, J.-B. Mathieu, O. Felfoul, A. Chanu, E. Aboussouan, S. Tamaz, P. Pouponneau, L. Yahia, G. Beaudoin, G. Soulez, and M. Mankiewicz, "A computer-assisted protocol for endovascular target interventions using a clinical MRI system for controlling untethered microdevices and future nanorobots," *Comput. Aided Surg. Off. J. Int. Soc. Comput. Aided Surg.*, vol. 13, no. 6, pp. 340–352, Nov. 2008.

[164] P. Vartholomeos, C. Mavroidis, and N. Hata, "Magnetic targeting of aggregated nanoparticles for advanced lung therapies: A robotics approach," 2010, pp. 861–868.

[165] K. B. Yesin, K. Vollmers, and B. J. Nelson, "Analysis and design of wireless magnetically guided microrobots in body fluids," in *IEEE International Conference on Robotics and Automation, 2004.*, 2004, vol. 2, pp. 1333–1338.

[166] K. B. Yesin, K. Vollmers, and B. J. Nelson, "Modeling and Control of Untethered Biomicrorobots in a Fluidic Environment Using Electromagnetic Fields," *Int. J. Robot. Res.*, vol. 25, no. 5–6, pp. 527–536, May 2006.

[167] J.-B. Mathieu and S. Martel, "In vivo validation of a propulsion method for untethered medical microrobots using a clinical magnetic resonance imaging

system," in *IEEE/RSJ International Conference on Intelligent Robots and Systems, 2009. IROS 2009.*, San Diego, CA, 2007, pp. 502–508.

[168] I. Fleming, M. Balicki, J. Koo, I. Iordachita, B. Mitchell, J. Handa, G. Hager, and R. Taylor, "Cooperative robot assistant for retinal microsurgery," *Med. Image Comput. Comput.-Assist. Interv. Miccai Int. Conf. Med. Image Comput. Comput.-Assist. Interv.*, vol. 11, no. Pt 2, pp. 543–550, 2008.

[169] J. B. Mathieu, G. Beaudoin, and S. Martel, "Method of propulsion of a ferromagnetic core in the cardiovascular system through magnetic gradients generated by an MRI system," *Biomed. Eng. Ieee Trans.*, vol. 53, no. 2, pp. 292–299, 2006.

[170] S. Martel, J.-B. Mathieu, O. Felfoul, A. Chanu, E. Aboussouan, S. Tamaz, P. Pouponneau, Lh. Yahia, G. Beaudoin, G. Soulez, and M. Mankiewicz, "Automatic navigation of an untethered device in the artery of a living animal using a conventional clinical magnetic resonance imaging system," *Appl. Phys. Lett.*, vol. 90, no. 11, pp. 114105–114105–3, 2007.

[171] K. Belharet, D. Folio, and A. Ferreira, "MRI-based microrobotic system for the propulsion and navigation of ferromagnetic microcapsules," *Minim. Invasive Ther. Allied Technol. Mitat Off. J. Soc. Minim. Invasive Ther.*, vol. 19, no. 3, pp. 157–169, Jun. 2010.

[172] L. Arcese, M. Fruchard, and A. Ferreira, "Nonlinear modeling and robust controller-observer for a magnetic microrobot in a fluidic environment using MRI gradients," 2009, pp. 534–539.

[173] S. Martel, O. Felfoul, and M. Mohammadi, "Flagellated bacterial nanorobots for medical interventions in the human body," in *Biomedical Robotics and Biomechatronics, 2008. BioRob 2008. 2nd IEEE RAS & EMBS International Conference on. 2008*, Scottsdale, AZ, 2008, pp. 264–269.

[174] A. Luciani, C. Wilhelm, P. Bruneval, P. Cunin, G. Autret, A. Rahmouni, O. Clément, and F. Gazeau, "Magnetic targeting of iron-oxide-labeled fluorescent hepatoma cells to the liver," *Eur. Radiol.*, vol. 19, no. 5, pp. 1087–1096, May 2009.

[175] J. Riegler, J. A. Wells, P. G. Kyrtatos, A. N. Price, Q. A. Pankhurst, and M. F. Lythgoe, "Targeted magnetic delivery and tracking of cells using a magnetic resonance imaging system," *Biomaterials*, vol. 31, no. 20, pp. 5366–5371, 2010.

[176] M. Muthana, S. D. Scott, N. Farrow, F. Morrow, C. Murdoch, S. Grubb, N. Brown, J. Dobson, and C. E. Lewis, "A novel magnetic approach to enhance the efficacy of cell-based gene therapies," *Gene Ther.*, vol. 15, no. 12, pp. 902–910, Jun. 2008.

[177] P. Pouponneau, J.-C. Leroux, and S. Martel, "Magnetic nanoparticles encapsulated into biodegradable microparticles steered with an upgraded magnetic resonance imaging system for tumor chemoembolization," *Biomaterials*, vol. 30, no. 31, pp. 6327–6332, Oct. 2009.

[178] N. Olamaei, F. Cheriet, G. Beaudoin, and S. Martel, "MRI visualization of a single 15 μm navigable imaging agent and future microrobot," *Conf. Proc. Annu. Int. Conf. Ieee Eng. Med. Biol. Soc. Ieee Eng. Med. Biol. Soc. Conf.*, vol. 2010, pp. 4355–4358, 2010.

[179] S. Martel, "Microrobotic navigable entities for Magnetic Resonance Targeting," *Conf. Proc. Annu. Int. Conf. Ieee Eng. Med. Biol. Soc. Ieee Eng. Med. Biol. Soc. Conf.*, vol. 2010, pp. 1942–1945, 2010.

[180] M. P. Kummer, J. J. Abbott, B. E. Kratochvil, R. Borer, A. Sengul, and B. J. Nelson, "OctoMag: An Electromagnetic System for 5-DOF Wireless Micromanipulation," *Robot. Ieee Trans.*, vol. 26, no. 6, pp. 1006–1017, Dec. 2010.

[181] L. Arcese, A. Cherry, M. Fruchard, and A. Ferreira, "Dynamic behavior investigation for trajectory control of a microrobot in blood vessels," 2010, pp. 5774–5779.

[182] K. Belharet, D. Folio, and A. Ferreira, "Three-Dimensional Controlled Motion of a Microrobot using Magnetic Gradients," *Adv. Robot.*, vol. 25, no. 8, pp. 1069–1083, Jan. 2011.

[183] S. K. Pulfer, S. L. Ciccotto, and J. M. Gallo, "Distribution of small magnetic particles in brain tumor-bearing rats," *J. Neurooncol.*, vol. 41, no. 2, pp. 99–105, Jan. 1999.

[184] B. Chertok, A. E. David, and V. C. Yang, "Delivery of functional proteins to brain tumor using MRI-monitored, magnetically-targeted nanoparticles," *J. Controlled Release*, vol. 132, no. 3, pp. e61–e62, Dec. 2008.

[185] Z. G. Forbes, B. B. Yellen, K. A. Barbee, and G. Friedman, "An approach to targeted drug delivery based on uniform magnetic fields," *Ieee Trans. Magn.*, vol. 39, no. 5, pp. 3372–3377, 2003.

[186] B. B. Yellen, Z. G. Forbes, K. A. Barbee, and G. Friedman, "Model of an approach to targeted drug delivery based on uniform magnetic fields," in *Magnetics Conference, 2003. INTERMAG 2003. IEEE International*, 2003, p. EC– 06.

[187] B. B. Yellen, Z. G. Forbes, D. S. Halverson, G. Fridman, K. A. Barbee, M. Chorny, R. Levy, and G. Friedman, "Targeted drug delivery to magnetic implants for therapeutic applications," *J. Magn. Magn. Mater.*, vol. 293, no. 1, pp. 647–654, 2005.

[188] M. O. Avilés, A. D. Ebner, and J. A. Ritter, "Implant assisted-magnetic drug targeting: Comparison of in vitro experiments with theory," *J. Magn. Magn. Mater.*, 2008.

[189] G. H. Iacoba, O. Rotariub, N. J. Strachanband, and U. O. Hafelic, "Magnetizable needles and wires-modeling an efficient way to target magnetic microspheres in vivo," *Biorheology*, vol. 41, pp. 599–612, 2004.

[190] M. E. Hayden and U. O. Hafeli, "'Magnetic bandages' for targeted delivery of therapeutic agents," *J. Phys. Condens. Matter*, vol. 18, no. 38, pp. S2877–S2891, 2006.

[191] U. O. Hafeli, K. Gilmour, A. Zhou, S. Lee, and M. E. Hayden, "Modeling of magnetic bandages for drug targeting: Button vs. Halbach arrays," *J. Magn. Magn. Mater. Proc. Sixth Int. Conf. Sci. Clin. Appl. Magn. Carriers - Scamc-06*, vol. 311, no. 1, pp. 323–329, 2007.

[192] A. J. Rosengart, M. D. Kaminski, H. T. Chen, P. L. Caviness, A. D. Ebner, and J. A. Ritter, "Magnetizable implants and functionalized magnetic carriers: A novel approach for noninvasive yet targeted drug delivery," *J. Magn. Magn. Mater.*, vol. 293, no. 1, pp. 633–638, 2005.

[193] P. J. Cregg, K. Murphy, and A. Mardinoglu, "Calculation of nanoparticle capture efficiency in magnetic drug targeting," *J. Magn. Magn. Mater.*, vol. 320, no. 23, pp. 3272–3275, 2008.

[194] R. E. Rosensweig, *Ferrohydrodynamics*. Mineola, NY: Dover Publications, Inc., 1985.

[195] A. Senyei, K. Widder, and G. Czerlinski, "Magnetic Guidance of Drug-Carrying Microspheres," *J. Appl. Phys.*, vol. 49, no. 6, pp. 3578–3583, 1978.

[196] F. P. Incropera, *Fundamentals of Heat and Mass Transfer*. Hoboken, NJ: John Wiley, 2007.

[197] E. M. Renkin, "Filtration, diffusion, and molecular sieving through porous cellulose membranes," *J. Gen. Physiol.*, vol. 38, no. 2, pp. 225–243, 1954.

[198] F. E. Curry and C. C. Michel, "A fiber matrix model of capillary permeability," *Microvasc. Res.*, vol. 20, no. 1, pp. 96–99, Jul. 1980.

[199] R. E. Beck and J. S. Schultz, "Hindered Diffusion in Microporous Membranes with Known Pore Geometry," *Science*, vol. 170, no. 3964, pp. 1302–1305, Dec. 1970.

[200] E. Wisse, F. Jacobs, B. Topal, P. Frederik, and B. De Geest, "The size of endothelial fenestrae in human liver sinusoids: implications for hepatocyte-directed gene transfer," *Gene Ther.*, vol. 15, no. 17, pp. 1193–1199, Apr. 2008.

[201] W. M. Deen, "Hindered transport of large molecules in liquid-filled pores," *Aiche J.*, vol. 33, no. 9, pp. 1409–1425, Sep. 1987.

[202] A. G. Ogston, B. N. Preston, and J. D. Wells, "On the transport of compact particles through solutions of chain-polymers," *Proc. R. Soc. Lond. Math. Phys. Sci.*, vol. 333, no. 1594, p. 297, 1973.

[203] K. E. Kadler, D. F. Holmes, J. A. Trotter, and J. A. Chapman, "Collagen fibril formation," *Biochem. J.*, vol. 316 (Pt 1), pp. 1–11, May 1996.

[204] J. A. Chapman, "The regulation of size and form in the assembly of collagen fibrils in vivo," *Biopolymers*, vol. 28, no. 8, pp. 1367–1382, Aug. 1989.

[205] J. W. Ryoo and R. J. Buschmann, "Comparison of intralobar non-parenchyma, subcapsular non-parenchyma, and liver capsule thickness," *J. Clin. Pathol.*, vol. 42, no. 7, pp. 740–744, Jul. 1989.

[206] O. Ohtani, "Three-dimensional organization of the collagen fibrillar framework of the human and rat livers.," *Arch. Histol. Cytol.*, vol. 51, no. 5, pp. 473–488, 1988.

[207] L. J. Nugent and R. K. Jain, "Extravascular diffusion in normal and neoplastic tissues," *Cancer Res.*, vol. 44, no. 1, pp. 238–244, 1984.

[208] E. M. Renkin and F. E. Curry, "Transport of water and solutes across capillary endothelium," *Membr. Transp. Biol.*, vol. 4, pp. 1–45, 1979.

[209] A. J. Lemke, M. I. S. von Pilsach, A. Lubbe, C. Bergemann, H. Riess, and R. Felix, "MRI after magnetic drug targeting in patients with advanced solid malignant tumors," *Eur. Radiol.*, vol. 14, no. 11, pp. 1949–1955, 2004.

[210] D. A. Fleisch, *A Student's Guide to Maxwell's Equations*. Cambridge, UK; New York: Cambridge University Press, 2008.

[211] D. Fukumura and R. K. Jain, "Tumor microenvironment abnormalities: Causes, consequences, and strategies to normalize," *J. Cell. Biochem.*, vol. 101, no. 4, pp. 937–949, 2007.

[212] A. Nacev, C. Beni, O. Bruno, and B. Shapiro, "The Behaviors of Ferro-Magnetic Nano-Particles In and Around Blood Vessels under Applied Magnetic Fields," *J. Magn. Magn. Mater.*, vol. 323, no. 6, pp. 651–668, 2011.

[213] A. Nacev, C. Beni, O. Bruno, and B. Shapiro, "Magnetic Nanoparticle Transport within Flowing Blood and Into Surrounding Tissue," *Nanomed.*, vol. 5, no. 9, pp. 1459–66, 2010.

[214] R. Jurgons, C. Seliger, A. Hilpert, L. Trahms, S. Odenbach, and C. Alexiou, "Drug loaded magnetic nanoparticles for cancer therapy," *J. Phys.-Condens. Matter*, vol. 18, no. 38, pp. S2893–S2902, 2006.

[215] A. Sarwar, R. Lee, D. Depireux, and B. Shapiro, "Magnetic Injection of Nanoparticles at a Human Head Working Distance into Rat Inner Ears," *J. Magn. Magn. Mater.*, vol. accepted, Sep. 2012.

[216] Y. Okuhata, "Delivery of diagnostic agents for magnetic resonance imaging," *Adv. Drug Deliv. Rev.*, vol. 37, no. 1–3, pp. 121–137, 1999.

[217] P. Decuzzi, R. Pasqualini, W. Arap, and M. Ferrari, "Intravascular Delivery of Particulate Systems: Does Geometry Really Matter?," *Pharm. Res.*, vol. 26, no. 1, pp. 235–243, 2009.

[218] B. Shapiro, R. Probst, H. E. Potts, D. A. Diver, and A. Lubbe, "Control to concentrate drug-coated magnetic particles to deep-tissue tumors for targeted cancer chemotherapy," in *46th IEEE Conference on Decision and Control*, New Orleans, LA, 2007, pp. 3901–3906.

[219] C. I. Mikkelsen, "Magnetic separation and hydrodynamic interactions in microfluidic systems," Technical University of Denmark, 2005.

[220] A. Lubbe and C. Bergemann, 2005.

[221] C. Simon, "Magnetic drug targeting. New paths for the local concentration of drugs for head and neck cancer," *HNO*, vol. 53, no. 7, pp. 600–601, 2005.

[222] P. O. Vaccaro, K. Kubota, and T. Aida, "Strain-driven self-positioning of micromachined structures," *Appl Phys Lett*, vol. 78, no. 19, pp. 2852–4, 2001.

[223] R. Engel-Herbert and T. Hesjedal, "Calculation of the magnetic stray field of a uniaxial magnetic domain," *J. Appl. Phys.*, vol. 97, no. 7, pp. 74504–74505, 2005.

[224] P. C. Hiemenz, *Principles of colloid and surface chemistry*, 3rd ed., rev. and expanded. New York: Marcel Dekker, 1997.

[225] R. D. Braun, A. Abbas, S. O. OBukhart, and W. Willson-III, "Hemodynamic Parameters in Blood Vessels in Choroidal Melanoma Xenografts and Rat Choroid," *Invest. Ophthalmol. Vis. Sci.*, vol. 43, pp. 3045–3052, 2002.

[226] A. J. Fisher, N. W. Schrader, and B. Klitzman, "Effects of chronic hypoxia on capillary flow and hematocrit in rat skeletal muscle," *Am. J. Physiol.- Heart Circ. Physiol.*, vol. 262, no. 6, pp. 1877–1883, 1992.

[227] J. W. Roy and H. N. Mayrovitz, "Microvascular blood flow in the normotensive and spontaneously hypertensive rat," *Hypertens. J. Am. Heart Assoc.*, vol. 4, pp. 264–271, 1982.

[228] R. Ganguly, A. P. Gaind, S. Sen, and I. K. Puri, "Analyzing ferrofluid transport for magnetic drug targeting," *J. Magn. Magn. Mater.*, vol. 289, pp. 331–334, 2005.

[229] J. P. Woodcock, "Physical properties of blood and their influence on blood-flow measurement.," *Reports Prog. Phys.*, vol. 39, pp. 65–127, 1976.

[230] W. W. Nichols and M. F. O'Rourke, *McDonald's Blood Flow in Arteries: Theoretical, Experimental and Clinical Principles*. London, UK: Hodder Arnold, 2005.

[231] J. Douglas, "Alternating direction methods for three space variables," *Numer. Math.*, vol. 4, no. 1, pp. 41–63, 1962.

[232] J. Douglas and C. M. Pearcy, "On convergence of alternating direction procedures in the presence of singular operators," *Numer. Math.*, vol. 5, no. 1, pp. 175–184, 1963.

[233] J. Douglas and J. E. Gunn, "A general formulation of alternating direction methods," *Numer. Math.*, vol. 6, no. 1, pp. 428–453, Dec. 1964.

[234] D. W. Peaceman and H. H. Rachford Jr, "The numerical solution of parabolic and elliptic differential equations," *J. Soc. Ind. Appl. Math.*, pp. 28–41, 1955.

[235] X. L. Li, K. L. Yao, and Z. L. Liu, "CFD study on the magnetic fluid delivering in the vessel in high-gradient magnetic field," *J. Magn. Magn. Mater.*, vol. 320, no. 11, pp. 1753–1758, 2008.

[236] F. Yuan, M. Dellian, D. Fukumura, M. Leunig, D. A. Berk, V. P. Torchilin, and R. K. Jain, "Vascular Permeability in a Human Tumor Xenograft: Molecular Size Dependence and Cutoff Size," *Cancer Res.*, vol. 55, pp. 3752–3756, 1995.

[237] *Molecular biology of the cell*, 5th ed. New York: Garland Science, 2008.

[238] N. Willmott and J. M. Daly, Eds., *Microspheres and regional cancer therapy*. Boca Raton, Florida: CRC Press, 1994.

[239] B. Shapiro, "Towards dynamic control of magnetic fields to focus magnetic carriers to targets deep inside the body," *J. Magn. Magn. Mater.*, vol. 321, no. 10, p. 1594, May 2009.

[240] A. Nacev, R. Probst, S. Kim, A. Komaee, A. Sarwar, R. Lee, D. Depireux, M. Emmert-Buck, and B. Shapiro, "Towards Control of Magnetic Fluids in Patients: Directing Therapeutic Nanoparticles to Disease Locations," *Ieee Control Syst. Mag.*, vol. 32, no. 3, pp. 32–74, Jun. 2012.

[241] B. Shapiro, R. Probst, H. E. Potts, D. A. Diver, and A. S. Lubbe, *Dynamic Control of Magnetic Fields to Focus Drug-Coated Nano-Particles to Deep Tissue Tumors*. 2008.

[242] P. R. Bergethon, *The physical basis of biochemistry: the foundations of molecular biophysics*. New York: Springer, 1998.

[243] L. S. Lerner, *Physics for scientists and engineers*. Jones and Bartlett, 1997.

[244] R. P. Feynman, R. B. Leighton, and M. Sands, *The Feynman Lectures on Physics*. Addison-Wesley Publishing Company, 1964.

[245] D. R. Lide, *Handbook of Chemistry and Physics*, 82nd ed. New York: CRC Press LLC, 2001.

[246] J. F. Schenck, "The role of magnetic susceptibility in magnetic resonance imaging," *Med. Phys.*, vol. 23, no. 6, pp. 815–850, 1996.

[247] A. Vignaud, X. Maître, G. Guillot, E. Durand, L. de Rochefort, P. Robert, V. Vivès, R. Santus, and L. Darrasse, "Magnetic susceptibility matching at the air-tissue interface in rat lung by using a superparamagnetic intravascular contrast agent: Influence on transverse relaxation time of hyperpolarized helium-3," *Magn. Reson. Med.*, vol. 54, no. 1, pp. 28–33, 2005.

[248] R. L. Panton, *Incompressible Flow*, 2nd ed. New York, NY: John Wiley & Sons, Inc., 1996.

[249] J. L. Sutterby, "Falling sphere viscometry. I. Wall and inertial corrections to Stokes' law in long tubes," *J. Rheol.*, vol. 17, p. 559, 1973.

[250] V. S. Mendelev and A. O. Ivanov, "Ferrofluid aggregation in chains under the influence of a magnetic field," *Phys. Rev. E*, vol. 70, no. 5, p. 51502, 2004.

[251] M. Wu, Y. Xiong, Y. Jia, H. Niu, H. Qi, J. Ye, and Q. Chen, "Magnetic field-assisted hydrothermal growth of chain-like nanostructure of magnetite," *Chem. Phys. Lett.*, vol. 401, no. 4–6, pp. 374–379, 2005.

[252] A. Y. Zubarev, S. Odenbach, and J. Fleischer, "Rheological properties of dense ferrofluids. Effect of chain-like aggregates," *J. Magn. Magn. Mater.*, vol. 252, pp. 241–243, 2002.

[253] G. Karp, *Cell and molecular biology: concepts and experiments*, 2nd ed. New York: J. Wiley, 2008.

[254] J. D. Anderson, *Fundamentals of aerodynamics*, 4th ed. Boston: McGraw-Hill Higher Education, 2007.

[255] N. P. Smith, A. J. Pullan, and P. J. Hunter, "An anatomically based model of transient coronary blood flow in the heart," *Siam J. Appl. Math.*, pp. 990–1018, 2001.

[256] I. Hilger, R. Hergt, and W. A. Kaiser, "Use of magnetic nanoparticle heating in the treatment of breast cancer," in *Nanobiotechnology, IEE Proceedings*, 2005, vol. 152, pp. 33–39.

[257] C. S. Lee, H. Lee, and R. M. Westervelt, "Microelectromagnets for the control of magnetic nanoparticles," *Appl. Phys. Lett.*, vol. 79, no. 20, pp. 3308–3310, 2001.

[258] K. M. Kirk and H. Merte, "A mixed natural/forced convection nucleate boiling heat transfer criteria," 1994, vol. 135, p. 479.

[259] O. P. Bruno and M. Lyon, "High-order unconditionally stable FC-AD solvers for general smooth domains I: Basic elements," *J. Comput. Phys.*, vol. 229, no. 6, pp. 2009–2033, 2010.

[260] C. E. Beni, O. P. Bruno, A. N. Nacev, and B. Shapiro, "A fast high-order algorithm enabling efficient solution of a drug-delivery problem," vol. under-preparation, 2011.

[261] A. B. Comsol, "COMSOL multiphysics user's guide," *Comsol Ab Burlingt. Ma Usa*, 2005.

[262] K. Spitz and J. Moreno, *A practical guide to groundwater and solute transport modeling*. New York: John Wiley, 1996.

[263] D. M. Young, "Iterative Solution of Large Linear Systems," *Dover*, 2003.

[264] O. P. Bruno, Y. Han, and M. M. Pohlman, "Accurate, high-order representation of complex three-dimensional surfaces via {F}ourier continuation analysis," *J. Comput. Phys.*, vol. 227, no. 2, pp. 1094–1125, 2007.

[265] R. M. Berne and M. N. Levy, *Cardiovascular Physiology*. St. Louis, MO: Mosby, 1967.

[266] K. J. Widder, A. E. Senyei, and D. F. Ranney, "Magnetically responsive microspheres and other carriers for the biophysical targeting of antitumor agents," *Adv. Pharmacol. Chemother.*, vol. 16, p. 213, 1979.

[267] K. D. Caldwell, G. Karaiskakis, M. N. Myers, and J. Calvin Giddings, "Characterization of Albumin Microspheres by Sedimentation Field-Flow Fractionation," *J. Pharm. Sci.*, vol. 70, no. 12, 1981.

[268] A. Lubbe, 2008.

[269] D. W. Holdsworth, C. J. D. Norley, R. Frayne, D. A. Steinman, and B. K. Rutt, "Characterization of common carotid artery blood-flow waveforms in normal human subjects," *Physiol. Meas.*, vol. 20, pp. 219–240, 1999.

[270] A. Kirpalani, H. Park, J. Butany, K. W. Johnston, and M. Ojha, "Velocity and wall shear stress patterns in the human right coronary artery," *J. Biomech. Eng.*, vol. 121, p. 370, 1999.

[271] D. N. Ku, "Blood flow in arteries," *Annu. Rev. Fluid Mech.*, vol. 29, no. 1, pp. 399–434, 1997.

[272] J. G. Myers, J. A. Moore, M. Ojha, K. W. Johnston, and C. R. Ethier, "Factors influencing blood flow patterns in the human right coronary artery," *Ann. Biomed. Eng.*, vol. 29, no. 2, pp. 109–120, 2001.

[273] R. Ganguly, B. Zellmer, and I. K. Puri, "Field-induced self-assembled ferrofluid aggregation in pulsatile flow," *Phys. Fluids*, vol. 17, pp. 097104(1–8), 2005.

[274] A. Nacev, S. H. Kim, J. Rodriguez-Canales, M. A. Tangrea, B. Shapiro, and M. R. Emmert-Buck, "A dynamic magnetic shift method to increase nanoparticle concentration in cancer metastases: a feasibility study using simulations on autopsy specimens," *Int. J. Nanomedicine*, vol. 6, no. 1, pp. 2907–2923, Jul. 2011.

[275] R. K. Jain, "Molecular regulation of vessel maturation," *Nat. Med.*, vol. 9, no. 6, pp. 685–693, 2003.

[276] D. Burke, P. Carnochan, C. Glover, and T. G. Allen-Mersh, "Correlation between tumour blood flow and fluorouracil distribution in a hypovascular liver metastasis model," *Clin. Exp. Metastasis*, vol. 18, no. 7, pp. 617–22, 2000.

[277] L. H. Gray, A. D. Conger, M. Ebert, S. Hornsey, and O. C. Scott, "The concentration of oxygen dissolved in tissues at the time of irradiation as a factor in radiotherapy," *Br. J. Radiol.*, vol. 26, no. 312, pp. 638–48, 1953.

[278] R. K. Jain, "Determinants of tumor blood flow: A review," *Cancer Res.*, vol. 48, no. 10, pp. 2641–58, 1988.

[279] R. K. Jain, "Normalization of Tumor Vasculature: An Emerging Concept in Antiangiogenic Therapy," *Science*, vol. 307, no. 5706, pp. 58–62, 2005.

[280] G. M. Tozer, C. Kanthou, and B. C. Baguley, "Disrupting tumour blood vessels," *Nat. Rev. Cancer*, vol. 5, no. 6, pp. 423–35, 2005.

[281] H. Iinuma, K. Maruyama, K. Okinaga, K. Sasaki, T. Sekine, O. Ishida, N. Ogiwara, K. Johkura, and Y. Yonemura, "Intracellular targeting therapy of cisplatin-encapsulated transferrin-polyethylene glycol liposome on peritoneal dissemination of gastric cancer," *Int J Cancer*, vol. 99, no. 1, pp. 130–7, 2002.

[282] L. Brannon-Peppas and J. O. Blanchette, "Nanoparticle and targeted systems for cancer therapy," *Adv Drug Deliv Rev*, vol. 56, no. 11, pp. 1649–59, 2004.

[283] F. X. Gu, R. Karnik, A. Z. Wang, F. Alexis, E. Levy-Nissenbaum, S. Hong, R. S. Langer, and O. C. Farokhzad, "Targeted nanoparticles for cancer therapy," *Nano Today*, vol. 2, no. 3, pp. 14–21, 2007.

[284] D. Peer, J. M. Karp, S. Hong, O. C. Farokhzad, R. Margalit, and R. Langer, "Nanocarriers as an emerging platform for cancer therapy," *Nat Nanotechnol*, vol. 2, no. 12, pp. 751–60, 2007.

[285] P. M. Winter, S. D. Caruthers, A. Kassner, T. D. Harris, L. K. Chinen, J. S. Allen, E. K. Lacy, H. Zhang, J. D. Robertson, S. A. Wickline, and G. M. Lanza, "Molecular imaging of angiogenesis in nascent Vx-2 rabbit tumors using a novel alpha(nu)beta3-targeted nanoparticle and 1.5 tesla magnetic resonance imaging," *Cancer Res*, vol. 63, no. 18, pp. 5838–43, 2003.

[286] N. K. Devaraj, E. J. Keliher, G. M. Thurber, M. Nahrendorf, and R. Weissleder, "18F labeled nanoparticles for in vivo PET-CT imaging," *Bioconjug. Chem.*, vol. 20, no. 2, pp. 397–401, 2009.

[287] P. Decuzzi, B. Godin, T. Tanaka, S. Y. Lee, C. Chiappini, X. Liu, and M. Ferrari, "Size and shape effects in the biodistribution of intravascularly injected particles," *J. Controlled Release*, vol. 141, no. 3, pp. 320–327, 2010.

[288] O. Feron, "Tumor-Penetrating Peptides: A Shift from Magic Bullets to Magic Guns," *Sci. Transl. Med.*, vol. 2, no. 34, p. –, 2010.

[289] G. J. Kim and S. Nie, "Targeted cancer nanotherapy," *Mater. Today*, vol. 8, no. 8, pp. 28–33, 2005.

[290] G. Orive, R. M. Hernández, A. R. Gascón, and J. L. Pedraz, "Micro and nano drug delivery systems in cancer therapy," *Cancer Ther.*, vol. 3, pp. 131–138, 2005.

[291] J. H. Park, G. von Maltzahn, M. J. Xu, V. Fogal, V. R. Kotamraju, E. Ruoslahti, S. N. Bhatia, and M. J. Sailor, "Cooperative nanomaterial system to sensitize, target, and treat tumors," *Proc. Natl. Acad. Sci. U. S. A.*, vol. 107, no. 3, pp. 981–986, 2010.

[292] K. N. Sugahara, T. Teesalu, P. P. Karmali, V. R. Kotamraju, L. Agemy, O. M. Girard, D. Hanahan, R. F. Mattrey, and E. Ruoslahti, "Tissue-Penetrating Delivery of Compounds and Nanoparticles into Tumors," *Cancer Cell*, vol. 16, no. 6, pp. 510–520, 2009.

[293] T. Tanaka, P. Decuzzi, M. Cristofanilli, J. H. Sakamoto, E. Tasciotti, F. M. Robertson, and M. Ferrari, "Nanotechnology for breast cancer therapy," *Biomed. Microdevices*, vol. 11, no. 1, pp. 49–63, 2009.

[294] M. L. Flenniken, D. A. Willits, A. L. Harmsen, L. O. Liepold, A. G. Harmsen, M. J. Young, and T. Douglas, "Melanoma and Lymphocyte Cell-Specific Targeting Incorporated into a Heat Shock Protein Cage Architecture," *Chem. Biol.*, vol. 13, no. 2, pp. 161–170, Feb. 2006.

[295] E. V. Batrakova, T. Y. Dorodnych, E. Y. Klinskii, E. N. Kliushnenkova, O. B. Shemchukova, O. N. Goncharova, S. A. Arjakov, V. Y. Alakhov, and A. V. Kabanov, "Anthracycline antibiotics non-covalently incorporated into the block copolymer micelles: in vivo evaluation of anti-cancer activity," *Br. J. Cancer*, vol. 74, no. 10, pp. 1545–1552, Nov. 1996.

[296] W. J. Gradishar, S. Tjulandin, N. Davidson, H. Shaw, N. Desai, P. Bhar, M. Hawkins, and J. O'Shaughnessy, "Phase III trial of nanoparticle albumin-bound paclitaxel compared with polyethylated castor oil-based paclitaxel in women with

breast cancer," *J. Clin. Oncol. Off. J. Am. Soc. Clin. Oncol.*, vol. 23, no. 31, pp. 7794–7803, Nov. 2005.

[297] W. Wu, S. Wieckowski, G. Pastorin, M. Benincasa, C. Klumpp, J.-P. Briand, R. Gennaro, M. Prato, and A. Bianco, "Targeted Delivery of Amphotericin B to Cells by Using Functionalized Carbon Nanotubes," *Angew. Chem. Int. Ed.*, vol. 44, no. 39, pp. 6358–6362, Oct. 2005.

[298] P. A. Voltairas, D. I. Fotiadis, and L. K. Michalis, "Hydrodynamics of magnetic drug targeting," *J. Biomech.*, vol. 35, no. 6, pp. 813–821, 2002.

[299] O. Pagani, E. Senkus, W. Wood, M. Colleoni, T. Cufer, S. Kyriakides, A. Costa, E. P. Winer, and F. Cardoso, "International Guidelines for Management of Metastatic Breast Cancer: Can Metastatic Breast Cancer Be Cured?," *Jnci J. Natl. Cancer Inst.*, 2010.

[300] H. Kennecke, R. Yerushalmi, R. Woods, M. C. U. Cheang, D. Voduc, C. H. Speers, T. O. Nielsen, and K. Gelmon, "Metastatic Behavior of Breast Cancer Subtypes," *J. Clin. Oncol.*, vol. 28, no. 20, pp. 3271–3277, 2010.

[301] N. Terayama, T. Terada, and Y. Nakanuma, "An immunohistochemical study of tumour vessels in metastatic liver cancers and the surrounding liver tissue," *Histopathology*, vol. 29, no. 1, pp. 37–43, 1996.

[302] N. Terayama, T. Terada, and Y. Nakanuma, "Histologic growth patterns of metastatic carcinomas of the liver," *Jpn. J. Clin. Oncol.*, vol. 26, no. 1, pp. 24–29, 1996.

[303] V. P. Torchilin, *Nanoparticulates as drug carriers*. London; Hackensack: Imperial College Press ; Distributed by World Scientific Pub., 2006.

[304] A. Sarwar, A. Nemirovski, and B. Shapiro, "Optimal Halbach Permanent Magnet Designs for Maximally Pulling and Pushing Nanoparticles," *J. Magn. Magn. Mater.*, vol. 324, no. 5, pp. 742–754, Mar. 2012.

[305] I. Alagkiozidis, A. Facciabene, M. Tsiatas, C. Carpenito, F. Benencia, S. Adams, Z. Jonak, C. H. June, D. J. Powell, and G. Coukos, "Time-dependent cytotoxic drugs selectively cooperate with IL-18 for cancer chemo-immunotherapy," *J. Transl. Med.*, vol. 9, no. 1, p. 77, 2011.

[306] R. J. Lopez, *Maple via calculus: a tutorial approach*. Boston: Birkhäuser, 1994.

[307] T. Hastie, R. Tibshirani, and J. H. Friedman, *The elements of statistical learning data mining, inference, and prediction*. New York: Springer, 2009.

[308] C. C. Berry and A. S. G. Curtis, "Functionalisation of magnetic nanoparticles for applications in biomedicine," *J. Phys. Appl. Phys.*, vol. 36, no. 13, pp. R198–R206, Jul. 2003.

[309] A. K. Gupta, R. R. Naregalkar, V. D. Vaidya, and M. Gupta, "Recent advances on surface engineering of magnetic iron oxide nanoparticles and their biomedical applications," *Nanomed.*, vol. 2, no. 1, pp. 23–39, Feb. 2007.

[310] H. Chen, A. D. Ebner, M. D. Kaminski, A. J. Rosengart, and J. A. Ritter, "Analysis of magnetic drug carrier particle capture by a magnetizable intravascular stent–2: Parametric study with multi-wire two-dimensional model," *J. Magn. Magn. Mater.*, vol. 293, no. 1, pp. 616–632, 2005.

[311] M. G. Allen, M. Scheidl, and R. L. Smith, "Design and fabrication of movable silicon plates suspended by flexible supports," in *MicroElectroMechanical Systems Workshop*, Salt Lake City, USA, 1989, p. 76.

[312] C. Seliger, R. Jurgons, F. Wiekhorst, D. Eberbeck, L. Trahms, H. Iro, and C. Alexiou, "In vitro investigation of the behaviour of magnetic particles by a circulating artery model," *J. Magn. Magn. Mater.*, vol. 311, no. 1, pp. 358–362, Apr. 2007.